eman ta zabal zazu

Universidad del País Vasco
Euskal Herriko Unibertsitatea

Departamento de Fisica de Materiales - Materialen Fisika Saila

PhD Thesis

Electrospinning of Biomolecules

Wiwat Nuansing

Supervisor

Alexander M. Bittner

June, 2014

This PhD thesis has been performed at:

CIC nanoGUNE Consolider
Self-assembly group
Donostia-San Sebastián, SPAIN

Abstract

Electrospinning is a simple and versatile technique used for the fabrication of continuous micro and nanofibers, mainly from polymer solutions and polymer melts. The process is based on applying a high voltage (kV range) to a liquid, which forms a jet that can be collected in dry form on a grounded substrate. Nonpolymeric molecules (monomers) can usually not be electrospun, they have to be mixed with polymers to achieve sufficiently high viscosity and intermolecular entanglement in solution. However, many peptides and proteins can self-assemble in 3D (bulk crystals), in 2D (for example membrane proteins), and in 1D (natural fibrils) by intermolecular interactions, e.g. Van der Waals, electrostatic interactions, hydrogen bonds, and π-stacking interactions.

This study demonstrates that the electrospinning of biomolecules (polymers and also molecules/ monomers) is possible in pure form. For this, they have to show self-assembly in 1D, 2D, or 3D; they have to be dissolved in a suitable organic solvent at high concentration; and the electrospinning parameters have to be optimized. Based on these conditions, short aromatic peptides and globular proteins can be spun into continuous fibers. Furthermore, techniques such as microliter electrospinning from a single droplet can produce protein nanofibers equally well. For some proteins, the fibers contain short stretches with diameters down to 5 nm, close to the size of a single large protein molecule. With the same setup, DNA molecules bundle into nanoscale fibers of centimeter length. Some stretches of these fibers coil into intriguing pot-like hollow structures, based on rope coiling from the highly viscous jet.

The chemical and physical properties of the biomolecular fibers were studied. Raman and infrared spectroscopy of the aromatic peptides (molecules and fibers) provide information on molecular vibrations, and are compared to simulation results obtained on free single molecules in vacuum. This comparison shows substantial differences between assembled and free molecules for the O-H and N-H stretching and bending vibrations, caused by extensive hydrogen bonding in the solid. However, the aromatic residues also provide possibilities for intermolecular π-stacking. This additional interaction is supposed to support assembly to fibers, while electrospinning assists the molecular alignment. Nanoscale analysis of the ultrasmall protein fibers was based on SEM, AFM, and infrared near-field microscopy. The amide bands, observed in nano-, micro- and macroscale infrared and Raman spectra, combined with (macroscale) circular dichroism spectroscopy, allow to assign secondary structures, and to address the question of protein denaturation.

Resumen

El electrohilado *(electrospinning)* es una técnica sencilla y muy versátil que se utiliza para la fabricación continua de micro y nanofibras, principalmente a partir de polímeros y polímeros fundidos. El fundamento de esta técnica está basado en la aplicación de un alto voltaje (kV) a una solución líquida, la cuál forma un chorro que es recogido en forma seca en un sustrato o colector que está conectado a tierra. Las moléculas no poliméricas (monómeros) en general no pueden ser electrohiladas, por lo que tienen que ser mezcladas con algún polímero para conseguir una viscosidad suficientemente alta y un entrelazado intermolecular en la solución. Sin embargo, muchos péptidos y proteínas pueden auto-ensamblarse en 3D (cristales), en 2D (proteínas de membrana) y en 1D (fibrillas naturales) por interacciones intermoleculares, como por ejemplo, fuerzas de Van der Waals, interacciones electrostáticas, enlaces de hidrógeno, e interacciones por apilamiento-π.

En este estudio se demuestra el electrohilado de biomoléculas (polímeros y también moléculas/ monómeros) es posible en su forma pura. Para ello, estas biomoléculas tienen que mostrar autoensamblaje en 1D, 2D o 3D; tienen que ser disueltas en un disolvente orgánico adecuado a elevada concentración y los parámetros del proceso tienen que ser optimizados. Se han desarrollado cuatro conFig.ciones para la técnica de electrohilado (ver esquemas en Fig. 1). La conFig.ción convencional (Fig. 1a) es adecuada para el estudio del electrohilado de péptidos y proteínas, cuando se dispone de soluciones concentradas de al menos 0,1 ml, sin embargo, algunas sustancias se encuentran disponibles sólo en pequeñas cantidades, y en general el ensayo de nuevos procesos bajo diferentes parámetros es más simple y rápido a partir de pequeñas cantidades. Esto último requiere la conFig.ción del microelectrohilado (microliter electrospinning) (Fig. 1b), el cuál funciona con algunos l de solución. Las conFig.ciones tercera (Fig. 1c) y cuarta (Fig. 1d) se han desarrollado específicamente para reducir el diámetro de las fibras de proteínas por debajo de 10 nm.

Resultados: Los resultados experimentales explicados en ambos capítulos 4 y 5 (ver el resumen en la Fig. 2) apoyan la hipótesis de este trabajo: el electrohilado de biomoléculas puras, sin ser mezcladas con polímeros, es posible cuando muestran autoensamblaje en 1D, 2D o 3D; cuando se pueden disolver en un disolvente orgánico adecuado a alta concentración; y cuando se optimizan los parámetros del proceso (voltaje, distancia, velocidad de flujo, humedad del aire). En los péptidos aromáticos, las interacciones intermoleculares (principalmente los enlaces de hidrógeno y las interacciones de apilamiento π-π) determinan el autoensamblaje. La fuerza electrostática ejercida por el proceso de electrohilado ayuda al ensamblado de péptidos para organizarse en forma

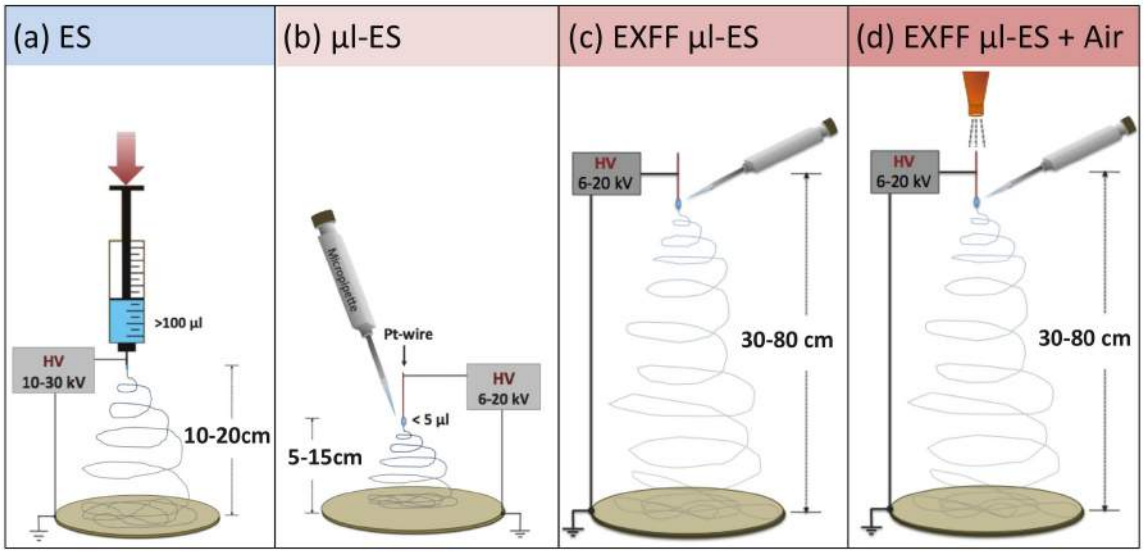

Figure 1: Esquema de las conFig.ciones de la técnica de electrohilado desarrolladas en este trabajo. (a) Electrohilado convencional, (b) microelectrohilado, (c) microelectrohilado a gran distancia, (d) microelectrohilado a gran distancia con una corriente de aire.

de largas fibras. El electrohilado de las proteínas globulares puras es posible; sin embargo, están normalmente desnaturalizadas: sus estructuras secundarias (hélices alfa, hojas beta, etc.) han cambiado previamente en solución con el disolvente orgánico. El electrohilado en sí parece ser mucho menos perjudicial.

Los mecanismos propuestos: Se propone que las interacciones no covalentes (fuerzas electrostáticas, enlaces de hidrógeno, o fuerzas de Van der Waals) desempeñan un papel vital en la estabilización de la formación de fibras y este papel es similar al autoensamblaje en solución de los péptidos aromáticos. La Fig. 3b presenta esquemáticamente el mecanismo propuesto en comparación con el electrohilado de polímeros (Fig. 3a): Inicialmente, los residuos aromáticos presentes en el péptido causan apilamiento- de las moléculas, lo que resulta en una pequeña agregación. Entonces, el electrohilado da lugar a la formación de fibras. La Fig. 3c muestra el mecanismo de una solución de GFG que se autoensambla en fibras antes del electrohilado. En el caso de sustancias derivadas del flúor, como 9FM y Fmoc-NH_2, el chorro de la solución se rompe en gotitas, que más tarde solidifican por evaporación del disolvente (Fig. 3d). Esto es posible ya que las interacciones moleculares no son lo suficientemente fuertes para estabilizar la estructura de fibras.

Predicciones: Los parámetros de la técnica de electrohilado son muy difíciles de predecir, por lo que suelen estar totalmente basados en pruebas empíricas. Más difícil aún de predecir es la capacidad de electrohilado - probablemente todas las sustancias se pueden hilar, dependiendo de los parámetros que aún no han sido evaluados. Para los péptidos, el hilado podría predecirse con tres métodos; método 1) basado en el aceptor de electrones (AN) y en el número de donantes (DN) del disolvente; método 2) utilizando espectros Raman polarizados del péptido, que son gen-

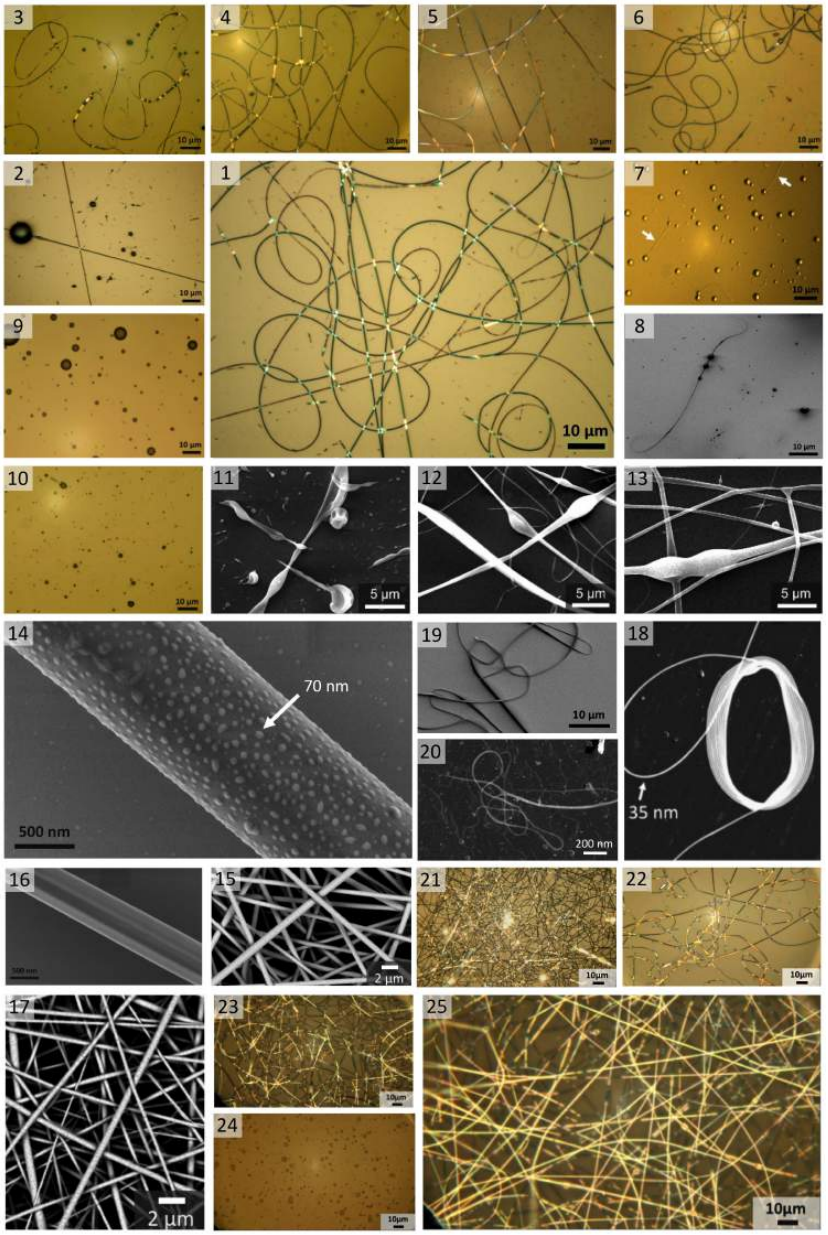

Figure 2: Resumen de resultados de diferentes sustancias electrohiladas: Micrografías ópticas (color) y electrónicas (blanco/negro).
(1) FF,
(2) Fmoc-FG,
(3-4) GF,
(5) GFG,
(6) $(Fmoc\text{-}C)_2$,
(7-8) Fmoc-G,
(9) 9FM,
(10) $Fmoc\text{-}NH_2$,
(11) TPP,
(12) FF-TPP,
(13) FF/FF-TPP,
(14-15) hidrofobinas-A,
(16-17) hidrofobinas-B,
(18) ADN de doble hebra,
(19) insulina,
(20-21) albúmina,
(22) hemoglobina,
(23-24) lisozima, y
(25) caseína.

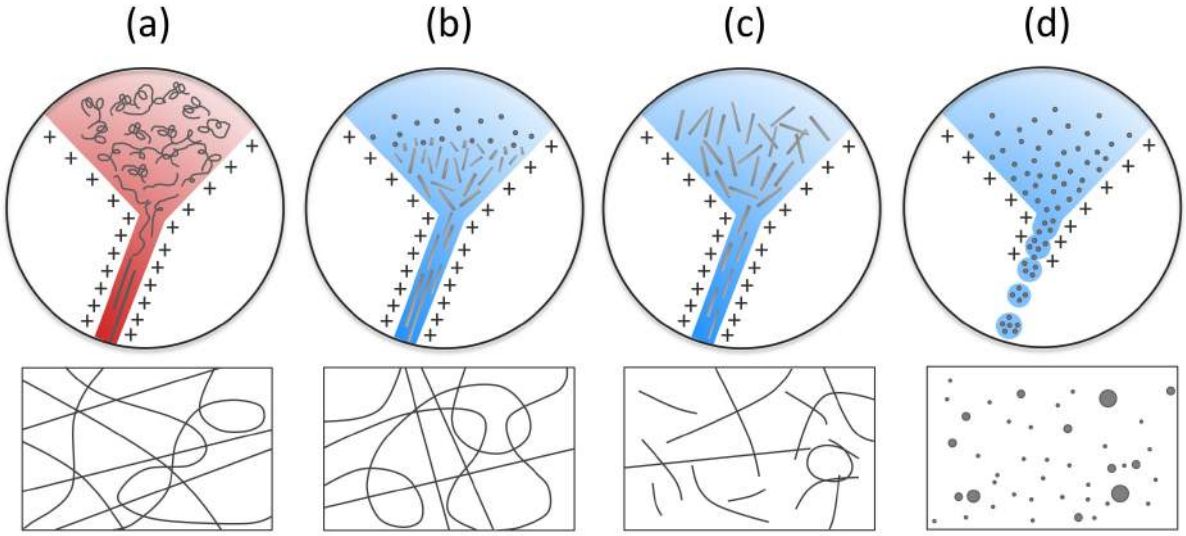

Figure 3: Esquema de los mecanismos propuestos en el electrohilado de (a) polímero estándar, (b) FF, GF, Fmoc-FG, Fmoc-G, $(Fmoc\text{-}C)_2$, (c) GFG, y (d) 9FM, $Fmoc\text{-}NH_2$.

eralmente analizados (por ejemplo, en forma de polvo); y método 3) basado en la caracterización reológica de la solución del péptido. El tercer método se ha aplicado y ensayado para las proteínas globulares y los resultados indican que el valor mínimo del número Ohnesorge (*Oh*) requerido para el electrohilado es ≈10.

Conclusiones: Como resultado de este trabajo a continuación se resumen las bases generales para los disolventes adecuados, las condiciones de optimización y los parámetros para la técnica de electrohilado.

- **Selección de sustancias:** El péptido debe ser capaz de autoensamblarse, por lo que debería tener muchas propiedades para formar enlaces intermoleculares, especialmente enlaces de hidrógeno. Los grupos laterales aromáticos pueden dirigir el ensamblado, pero parece que dejan menos opciones para que se formen los enlaces de hidrógeno, por lo tanto, es preferible seleccionar péptidos aromáticos cortos (ya que sus grupos terminales pueden entonces dominar el ensamblado). Las proteínas globulares tales como la albúmina, la hemoglobina, la caseína, la lisozima y la insulina también se pueden electrohilar sin la adición de polímeros. Las proteínas fibrosas (no probadas en este trabajo) deben comportarse bastante similarmente a los polímeros, y se supone que se electrohilarán sin problemas.

- **Disolución:** Los péptidos aromáticos y las proteínas globulares deben disolverse en un disolvente altamente electrofílico (AN - DN ≥ 88), por ejemplo, en hexafluoroisopropanol (HFIP) o en ácido trifluoroacético (TFA). La concentración de la solución debe ser alta (por encima del ≈5 % en peso o incluso mayor que el 10 %), con el fin de conseguir fuertes interacciones intermoleculares, y para lograr las propiedades reológicas adecuadas (los resultados sugieren un número Ohnesorge (*Oh*) por encima de 10).

- **Electrohilado:** El voltaje aplicado, la distancia al colector, la velocidad de flujo, y la humedad del aire (especialmente para el electrohilado de proteínas) son parámetros importantes, que afectan a la morfología de las fibras. Para las biomoléculas estudiadas, las condiciones de optimización típicas son 10−15 kV, 12−15 cm, 0.2−0.5 ml/h (para la conFig.ción de micro-electrohilado la velocidad de flujo debe ser lo más pequeña posible), y por debajo del 30 % de humedad. Para formar fibras ultrafinas de proteínas (< 20 nm de diámetro), el electrohilado debe realizarse definiendo una distancia extrema entre la solución y el colector (60−75 cm), con un voltaje de 20−35 kV, y aplicando una corriente de aire adicional de ∼1 $m.s^{-1}$ (por encima de la punta, ver Fig. 1d).

Aplicaciones: Para la posible aplicación de fibras electrohiladas formadas puramente de biomoléculas, es interesante que las fibras de péptidos y proteínas (de 100 nm hasta micrómetros) muestren morfologías similares a las de las fibras típicas de polímeros biocompatibles. Además, su química sugiere una muy alta biocompatibilidad que debería permitir su uso en aplicaciones biológicas y médicas altamente críticas, por ejemplo, la proliferación y diferenciación de células madre. Los andamios hechos de fibras de proteínas puras o péptidos presentan intrínsecamente grupos químicos a las células, además, seleccionando proteínas (o secuencias de aminoácidos) de familias de proteínas que se adhieren de forma natural a las células, permitiría la creación de un entorno morfológica y bioquímicamente optimizado. Recientemente en nanoGUNE se han llevado a cabo relevantes experimentos en el uso de fibras y células, y varias publicaciones están siendo preparadas (la discusión detallada de esta aplicación está fuera del alcance de esta tesis). En términos más generales, las estructuras biofuncionales electrohiladas están siendo estudiadas para varios fines médicos, por ejemplo, en el vendaje para heridas, en ingeniería de tejidos, en la administración y la liberación controlada de fármacos, y en aplicaciones en enfermedades neurodegenerativas. Muchos de estos estudios están siendo ahora trasladados desde la investigación hacia el desarrollo.

Para biomoléculas con una funcionalidad menos específica, la morfología de la fibra, la mecánica y la química de superficie pueden proporcionar una ventaja sobre los polímeros. Estas moléculas tienen que estar disponibles en grandes cantidades, tales como la caseína de la leche, los azúcares de las plantas, y las hidrofobinas (propias de hongos, pero producidas por bacterias). Estas moléculas pueden ser electrohiladas y aplicadas, por ejemplo, en aplicaciones textiles, para prendas de ropa protectoras, para el envasado, o como filtros. De la misma manera que las nanofibras cerámicas se forman a partir de plantillas de fibras de polímeros electrohiladas, estas biomoléculas también pueden servir como fuentes de polímeros naturales para la producción de nanofibras mineralizadas. En este caso, el revestimiento cerámico proporciona la funcionalidad, que puede ser dirigida a un amplio rango de aplicaciones en energía y dispositivos electrónicos.

This thesis is dedicated to my grandmother and everyone who is subject to Birth,

Old age,

Sickness,

and Death.

Contents

Chapter 1

Introduction

1.1 Background and Motivation

One-dimensional (1D) nanostructured materials such as nanowires, nanorods, nanowhiskers, nanotubes and nanofibers have been intensively studied worldwide owing to their potential technological applications in many areas. The wide range use of 1D nanostructures stems from the ability to precisely control or fine tune their dimensions, chemical compositions, surface properties, phase purity, and crystal structure [1, 2]. For example, fibrous networks play a significant role in bioengineering applications such as tissue engineering scaffolds. Nanofibers have been commercialized in various applications such as filter media, nano-sensors, protective clothing, tissue scaffolds, and wound dressings. Business Communications Company, Inc. Research (BCC) published a research report on nanofibers (report code NAN043C, 2013 [3]), which states that the global nanofiber market increased from $128.3 million in 2011 to $151.7 million in 2012. The market is projected to grow to reach a global revenue of $570.2 million by 2017. The BCC has identified nine main areas where nanofibers have current and potential future applications. These consist of automotive and aerospace, consumer, defense and security, electronics, energy, mechanical/chemical, medical/biological/pharmaceutical, sensors and instrumentation, and thermal and acoustic insulation. The largest segment of the market is mechanical and chemical products. The second and the third largest segments are energy and electronic products, respectively.

A special case: Organic nanofibers and nanotubes, e.g. assembled tobacco mosaic virus (TMV) nanotubes and peptide self-assembly [4–9], are currently under investigation. Compared with inorganic 1D materials, they feature various "built-in" advantages. These advantages include mechanical flexibility and good control over chemical composition. Technical applications such as tissue scaffolds require the ability to control (or to finely tune) the material's dimensions and surface properties [1, 2], both of which are difficult tasks for all nanofibers.

Special importance: Polymer nanofibers are defined as fibers with diameters less than 1000 nm. For example, Fig. 1.1 shows composite polyvinylpyrrolidone (PVP)/titanium dioxide (TiO_2)[1] nanofibers fabricated by electrospinning of a solution of PVP and Ti complex, followed by calcination (heating in air) [14] compared to a human hair with around 100 μm of diameter. When the diameters of fibers are reduced from micrometers to submicrons (10−100 nm), their surface area to volume ratio will be hugely increased. Furthermore, their surface functionalities and mechanical performance (e.g. stiffness and tensile strength) can be improved compared to other known forms of materials such microfibers or films [15–17].

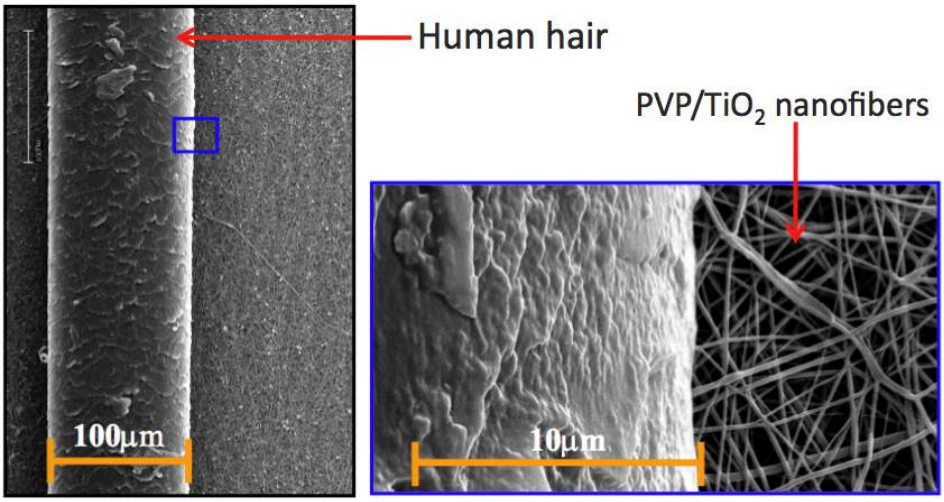

Figure 1.1: SEM micrographs of a human hair compared to composite polyvinylpyrrolidone (PVP)/titanium dioxide (TiO_2) nanofibers fabricated by electrospinning and calcination.

Nanofibers can be produced by several techniques including top-down and bottom-up approaches. Some example techniques are template synthesis, drawing, phase separation, self-assembly and electrospinning.

Template synthesis uses a template or mold to produce nanofibers (see Fig. 1.2a). This method is similarly to standard manufacturing of polymer fibers, which is called melt spinning (or extrusion). In the extrusion, molten polymer is delivered from an extruder or a metal-grid melter located upstream of the spinning machine. The molten polymer passes through a filter and a spinneret. The emerging molten filaments are quenched by cross-flow air, and then solid state fiber is obtained [18]. For nanoscale fiber production, the filter has pores in the rage of the nanometer. For example fabrication of polyacrylonitrile (PAN) nanofibers [19, 20], an aluminum oxide membrane with average pore diameters of ~100 nm is used as a sieve (see Fig. 1.2b). PAN solution is pressed into one side of the porous membrane. Hence, nanofibers are extruded. They can be contacted with a solidifying solution. The nanofibers diameter is determined by the pores or the templates. Figure

[1]Nanocrystalline TiO_2 is widely studied for its potential applications in chemical sensors, photoelectrochemical cells, optical filters, and systems with enhanced catalytic activity [10–13].

1.2c shows a cross-sectional scanning electron microscope (SEM) image of PAN nanofibers, the average diameter of the nanofiber tips and interfiber distances are 100 nm and 500 nm, respectively. The length of the fibers is approximately 10 μm. Therefore, diameter of nanofibers can be easily controlled by using different templates. Disadvantages of this technique are that they do not work on the industrial scale, the length of fibers is limited in the range of the micrometer and the diameter is rather large.

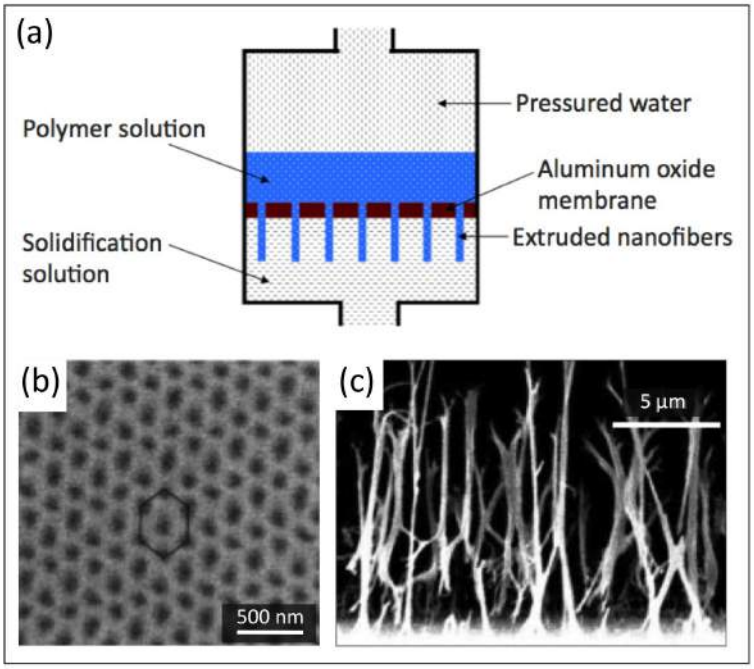

Figure 1.2: (a) Schematic of template synthesis technique (adapted from [23]). SEM micrographs of (b) the as-prepared anodic aluminum oxide membrane, (c) cross-sectional view of the as-synthesized PAN nanofibers using the template synthesis technique (adapted from [19, 20]).

Drawing (or cold drawing) is a standard manufacturing of plastic fibers. In industry, the drawing (or stretching) method is usually followed the extrusion process in order to reduce the cross-section of the extruded polymer fibers. Furthermore, this process improves some properties of the fibers in higher tensile strength, lower elongation, and more oriented crystallization [18]. The similarity of this technique to the drawing of nanofiber method is that the process mechanically draws from viscous or melts polymers directly. However, this is a low-throughput nanofiber production method [21]. Figure 1.3a shows schematic of poly(trimethylene terephthalate) (PTT) nanofiber produced by direct drawing process from molten PTT. Firstly, an iron or silica rod with radius of approximately 125 μm is approached and immersed into the molten PTT (temperature controlled at ~250 °C). Then, the rod conglutinated PTT is slowly drawn out with a speed of 0.1−1.0 m/s. Figure 1.3b shows SEM micrograph of a PTT nanofiber produced by this technique with diameter of 150 nm [22]. The main disadvantage of this process is the formation of discontinuous fibers, as can be seen in the schematics. Therefore, it can only produce nanofibers in laboratory scale and along the direction of drawing. However, this technique shows an advantage for small equipment.

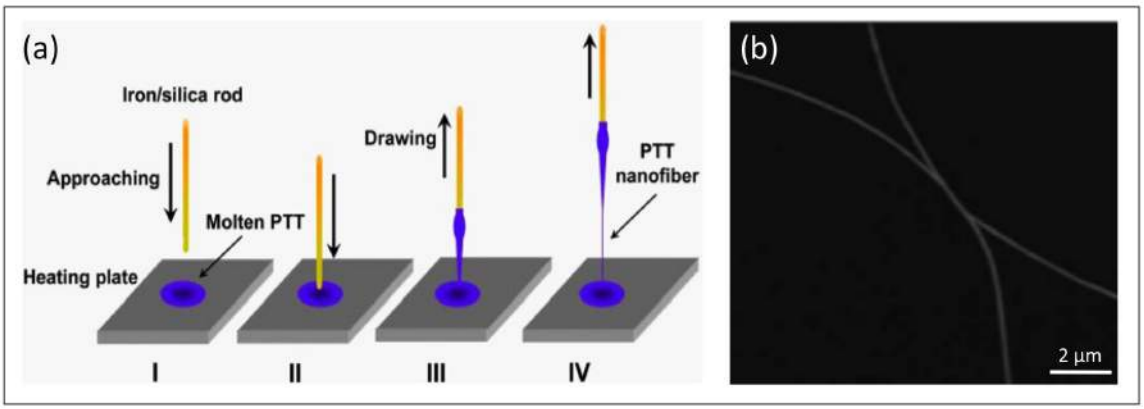

Figure 1.3: (a) Schematic of a poly(trimethylene terephthalate) (PTT) nanofiber fabricated by the drawing technique and (b) SEM micrograph of the PTT nanofibers with diameter of 150 nm (adapted from [22]).

One of the simplest nanofibers production method based on drawing technique is the **"ruler drawing"**. It only needs an orange peel and a plastic (polystyrene) ruler. From Fig. 1.4a-d, firstly, the orange peel is pressed in order to spread an organic solvent (limonene) from the peel onto the ruler. After that the wetted ruler is attached to a hand and then drawn back with a speed of ~0.1 m/s. Dissolution of polystyrene is stretched, resulting micro- and nanofibers aligned between the ruler and hand.[2] Figure 1.4e shows an optical image of fibers with various diameters from few μm down to hundreds nm. Furthermore, the alignment of fibers can be controlled by rotating the substrate (see Fig. 1.4f).

Phase separation can directly produce a nanofiber matrix. Since this process is limited to specific polymers, it is not a standard process in industrial scale. A polymer is firstly dissolved and mixed with a second solvent before undergoing gelation (see schematic in Fig. 1.5a). Immiscibility is the main mechanism of this process, causing the separation of phases for example production of Poly(L-lactic acid) (PLLA) nanofibers reported by P.X. Ma and R. Zhang [24]. Figure 1.5b shows SEM micrograph of PLLA fibrous matrices prepared from PLLA/Tetrahydrofuran (THF) 1.0 %(wt/v) solution at a gelation temperature of 8 °C. Furthermore, the mechanical properties of the matrix can be tailored by adjusting polymer concentration. A disadvantage is that the fiber dimensions cannot be controlled because they formed a porous structure or a continuous network. However, the fiber network can enhance the cell attachment and it is suitable for scaffold applications.

[2] Around 1990s, this technique is a mysterious experiment for kids in Thailand, the fibers are believed to come from orange peel. However, vibrational spectroscopy results (see Appendix A) concluded that the fibers are polystyrene. This means organic natural solvent (limonene) spread out from the orange peel dissolved polystyrene. Then it is stretched and leaving micro- and nanofibers.

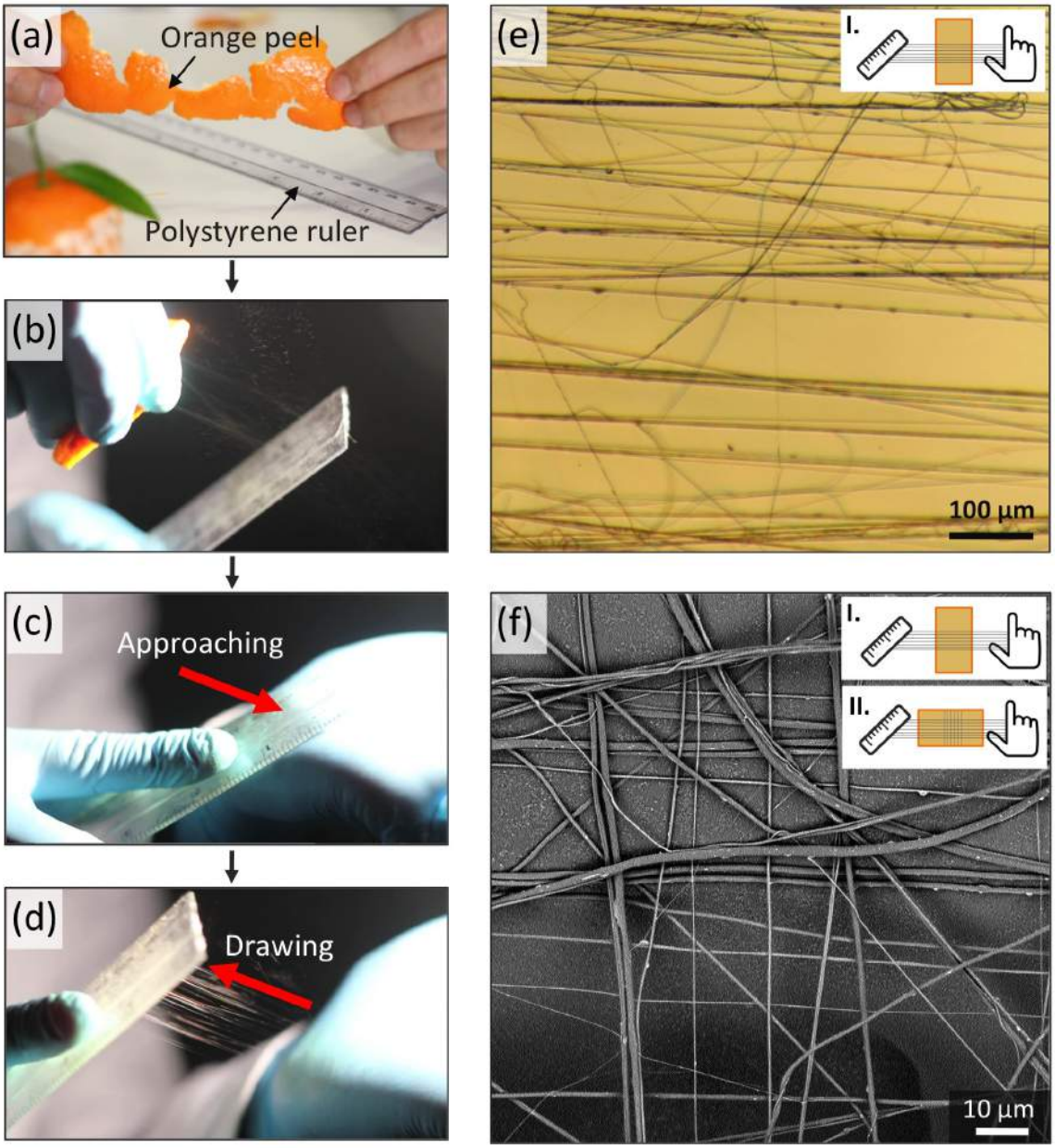

Figure 1.4: Photos demonstrating the ruler drawing technique (a) only an orange peel and a plastic (polystyrene) ruler are needed; (b) the orange peel is pressed in order to spread an organic solvent onto the ruler; (c) the wetted ruler is attached to a hand; and finally (d) the ruler is drawn back with a speed of ~0.1 m/s. (e) Optical image of aligned micro- and nanofibers on a glass substrate, and (f) SEM micrograph of two steps aligned fibers produced on a carbon tape.

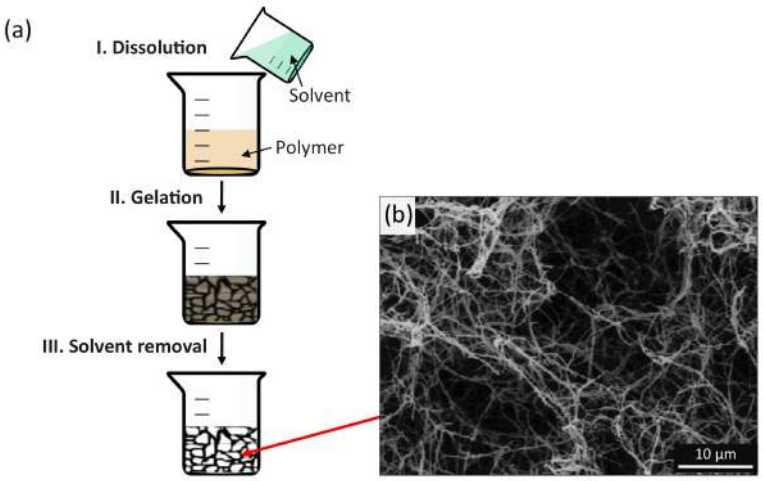

Figure 1.5: (a) Schematic of the phase separation technique (adapted from [23]) and (b) SEM micrograph of the PLLA fibrous matrices prepared from a PLLA/THF 1.0 %(wt/v) solution at a gelation temperature of 8 °C (adapted from [24]).

Self-assembly is one of bottom-up nanomaterial fabrication and a good technique for producing very small nanofibers (lower than 100 nm to few nm) with length of several micrometers. The main mechanism is based on the intermolecular forces that bring small units (molecules) together. Hartgerink et al. [25] reported that pH-induced self-assembly of a peptide amphiphile produced a nanostructured fibrous scaffold with 7 nm of diameter. But this technique can only produce nanofibers on the laboratory scale and cannot control the fiber dimensions. Another example is self-assembly of Fluorenylmethoxycarbonyl (Fmoc) protected aromatic amino acids derived from phenylalanine (Phe) [26]. Figure 1.6 shows schematic of the self-assembly process in solution. Firstly, a peptide is dissolved in dimethyl sulfoxide (DMSO). Then, the aqueous solution is diluted with water. After 5−30 min, the peptide molecules are self-assembled and they formed a hydrogel, which is a 3D network of peptide nanofibers capable of entrapping water molecules and present a self-supporting structure [27]. Some of the disadvantages of the self-assemby technique are its limitation to the laboratory scale production of nanofibers and the lack of fine control of the fiber dimensions [21, 23].

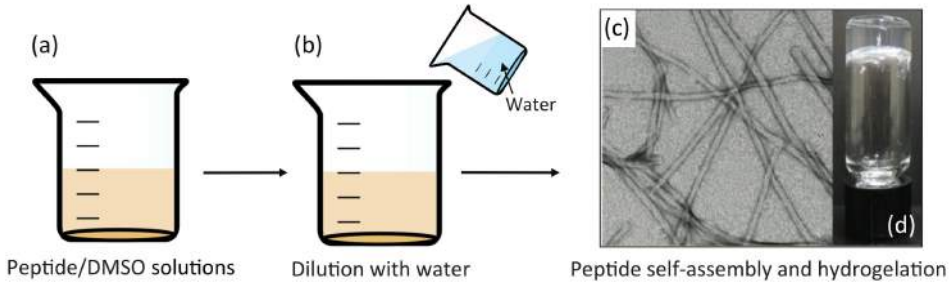

Figure 1.6: (a-b) Schematic of peptide self-assembly technique, (c) TEM micrograph of peptide self-assembled nanofibers, and (d) digital photo of their hydrogeletion (adapted from [26]).

Electrospinning (ES) seems to be the only technique that can produce nanofibers on an industrial scale. In addition, the fiber length can be increased up to several meters. The diameter and fiber directions can be controlled depending on materials, instrument setup and process parameters. Moreover, this technique is very simple, convenient, and has low operating cost [15, 17, 28–31]. Figure 1.7a shows a simple schematic of the electrospinning technique. The conventional ES system needs a plastic syringe connected to a metal needle and a high voltage power supply (HV). When a polymer solution is loaded into the syringe, and a high voltage of around 10−30 kV is applied, extremely long nanofibers are quickly produced and collected on a metal collector below. The mechanism of the process is very fast and has a similar appearance to spraying or nebulization of a solution (Fig. 1.7b). A high-speed camera can be used to illustrate that the spraying is in fact a continuous single nanofiber, forming during the process as shown in Fig. 1.7c.

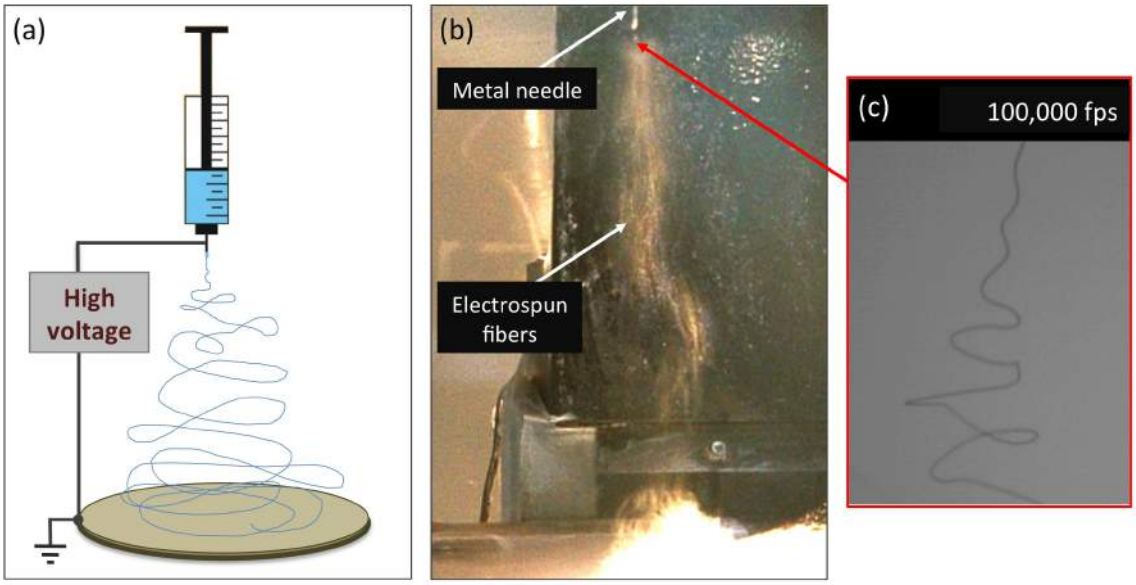

Figure 1.7: Electrospinning technique, (a) simple schematic of a conventional system, (b) electrospinning process recorded by a video camera, (c) recorded by a high-speed camera at 100,000 fps.

Figure 1.8 shows an overview of the materials which can be fabricated into nanofibers by using electrospinning. Over one hundred years after, Cooley and Morton first patented electrospinning in 1902 [32], more than 200 polymers have been electrospun [33] (see example of electrospun polymers and biopolymers in Fig. 1.9). Polymer nanofibers can be used as a template for fabrication of ceramic nanofibers, in excess of 100 different ceramic materials have been fabricated based on polymer fibers [34] (see example of electrospun ceramic nanofibers in Fig. 1.10). Apart from this, less than 20 pure biomolecules (such as proteins, carbohydrates, nucleic acids, and lipids) have been successfully electrospun for biomedical applications [35, 36]. Nevertheless, electrospinning of pure monomeric peptides has not been widely explored.

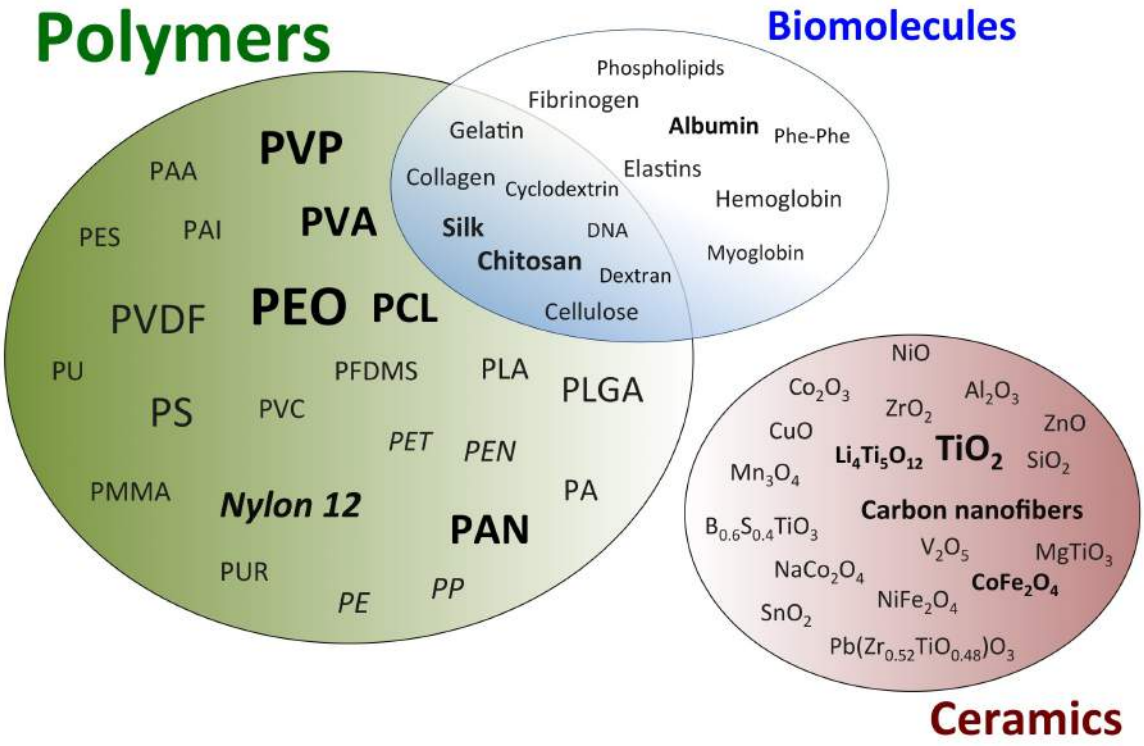

Figure 1.8: An overview of materials from which nanofibers can be fabricated by using electrospinning. They are divided into three groups; >200 of polymers, >100 of ceramic composites, and <20 of biomolecules.

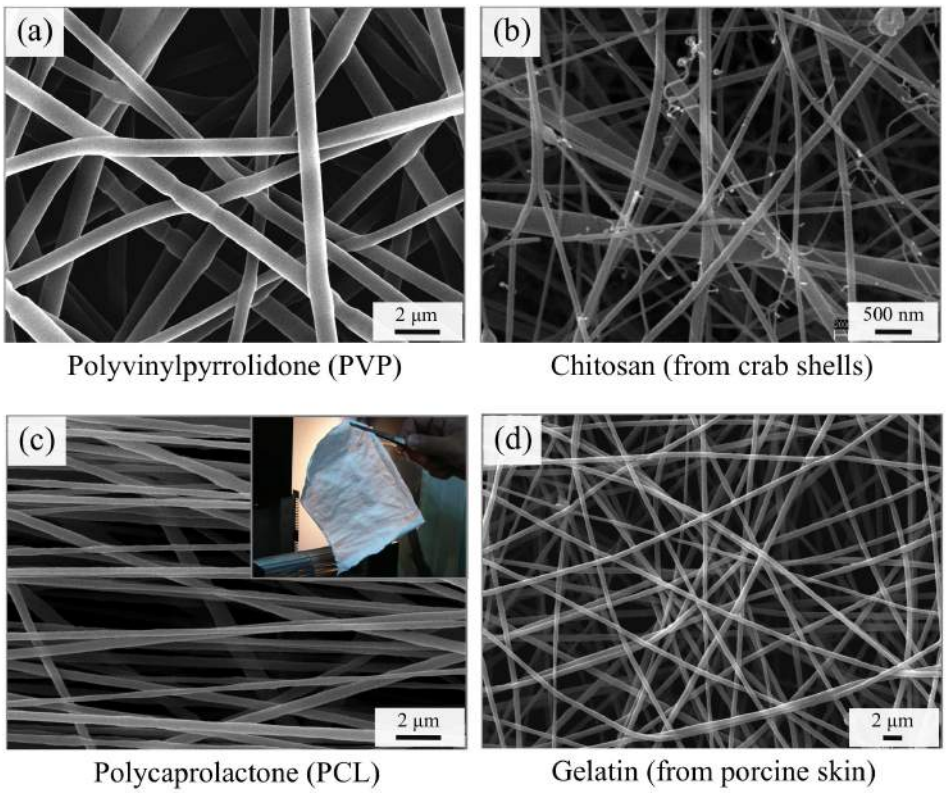

Figure 1.9: SEM images of electrospun polymers and biopolymers (a) polyvinylpyrrolidone, (b) chitosan, (c) polycaprolactone, inset is a digital photo of fibers a fiber mat, and (d) gelatin. Results obtained at Khon Kaen University, Thailand.

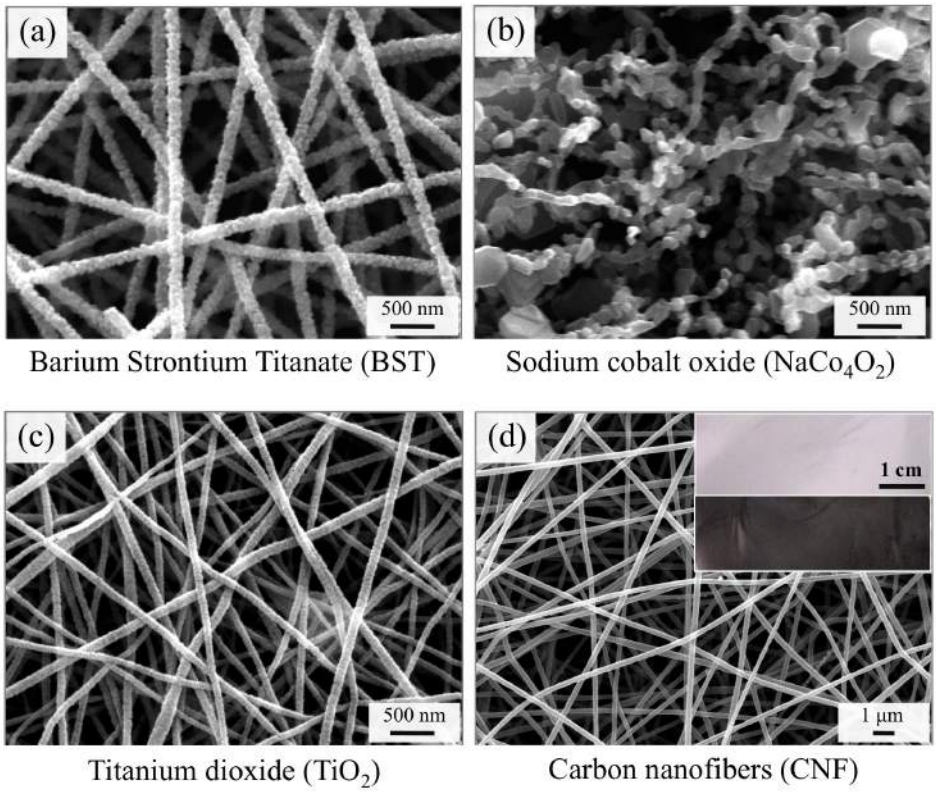

Figure 1.10: SEM images of 1D materials formed using templates of electrospun polymer fibers; (a) barium strontium titanate [37], (b) sodium cobalt oxide [38], (c) titanium dioxide [14], and (d) carbon nanofibers; inset is a digital photo of a carbon nanofiber mat before (upper) and after carbonization. Results obtained at Khon Kaen University, Thailand.

1.2 Electrospinning of monomers

Monomers usually cannot be electrospun because only polymer solutions or melts are adequately viscous and contain sufficient chain entanglements [39, 40]. However, many peptides and proteins can self-assemble in 3D (bulk crystals), in 2D (for example membrane proteins), and in 1D (natural fibrils such as collagen). This occurs by intermolecular interactions, e.g. Van der Waals, electrostatic interactions, hydrogen bonds, and π-stacking interactions. When self-assembling molecules combine together to form well ordered supramolecular structures, they can assemble to nanofibers or nanotubes.

- **Examples 1:** Ghadiri et al. were the first group to describe the conversion of cyclic polypeptides into nanotubes [41, 42]. The results demonstrated that cyclic peptides can form artificial transmembrane channels for ion and glucose transport, and antibacterial activity [43].
- **Examples 2:** In recent years, Gazit et al. published important works on self-assembly of short aromatic peptides. They demonstrated that the short aromatic peptide diphenylalanine (Phe-Phe, FF) can self-assemble in solution to mimic amyloid fibrils because aromatic stacking interactions provide an energetically favorable contribution towards the self-assembly of amyloid structures (which are mainly based on hydrogen bonding). Related protein fibrils can result in neurodegenerative diseases, e.g. Alzheimer's disease, Parkinson's disease [44, 45]. Self-assembly of FF nanostructures have been investigated for applications in bionanotechnology and nanodevices [46, 47].
- **Example 3:** Besides natural aromatic side chains in peptides such phenylalanine, the protecting group fluorenylmethoxycarbonyl (Fmoc) with a series of amino acid or dipeptides Alanine (Ala), Glycine (Gly), Serine (Ser), Leucine (Leu), Lysine (Lys), Valine (Val), and Tyrosine (Tyr) can form a nanofibrous hydrogel based on intermolecular π-π and also dipole-dipole interactions [26, 48–52].

Singh et al. has been the only group to report electrospinning of pure monomeric peptide FF, using π-π interactions between aromatic rings to provide molecular entanglements, resulting in the stabilization of nanofibers [53]. Thus, this thesis extends their experiments with other peptides containing aromatic groups to demonstrate that non-covalent interactions can be used to replace covalent bonds in conventional polymer electrospinning. Furthermore, the results and some conclusions are adapted for electrospinning of proteins, made up of hundreds or thousands of amino acids.

1.3 Objectives of this work

Motivation: Electrospinning of biomolecules, i.e. peptides, and globular proteins is not yet understood, and there are few reports comparing polymer or ceramic nanofibers. Typically, monomers such as a peptide cannot be electrospun without polymer blends because it has a low molecular weight (in this work relative molecular masses M_r are around 200−700) and no covalent bonds.

Figure 1.11 compares electrospinning of polymer and monomer. The solution jet of monomer formed when a high voltage was applied, but it is broken after a few whippings, resulting in small droplets, rather than long fibers.

Moreover, a conventional electrospinning system needs solution volumes in range of milliliters up to liters for laboratory and industrial scale, respectively. For biomolecules, conventional electrospinning requires at least milliliters of highly concentrated solutions of self-assembling molecular units. The minimum amount of material is thus in the range of 100 mg. However, many biomolecules, especially peptides and proteins, are only available in mg or μg amounts. Commercialized electrospinning setups offer only laboratory and industrial scale equipment (see example of some companies in Fig. 1.12), no company provides an electrospinning system for small amounts of substance.

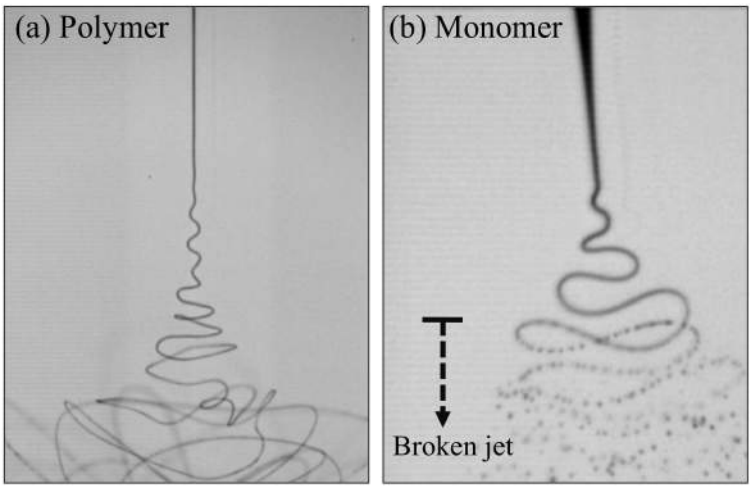

Figure 1.11: High speed images of the solution jet during the electrospinning of polymer solutions when (a) the jet is continuously stretched into nanofibers and (b) monomer solution jet is broken after instability whipping occurred, resulting small droplets similar to a spraying process.

Two specific problems of this work are;

- Experiment: Which molecules, solvents, solution preparation and electrospinning parameters are suitable for producing long fibers?
- Theory: Why and how can electrospinning of biomolecule solution form long fibers?

Idea or hypothesis: Select biomolecule substances that can assemble into 1D supramolecular structures, i.e. nanofibers, and nanotubes. This self-assembly is entirely based on non-covalent interactions. Hence, biomolecules may be successfully electrospun if their intermolecular interactions are increased and if the electrospinning parameters are properly chosen.

> Electrospinning of pure biomolecules without polymer blends is possible, when they show self-assembly in 1D, 2D, or 3D, when they can be dissolved in a suitable organic solvent at high concentration, and when electrospinning parameters are optimized.

Therefore, the objectives of this work are focused on;

1. Developing a new electrospinning system that is suitable and convenient for a substance available in small amounts.
2. Studying the possibility of electrospinning fibers from biomolecules:
   (a) starting from dipeptides containing phenyl side groups (e.g. FF, GF)[3], then
   (b) peptides containing larger aromatic groups (e.g. Fmoc-FG, Fmoc-G, $(Fmoc\text{-}C)_2$), and finally
   (c) polypeptide chains such as globular proteins (albumin, hemoglobin, casein, lysozyme, insulin, and hydrophobins) and also double-stranded DNA.
3. Evaluating molecular conformation of biomolecules, which are subjected to a high voltage.
4. Reducing the diameter of biomolecule fibers close to the size of a single molecule.

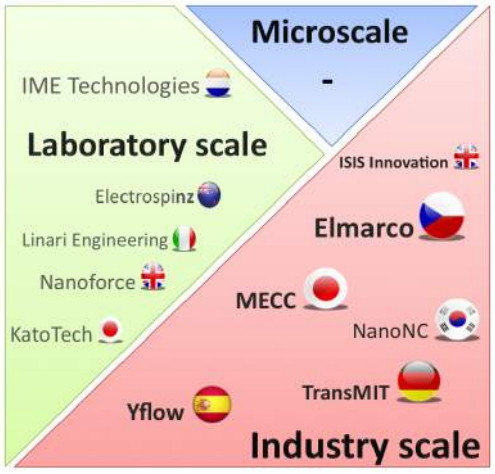

Figure 1.12: Example of some companies that develop commercial electrospinning systems on laboratory and industrial scales.

[3]The one letter codes and abbreviations are given for amino acid and amino protecting group; F is phenylalanine (Phe), G is glycine (Gly), C is cysteine (Cys), and Fmoc is fluorenylmethyloxycarbonyl. Their molecular structures are presented in Chapter 3.

1.4 Expected impact

The thesis is expected to have the following impacts: extend the ability to electrospin biomolecule materials, in particular small peptides and polypeptides. A. Dasgupta et al. collected and reported 190 peptides that can undergo self-assembly in solution and form hydrogels [27]. This means that if the hypothesis of this work is correct, not only the choice of biomolecule substance for electrospinning can be sharply increased, but also improvements can be made for the potential applications of nanofibers in life science area, e.g. wound dressing, tissue engineering, and biomedical applications. Furthermore, uniform fibers of proteins and DNA with diameters less than 100 nm would be useful for further characterization or applications in nanodevices.

Apart from applications, this work is primarily focused on electrospinnability of monomers, i.e. short aromatic peptides, which can self-assemble to nanofibers such as the model system for amyloids. Amyloid fiber assembly takes years *in vivo*, and days to weeks *in vitro* but electrospinning could speed up the process to millisecond. This advantage can help enable a better understanding of fiber assembly, and maybe find new pathways of molecular assembly under shear forces, as present in electrospinning.

A prototype of a microliter electrospinning system may be developed to fulfill the commercial need for an electrospinning system for μg amounts, e.g. peptides and proteins. In addition, this might also be a useful electrospinning system for educational proposes in a high school or for undergraduate studies.

1.5 Overview of the thesis

This thesis is divided into 6 chapters, first part provides background information: Introduction (Chapter 1), theoretical background (Chapter 2) and methodology (Chapter 3). Second part: Report on new results (processes, materials), experimental results (Chapter 4, 5), and finally the conclusion (Chapter 6).

- **In Chapter 2**, the theoretical aspects of the electrospinning processes and electrospinning setup will be explained together with a basic mathematical description of these processes. A description of the biomolecules selected in this work are employed and the literature related to them are reviewed.
  ► *This chapter supports the hypothesis; why the electrospinning of pure biomolecules might be possible.*
- **In Chapter 3**, details on the methodology consist of solution preparation, electrospinning setup, characterization techniques and computation of molecular vibrations will be provided. Some biomolecules are available in small amounts, therefore both the conventional and microliter electrospinning setup are developed and will be presented. In addition, this chapter

also includes a special technique used for fabrication sub 100 nm protein fibers.
► *Objective 1 will be mentioned in this chapter.*

- **In Chapter 4**, the first part of the experimental results on the electrospinning of short aromatic peptides will be presented and discussed. After that, optimized parameters and conditions for producing fibers from such peptides are concluded. The next part of this chapter, prediction of electrospinnability of a peptide will be proposed by using electron acceptor and donor number of the solvent, polarized Raman spectroscopy, and some remarks on rheology of the solutions.
► *Objective 2(a), 2(b), and 3 will be mentioned in this chapter.*

- **In Chapter 5**, the second part of the experimental results will be provided. This part attempts the electrospinning of globular proteins, i.e. albumin, hemoglobins, casein, lysozyme, insulin and hydrophobins into fibers without polymer blends using some conclusions from Chapter 4. For albumin, this protein was electrospun into nanofibers with a small diameter close to single molecules. In addition, double-stranded DNA was tested with electrospinning (absence of polymer) and significant results are presented.
► *Objective 2(c), 3, and 4 will be mentioned in this chapter.*

- **In Chapter 6**, a summary of all experimental results will be concluded with suggestions of possible applications for this work.

1.6 References

[1] J. Hu, T.W. Odom, C.M. Lieber. Chemistry and Physics in One Dimension: Synthesis and Properties of Nanowires and Nanotubes, *Acc. Chem. Res.*, **32**: 435-445, 1999.

[2] Y. Xia, P. Yang, Y. Sun, Y. Wu, B. Mayers, B. Gates, Y. Yin, F. Kim, H. Yan. One-Dimensional Nanostructures: Synthesis, Characterization, and Applications, *Adv. Mater.* **15**: 353-389, 2003.

[3] BCC Research. Nanofibers: Technologies and Developing Markets, Report Code *NAN043C*, 2013.

[4] D.T. Bong, T.D. Clark, J.R. Granja, M.R. Ghadiri. Self-Assembling Organic Nanotubes, *Angew. Chem. Int. Ed.* **40**: 988-1011, 2001.

[5] M.A.B. Block, C. Kaiser, A. Khan, S. Hecht. Discrete organic nanotubes based on a combination of covalent and non−covalent approaches, *Top. Curr. Chem.* **245**: 89-150, 2005.

[6] A.P.H.J. Schenning, E.W. Meijer. Supramolecular electronics; nanowires from self-assembled π-conjugated systems, *Chem. Commun.* **14**: 3245-3258, 2005.

[7] A.M. Bittner. Biomolecular rods and tubes in nanotechnology, *Naturwissenschaften* **92**: 51-64, 2005.

[8] L. Zang, Y. Che, J.S. Moore. One-Dimensional Self-Assembly of Planar π-Conjugated Molecules: Adaptable Building Blocks for Organic Nanodevices, *Acc. Chem. Res.* **41**: 1596-1608, 2008.

[9] R.V. Ulijin, A.M. Smith. Designing peptide based nanomaterials, *Chem. Soc. Rev.* **37**: 664-675, 2008.

[10] J.C. Parker, R.W. Siegel. Calibration of the Raman spectrum to the oxygen stoichiometry of nanophase TiO_2, *Appl. Phys. Lett.* **57**: 943, 1990.

[11] M. Anpo. Utilization of TiO_2 photocatalysts in green chemistry, *Pure Appl. Chem.* **72**: 1265, 2000.

[12] M. Grätzel. Photoelectrochemical cells, *Nature* **414**: 338, 2001.

[13] Z. Guan, X. Zhang, Y. Ma, Y. Cao, J. Yao. Photocatalytic activity of TiO_2 prepared at low temperature by a photo-assisted sol-gel method, *J. Mater. Res.* **16**: 907, 2001.

[14] W. Nuansing, S. Ninmuang, W. Jarernboon, S. Maensiri. Structural characterization and morphology of electrospun TiO_2 nanofiber, *Mater. Sci.Eng. B* **131**: 147-155, 2006.

[15] Z.M. Huang, Y.Z. Zhang, M. Kotaki, S. Ramakrishna. A review on polymer nanofibers by electrospinning and their applications in nanocomposites, *Comp. Sci. Tech.* **63**: 2223-2253, 2003.

[16] A. Frenot, I.S. Chronakis. Polymer nanofibers assembled by electrospinning, *Curr. Opin. Coll. Interf. Sci.* **8**: 64-75, 2003.

[17] D. Li, Y. Xia. Electrospinning of Nanofibers: Reinventing the Wheel?, *Adv. Mater.* **16**: 1151-1170, 2004.

[18] A. Anton, B.R. Baird. Polyamides, Fibers, *In the Encyclopedia of Polymer Science and Technology*, John Wiley, New York, 2001.

[19] L. Feng, S. Li, H. Li, J. Zhai, Y. Song, L. Jiang, D. Zhu. Super-Hydrophobic Surface of Aligned Polyacrylonitrile Nanofibers, *Angew. Chem. Int. Ed.* **41**: 1221-1223, 2002.

[20] L. Feng, S. Li, Y. Li, H. Li, L. Zhang, J. Zhai, Y. Song, B. Liu, L. Jiang, D. Zhu. Super-Hydrophobic Surfaces: From Natural to Artificial, *Adv. Mater.* **14**: 1857-1860, 2002.

[21] V. Beachley, X. Wen. Polymer nanofibrous structures: Fabrication, biofunctionalization, and cell interactions, *Prog. Polym. Sci.* **35**: 868-892, 2010.

[22] X. Xing, Y. Wang, B. Li. Nanofiber drawing and nanodevice assembly in poly(trimethylene terephthalate), *Optics Express* **16**: 10815-10822, 2008.

[23] S. Ramakrishna, K. Fujihara, W.E. Teo, T.C. Lim, Z. Ma. An Introduction to Electrospinning and Nanofibers, *Singapore: World Scientific Publishing*, 2005.

[24] P.X. Ma, R. Zhang. Synthetic nano-scale fibrous extracellular matrix, *J. Biomed. Mater. Res.* **46**: 60-72, 1999.

[25] J.D. Hartgerink, E. Beniash, S.I. Stupp. Self-Assembly and Mineralization of Peptide-Amphiphile Nanofibers, *Science* **294**: 1684-1688, 2001.

[26] D.M. Ryan, T.M. Doran, S.B. Anderson, B.L. Nilsson. Effect of *C*-Terminal Modification on the Self-Assembly and Hydrogelation of Fluorinated Fmoc-Phe Derivatives, *Langmuir* **27**: 4029-4039, 2011.

[27] A. Dasgupta, J.H. Mondal, D. Das. Peptide hydrogels, *RSC Adv.* **3**: 9117-9149, 2013.

[28] A. Greiner, J.H. Wendorff. Electrospinning: A Fascinating Method for the Preparation of Ultrathin Fibers, *Angew. Chem. Int. Ed.* **46**: 5670-5703, 2007.

[29] C.J. Luo, S.D. Stoyanov, E. Stride, E. Pelan, M. Edirisinghe. Electrospinning versus fibre production methods: from specifics to technological convergence, *Chem. Soc. Rev.* **41**: 4708-4735, 2012.

[30] P. Raghavan, D.H. Lim, J.H. Ahn, C. Nah, D.C. Sherrington, H.S. Ryu, H.J. Ahn. Electrospun polymer nanofibers: The booming cutting edge technology, *React. Funct. Polym.* **72**: 915-930, 2012.

[31] S. Agarwal, A. Greiner, J.H. Wendorff. Functional materials by electrospinning of polymers, *Prog. Polym. Sci.* **38**: 963-991, 2013.

[32] W.E. Teo, S. Ramakrishna. A review on electrospinning design and nanofiber assemblies, *Nanotech.* **17**: R89-R106, 2006.

[33] N. Bhardwaj, S.C. Kundo. Electrospinning: A fascinating fiber fabrication technique, *Biotech. Adv.* **28**: 325-347, 2010.

[34] Y. Dai, W. Liu, E. Formo, Y. Sun, Y. Xia. Ceramic nanofibers fabricated by electrospinning and their applications in catalysis, environmental science, and energy technology, *Polym. Adv. Technol.* **22**: 326-338, 2011.

[35] D. Liang, B.S. Hsiao, B. Chu. Functional Electrospun Nanofibrous Scaffolds for Biomedical Applications, *Adv. Drug Deliv. Rev.* **59**: 1392-1412, 2007.

[36] D.B. Khadka, D.T. Haynie. Protein- and peptide-based electrospun nanofibers in medical biomaterials, *Nanomedicine: NBM* **8**: 1242-1262, 2012.

[37] S. Maensiri, W. Nuansing, J. Klinkaewnarong, P. Laokul, J. Khemprasit. Nanofibers of barium strontium titanate (BST) by sol-gel processing and electrospinning, *J. Colloid Interface Sci.* **297**: 578-583, 2006.

[38] S. Maensiri, W. Nuansing. Thermoelectric oxide $NaCo_2O_4$ nanofibers by electrospinning, *Mater. Chem. Phys.* **99**: 104-106, 2006.

[39] S.L. Shenoy, W.D. Bates, H.L. Frisch, G.E. Wnek. Role of chain entanglements on fiber formation during electrospinning of polymer solutions: good solvent, non-specific polymer-polymer interaction limit, *Polymer* **46**: 3372-3384, 2005.

[40] S.L. Shenoy, W.D. Bates, G. Wnek. Correlations between electrospinnability and physical gelation, *Polymer* **46**: 8990-9004, 2005.

[41] M.R. Ghadiri, J.R. Granja, L.K. Buehler. Artificial transmembrane ion channels from self-assembling peptide nanotubes, *Nature* **369**: 301-304, 1994.

[42] J.D. Hartgerink, J.R. Granja, R.A. Milligan, M.R. Ghadiri. Self-Assembling Peptide Nanotubes, *J. Am. Chem. Soc.* **118**: 43-50, 1996.

[43] K. Rosenthal-Aizman, G. Svensson, A. Unden. Self-Assembling Peptide Nanotubes from Enantiomeric Pairs of Cyclic Peptides with Alternating D and L Amino Acid Residues, *J. Am. Chem. Soc.* **126**: 3372-3373, 2004.

[44] S. Gilead, E. Gazit. Self-organization of Short Peptide Fragments: From Amyloid Fibrils to Nanoscale Supramolecular Assemblies, *Supramol. Chem.* **17**: 87-92, 2005.

[45] E. Gazit. Self Assembly of Short Aromatic Peptides into Amyloid Fibrils and Related Nanostructures, *Prion* **1**: 32-35, 2007.

[46] X. Yan, P. Zhu, J. Li. Self-assembly and application of diphenylalanine-based nanostructures, *Chem. Soc. Rev.* **39**: 1877-1890, 2010.

[47] A. Lakshmanan, S. Zhang, C.A.E. Hauser. Short self-assembling peptides as building blocks for modern nanodevices, *Trends Biotechnol.* **30**: 155-165, 2012.

[48] Y. Zhang, H. Gu, Z. Yang, B. Xu. Supramolecular Hydrogels Respond to Ligand-Receptor Interaction, *J. Am. Chem. Soc.* **125**: 13680-13681, 2003.

[49] S. Toledano, R.J. Williams, V. Jayawarna, R.V. Ulijn. Enzyme-Triggered Self-Assembly of Peptide Hydrogels via Reversed Hydrolysis, *J. Am. Chem. Soc.* **128**: 1070-1071, 2006.

[50] V. Jayawarna, M. Ali, T.A. Jowitt, A.F. Miller, A. Saiani, J.E. Gough, R.V. Ulijn. Nanostructured Hydrogels for Three-Dimensional Cell Culture Through Self-Assembly of Fluorenylmethoxycarbonyl- Dipeptides, *Adv. Mater.* **18**: 611-614, 2006.

[51] D.M. Ryan, S.B. Anderson, F.T. Senguen, R.E. Youngman, B.L. Nilsson. Self-assembly and hydrogelation promoted by F_5-phenylalanine, *Soft Matter* **6**: 475-479, 2010.

[52] D.M. Ryan, T.M. Doran, B.L. Nilsson. Complementary π-π Interactions Induce Multicomponent Coassembly into Functional Fibrils, *Langmuir* **27**: 11145-11156, 2011.

[53] G. Singh, A.M. Bittner, S. Loscher, N. Malinowski, K. Kern. Electrospinning of Diphenylalanine Nanotubes, *Adv. Mater.* **20**: 2332-2336, 2008.

Chapter 2

Theoretical Background

Principle, parameters, and setup systems of electrospinning are explained in the first part. A brief review gives a general idea how electrospinning works, and which parameters play an important role in the process. The second and the third parts give theoretical backgrounds for biomolecules including their chemical structures and self-assembly properties.

2.1 Electrospinning

Recently, the electrospinning has attracted much attention because it can produce nanofibers that range from μm down to few nm in diameter. Moreover, this technique is a simple, convenient process that can produce nanofibers on the laboratory and the industrial scale as was introduced in Chapter 1. Figure 2.1 shows a simple schematic of the standard electrospinning. A polymer solution or melt is fed through a capillary tube or a small needle, which is polarized electrically. A jet is ejected and travels to the grounded collector. It undergoes thinning, and more and more very rapid bending ("whipping") as it travels, which makes it appear spraying droplets or fibers to the human eyes. In fact, only one single fiber is ejected, but it bends and oscillates, so fast that high-speed cameras are required to observe it. The solvent evaporates, leaving behind a charged fiber deposited on a collector [1, 2], which usually is grounded such that the fiber is discharged. Electrospinning is a simple technique but there are various parameters that affect the fiber diameter, e.g. applied voltage V, distance from the tip to the collector H, flow rate Q, and liquid properties (density ρ, viscosity η, conductivity κ, surface tension γ, permittivity ε).

The principle of electrospinning is based on the effect of an electric force to a high viscosity fluid. If a high viscosity solution drops from a capillary or a needle without an electric field, a big droplet ~2 mm of diameter is generated (see a polymer solution droplet process in Fig. 2.2a-e). In this case, the gravitational force moves the droplet. This is not the case for electrospinning, so all following considerations are equally valid for horizontal on upside-down arrangements. The only exceptions are (unwanted) droplets, which can be so large that their mass matters.

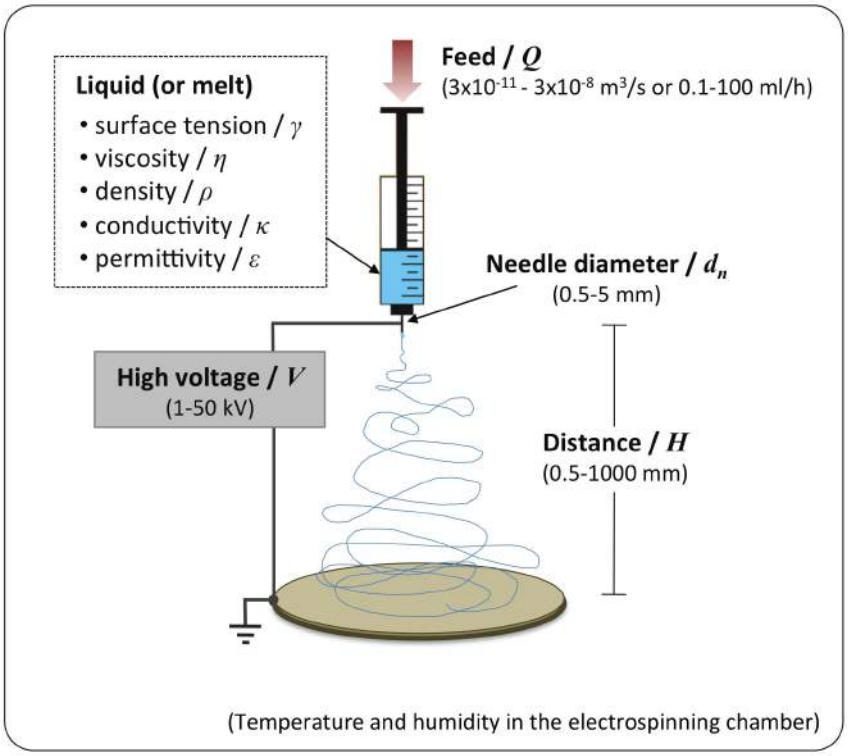

Figure 2.1: A simple schematic of standard electrospinning and parameters.

When starting the electrospinning process (see Fig. 2.2f-j), the solution is charged above a critical high voltage, resulting in the Taylor cone shape 0.1−1 mm in diameter is formed by electric force. Just after 0.05 ms, a solution jet is created with a diameter between 1−10 μm. Further away from the cone, the solution jet has an instability, and whipping occurs in which the jet travels and rapidly elongates between the tip and the collector. About 3 ms later, the shape of the cone is changed to a rounded shape, here is a steady state of the droplet (depended on flow rate and applied voltage, see Fig. 2.3). At the final step, a bending thin solution jet travels in a space between the tip of needle and the collector (generally 10−20 cm). During this process, the evaporation of a solvent reduces the diameter down to the nanometer range and obtains a continuous nanofiber on the collector.

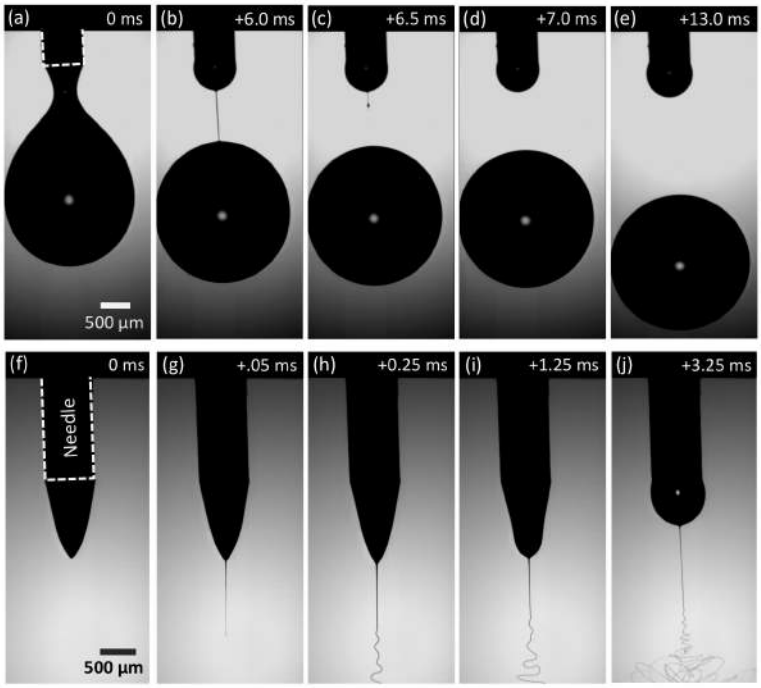

Figure 2.2: High-speed images of polymer solution (polyacrylonitrile/dimethylformamide, PAN/DMF) recorded at 20,000 fps, show the evolution in time of; (a-e) falling droplet from a needle at 0 kV; (f-j) electrospinning process at 10 kV, the time zero is recorded when the droplet of PAN/DMF solution transformed to a conical shape (Taylor cone). Just after 0.05 ms, a solution jet is emerged from the tip of the cone. The solution jet has an instability, so whipping occurs in which the jet travels and rapidly elongates between the tip and the collector. About 3 ms later, the shape of the cone is changed to a rounded shape, here is a steady state of the droplet.

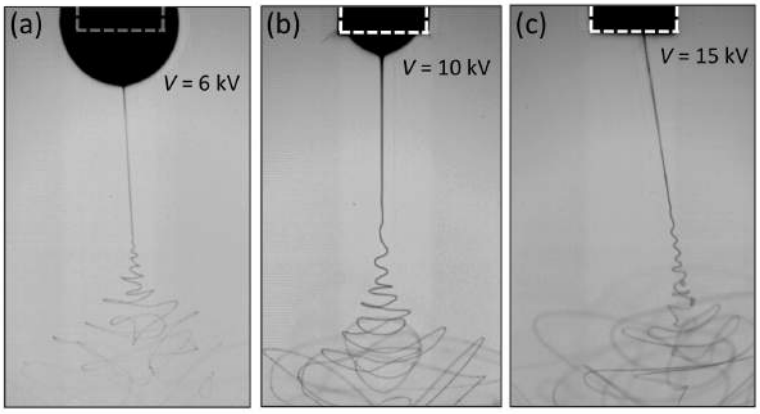

Figure 2.3: High-speed images of PAN/DMF solution recorded at 20,000 fps, demonstrate shape and size of the hanging droplet, depended on flow rate and applied voltage. In case the flow rate is fixed at 0.5 ml/h, and the distance is fixed at 15 cm; (a) V = 6 kV, the droplet size increases, (b) V = 10 kV, here is a steady state of the droplet, and (c) V = 15 kV, the droplet size decreases.

Therefore, the electrospinning process can be divided into three regimes (see Fig. 2.4).

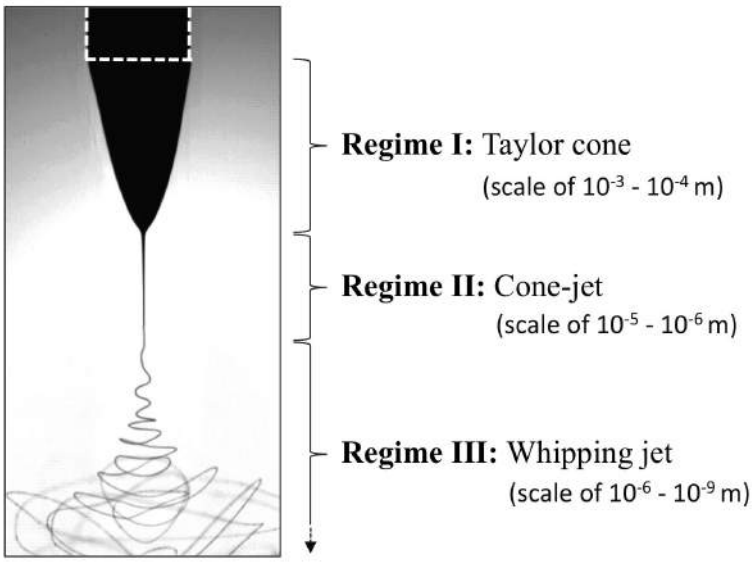

Figure 2.4: Three regimes of electrospinning process; (I) Taylor cone, (II) cone-jet, and (III) whipping jet.

Regime I. Taylor Cone: In the first step, the conical formation occurs from a combination of charge repulsion and surface tension, which always tries to form spherical droplets (see schematic of experimental setup in Fig. 2.5). When the high voltage is applied to the needle, an electric field is generated between the needle and collector. Therefore, an electric stress is induced on the droplet with both normal and tangential components. At the optimized parameters of electric field, the electrical stress will overcome the surface tension of the solution leading to the Taylor cone. In the case of a cones surface has an equipotential and the cone exists in a steady state equilibrium, a critical voltage V_c can be estimated by Eq. 2.1, which was identified by Taylor [3–5].

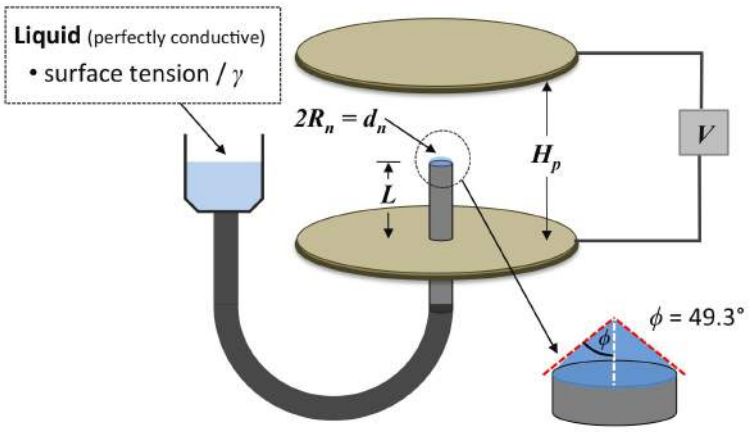

Figure 2.5: Schematic of the two-plate apparatus (adapted from [5]).

$$V_{c\,(cgs)}^2 = \frac{4H_p^2}{L^2}\left(ln\frac{2L}{R_n} - \frac{3}{2}\right)2\pi\gamma R_n cos\phi\,, \tag{2.1}$$

where H_p is the distance between tip of the needle and the collector, L is the length of the needle, R_n is the radius of the needles orifice, and γ is the surface tension of the solution. All quantities are in the centimeter-gram-seconds (cgs) units; V_c = statvolt; H_p, L, R_n = cm; and γ = dyne/cm. The ϕ is the Taylor cone angle, which is a semi-vertical angle required to form a cone shape just before a jet formation. For an electrically conductive solution, the ϕ is 49.3°. Hence, $2cos\phi$ = 1.30 and then;

$$V_{c\,(cgs)}^2 = \frac{4H_p^2}{L^2}\left(ln\frac{2L}{R_n} - \frac{3}{2}\right)1.30\pi\gamma R_n\,. \tag{2.2}$$

Since one statvolt equals 2.998x10^2 V and one dyne equals 10^{-5} N in the meter-kilogram-seconds (mks) units, therefore the Eq. 2.2 must be multiplied by factor 0.9x10^{10};

$$V_{c\,(mks)}^2 = \frac{4H_p^2}{L^2}\left(ln\frac{2L}{R_n} - \frac{3}{2}\right)1.30\pi\gamma R_n\left(0.9\times10^{10}\right)\,. \tag{2.3}$$

Note that the Taylor cone angle of the polymer solutions fed in electrospinning is smaller than 49.3° because these solutions are not perfectly conductive. In case of the PAN/DMF solution (shown in Fig. 2.2f), the Taylor cone has the angle about 35°. Yarin et al. reported the experimental and theoretical studies of the Taylor cone angle of the polymer solution, finding that the angle is equal 33.5° [6]. Therefore, the value of V_c for electrospinning might be a bit higher than Eq. 2.3 (the $2cos\phi$ is 1.67 rather than 1.30) as following:

$$V_{c\,(mks)}^2 = \frac{4H_p^2}{L^2}\left(ln\frac{2L}{R_n} - \frac{3}{2}\right)1.67\pi\gamma R_n\left(0.9\times10^{10}\right)\,. \tag{2.4}$$

For example, PAN/DMF solution (the surface tension γ is ~30 mN/m [7]) fed through a needle with the radius R_n of 0.3 mm, the length L is 5 cm, and the distance to the collector is 10 cm, so the H_p is ≈0.1 m. The V_c can be estimated by Eq. 2.4. For this case, the V_c is ~5 kV.

Regime II. Cone-jet: Above V_c, the tangential electric stress accelerates charge carriers in the solution toward the grounded collector in an attempt to complete the circuit (see Fig. 2.6). The drift velocity of ions in a solution can be calculated by multiplying the electric field by the ion mobility. It is so high that it causes the cone to eject either a spray or a jet of the solution, depending on its viscosity [8, 9]. The speed of the solution jet increases when far away from the needle tip and increasing with applied voltage. The values have been estimated using a high-speed camera or a laser doppler velocimetry to be about 0.5−5 m/s [10, 11]. In the case of polymer fluids, a solution jet diameter d_j in this regime can be predicted by the nonlinear rheological constitutive equation

(Eq. 4.1) [12, 13].

$$d_j = 4\left(\gamma\varepsilon_0\frac{Q^2}{I^2}\right)^{1/3}, \tag{2.5}$$

where d_j is a jet diameter, γ is a surface tension, and ε_0 is permittivity of a vacuum.

The electrohydrodynamic of the cone-jet regime was experimentally investigated [14–16] and a scaling law of the current I versus the flow rate Q has been reported in two cases; for highly conducting liquids (polar liquids), $I \sim Q^{1/2}$ [17], and for low polarity liquids, $I \sim Q^{1/4}$ [18]. This translates into $d_j \sim Q^{1/3}$ and $d_j \sim Q^{1/2}$, respectively.

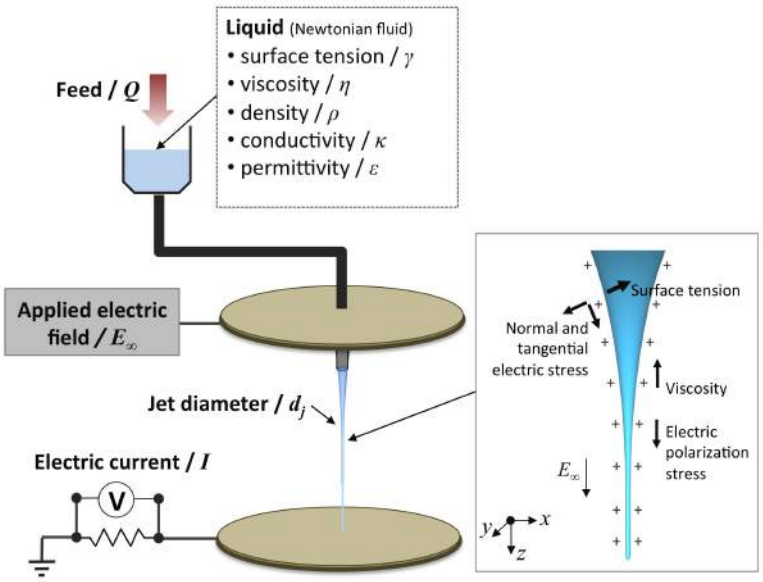

Figure 2.6: Schematic of the parallel-disk fiber spinner apparatus (adapted from [19]). Square box is the diagram of forces acting on a droplet of the viscous solution (adapted from [9]).

Regime III. Whipping jet: After the solution jet is ejected from the bottom of the Taylor cone, it will remain stable for a certain distance, depending on the solution properties and electrical configuration. The straight solution jet can be defined where the flow direction is parallel to the axis of the jet (z-direction). But in the instability region as shown in Fig. 2.4, a bending perturbation is continuously present. The bending motion accelerates rapidly and forms an irregular coil under the influence of the charge carried with the jet. Therefore, the Coulomb forces perturb the electrospinning jet [11]. The trajectory of each short segment of the coil is roughly perpendicular to its axis. The continuing electrical bending generates a coil with many turns, which expands in diameter as the jet continues to elongate in response to the Coulomb repulsion of the charge. Additionally, the effect of solvent evaporation has to be considered. Therefore, both the elongation, forced by the electric field, and the evaporation thin the jet.

A quantitative analysis of the whipping jet has been developed by Hohman et al. and Fridrikh et al. The jet is treated as a slender viscous object and assumes that the fluid is the Newtonian and elastic effects due to the solvent evaporation are neglected. The equation of motion for normal displacement x derives as Eq. 2.6 [19–22].

$$\rho\pi d_j^2\ddot{x} = \underbrace{2\pi d_j\sigma_0 E_\infty\cdot\hat{n}}_{\text{Term I: Thinning jet}} + \underbrace{\left(\pi\gamma + \frac{d_j\varepsilon_0}{2}(\varepsilon-1)(E_\infty\cdot\hat{t})^2 - \frac{2\pi^2 d_j\sigma_0^2}{\varepsilon_0}(2ln\chi-3)\right)\frac{d_j}{R_w}}_{\text{Term II: Whipping jet}}, \tag{2.6}$$

where d_j is a jet diameter, σ_0 is a surface charge density, γ is a surface tension, ε is the permittivity of the fluid (the permittivity of air ($\bar{\varepsilon}$) equals 1.0006, so $\bar{\varepsilon}\cdot\varepsilon_0 \approx \varepsilon_0$), E_∞ is an electric field vector, $\hat{n}$ and $\hat{t}$ are the unit vectors which are normal and tangential to the centerline of the jet, $\chi \sim R_w/d_j$ (R_w is radius of whipping curvature, so the χ is around 10^3–10^4).

The "Term I" is an electrostatic force due to the external electric field interacts on the surface charge of the jet. The "Term II" is the normal stress, affecting the whipping instability of the jet. This "Term II" consists of the stability and the instability term as described below;

- **Stability term:** $\pi\gamma + \frac{d_j\varepsilon_0}{2}(\varepsilon-1)(E_\infty\cdot\hat{t})^2$ This part is the stabilizing effect due to surface tension and the electric field in the direction of the jet ($E_\infty\cdot\hat{t}$). When the jet diameter (d_j) is very small, the effect from the surface tension is more importance than the electric field.
- **Instability term:** $-\frac{2\pi^2 d_j\sigma_0^2}{\varepsilon_0}(2ln\chi-3)$ This term is the instability, affected by the surface charge repulsion.

Whipping of the jet can be estimated by comparison between stability (the effect from the surface tension) and instability (the effect from the surface charge repulsion). When

$$\pi\gamma \geq 2\pi^2 d_j(z)\,\sigma_0(z)^2\,(2ln\chi-3)/\varepsilon_0, \tag{2.7}$$

the "Term II" is positive, so the jet is stable. Conversely, when the surface charge repulsion dominates, the jet becomes unstable and the whipping jet grows. Because of this whipping instability, the jet dramatic stretches; hence, the terminal fiber diameter (d_f) is achieved. The value of d_f can be predicted by

$$d_f = \left(\gamma\varepsilon_0\frac{Q^2}{I^2}\frac{2}{\pi(2ln\chi-3)}\right)^{\frac{1}{3}}. \tag{2.8}$$

Because $ln\chi$ varies not much, the Eq. 2.8 can be compared with the Eq. 4.1: $d_f \approx 0.1 d_j$, so the whipping causes shrinking by a factor of ≈ 10. However, Eq. 2.8 ignores evaporation of the fluid and the elastic effects, so the d_f is higher than the experiment results. There is no complete theory exists that can describe or predict the process with quantitative accuracy. Nevertheless, the

Table 2.1: The list of process conditions and solution parameters affects to electrospun nanofibers.

Parameters	Effect to diameter of the fibers	Eq.
Process conditions:		
($V > V_c$) Applied voltage*	⇓	(2.4)
(H) Distance to collector*	⇓	(2.4)
(Q) Flow rate*	⇑	(2.8)
(I) Current	⇓	(2.8)
Solution parameters:		
(η) Viscosity*	⇑	-
(κ) Conductivity*	⇓?	(2.8)
(ε) Dielectric constant of liquid	⇑	(2.8)
(γ) Surface tension	⇑	(2.4 and 2.8)

* most important variables
⇑ diameter of the fibers increases
⇓ diameter of the fibers decreases
? not always

Eq. 2.4 and 2.8 present some parameters affecting to diameter of the fiber as shown in Table 2.1. The conclusions point out that a small fiber can be produced by electrospinning at a high applied voltage, and at a low liquid flow rate, also the collector should be placed very far from the tip.

Notice that viscosity of liquid is not included in all equations presented above. Some common dimensionless groups in fluid mechanics might give the clues about the effects from the viscosity, e.g. the Reynolds number (Re), the Weber number (We), and the Capillary number (Ca) [23–26]. However, the Re, We and Ca vary with the characteristic flow speed (υ). In some cases a jet can be self-thinning, so the internal velocity in the fluid is much faster than the characteristic velocity υ [27]. This requires a dimensionless number that is independent of the velocity. The process speed can be examined in term of "time scale", e.g. an inertial or the Rayleigh time-scale ($t_R \sim \sqrt{\rho d^3/\gamma}$), viscous time scale ($t_{vis} \sim \eta d/\gamma$), and a polymeric time scale ($t_{poly} \sim \lambda$, where λ is a relaxation time). d is a characteristic length scale (generally is drop diameter or jet diameter (d) $\sim d_j$. For free-surface flows of Newtonian fluid,

- **The Ohnesorge number** (Oh) is defined as the ratio of the viscous time scale to the Rayleigh time-scale ($Oh = t_{vis}/t_R$), so the Oh is estimated by

$$Oh \sim \frac{\eta}{\sqrt{\rho d \gamma}} . \tag{2.9}$$

  In addition, this number means also relative effect from the viscous force to surface tension. Hence, the Oh can be thought of as $Oh \equiv \sqrt{We}/Re$, or $Oh^2 \equiv Ca/Re$ [28]. The Ohnesorge number is commonly used to characterize the jet breakup (independent of the process velocity) for an inkjet printing or a spraying technology. If the Oh is low ($Oh < \sim 1$), droplets and

also satellite droplets will form [29, 30]. A high Oh ($Oh > \sim 1$) causes the viscous forces to prevent the formation of droplets. For a liquid with $\eta \geq 0.1$ Pa.s ($100 \cdot \eta_{water}$), this Ohvalue ($Oh > \sim 1$) is fulfilled even for the largest jets in electrospinning ($d \approx 1$ mm) since $\rho \approx 1000$ kg/m^3 and $\gamma \approx 0.01$ N/m vary little.

For free-surface flows of the viscoelestic or the non-Newtonain fluids (e.g. polymer solution), they can be characterized by a dimensionless number called the Deborah number, originally proposed by M. Reiner [31].

- **The Deborah number** (De) is defined as the ratio of the polymeric relaxation time to the Rayleigh time-scale ($De = t_{poly}/t_R$):

$$De \sim \frac{\lambda}{\sqrt{\rho d^3/\gamma}} . \tag{2.10}$$

  The De physically represents the relative between response time and observation time (here means the observation of a breakup into droplets). For a liquid with $\rho \approx 1000$ kg/m^3, $\gamma \approx 0.01$ N/m, and $d \approx 1$ mm downs to 100 nm, the t_R varies from 10^{-2} to 10^{-8} s. Furthermore, the De is defined to account for the degree of non-Newtonian behavior in a fluid flows. At a high De, a material behaves like in the non-Newtonian regime.

McKinley et al. reported the usage of the Oh and De to define a two-dimensional "operating space" for an inkjet printing and and electrospinning or other self-thinning free surface processes involving non-Newtonian fluids [24,25]. The operating diagram in Fig. 2.7 proposes that the inkjet printing needs neither long elastic tails nor inertially-induced satellites; hence, the dimensionless numbers of the suitable liquid should be $De \approx Oh \approx 1$. While the electrospinning requires a liquid which can form a uniform filament without beads, so the fluid rheology and the geometry should be $De \geq Oh \geq 1$. To achieve these conditions; all three inequalities must be fulfilled as following:

- **Ineq. 1:** The first inequality is $Oh \geq 1$ (see Eq. 2.9), because the density of the liquid ρ (in the order of magnitude 1000 kg/m^3 = 1 g/ml) and the surface tension γ (in the order of magnitude 10 mN/m) are rather constant. Hence, the Oh depends on the jet diameter d_j, but more strongly on the viscosity of the liquid η. For the lowest viscosity considered in the electrospinning ($\eta_{pure\ water}$ = 1 mPa.s), one finds $Oh < 1$ above 100 nm jet diameter. So the electrospinning, which starts from a thicker jet, is impossible for low viscosities. The critical range ($Oh = 1$) translates into a minimal viscosity of around 10 mPa.s (comparable to ethylene glycol), for which the jet needs to be thinner than 10 μm, which is already in the case that closes to the jet source (a droplet or and orifice).

- **Ineq. 2:** The next inequality is $De \geq 1$ (see Eq. 2.10). The typical system time or the observation time is t_R, the time required for breaking up into droplets according to the Rayleigh-Plateau instability. Again ρ and γ can be taken as nearly constant. The t_R values span an extreme range: 10 ps for a quasi-molecular jet of 1 nm diameter (this is comparable to the reorientation times of molecules in solution, which would indeed lead to break-up of such

the jet); 10 μs for a 10 μm jet, closing to the source. The problem is that the relaxation times λ are not well known. Stelter et al. [32] find the values in the ms to s range, measured by elongational viscosimetry (measure stretching of a liquid jet with the capillary break-up elongational rheometry (CABER) method). The lower technical limit is in the ms range, such that $De \geq 1$ is always fulfilled. Of course a relaxation time and thus a non-Newtonian behavior with respect to stretching have to be present.

- **Ineq3:** In the final inequality, the electrospinning also requires $De \geq Oh$. This means that

$$\frac{\lambda}{\sqrt{\rho d^3/\gamma}} \geq \frac{\eta}{\sqrt{\rho d \gamma}}\,, \tag{2.11}$$

this simplifies to

$$\lambda \geq \frac{\eta d}{\gamma}\,. \tag{2.12}$$

Setting $\gamma \approx 10$ mN/m, the most challenging case would combine the thickest jet of 10 μm diameter with the highest viscosity that is usually handled (10000 mPa.s, corresponding to a honey). Even this situation would merely require the relaxation time above 10 ms, which is easily reached by sing the polymer solutions [32]. As for the argument of $De \geq 1$, a relaxation time and a non-Newtonian behavior with respect to stretching must be present.

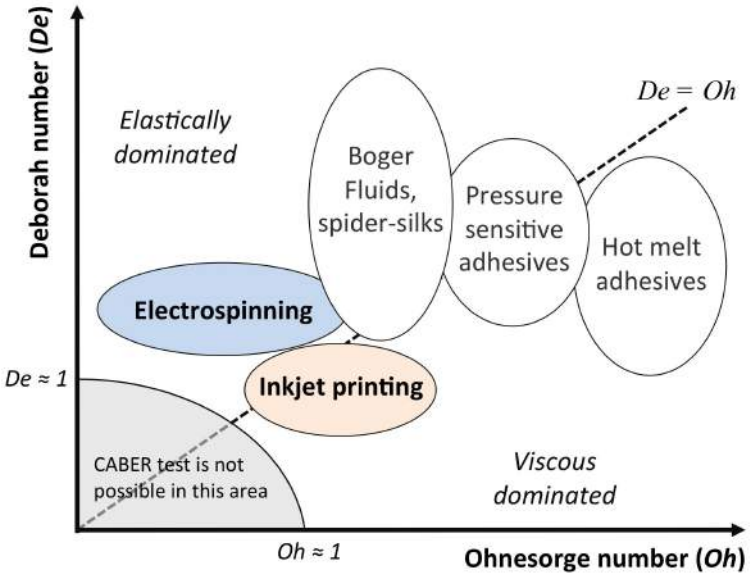

Figure 2.7: Operating diagram for complex fluids organized in terms of the natural time scales for capillary, viscous, and elastic phenomena (adapted from the work of McKinley [24]). Gray area indicates the *De* and *Oh* that cannot be measured by the CABER method. The low limit of the *Oh* is found to be 0.14 reported by McKinley and co-workers [33].

The qualitative analysis of the whipping jet (include the effect from the viscosity) based on the viscoelastic models and use of the relaxation time has been developed by Reneker et al. [34], and improved the paths of the jet by Kowalewski et al. [35]. Both models can demonstrate the whipping instability in the regime III and reproduce qualitatively nanofiber bending. However, the models cannot predict the process with quantitative accuracy except semiquantitative for the Newtonian fluid.

2.2 Biomolecules

A biomolecule is a molecule that naturally occurs in living organisms [36]. There are four major classes of biomolecules based on their structures and functions.

2.2.1 Proteins

Proteins are the majority biomolecules produced in a cell. These molecules are responsible for many functions and structures in all living organisms. Without proteins, life on the planet earth may not exist. Subunit of proteins is "amino acids". There are over 100 natural amino acids. However, only 22 of them are standard amino acids- 20 are encoded by the universal genetic code and two (selenocysteine, pyrrolysine) are incorporated into proteins by unique synthetic mechanisms. All standard amino acids (except the pyrrolysine) can be found in eukaryotes. Binding of only 22 amino acids with different orders makes up long chains, so called polypeptides, with different sequence, forming millions of different proteins in living beings.

Structures of protein are divided into four levels, i.e. primary, secondary, tertiary, and quaternary structure. For example the hormone insulin (see Fig. 2.8), which is a protein consisting of two polypeptides called "A chain" and "B chain" as an example. The primary structure of insulin is a sequence of amino acids, 21 amino acids for the A chain and 30 for the B chain. The amino acids in the sequence are linked together chemically. In addition, there are noncovalent interactions (e.g. hydrogen bonds) among them, so the secondary structure of a protein occurs, i.e. α-helices, β-strands, and loops (see in the secondary structure, Fig. 2.8). The third level presents when the secondary structures folded to compose a protein, this case is a monomer of insulin (active form, means it can control metabolic processes). The tertiary structure is mainly stabilized by disulphide bonds between thiol groups (-SH) on the Cys residues. The last level is the quaternary structure, which is a combination of tertiary structures to create a larger unit or complex. For example, six insulin molecules form into granule (by interactions between hydrophobic surfaces) around two zinc ions. This form is inactive, but allows the insulin to be stored in bloodstream.

Because of the huge numbers of protein, they can be classified in different ways based on their solubility, shape, composition, function, and etc. On the basis of shapes, it is divided into three major classes as follows.

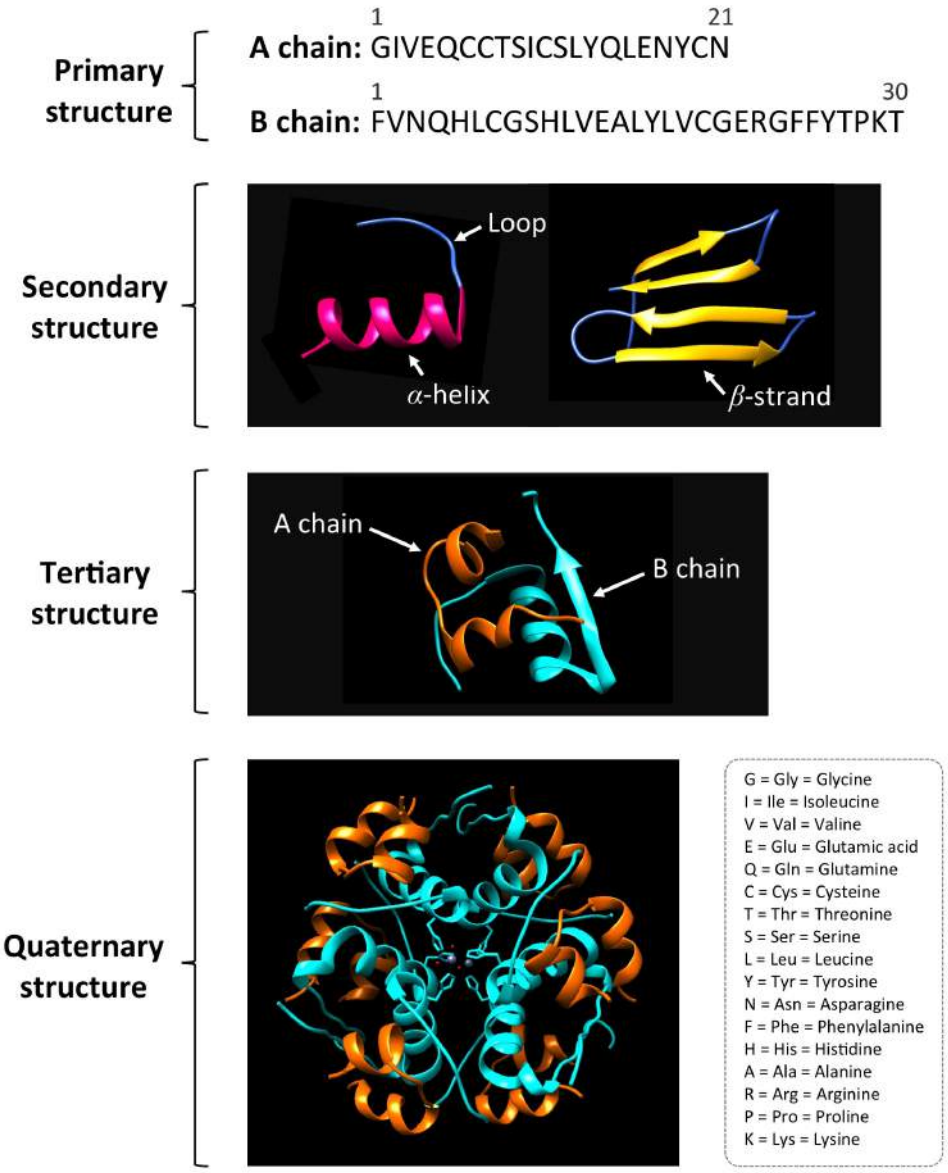

Figure 2.8: Structure levels of hormone insulin, which is a protein consisting of two polypeptides called "A chain" and "B chain". The primary structure is a sequence of amino acids, 21 amino acids for the A chain and 30 for the B chain. Because hydrogen bonds between amino acids in the sequence, the secondary structure of a protein occurs, i.e. α-helices, β-strands, and loops. The tertiary structure is based on folding all secondary structures into the final 3D shape, as here shown for the insulin monomer. Finally, the quaternary structure can occur when tertiary structures (or non-protein structures) are combined to protein complexes, e.g. six insulin molecules form into granule (hexamers insulin).

Fibrous proteins or scleroproteins are elongated proteins, the shape forms long ribbon-like or fiber (aspect ratio >10). They are not soluble in water or in solution of dilute acids. These proteins generally have protection and structural support functions, so they are the most abundant proteins in the animals (by mass). Examples of fibrous proteins are collagens (in tendons, bone, connective tissue), keratins (in wool, fingernails), myosins (in muscle tissue), elastins (blood vessels, ligaments), and fibrins (blood clots). Since they naturally form fiber-like shapes, it was possible for them to electrospin into fibers. Most fibrous proteins have dissolved in an organic solvent such as hexafluoroisopropanol (HFIP) and then electrospun into fibers, i.e. collagens from calfskin and human placenta [37], fibrinogens from human and bovine [38], elastins from bovine [39]. Both biocompatibility and mechanical properties, the fiber mats of fibrous proteins are considered promising for tissue-engineering scaffold. In the case the electrospun fibrous proteins displays poor mechanical properties such as the soluble elastin, blends with synthetic polymers can improve the structural of the scaffold [40].

Globular proteins or spheroproteins are very compactly and extensively folded proteins, hence their 3D structures tend to be formed into a spherical or globe-like shape (aspect ratio ≤10). They are soluble in water, and can therefore travel through the blood and perform various functions, e.g. catalyzing metabolic reactions, transporting molecules, regulation, and transmitting biological messages. The number of different kinds of globular protein is much larger than the fibrous protein. For example; insulin (a hormone for controlling glucose metabolism and the first protein was sequenced by Frederick Sanger in 1949), hemoglobin (an oxygen transporter in blood and one of the first protein was solved its structures by Max Perutz in 1958), myoglobin (an oxygen transporter in muscles, its structure was solved by Sir John Cowdery Kendrew in the same year), albumin (main protein of human blood serum and egg white, which is one of the first proteins from animal sources recognized as a distinct class of biomolecules by Antoine Fourcroy in 1789). Because of the spherical shape, only few pure globular proteins have been electrospun into fiber compared to huge numbers of proteins in this class: hemoglobin, myoglobin [41], and bovine serum albumin (BSA) [42]. In these cases, the globular proteins were dissolved in an organic solvent such as trifluroethanol (TFE) to obtain electrospun fiber. Zussman and co-workers proposed that the dissolved BSA proteins are opened and elongated, which are suitable for electrospinning [42]. However, this mechanism is not clearly understood. It is possible that the globular proteins become denatured when it is dissolved and also between the electrospinning process. The opened and elongated proteins, in most cases, are denatured, and therefore lose their function (not only geometry changes).

Membrane proteins are embedded in cell membrane, and play important roles in the membrane functions, e.g. transporting of molecules and ions, relaying signals through a cell, and controlling adhesion of a cell to another cell. The most common shapes are bundles of α-helices (found in all types of biological membranes) and barrel-shape arrangement of β-sheets. More than 25% of human proteins are membrane proteins but the structure of less than 1% has been resolved [43]. Electrospinning of pure membrane proteins have not been yet reported.

2.2.2 Nucleic acids

Nucleic acids are one of the organic macromolecules found in all living cells, and was first discovered in the nucleus of cells. These molecules serve as informational molecules because their primary structure contains a genetic code, which guide the synthesis of proteins and they can duplicate themselves. Subunit of nucleic acids is "nucleotide". A nucleotide has three chemically distinct components consisting of a monosaccharide (5-carbon sugar), a nitrogenous base, and a phosphate group (negative ion).

There are two types of 5-carbon sugar in the nucleic acids, which are polymers found in all living cells. In case the sugar is deoxyribose, the polymer is deoxyribonucleic acid (DNA), which is found mainly in the nucleus of the cell. While when the sugar is ribose, the polymer is ribonucleic acid (RNA), which is found mainly in the cytoplasm of the cell. The DNA contains the genetic codes to produce RNA, while the RNA contains the codes for the primary sequence of amino acids to synthesis proteins. For the nitrogenous base, five bases are used in the construction of nucleotides. The five bases are divided into two classes; 1) purines (double-ringed structures) including adenine (A), guanine (G); 2) pyrimidines (single-ringed structures) including thymine (T), cytosine (C), and uracil (U). The DNA double helix structure is stabilized primarily by hydrogen bonds between these bases (A-T and G-C), including base-stacking interactions among the aromatic rings. Counter-ions such as Na^+, K^+, and Mg^{2+} are essential to stabilize the double-helical structure because each phosphate group of nucleotide has one negative charge, so the backbone of polynucleotides are highly negative charged and have strong repulsion between the two strands.

Electrospinning of calf thymus Na-DNA (counter-ion is Na^+) in an aqueous solution has been first reported by Fang et al. [44]. The diameter of electrospun DNA is 30−80 nm, electron microscopy results supposed that a single DNA fiber with the diameter of 62 nm consists of ~600 DNA molecules. Takahashi et al. is another group who can electrospin pure salmon testis DNA onto a mica substrate [45].

2.2.3 Carbohydrates

Carbohydrates or polysaccharides are long chains of sugars. These molecules are responsible for the energy source of a cell, constructing structures such as cell wall of green plants, and also forming a part of DNA and RNA. Subunit of carbohydrates is "monosaccharide" (saccharide means sugar or sweetness, sugar is derived from French *sucre*, from Arabic *sukkar*). All simple subunits have the general empirical formula $(CH_2O)_n$, where n is an integer number ranging from 3 to 9 (usually 5 or 6). The saccharides are aldehydes or ketones (C=O group) that have at least one (usually 4 or 5) hydroxyl group. In aldehydes, the C=O group is bond to one carbon and one hydrogen atom, while in ketones, to two other carbon atoms. Examples of saccharides are glucose (the major source of energy for a cell), galactose (found most readily in milk and dairy products) and fructose (found in most vegetables and fruit). The saccharide can be covalently linked to another biomolecule subunit, e.g. an amino acid or a lipid. These compounds occur in such as

glycoproteins and glycolipids. Generally, monosaccharides bind chemically together and form polysaccharides such as carbohydrate structures including cellulose and starch.

Some carbohydrates have been electrospun, e.g. a bacterial polysaccharide (dextran) [46], chitosan [47], cellulose [48], cyclodextrin [49]. In particular, Stijnman et al. investigated electrospinnability of food-grade polysaccharides and reported that aqueous solutions of dextran, pullulan, and maltodextrin (glucidex DE2) can be electrospun to fibers when the solutions have concentrations of 15−50 %(wt/wt) and present a weak shear thinning at shear rates below 1000 s^{-1} [50].

2.2.4 Lipids

Lipids are broadly defined as hydrophobic or amphiphilic small molecules. These molecules are responsible for storing energy, signaling, and also serve as structural components of cell membranes. The characteristic properties of lipid are generally not soluble in water but soluble in nonpolar solvents. Lipids are composed of long hydrocarbon chains (-CH_2-). For example, fatty acids, $CH_3(CH_2)_{n-2}COOH$ with $n > 10$. Some lipids are phosphorylated, i.e. containing phosphate group. These are phospholipids (found in cell membrane) such as lecithin.

McKee et al. reported that lecithin can transform from amphiphilic molecules to entangled wormlike micelles when the lecithin is dissolved in a mixture of chloroform and dimethylformamide at high concentration (above 40 %(wt/wt)). The cylindrical micelles can be overlapped and entangled similar to polymers. Hence high concentrated lecithin can electrospin and forms fiber network [51].

2.3 Peptides

Peptides are compounds containing two or more amino acid residues linked together chemically by peptide bonds. If there are only two amino acids, the peptide is called a dipeptide. Similarly there are tripeptides, tetrapeptides, containing three and four amino acids, respectively. If the number of amino acids in the chain is around ten or more, such substances are called “polypeptides”, while large polypeptides are called “proteins”. There is no particular agreed size at which a large polypeptide becomes a small protein, but generally polypeptides have molecular weights of a few kDa, while proteins have molecular weights of tens of kDa. In this thesis, short aromatic peptides were used in Chapter 4, their molecular weights are below a thousand. In Chapter 5, globular proteins were studied. They have molecular weight higher than 10 kDa, except for insulin which has the molecular weight of around 6 kDa, so it can be called a polypeptide.

2.3.1 Structure of peptides

Peptide comprises amino acids, which are organic compounds containing an amino group (-NH_2), a carboxylic acid group (-COOH), and any of various side groups (*R*-group) (see Fig. 2.9a). Generally, the amino group is attached to a carbon atom (C_α) next to the carboxyl group. In addition, the side group and a hydrogen atom are attached to this carbon atom. Hence, the C_α is a chiral carbon atom. Therefore, all amino acids are chiral molecules (except for glycine because this amino acid has two hydrogen atoms attached to the C_α) that can exist in two enantiomers called L- and D-amino acids.

Amino acids act as a subunit of peptide and protein (all amino acids that naturally occur in proteins are L-form). They are linked together by peptide bonds between the -NH_2 group of one amino acid and the -COOH group of another amino acid. Amino acids can bind together in this way to form dipeptides, polypeptides and proteins. Figure 2.9b shows two amino acids of phenylalanine (Phe or F) linked together by a peptide bond between the -NH_2 and -COOH group, water is eliminated, and the final product is a dipeptide "diphenylalanine" (Phe-Phe or FF). A peptide containing aromatic amino acids, e.g. phenylalanine (Phe), Tyrosine (Tyr), can be defined as an "aromatic peptide". If this peptide contains a few amino acids, it can be specified as "short aromatic peptide".

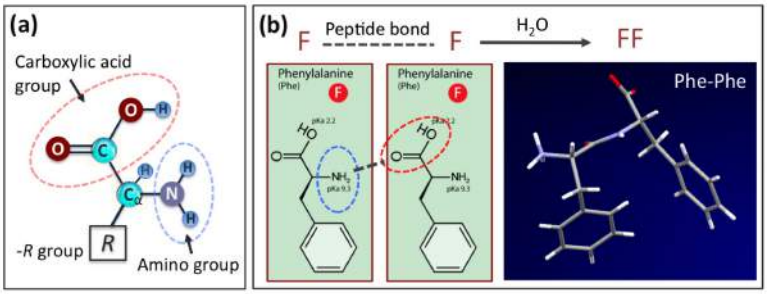

Figure 2.9: (a) Structure of amino acid with an amino group (-NH_2), a carboxylic acid group (-COOH), and any of various side groups (*R*-group), (b) Example of dipeptide Phe-Phe, linked by peptide bond between two amino acids of Phe.

Peptides used in this thesis mainly contain amino acid phenylalanine (Phe), glycine (Gly) and cysteine (Cys). Figure 2.10 illustrates their molecular structures with pK_a values, which represent the ionization state of the site under physiological conditions. The pK_a is defined by Eq. 2.13. In case the pH is higher than the pK_a, the site is mostly deprotonated. Conversely, when the pH is lower than the pK_a, the site is mostly protonated. This means that in the range of weak or medium strong acids (pH>4) and weak bases (pH<9), the carboxylic acid protonates the amine group, so peptides are normally zwitterions H_3N^+-CHR-COO^-. In medium strong to strong acids (pH<2), they are protonated H_3N^+-CHR-COOH (cationic).

$$pK_a = pH + lg\left(\frac{conc.\ protonated}{conc.\ unprotonated}\right) \tag{2.13}$$

Each amino acid has the following properties:

- **Phenylalanine:** Phe is an essential amino acid because it cannot be synthesized in the human body. Its chemical formula is $NH_2CH(CH_2C_6H_5)COOH$. It is classified as nonpolar because of the hydrophobic nature of the aromatic side group. The hydrophobic property of Phe is stronger than other amino acids that contain aromatic side groups, i.e. tyrosine (Tyr, Y) and tryptophan (Trp, W). Its strong hydrophobicity allows the structure of Phe always buried inside hydrophilic proteins. The π electrons of the phenyl ring interact with other molecules containing π electrons, and this stabilizes the protein by stacking to other aromatic structures.

- **Glycine:** Gly is a non-essential amino acid that can be manufactured in the liver. It is the only amino acid that does not have enantiomer. Its chemical formula is NH_2CH_2COOH, and it is the smallest among the 20 amino acids commonly found in proteins. Because of its small size, Gly can be placed into tight spaces of proteins where other bigger amino acids can not fit. Most proteins contain small amount of Gly, except for collagen which contains 35%. The presence of Gly residues tends to interrupt the helix formation. Gly is often found in portions of proteins involved in turns.

- **Cysteine:** Cys is a semi-essential amino acid. It can be biosynthesized in human body, except for infants, the elderly or patients with metabolic disease. Its chemical formula is $NH_2CH(CH_2SH)COOH$. The SH group can be deprotonated by bases. Cys is slightly hydrophobic. The side group of Cys is sulfhydryl (or thiol), which is more reactive than hydroxyl group, and two of them form stable disulfide bonds (S-S) upon oxidation (removal of H atoms). The most important characteristic of Cys may be its ability to stabilize protein structure by forming disulfide linkages with other cysteine molecules. These covalent cross links add stability to the 3D structures of proteins.

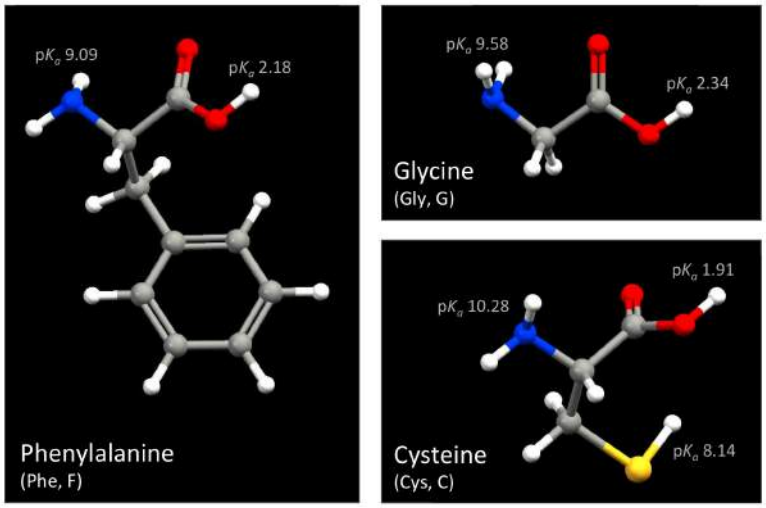

Figure 2.10: 3D molecular structures of amino acid Phe, Gly and Cys with their pK_a values. The 3D structures are downloaded from PubChem database [52] and imaged by the Mercury software 2.2 (Build RC5) [53], carbon, oxygen, nitrogen, sulfur, and hydrogen atoms are represented in grey, red, blue, yellow, and white, respectively.

2.3.2 Self-assembly of peptides

As mentioned in the introduction (section 1.1), nanofibers can be produced by self-assembly. The production is based on a bottom-up approach for fabricating nanostructures. Molecular self-assembly can form 3D crystals or 1D nanofibers and nanotubes. This occurs by intermolecular interactions, e.g. Van der Waals, electrostatic interactions, hydrogen bonds, and π-stacking interactions [54]. This section describes three main model systems to archive formation of nanostructures based on non-covalent interactions of peptides.

- **Assembly of cyclic peptides:** (see Fig. 2.11a) Ghadiri and coworkers were the first group to describe the formation of cyclic polypeptides (e.g. octapeptide *cyclo*[-(L-Gln-D-Ala-L-Glu-D-Ala)$_2$-]) to nanotubes [55, 56]. The L, D, L, D,.... sequency with the non natural D-amino acids express all side chains outward. The nanotube formation is based on the stacking of closed cyclic structures to form an array of tubes. E.g. *cyclo*-[(L-Glu-D-Leu)]$_4$, and *cyclo*-[(L-Lys-D-Leu)]$_4$, were assembled under favorable conditions to reach a continuous hydrogen-bonded hollow tubular structure. Characterization by FTIR supports that the self-assembled nanotubes have characteristic features of hydrogen-bonded β-sheet structure [55, 57]. Moreover, the results demonstrated that cyclic peptides are able to form artificial transmembrane channels for ion and glucose transport, and antibacterial activity [56, 58–61].

- **Assembly by hydrophobic interactions:** (see Fig. 2.11b) This model uses designed peptide-amphiphile molecules to self-assemble into nanofibers based on hydrophobic interactions. The first system were designed and reported by Hartgerink et al. who found that the building blocks contain a hydrophobic alkyl tail (see Fig. 2.11b, in the region 1) and hydrophilic peptide regions (see Fig. 2.11b, in the region 2-5). The hydrophobic parts of the peptide form a water-protected core and the hydrophilic parts are directed to the aqueous phase, resulting formation of nanofibers [62, 63]. The hydrophilic regions can be designed with various peptides, e.g. peptide RGD (Arginine-Glycine-Aspartic acid) for increasing the cell adhesion [63, 64], IKVAV (Isolucine-Lysine-Valine-Alanine-Valine) to promote neurite sprouting and to direct neurite growth [65]. Similarly system was reported by Vauthey et al. who found that both hydrophobic and hydrophilic parts are amino acid moieties (7-8 residue peptides) [66]. Each building block is about 2-3 nm in length and has properties very similar to biological surfactant molecules, hence this designed peptide was called “surfactant-like peptides”. For example the peptides are AAAAAAD, VVVVVVD, VVVVVVDD, and LLLLLLDD. Aspatic acid (D) conveys negative charges and hydrophilic, while alanine (A), valine (V), and Leucine (L) establish hydrophobic tails.

- **Assembly by aromatic interactions:** (see Fig. 2.11c) Recently, Gazit and coworkers reported that aromatic stacking interactions may provide energetic contribution in the self-assembly of amyloid structures (which are mainly based on hydrogen bonding). They demonstrated that the short aromatic peptide diphenylalanine (Phe-Phe, FF) can self-assemble in solution to mimic amyloid fibrils. Similar fibrils can result in neurodegenerative diseases, e.g. Alzheimer’s disease, Parkinson’s disease [67, 68]. Ulijn and coworkers reported self-assembly of dipeptides linked to fluorenylmethoxycarbonyl (Fmoc), the result shows that these substances can form nanofibers, useful as a scaffold material in 3D cell culture. Similar to works of Gazit, the self-assembly of Fmoc-dipeptides is driven by hydrogen bonding

and π-π interactions, that is, the attractive interactions between π electrons in the aromatic fluorenyl rings [69–71].

2.3.3 Hydrogen bonding and π-stacking interactions

Electrospinning of pure peptides in this thesis are based on noncovalent interactions, the same as previous self-assembly model of aromatic peptides, which are mainly formed by hydrogen bondings and π-stacking interactions. The hydrogen bonding interaction is an electrostatic attractive interaction between the hydrogen (H) atom and a highly electronegative atom, e.g. nitrogen (N), oxygen (O) or fluorine (F). This interaction can be both intermolecular (e.g. interaction between water molecules) and intramolecular (e.g. interaction inside DNA, interaction in protein folding and protein structures such as α-helices, β-sheets). The strength of hydrogen bond is generally 5−30 kJ/mol, which is stronger than a van der Waals interaction but much weaker than covalent bonds (for a C-H covalent bond is approximately 420 kJ/mol). The hydrogen bondings is strongest when the hydrogen-bond donor (H atom) and the hydrogen-bond acceptor (e.g. N and O atom) lie along a straight line. In addition, the length of hydrogen bonds is longer than the covalent bonds (measured from the hydrogen atom to heteroatom (e.g. O, N, F) is in range of 0.15−0.26 nm) [72]. For self-assembling dipeptides, the head-to-tail hydrogen-bonded chains are energetically dominating interactions to stabilize the assembly of nanostructures [73].

Van der Waals interactions comprise of π-stacking interactions, which are attractive noncovalent interactions and between aromatic rings, e.g. intramolecular π-stacking interactions in nucleobase stacking within DNA and RNA molecules, and intermolecular π-π interactions of aromatic peptides. Bernstein et al. and Gazit demonstrated that there are four possible configurations for axially symmetric aromatic systems consisting of 1) parallel staggered, 2) T-shape, 3) parallel displaced, which are in an off-centered parallel orientation and 4) herringbone (see Fig. 2.12) [74–76]. McGaughey et al. determined the preferred positions and orientations of aromatic side chains of aromatic amino acids Phe, Tyr, His, and Trp. They found that the parallel displaced is 2−3 kJ/mol more stable than the T-shape structure for the Phe [77]. Moreover, characterization of π-stacking in a group of proteins with known structures point out that the most usual organization of π-π interactions in proteins is the parallel displaced π-stackings [76].

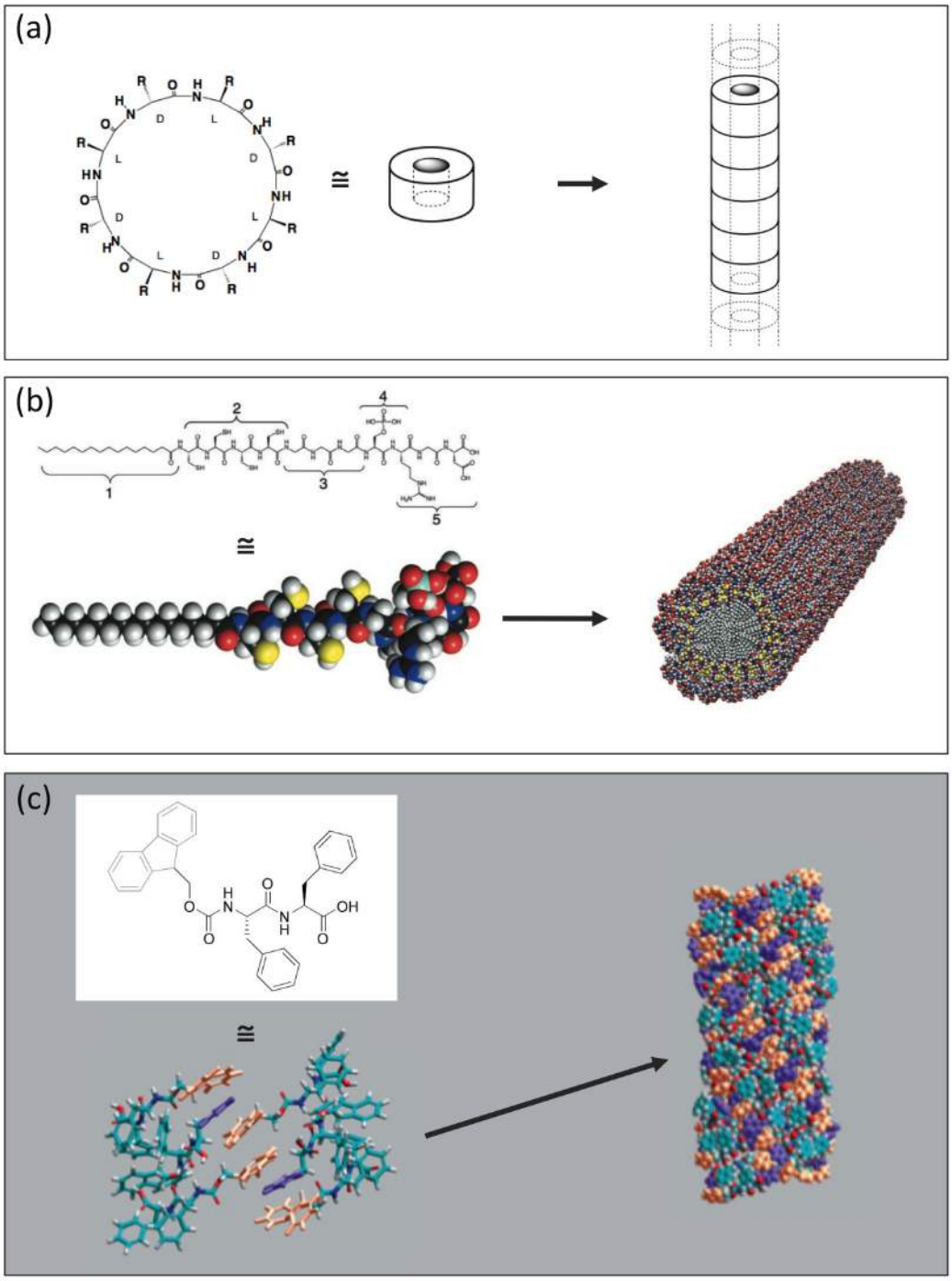

Figure 2.11: Schematics of peptide self-assembly based on; (a) cyclic peptides, a nanotube formed by the stacking of closed cyclic structures, which is made up of D- and L-isomers amino acid, adapted from [58]; (b) hydrophobic interactions, the building blocks contain a hydrophobic alkyl tail (region 1) and hydrophilic peptide regions (region 2-5), adapted from [62]; (c) aromatic interactions, aromatic peptide Fmoc-Phe-Phe self-assembled by interlocking of Fmoc groups and π-stacked pairs of phenyl rings, adapted from [71].

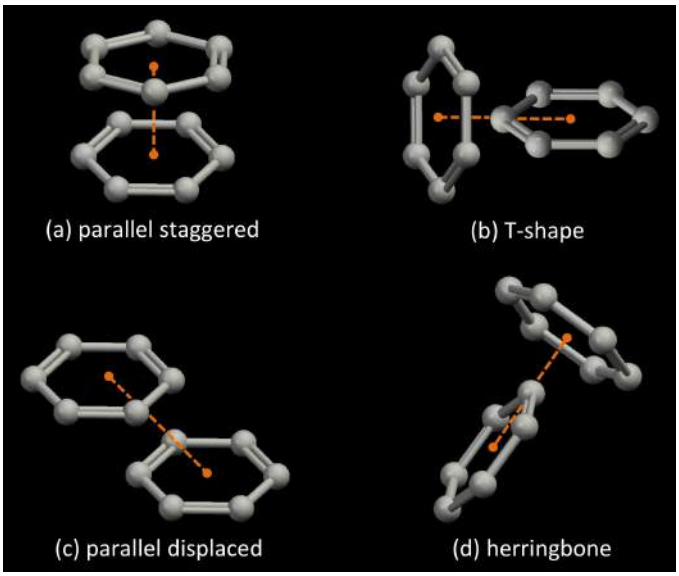

Figure 2.12: Schematic diagram of the four possible configurations found for axially symmetric aromatic systems; (a) parallel staggered, (b) T-shape, (c) parallel displaced, and (d) herringbone, adapted from [75].

▲ Summary

The first section (Chapter 2.1) describes the electrospinning process and the solution jet. At the critical voltage V_c, a Taylor cone creates (Eq. 2.4). Above V_c, a straight solution jet forms. The jet diameter d_j can be predicted by Eq. 2.5. When the surface charge repulsion dominates, the jet is unstable, hence whipping jet grows and fiber diameter reduces. The terminal fiber diameter d_f can be estimated by Eq. 2.8. For low-viscosity solution, however, the jet tends to break-up and droplets form. *De* and *Oh* numbers might be predict electrospinnability of a fluid (Eq. 2.9 and 2.10).

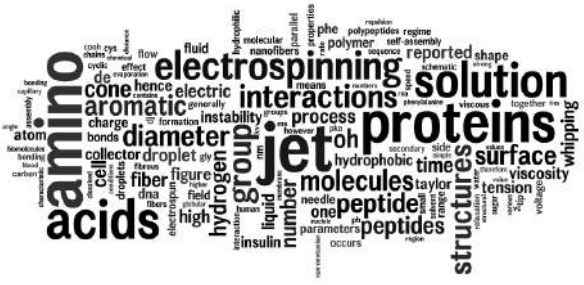

The second and third section explain the nature of biomolecules, especially, the amino acids and proteins. Some of them can be self-assembled into 1D nanofibers and nanotubes based on non-covalent interactions such as hydrogen bonding and π-π stacking interactions. Therefore, studying in this thesis focused on aromatic peptides and globular proteins. Selection of these biomolecules will be detailed in the next chapter.

Some equations described in this chapter will be used and discussed in the further parts of thesis as set out below.

• Eq. 2.4 : $V_c = f(H_p, L)$	Ch. 4	Taylor cone formation
• Eq. 4.1 : $d_j = f(Q, I)$	Ch. 4, 5	Diameters of electrospun fiber (≥100 nm)
• Eq. 2.8 : $d_f = f(Q, I)$	Ch. 4, 5	Diameters of electrospun fiber (≤10 nm)
• Eq. 2.9 : $Oh \geq 1$	Ch. 3	Solution preparation
	Ch. 4, 5	Droplets and fibers formation

2.4 References

[1] J.M. Deitzel, J. Kleinmeyer, D. Harris, N.C. Beck Tan. The effect of processing variables on the morphology of electrospun nanofibers and textiles, *J. Phys. Chem. B* **42**: 261-272, 2001.

[2] Z.M. Huang, Y.Z. Zhang, M. Kotaki, S. Ramakrishna. A review on polymer nanofibers by electrospinning and their applications in nanocomposites, *Comp. Sci. Tech.* **63**: 2223-2253, 2003.

[3] G. Taylor. Disintegration of water drops in an electric field, *Proc. R. Soc. London, Series A* **280**: 383-397, 1964.

[4] G. Taylor. The circulation produced in a drops by an electric field, *Proc. R. Soc. London, Series A* **291**: 159-166, 1966.

[5] G. Taylor. Electrically driven jets, *Proc. R. Soc. London, Series A* **313**: 453-475, 1969.

[6] A.L. Yarin, S. Koombhongse, D.H. Reneker. Taylor cone and jetting from liquid droplets in electrospinning of nanofibers, *J. Appl. Phys.* **90**: 4836-4846, 2001.

[7] J. Sutasinpromprae, S. Jitjaicham, M. Nithitanakul, C. Meechaisue, P. Supaphol. Preparation and characterization of ultrafine electrospun polyacrylonitrile fibers and their subsequent pyrolysis to carbon fibers, *Polym. Int.* **55**: 825-833, 2006.

[8] A.M. Gañán-Calvo, J. Dávila, A. Barrero. Current and droplet size in the electrospraying of liquid scaling laws, *J. Aerosol Sci* **28**: 249-275, 1997.

[9] R.P.A. Hartman, D.J. Brunner, D.M.A. Camelot, J.C.M. Marijnissen, B. Scarlett. Electrohydrodynamic atomization in the cone-jet mode: Physical modeling of the liquid cone and jet, *J. Aerosol Sci.* **30**: 823-849, 1999.

[10] L.M. Bellan, H.G. Craighead, J.P. Hinestroza. Direct measurement of fluid velocity in an electrospinning jet using particle image velocimetry, *J. Appl. Phys.* **102**: 094308, 2007.

[11] D.H. Reneker, A.L. Yarin. Electrospinning jets and polymer nanofibers, *Polymer* **49**: 2387-2425, 2008.

[12] A.F. Spivak, Y.A. Dzenis, D.H. Reneker. A model of steady state jet in the electrospinning process, *Mech. Res. Commun.* **27**: 37-42, 2000.

[13] M.M. Munir, A.B. Suryamasa, F. Iskandara, K. Okuyama. Scaling law on particle-to-fiber formation during electrospinning, *Polymer* **50**: 4935-4943, 2009.

[14] M. Mutoh, S. Kaieda, K. Kamimura. Convergence and disintegration of liquid jets induced by an electrostatic field, *J. Appl. Phys.* **50**: 3174-3179, 1979.

[15] D.P.H. Smith. The electrohydrodynamic atomization of liquids, *IEEE Trans. Ind. Appl.* **IA-22**: 527-535, 1986.

[16] M. Cloupeau, B. Prunet-Foch. Electrostatic spraying of liquids in cone-jet mode, *J. Electrostat.* **22**: 135-159, 1989.

[17] J.F. Mora, I.G. Loscertales. The current emitted by highly conducting Taylor cones, *J. Fluid Mech.* **260**: 155-184, 1994.

[18] A.M. Gañán-Calvo, J.C. Lasheras, J. Dávila, A. Barrero. The electrostatic spray emitted from an electrified conical meniscus, *J. Aerosol Sci.* **25**: 1121-1142, 1994.

[19] S.V. Fridrikh, J.H. Yu, M.P. Brenner, G.C. Rutledge. Controlling the fiber diameter during electrospinning, *Phys. Rev. Lett.* **90**: 144502, 2003.

[20] Y.M. Shin, M.M. Hohman, M.P. Brenner, G.C. Rutledge. Experimental characterization of electrospinning: the electrically forced jet and instabilities, *Polymer* **42**: 9955-9967, 2001.

[21] M.M. Hohman, M. Shin, Gr. Rutledge, M.P. Brenner. Electrospinning and electrically forced jets. I. Stability theory, *Phys. Fluids* **13**: 2201-2220, 2001.

[22] M.M. Hohman, M. Shin, Gr. Rutledge, M.P. Brenner. Electrospinning and electrically forced jets. II. Applications, *Phys. Fluids* **13**: 2221-2236, 2001.

[23] J. Eggers. Nonlinear dynamics and breakup of free-surface flows, *Rev. Mod. Phys.* **69**: 865-926, 1997.

[24] G.H. McKinley. Dimensionless Groups For Understanding Free Surface Flows of Complex Fluids, *SOR Rheology Bulletin*, 2005.

[25] G.H. McKinley. Visco-elasto-capillary thinning and break-up of complex fluids, *SOR Rheology Bulletin*, 2005.

[26] J. Eggers, E. Villermaux. Physics of liquid jets, *Rep. Prog. Phys.* **71**: 036601, 2008.

[27] M.K. Tiwari, A.V. Bazilevsky, A.L. Yarin, C.M. Megaridis. Elongational and shear rheology of carbon nanotube suspensions, *Rheol. Acta* **48**: 597-609, 2009.

[28] G.H. McKinley, M. Renardy. Wolfgang von Ohnesorge, *Phys. Fluids* **23**: 127101, 2011.

[29] B. Derby. Inkjet printing of functional and structural materials: Fluid property requirements, feature stability and resolution, *Ann. Rev. Mater. Res.* **40**: 395-414, 2010.

[30] I.M. Hutchings, G.D. Martin. Inkjet Technology for Digital Fabrication, John Wiley Sons, ISBN: 978-0-470-68198-5, 2012.

[31] M. Reiner. The Deborah Number, *Physics Today* **17**: 62, 1964.

[32] M. Stelter, G. Brenn, A.L. Yarin, R.P. Singh, F. Durst. Validation and application of a novel elongational device for polymer solutions, *J. Rheol* **44**: 595-616, 2000.

[33] L.E. Rodd, T.P. Scott, J.J. Cooper-White, G.H. McKinley. Capillary Break-up Rheometry of Low-Viscosity Elastic Fluids, *Appl. Rheol.* **15**: 12-27, 2005.

[34] D.H. Reneker, A.L. Yarin, H. Fong, S. Koombhongse. Bending instability of electrically charged liquid jets of polymer solutions in electrospinning, *J. Appl. Phys.* **87**: 4531-4547, 2000.

[35] T.A. Kowalewski, S. Błoński, S. Barral. Experiments and modelling of electrospinning process, *Bull. Pol. Ac.: Tech.* **53**: 385-394, 2005.

[36] C. Branden, J. Tooze. Introduction to Protein Structure 2nd Edition, New York: Garland Publishing Company, 1998.

[37] J.A. Matthews, G.E. Wnek, D.G. Simpson, G.L. Bowlin. Electrospinning of Collagen Nanofibers, *Biomacromolecules* **3**: 232-238, 2002.

[38] G.E. Wnek, M.E. Carr, D.G. Simpson, G.L. Bowlin. Electrospinning of Nanofiber Fibrinogen Structures, *Nano Lett.* **3**: 213, 2003.

[39] M. Li, M.J. Mondrinos, M.R. Gandhi, F.K. Ko, A.S. Weiss, P.I. Lelkes. Electrospun protein fibers as matrices for tissue engineering, *Biomaterials* **26**: 5999, 2005.

[40] S.A. Sell, P.S. Wolfe, K. Garg, J.M. McCool, I.A. Rodriguez. G.L. Bowlin. The Use of Natural Polymers in Tissue Engineering: A Focus on Electrospun Extracellular Matrix Analogues, *Polymers* **2**: 522-553, 2010.

[41] C.P. Barnes, M.J. Smith, G.L. Bowlin, S.A. Sell, T. Tang, J.A. Matthews, D.G. Simpson, J.C. Nimtz. Feasibility of Electrospinning the Globular Proteins Hemoglobin and Myoglobin, *J. Eng. Fiber Fabr.* **1**: 16, 2006.

[42] Y. Dror, T. Ziv, V. Makarov, H. Wolf, A. Admon, E. Zussman. Nanofibers Made of Globular Proteins, *Biomacromolecules* **9**: 2749, 2008.

[43] F.P. Gao, T.A. Cross. Recent developments in membrane-protein structural genomics, *Genome Biol.* **6**: 244, 2005.

[44] X. Fang, D.H. Reneker. DNA Fibers by Electrospinning, *J. Macromol. Sci. Phys.* **B36**: 169-173, 1997.

[45] T. Takahashi, M. Taniguchi, T. Kawai. Fabrication of DNA Nanofibers on a Planar Surface by Electrospinning, *Jpn. J. Appl. Phys.* **44**: L860-L862, 2005.

[46] H. Jiang, D. Fang, B.S. Hsiao, B. Chu, W. Chen. Optimization and Characterization of Dextran Membranes Prepared by Electrospinning, *Biomacromolecules* **5**: 326-333, 2004.

[47] K. Ohkawa, D. Cha, H. Kim, A. Nishida, H. Yamamoto. Electrospinning of Chitosan, *Macromol. Rapid Commun.* **25**: 1600-1605, 2004.

[48] S. Xu, J. Zhang, A. He, J. Li, H. Zhang, C.C. Han. Electrospinning of native cellulose from nonvolatile solvent system, *Polymer* **49**: 2911-2917, 2008.

[49] A. Celebioglu, T. Uyar. Cyclodextrin nanofibers by electrospinning, *Chem. Commun.* **46**: 6903-6905, 2010.

[50] A.C. Stijnman, I. Bodnar, R.H. Tromp. Electrospinning of food-grade polysaccharides, *Food Hydrocolloids* **25**: 1393-1398, 2010.

[51] M.G. McKee, J.M. Layman, M.P. Cashion, T.E. Long. Phospholipid Nonwoven Electrospun Membranes, *Science* **311**: 353-355, 2006.

[52] National Center for Biotechnology Information. PubChem Compound Database; CID6140 (Phe), CID5862 (Cys), CID750 (Gly), http://pubchem.ncbi.nlm.nih.gov/ (accessed Feb. 14, 2014).

[53] C.F. Macrae, I.J. Bruno, J.A. Chisholm, P.R. Edgington, P. McCabe, E. Pidcock, L. Rodriguez-Monge, R. Taylor, J. van de Streek, P.A. Wood. Mercury CSD 2.0 - new features for the visualization and investigation of crystal structures, *J. Appl. Cryst.* **41**: 466-470, 2008.

[54] E. Gazit. Self-Assembly of Short Peptides for Nanotechnological Applications, In the NanoBioTechonology: BioInspired Devices and Materials of the Future, Ed. by O. Shoseyov, l. Levy, Humana Press Inc., Totowa, NJ: 385-395, 2008.

[55] M.R. Ghadiri, J.R. Granja, R.A. Milligan, D.E. McRee, N. Khazanovich. Self-assembling organic nanotubes based on a cyclic peptide architecture, *Nature* **366**: 324-327, 1993.

[56] M.R. Ghadiri, J.R. Granja, L.K. Buehler. Artificial transmembrane ion channels from self-assembling peptide nanotubes, *Nature* **369**: 301-304, 1994.

[57] J.D. Hartgerink, J.R. Granja, R.A. Milligan, M.R. Ghadiri. Self-Assembling Peptide Nanotubes, *J. Am. Chem. Soc.* **118**: 43-50, 1996.

[58] D.T. Bong, T.D. Clark, J.R. Granja, M.R. Ghadiri. Self-Assembling Organic Nanotubes, *Angew. Chem. Int. Ed.* **40**: 988-1011, 2001.

[59] K. Rosenthal-Aizman, G. Svensson, A. Unden. Self-assembling peptide nanotubes from enantiomeric pairs of cyclic peptides with alternating D and L amino acid residues, *J. Am. Chem. Soc.* **126**: 3372-3373, 2004.

[60] N. Ashkenasy, W.S. Horne, M.R. Ghadiri. Design of Self-Assembling Peptide Nanotubes with Delocalized Electronic States, *Small* **2**: 99-102, 2006.

[61] M. Yoshizaki, N. Nishio, J. Kuwahara, N. Nishino, T. Kato. Self-assembling Cyclic Hexapeptides for Peptide Nanotube Formation, *Proceedings of the 4th International Peptide Symposium*, 2007.

[62] J.D. Hartgerink, E. Beniash, S.I. Stupp. Self-Assembly and Mineralization of Peptide-Amphiphile Nanofibers, *Science* **294**: 1684-1688, 2001.

[63] J.D. Hartgerink, E. Beniash, S.I. Stupp. Peptide-amphiphile nanofibers: A versatile scaffold for the preparation of self-assembling materials, *Proc. Natl. Acad. Sci.* **99**: 5133-5138, 2002.

[64] M.O. Guler, S. Soukasene, J.F. Hulvat, S.I. Stupp. Presentation and Recognition of Biotin on Nanofibers Formed by Branched Peptide Amphiphiles, *Nano Lett.* **5**: 249-252, 2005.

[65] G.A. Silva, C. Czeisler, K.L. Niece, E. Beniash, D.A. Harrington, J.A. Kessler, S.I. Stupp. Selective Differentiation of Neural Progenitor Cells by High-Epitope Density Nanofibers, *Science* **303**: 1352-1355, 2004.

[66] S. Vauthey, S. Santoso, H. Gong, N. Watson, S. Zhang. Molecular self-assembly of surfactant-like peptides to form nanotubes and nanovesicles, *Proc. Natl. Acad. Sci.* **99**: 5355-5360, 2002.

[67] S. Gilead, E. Gazit. Self-organization of Short Peptide Fragments: From Amyloid Fibrils to Nanoscale Supramolecular Assemblies, *Supra. Chem.* **17**: 87-92, 2005.

[68] E. Gazit. Self Assembly of Short Aromatic Peptides into Amyloid Fibrils and Related Nanostructures, *Prion* **1**: 32-35, 2007.

[69] V. Jayawarna, M. Ali, T.A. Jowitt, A.F. Miller, A. Saiani, J.E. Gough, R.V. Ulijn. Nanostructured Hydrogels for Three-Dimensional Cell Culture Through Self-Assembly of Fluorenylmethoxycarbonyl-Dipeptides, *Adv. Mater.* **18**: 611-614, 2006.

[70] D.M. Ryan, T.M. Doran, S.B. Anderson, B.L. Nilsson. Effect of C-Terminal Modification on the Self-Assembly and Hydrogelation of Fluorinated Fmoc-Phe Derivatives, *Langmuir* **27**: 4029-4039, 2011.

[71] A.M. Smith, R.J. Williams, C. Tang, P. Coppo, R.F. Collins, M.L. Turner, A. Saiani, R.V. Ulijn. Fmoc-Diphenylalanine Self Assembles to a Hydrogel via a Novel Architecture Based on π-π Interlocked β-Sheets, *Adv. Mater.* **20**: 37-41, 2008.

[72] J.M. Berg, J.L. Tymoczko, L. Stryer. Chemical Bonds in Biochemistry, in the Biochemistry 5th edition, New York: W.H. Freeman; 2002.

[73] C.H. Görbitz. Structures of dipeptides: the head-to-tail story, *Acta Cryst. B* **66**: 84-93, 2010.

[74] C.A. Hunter, J.K.M. Sanders. The Nature of π-π Interactions, *J . Am. Chem. Soc.* **112**: 5525-5534, 1990.

[75] S. Sun, E.R. Bernstein. Aromatic van der Waals Clusters: Structure and Nonrigidity, *J. Phys. Chem.* **100**: 13348-13366, 1996.

[76] E. Gazit. A possible role for π-stacking in the self-assembly of amyloid fibrils, *FASEB J.* **16**: 77-83, 2002.

[77] G.B. McGaughey, M.Gagne, A.K. Rappe. π-Stacking Interactions. Alive and well in proteins, *J. Biol. Chem.* **273**: 15458-15463, 1998.

Chapter 3

Methodology

Three main steps will be undertaken to address the hypothesis of this thesis; 1) selection of substances and dissolution, 2) electrospinning of the solution, and 3) characterization of the electrospun fibers. The first section will enumerate choice of substances, solvents, and dissolution method. The second section will present electrospinning setups, which are developed and used in this work, starting from a conventional setup, typically suitable for the production of polymer nanofibers in laboratory scale. Then, a microliter electrospinning setup and special additional techniques will be detailed. The last two sections, characterization techniques and computation of molecular vibrations will be provided.

> **HYPOTHESIS:** Electrospinning of pure biomolecules without polymer blends is possible, when they show self-assembly in 1D, 2D, or 3D, when they can be dissolved in a suitable organic solvent at high concentration, and when electrospinning parameters are optimized.

3.1 Selection of substances and dissolution

To proof the hypothesis quoted above, the first part of experiments is focused on short aromatic peptides (see the results in Chapter 4) and then the choice of substance will be expanded into bigger biomolecules such as proteins (see the results in Chapter 5).

3.1.1 Peptides selection

Some self-assembling peptides can be assembled to amyloid-like structures as described in the introduction and the previous chapter. Therefore, short aromatic peptides were chosen for studying as listed in Table 3.1. The selected substances are: (1) H-Phe-Phe-OH or Phe-Phe (FF), it

Table 3.1: Choice of short aromatic peptides selected for electrospun fibers.

Name		**Chemical formula**	M_r	**Self-assembly in solution**
Short aromatic peptides:				
(1) H-Phe-Phe-OH	(FF)	$C_{18}H_{20}N_2O_3$	312	Y
(2) H-Gly-Phe-OH	(GF)	$C_{11}H_{14}N_2O_3$	222	Y
(3) H-Gly-Phe-Gly-OH	(GFG)	$C_{13}H_{17}N_3O_4$	279	Y
(4) Fmoc-Phe-Gly-OH	(Fmoc-FG)	$C_{26}H_{24}N_2O_5$	444	Y
(5) Fmoc-Gly-OH	(Fmoc-G)	$C_{17}H_{15}NO_4$	297	Y
(6) $(Fmoc\text{-}Cys\text{-}OH)_2$	$(Fmoc\text{-}C)_2$	$C_{36}H_{32}N_2O_8S_2$	685	Y
Fluorene derivates:				
(7) 9-Fluorenylmethanol	(9FM)	$C_{14}H_{12}O$	196	N
(8) $Fmoc\text{-}NH_2$	$(Fmoc\text{-}NH_2)$	$C_{15}H_{13}NO_2$	239	N
π stacking molecule:				
(9) Tetraphenylporphyrin derivate	(TPP)	$C_{44}H_{30}ON_4$	630	N

can be assembled to nanotubes or nanofibers, similar to amyloid fibrils [1–4] and can be spun by electrospinning technique [5]; (2-6) short peptides and Fmoc derivates, theses substances can be assembled to nanofibers [6–8] but have not yet been used in electrospinning; (7-8) Fluorene derivates, both molecules contain a basic π-stacking unit and (9) Tetraphenylporphyrin (TPP) derivate, this is a π stacking molecule. The substances (7-8) were selected for comparison of the spinnability to short aromatic peptides. All substances listed in Table 3.1 were purchased from Sigma-Aldrich (Madrid, Spain) and Bachem (Bubendorf, Switzerland). Exception for the TPP derivate was synthesized by Laboratory of BioInorganic Chemistry, at the University of Crete, Greece. Monoamino-tetraphenylporphyrine ($TPP\text{-}NH_2$) and diphenylalanine-TPP (FF-TPP) synthesized according to work of G. Charalambidis et al. [9], K. Ladomenou et al. [10] and references therein. All substances were used with no further purification.

3.1.2 Proteins selection

Peptides and proteins are biomolecule compounds consisting of amino acids and both show self-assembly in 3D, 2D, and 1D, e.g. bulk crystals, membrane proteins, natural fibrils, respectively. Hence, this work also selected some interesting proteins and larger biomolecules for studying their electrospinnability as shown in Table 3.2. Globular proteins that can be assembled and have been electrospun were selected; (1) albumin and (2) hemoglobin. Other globular proteins have not been electrospun were further studied; (3) casein and (4) lysozyme. Both globular proteins can be found in milk and hen egg white, respectively. Additionally, a tiny protein such as (5) insulin was tested its electrospinnability without polymer blends, and (6) hydrophobins can be assembled to 2D film but have not been used in electrospinning. Besides proteins, (7) double-stranded DNA was selected and included in the table.

Table 3.2: Choice of larger biomolecules selected for electrospun fibers.

Name		M_r	Self-assembly
(1) Albumin	(AL)	44,300	1D fibrils at low pH and heat treatment
(2) Hemoglobin	(HB)	64,500	3D quaternary of human HbA
(3) Casein	(CS)	24,000	3D micelles found in milk
(4) Lysozyme	(LZ)	14,307	1D fibrils at pH 2.0
(5) Insulin	(INS)	5,807	1D fibrils at low pH
(6) Hydrophobins	(HP-A)	40,000	2D monolayer on surfaces
	(HP-B)	17,000	2D monolayer on surfaces
(7) Double-stranded DNA	(dsDNA)	130,000	1D fibers in aqueous containing Mg^{2+}

The substances were purchased from Sigma-Aldrich (Madrid, Spain) and used with no further purification. Hydrophobins were donated from BASF (Ludwigshafen, Germany). Some details about production are listed below. Their properties, uses, chemistry will be described in more detail in Chapter 5.

1. Albumin (Sigma, A5503) from chicken egg white (can be named "Ovalbumin") lyophilized powder ≥ 98% purity.

2. Hemoglobin (Sigma, H7379) from human, lyophilized powder.

3. Casein (Sigma, C7078) from bovine milk, technical grade.

4. Lysozyme (Sigma, L1667) from human recombinant expressed in rice, ≥ 100,000 units/mg protein, ≥ 90% purity.

5. Insulin (Sigma, I2643) from human recombinant expressed in yeast (proprietary host), ≥ 98% purity.

6. Hydrophobins (BASF), from a recombinant production process described in [11]. There are two fusion proteins H*Protein A (HP-A) and H*Protein B (HP-B). Both are class I hydrophobins, the HP-A has molar mass of ~47 kDa, and ~19 kDa for the HP-B [11].

7. Deoxyribonucleic acid (DNA) sodium salt (Sigma, D1626) from salmon testes, approximately 2,000 base pairs.

3.1.3 Choices of the solvent

The electrospinning technique needs to dissolve the substance into a liquid form (melting is not possible for the short aromatic peptides because they are easily destroyed by heat). The choice of solvent plays a vital role in processes of electrospinning, since the properties of solution (e.g. concentration, viscosity, evaporation rate) strongly affect fiber formation.

Depending on the type of substance used, the suitable solvent might be following or a mixture (their properties are listed in Table 3.3).

- dichloromethane (DCM), CH_2Cl_2
- tetrahydrofuran (THF), C_4H_8O
- methanol (MeOH), CH_4O
- hexafluoroisopropanol (HFIP), $C_3H_2F_6O$
- trifluoroethanol (TFE), $C_2H_3F_3O$
- isopropyl alcohol (IPA), C_3H_8O
- ethanol (EtOH), C_2H_6O
- dimethylformamide (DMF), C_3H_7NO
- dimethyl sulfoxide (DMSO), C_2H_6SO
- *N*-methylpyrrolidone (NMP), C_5H_9NO
- trifluoroacetic acid (TFA), $C_2HF_3O_2$

After several trial experiments to find a suitable solvent, as shown in Table 3.3, the HFIP and DMF (gray label) are suitable to dissolve the short aromatic peptides. Despite the fact that DMSO and NMP can dissolve almost all peptides (+++), their vapor pressures are very low. A very low evaporation rate cannot give success in the electrospinning process. In contrast, HFIP can completely dissolve only some substances (++), but it is a highly polar solvent, has a high vapor pressure and low surface tension. Its physical properties are suitable for electrospinning because this technique needs a solution that easily evaporates and elongates after application of a high voltage. However, HFIP has low viscosity, this is not suitable for electrospinning as mentioned in Chapter 2. Electrospinning requires a liquid that has $Oh \geq 1$. Eq. 2.9 points out the viscosity of liquid must be high enough to achieve the inequality of the Oh. Otherwise, beads or droplets can be observed rather than fiber, caused by the high surface tension, but also by the low viscosity. Thus, a peptide solution will be prepared at high concentration in order to increase its viscosity as much as possible [5].

3.1.4 Dissolution method

Besides the requirement of viscosity mentioned in the previously section, homogenous solutions and completely dissolved materials are necessary for characterizing electrospinning. For the conventional electrospinning setup, the solution must be loaded into a syringe and fed through a small metal needle. If the substance was not dissolved homogenously, the electrospinning process cannot be stable. Moreover, the solution cannot feed through the needle, when the solution contains a precipitate.

Table 3.3: Physical properties of solvents selected to dissolve aromatic peptides; dissolution results.

Solvent (see text)	**Vapor pressure** (atm. at 25 °C)	**Surface tension** (mN/m at 25 °C)	**Boiling point** (°C)	**Viscosity** (mPa·s at 25 °C)	**Result**[1]
DCM	0.572	27.89	39.60	0.404	+
THF	0.213	26.40	65.96	0.460	++
MeOH	0.167	22.30	64.55	0.551	++
HFIP	0.158*	16.40	58.20	1.021	++
TFE	0.068	21.11*	78.00	1.730	0
IPA	0.060	21.79	82.24	2.043	+
EtOH	0.059	21.99	78.39	1.100	+
DMF	0.0036	36.76*	153.00	0.920*	+++
DMSO	0.0008	42.98	189.00	1.991	+++
NMP	0.0004	40.70	202.00	1.666	+++
TFA	0.128*	13.60	72.40	0.930*	++

[1] dissolution result, +++ completely dissolves almost all peptides, ++ completely dissolves some peptides, + dissolves some peptides, 0 cannot dissolve.
* measured at 20 °C.

Therefore, the selected substances were dissolved in a suitable solvent at a high concentration, 15−18 %(wt/wt). Although, some substances can be dissolved at higher or lower this range depending on their solubility in each solvent. The concentration of the substance solution was calculated and prepared in percentage by weight %(wt/wt) as shown in Eq. 3.1. Then the mixed solutions were ultrasonicated by an ultrasonic cleaner (USC300TH, VWR) for 30 min or more without additional of heat (except a bulk heating of the liquid over time), and shaken by a platform shaker (Titramax 1000, Heidolph) at 450−600 rpm for 3 h or more, in order to obtain homogenous solutions. In some cases, the solution was ultrasonicated at high temperature but not higher than around 60 °C for 30 min or until it was completely dissolved. Of each solution sample was prepared approximately 0.5−1 ml.

$$Concentration\ \%(wt/wt) = \left(\frac{mass\ of\ substance}{mass\ of\ solvent + mass\ of\ substance}\right)\ x\ 100 \tag{3.1}$$

> **OBJECTIVE 1:** Developing a new electrospinning system, which is suitable and convenient for a substance available in small amounts.

3.2 Electrospinning

To achieve the first objective, a conventional electrospinning system was built at the beginning. Then, a microliter electrospinning system was designed and developed. Detail of the electrospinning setups and processes will be described in this section. Some aspects on advanced electrospinning technologies will be briefly reviewed below.

3.2.1 Technological advances in electrospinning

As described in Chapter 1, a basic electrospinning equipment can be set up using a high voltage power supply and a solution controller, e.g. plastic syringe with a needle. However, electrospinning setup was designed and developed in several ideas beneficial to control physical properties and the mass production of nanofibers [12, 13]. This section presents some interesting techniques. They are divided into the following four groups.

3.2.1.1 Collector

For a standard setup, a conducting collector (square or circle metal sheet) connects to the negative pole of high voltage power supply. Electrospun fibers are randomly deposited onto the collector. When replacing with two conducting collectors (see Fig. 3.1a), fibers are aligned between the parallel collectors. This alignment is a result of the electric field (between the gap) forcing the charged nanofibers [14, 15]. Maximum gap size can be adjusted from few millimeters up to tens of centimeters depending on the concentration of the polymer solution (35−50 cm for polycaprolactone 8−20 %(wt/wt) [16], 18 cm for polyethylene oxide (PEO) 4.5 %(wt/wt) [17]). Another alignment technique is using a cylindrical collector with rotating speed of >1000 rpm (see Fig. 3.1b). Orientation of the fiber increases with increasing the rotating speed. However, the fiber will break, if linear speed of the rotating cylinder collector is too fast, e.g. 1.4 m/s (4500 rpm) is a suitable speed for alignment of collagen type I calfskin electrospun fibers [18]. A sharp tip stainless steel (apex diameter of 50 μm) can be used as a collector (see Fig. 3.1c). This technique obtains a coiling of PEO fiber to form free-standing hollow pottery (nanopottery), when distance between the sharp collector and a capillary tip is 2 mm [19]. Furthermore, using a static cylindrical collector with equally spaced circular protrusions (see Fig. 3.1d) can produce 3D fibrous tubes, which is attractive for biomedical, tissue engineering and filtration applications [20].

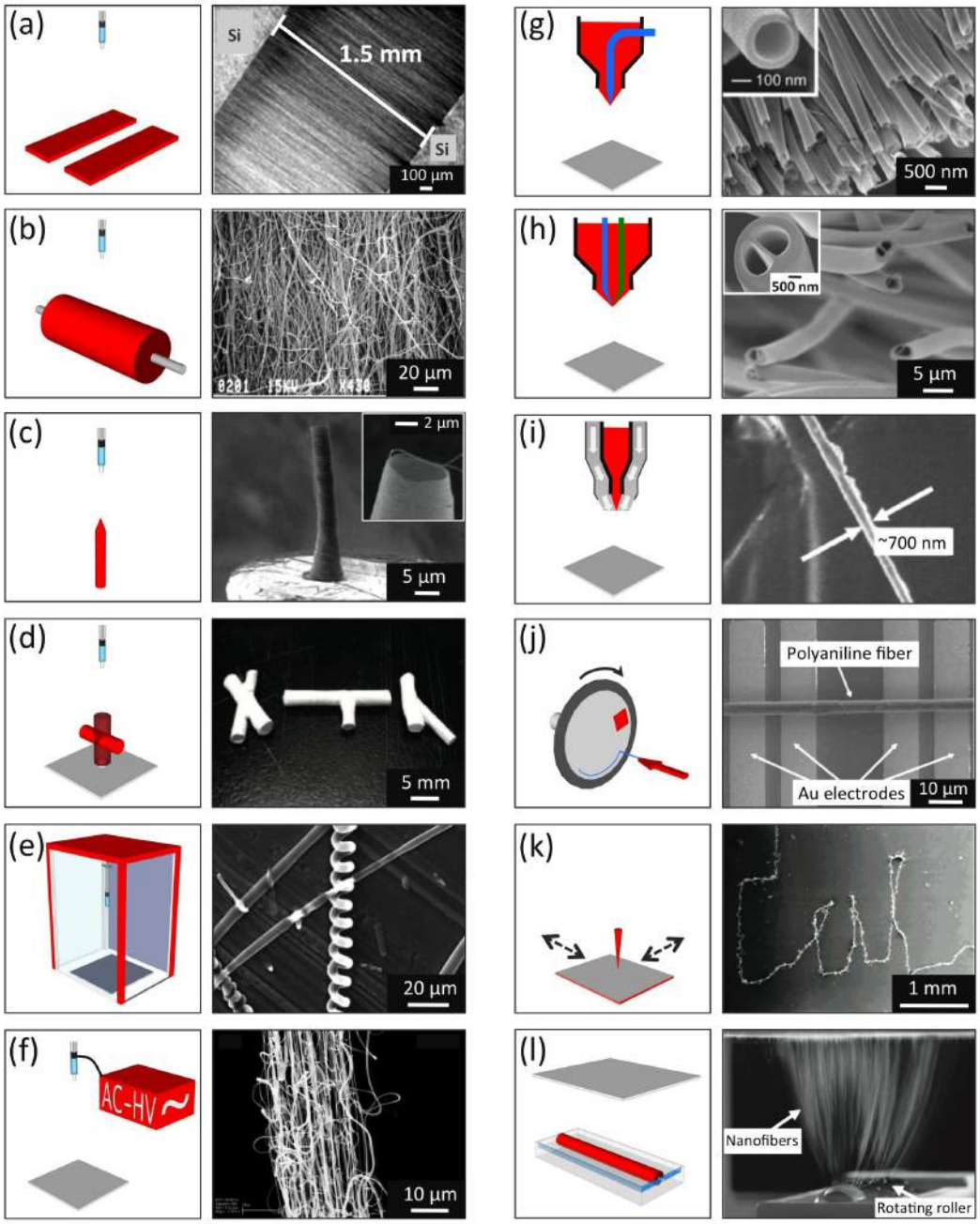

Figure 3.1: Schematics of electrospinning setup, some parts are modified from the standard setup (indicated with red color) with their fabrication results. (a) parallel collectors [14], (b) rotating drum [18], (c) sharp tip collector [19], (d) static cylindrical collector [20], (e) vacuum chamber [21], (f) AC electrospinning [25], (g) coaxial nozzle with two needles [27], (h) coaxial nozzle with three needles [28], (i) air-blowing assisted [32], (j) scanning tip [33], (k) near-field electrospinning [36], and (l) nozzle-less electrospinning [45].

3.2.1.2 Chamber

Typically, electrospinning is operated in an air environment inside a closed chamber, in which the processing can be carried out at controllable temperature or humidity. Furthermore, the closed system can protect a user from solvent evaporation and high voltage. Rangkupan et al. created a vacuum chamber for electrospinning (see Fig. 3.1e) which takes advantage of the increased electrical break down strength compared to the standard air environment. Small polypropylene fibers are produced with diameters from 0.3−30 μm because the high electrical forces the polymer melt [21].

3.2.1.3 High voltage power supply

A direct current (DC) high voltage power supply is the mostly used voltage source in electrospinning setups. This helps the process to be predicted with accuracy. There are few works using an alternating current (AC) power supply [22–24]. Maheshwari et al. reported using AC high voltage. A new fiber pattern was observed which strongly depends on the frequency. The AC electrospinning produces threads consisting of multiple strands fibers (see Fig. 3.1f) from poly(vinyl pyrolidine) 12 %(wt/wt) solution at AC frequency of 50 Hz, voltage of 3.33 kV, and distances 2−4 cm below the needle [25]. Therefore, AC electrospinning offers a possibility to produce fiber threads, which may be useful for textile and filtration applications.

3.2.1.4 Nozzle

For a simple setup, polymer solution is fed through a single needle diameter in the millimeter range. Another smaller needle can be inserted for feeding an immiscible solution. This setup is called “coaxial electrospinning”, it was first used for fabrication of monodisperse capsules with diameters of 0.15−10 μm [26]. Then, this technique was modified to fabricate a hollow fiber by loading a polymer solution into the outer needle (sheath) and heavy mineral oil into the inner (core) (see Fig. 3.1g). Hollow fibers are obtained after the mineral oil was removed by immersing the fibers in octane overnight [27]. Jiang et al. reported a multi-coaxial electrospinning that consists of two inner spinnerets (diameter is 0.17 mm) and one outer needle (diameter is 2.0 mm) [28]. The schematic of Fig. 3.1h shows the hollow fibers from the two inner spinnerets. These hollow fibers may be used for drug delivery or microfluidic applications. The cores of fibers can be filled with functional materials such as healing agents [29] and biopolymers [30].

Apart from coaxial electrospinning, the nozzle is modified by surrounding it with a hot air flow (see Fig. 3.1i), e.g. the electrospinning of hyaluronic acid (HA) solution, which has an unusually the high viscosity and the high surface tension [31]. The flowing air accelerates the evaporation rate of the solvent, reduces the solution viscosity, and introduces an additional pulling force helping the jet formation. Therefore, this technique can improve electrospinnability of polymers with limited low-temperature solubility, for example ultra-high molecular weight polyethylene [32].

To precisely control fiber deposition onto a substrate, the nozzle is replaced by a small tip (arrow-shaped, see Fig. 3.1j) made from silicon with diameter of about 0.5 mm [33–35]. The top side of the tip is deposited with gold to increase the conductivity. A polymer solution is loaded by dipping the tip into the solution, and then placing it far from a rotating collector of 0.5−1.5 cm. High voltage (4−6 kV) is applied to the tip through a gold wire, resulting in fiber depositsition on a substrate. However, the fiber deposition by this technique is limited to only one direction (along rotation direction). Few years later, Lin et al., reported a similar idea, but with the ability to direct-write deposition of nanofibers. The silicon tip is replaced by a tungsten electrode with a tip diameter of 25 μm. The distance to the collector is decreased down to the range of 0.5−3 mm, so this technique is called "near-field electrospinning (NFES)" [36]. In addition, the rotating collector is changed to a controllable *x*-*y* stage. When the collector moves fast enough (about 0.15−0.2 m/s), a straight fiber can be fabricated. Moreover, others patterns such as a letter can be drawn by controlling manually or with a programmable *x*-*y* stage [37–39].

One disadvantage of the standard electrospinning setup is low mass production rate. A single nozzle can produce fibers less then 0.003 kg/h [40, 41]. This problem has been improved by using multi-nozzle [42], however, there is a problem on strong interferences between the solution jets [40]. A high mass production of electrospinning based on nozzle-less technique has been operated in industrial scale with production rate of 0.171 kg/h [43]. There are significant differences between the nozzle-less technique and standard setup. The needle (spinneret) is replaced by other fiber generators, such as a rotating roller [44–46] (see Fig. 3.1l), disk [47], or spiral coil [48]. Partially part of the fiber generator was immersed into polymer solution and slowly rotates, therefore, unimmersed part of the generator was covered with a thin layer of the polymer solution. When a high voltage was applied, solution jets can be generated from the surface upward and the fibers deposited on the collector over the fiber generator. However, this technique requires a very high voltage (>40 kV) compared to a standard setup (<10 kV or higher) because the electric field cannot concentrate like on the tip of needle [47]. In addition, the solution was filled in an open bath; hence solvent can evaporate which increases the solution viscosity [49]. Thus, environmental conditions must be controlled during the process.

3.2.2 Electrospinning experimental setup

As introduced in Chapter 1, one problem and a challenge of this thesis is how to experiment with the small amounts of biomolecules substance, some techniques in the previous section can be modified and used, such as the scanning tip electrospinning (Fig. 3.1j) and the NFES (Fig. 3.1k). Both techniques work very well with polymer solution such as PEO in water, however, there are problems with a peptide dissolved in an organic solvent, evaporation happens quicker and the solution does not attach well to the tip, therefore, a home-built conventional setup and new techniques were designed and developed for studying electrospinning of biomolecules. There were four setups constructed and used in this thesis, the details and their schematics are described following.

3.2.2.1 Conventional electrospinning (ES)

Typically used for the production of polymer nanofibers in a laboratory scale, a solution of at least 0.1 ml is required for experimental conditions. The conventional setup used in this thesis consists of four parts; 1) high voltage, 2) solution flow rate control, 3) collector, and 4) chamber (see schematic in Fig. 3.2). Each part has components listed below.

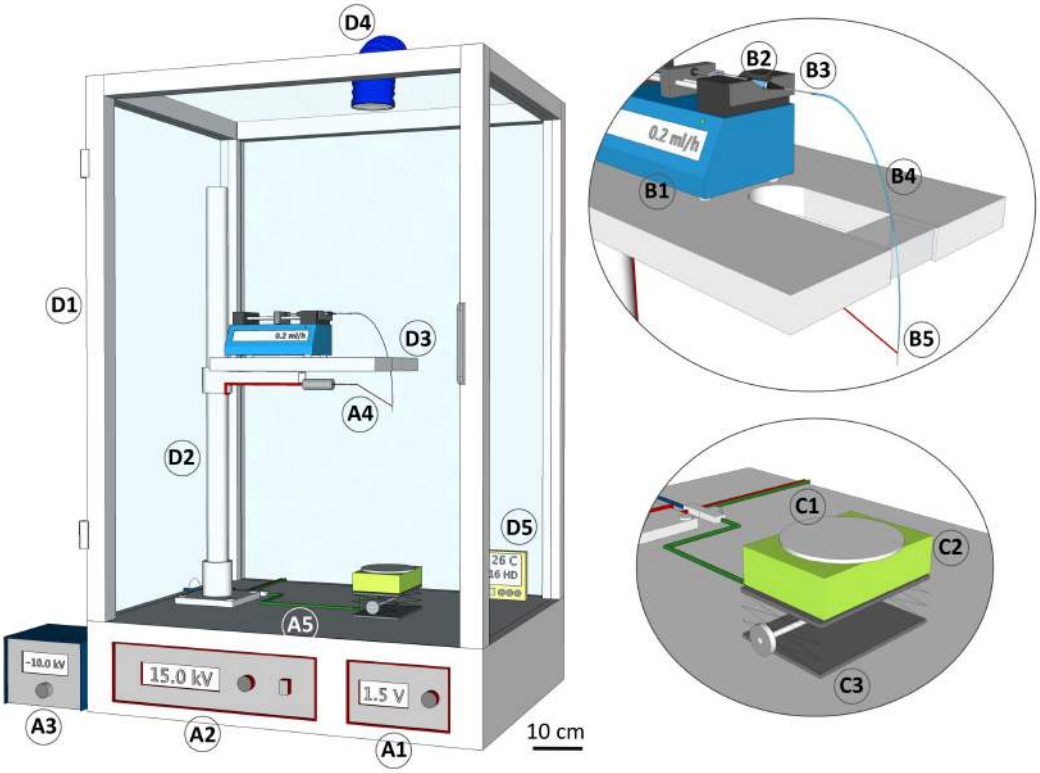

Figure 3.2: Schematic of the home-built conventional electrospinning setup consisting of four parts; (A1)-(A5) a high voltage, (B1)-(B5) a solution flow rate control, (C1)-(C3) a collector, and (D1)-(D5) a chamber.

Part 1: High voltage

(A1) Low voltage (0-10 volts) (PS303pro, Voltcraft) was applied to the control unit of high voltage

(A2) DC high voltage power supply (HP030R, AppliedKilovolts) used for applying a positive or negative voltage up to 30 kV (practical 25 kV, electric spark can exist above this value) of maximum at 0.25 mA. The exact number of high voltage generated from the home-built electrospinning system can be measured with a high voltage probe (80K-40, Fluke).

(A3) Another negative high voltage power supply (HP030, AppliedKilovolts) was applied to the

collector in order to achieve potential differences above 25 kV

(A4) High voltage cable connected to a needle

(A5) Electrical cable connected to a collector

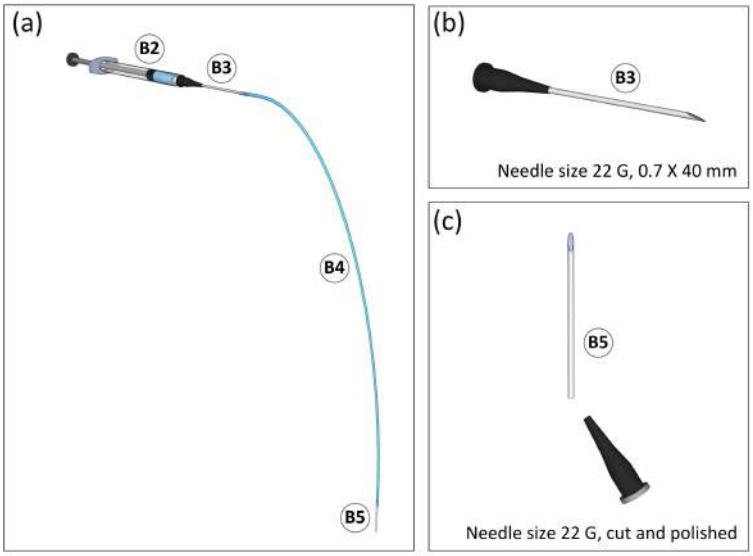

Figure 3.3: Schematic of the solution flow rate part; (a) solution was loaded into (B2) a 1 ml plastic syringe (Terumo), which is connected to (B3) a metal needle (size 22 G 0.7x40 mm, Terumo) through (B4) a teflon tube. The teflon tube was connected to (B5) another one cut-needle; (b), (c) the metal needles connected to the both ends of the teflon tube.

Part 2: Solution flow rate control

(B1) Syringe pump (11 Plus model, Harvard Apparatus) used to control the flow rate of solution at a certain rate, alternative: Home-built feeder made from a small digital linear actuator, used in case to fast check the electrospinnability of a solution. Advantage of the linear actuator is higher stability control than the syringe pump, when using close to a high voltage.

(B2) 1 ml plastic syringe (Terumo), which is connected to (B3)

(B3) Metal needle (size 22 G 0.7x40 mm, Terumo)

(B4) Teflon tube (inner diameter of 0.5 mm, Sigma-Aldrich)

(B5) Another metal needle (size 22 G 0.7x40 mm, Terumo), cut and polished (see schematic in Fig. 3.3)

Part 3: Collector

(C1) Easily removable disk collector made from aluminum with diameter 12 cm, covered with aluminum foil

(C2) Insulator foam sheet inserted between the collector and lift jack

(C3) Lift jack for fine adjustment distance between the collector and the needle

Part 4: Chamber

(D1) Closed setup made from polycarbonate sheets and aluminum frames

(D2) Pillar made from aluminum rod for supporting the second part, the distance between the needle and the collector can be roughly adjusted here

(D3) Wood plate for supporting the syringe pump

(D4) Air suction on top removes solvent and loose fibers

(D5) Thermo/hygrometer

3.2.2.2 Microliter electrospinning (μl-ES)

The conventional electrospinning setup used in the first stage requires highly concentrated solutions of self-assembling peptides of at least 0.1 ml per experiment. This solution volume means that the minimum amount of the substance is thus in the range of 10 mg. However, many biomolecules, especially peptides and proteins, are only available in μg amounts. In order to assess fiber formation potential even from such very small amounts of substance, a new technique named "microliter electrospinning" was created, based on an electrified wire. A concept related to the scanned tip electrospinning deposition setup (Fig. 3.1j) reported by J. Kameoka et al. [33–35]. The scanned tip made from silicon was replaced by a platinum (Pt) wire, which is more convenient to fabricate, do experiments, setting up and cleaning. Figure 3.4) shows a schematic of the microliter setup; the high voltage is applied to a platinum (Pt) wire of 0.25 mm diameter, onto which the solution is directly dropped from a micropipette. Building on the same physical processes with the conventional setup, the droplet attached to the wire is stretched, causing the formation of a fiber.

An electrified wire of the microliter electrospinning is used as the tip replaces the needle in conventional electrospinning. Besides supporting small amounts solution (<5 μl), the electrified tip is convenient for testing the electrospinnability of biomolecules solution. For a solution formed like a gel, conventional electrospinning with the needle cannot feed this solution but it can be tested with the microliter setup, moreover, some solution dried and stuck on the tip which can be removed easily with a paper wiper soaked in isopropanol or using a sonicator. Figure 3.5 shows components of the electrified tip consisting of; ① insulating tape, ② a cut-pipette tip, and ③ platinum (Pt) wire

diameter of 0.25 mm, 99.9% trace metals basis (Aldrich). About 3 cm of Pt wire was inserted into the cut-pipette tip, and wrapped with the insulating tape, these assembly steps are meant to help the tip to be easily handled and applied with a high voltage.

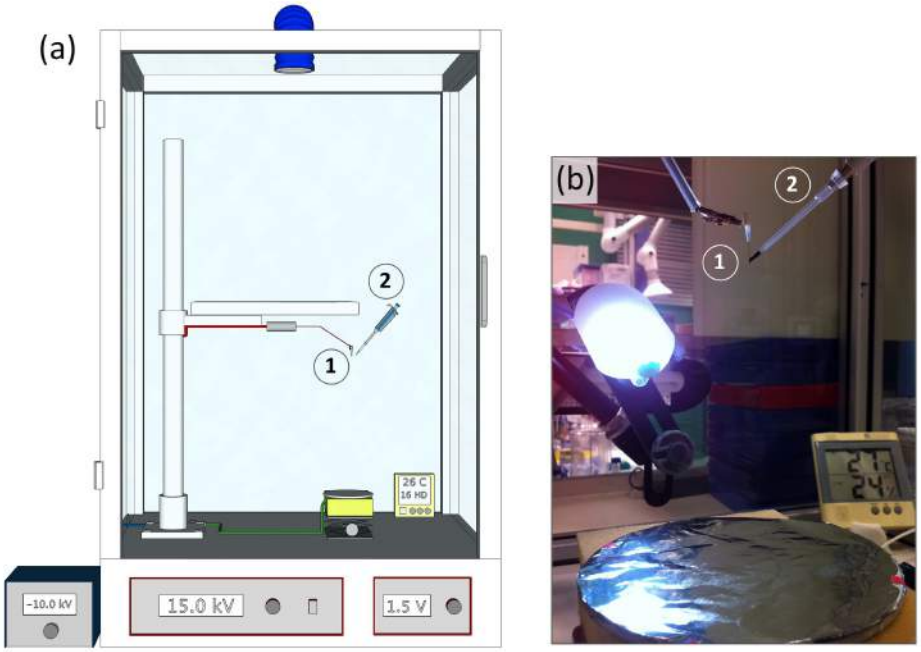

Figure 3.4: (a) Schematics of the microliter electrospinning setup; ① an electrified wire tip and ② a microliter pipette. (b) Digital photos of the microliter setup.

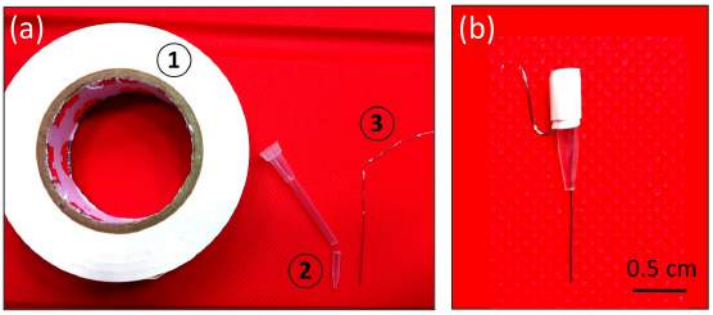

Figure 3.5: Digital photos of (a) components used for making a tip of microliter electrospinning; ① an insulating tape, ② a 100 μl pipette tip, and ③ a platinum wire of diameter 0.25 mm diameter, (b) an assembled tip.

3.2.2.3 Extreme far-field μl-ES (EXFF μl-ES)

This technique is used for the production of proteins nanofibers with diameters below 100 nm. The distance between the tip and the collector is increased to a range of 30−80 cm, while typical values are 10−20 cm for conventional electrospinning (far-field electrospinning, FFES), and 0.5−3.0 mm for near-field electrospinning (NFES) [36–39]. Figure 3.6 shows schematics of the electrospinning setup, the electrified wire is placed very far from the collector in the range of 30−80 cm. The distance between the needle and the collector or substrate is one of the important parameters in electrospinning, maybe it has a significant effect on the diameter of electrospun fibers depending on the properties of the solution. As explained in the theory section (Chapter 2), the solution has a longer flight time to be stretched and the solvent to evaporate when the collector was placed far from the needle, the result is the fiber diameter is decreased, however, it is possible that no fiber can be collected on the substrate, if the needle is placed too far from the collector, therefore, the distance is frequently varied to around 10−20 cm for conventional electrospinning. In the case of electrospinning of proteins, some nanofibers can be collected on a substrate, even the distance is increased up to 80 cm.

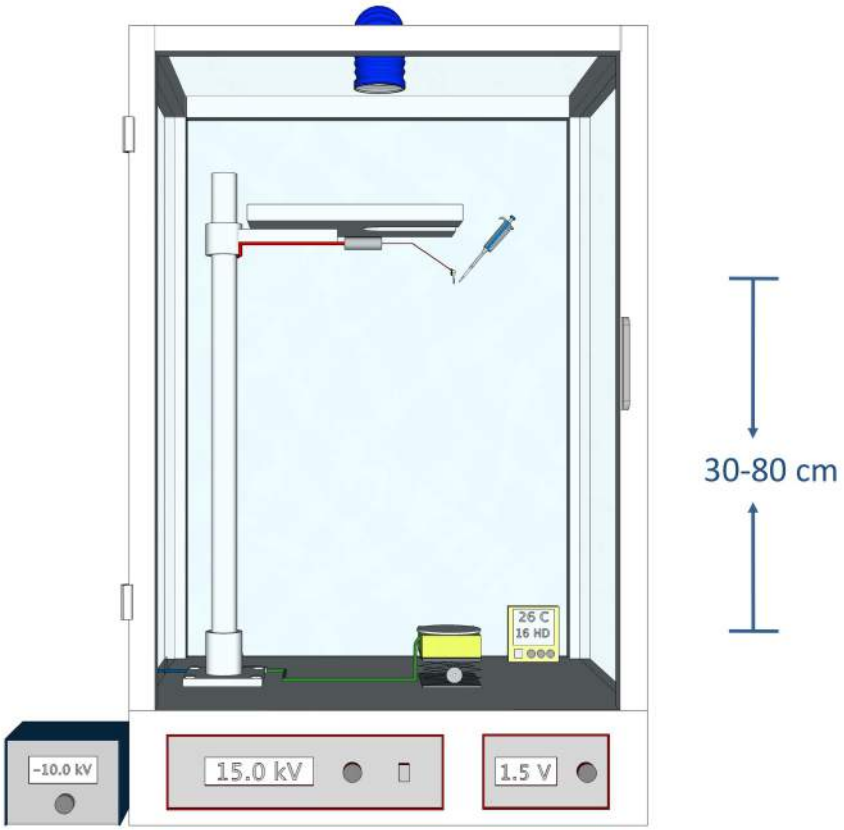

Figure 3.6: Schematics of the extreme far-field microliter electrospinning setup (EXFF μl-ES), distance between the electrified wire and the collector is increased to a range of 30 to 80 cm in order to reduce diameter of protein fiber less than 100 nm.

3.2.2.4 Extreme far-field μl-ES with an air stream (EXFF μl-ES + Air)

To reduce the diameter of protein nanofibers to below 10 nm, an air stream from a hot air generator (HLG 2000, Würth master) is placed above the tip, pointing downwards (see Fig. 3.7). The gap between the hot air gun and the electrified wire must be about 2 cm as an electric spark can occur if the gap is smaller than this value. The air flow rate was around 2500 cm^3/min through a 0.57 cm^3 nozzle, (hence speed 0.73 $m.s^{-1}$) and the temperature of between 35 to 45 °C.

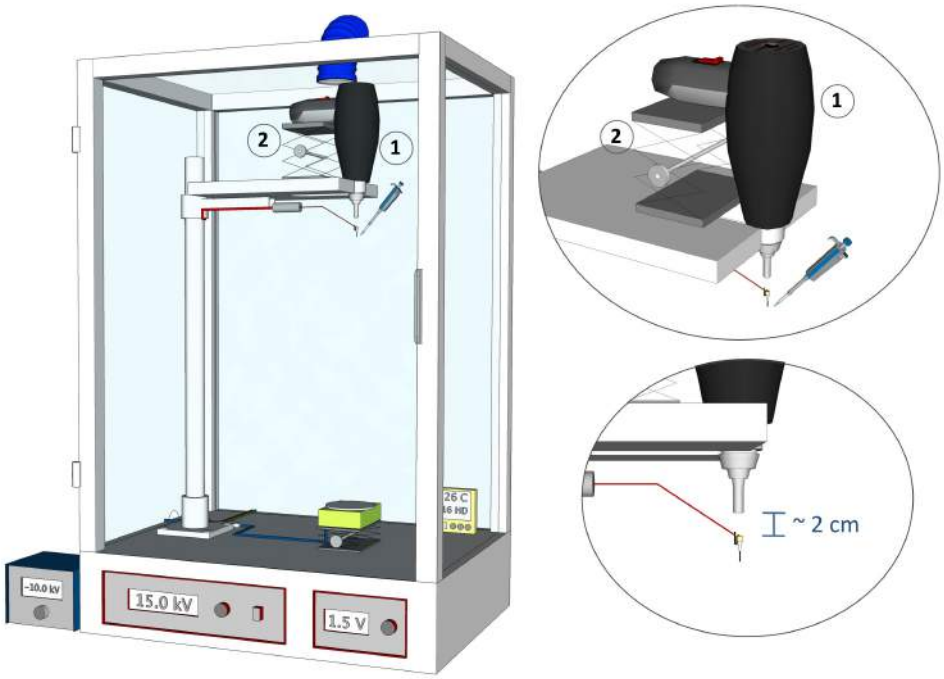

Figure 3.7: Schematics of the extreme far-field microliter electrospinning with an air stream setup (EXFF μl-ES + Air); ① A hot air generator is placed above the tip, ② a secondary lift jack is used for keeping gap between the hot air gun and the tip at around 2 cm.

3.2.3 Experimental procedure of electrospinning

First stage of experiments (Chapter 4), the home-built conventional electrospinning system was used to produce fibers from a peptide solution. Standard electrospinning processes are;

1. Load a solution at least 0.1 ml into a 1 ml plastic syringe, which is connected to a metal needle through a teflon tube in order to protect the syringe pump from the high voltage.
2. Control the solution flow rate to 0.2−0.5 ml/h using a syringe pump.
3. Adjust the distance between the needle and collector using a lift jack within a range of 10 to 20 cm.
4. Place a substrate over the collector plate to collect fibers for characterizations.

5. Apply a positive DC high voltage 10−30 kV to the needle and the negative pole connected to a collector plate (or vice versa).
6. Optimize electrospinning parameters, i.e. applied voltage, flow rate, distance between the needle and collector.

The ambient parameters, (e.g. temperature, humidity) affect the electrospinning process because the solvent evaporation rate increases with increasing temperature, and the humidity can increase or decrease the diameter of electrospun fibers, depending on the chemical nature of the substance. The electrospinning processes in this thesis were performed at a humidity < 30 %. A hot air gun (HLG 2000, Würth master) was used to reduce the humidity in the electrospinning chamber. The hot air gun was turned on until humidity inside the chamber was less than 30 %, monitored by a thermo/hygrometer (EM-913R, Oregon Scientific), as the temperature inside the chamber can increase slowly with time. The temperature and humidity were constantly recorded.

3.2.4 Substrates

During the electrospinning processes, a precleaned[1] glass slide (Menzel-Gläser Superfrost, Thermo Scientific) was cleaned with N_2 blowing and placed on the collector to collect a fiber for characterization with an optical microscope. For electron microscopy such as SEM, wet cleaned oxidized silicon (111) wafers were used. The wet cleaning processes are;

1. An oxidized silicon (111) wafer with dimension of 7 x 7 mm or bigger was washed with Milli-Q water.
2. Placed in acetone and sonicated in an ultrasonic bath for ∼15 min.
3. Sonicated again in isopropanol for ∼15 min.
4. The substrates were dried by blowing them with N_2.

3.3 Characterization Techniques

Biomolecular fibers were characterized with various techniques to study their physical and chemical properties. Characterization techniques will be detailed in this section, i.e. optical microscopy, electron microscopy, atomic force microscopy, X-ray diffraction, and circular dichroism spectroscopy. Furthermore, vibrational spectroscopy mainly used in this work for chemical analysis will be reviewed in more detail. Some additional techniques were included in the experimental results, e.g. polarized Raman spectroscopy, and nano-FTIR.

[1] wet cleaning as for wafers was used for dirty glass slides.

3.3.1 High-speed camera

The formation of fibers fabricated by electrospinning is shortened to milliseconds, much below than standard times for self-assembly in solution, e.g. for amyloid fibrils. The fiber formation processes cannot be recorded with a normal video camera. Therefore, a high-speed camera (Fastcam SA5, Photron) was implemented to visualize the electrospinning processes. A white light was generated by a Xenon lamp 300 W (Xenon NOVA 300, Karl Storz). The white light was sent through a fluid light cable (81594SB, Karl Storz) to a dispersing paper, which was placed at the back of the needle to illuminate the fiber formation process. The high-speed camera was focused at few millimeters around the tip of the needle and then recorded the electrospinning process. This method provided useful visual information on how the Taylor cone initiates, develops and produces electrospun fibers.

The Fastcam model SA5 has a memory of 8 GB, meaning that it can record the process for 0.75−5.46 s, depending on frame rate and resolution of the recording parameters. For example;

- An experiment focused on the area of the solution jet, the frame rate was set at 100,000 fps and 192 x 248 pixels of resolution. The limit for the record duration is 0.93 s. This record duration is small but long enough for electrospinning process.
- At a study of solution drop, the frame rate was set at 20,000 fps and 384 x 808 pixels of resolution. The limit for the record duration is 0.92 s.

Furthermore, the camera has various possibilities to start and stop the recording by setting a trigger mode parameter. Normally, when the trigger mode is set at “Start” mode, the electrospinning process will be recorded, directly after the trigger switch is pressed. The camera will record the process until its memory is full. In some cases, i.e. for recording a dropping process, if the trigger mode is set at “Center” mode, the dropping process will be recorded continuously before the trigger switch is pressed, and stopped after the switch is pressed when the memory is full. If the record duration time is 1 s, the dropping process will be recorded for 0.5 s before and for 0.5 s after the trigger switch is pressed.

3.3.2 Optical microscopy

The electrospun fibers on the collector substrate were first characterized by an optical microscope (BX50, Olympus) with a magnification up to 1,000X, equipped with a digital camera (D300, Nikon) to evaluate the electrospinnability property. Consistency measurements of sample fibers were performed by obtaining a measurement for the scale bar of an optical micrograph and then comparing a set of measurements of corresponding fiber diameters to that scale bar. The scale bars in optical micrographs were calibrated from a silicon calibration grating (TGX11, Mikromasch) at various magnifications. All images have the same dimension in pixels, and each pixel was converted into a micrometer scale with the GIMP (GNU Image Manipulation Program) software. The

diameter of the fibers was measured by the software ImageJ for Mac V.10.2 (Developed by National Institutes of Health). Although the average diameter measured by the optical microscope can have some error close to the diffraction limit (~300 nm for yellow light), it is fine enough for checking the electrospinnability, and has the advantage to be much faster than electron microscopy.

3.3.3 Scanning electron microscopy (SEM)

A tabletop scanning electron microscope (Tabletop-SEM) (Phenom, FEI) was used in this work for producing high resolution images of peptide fiber samples deposited on a glass slide substrate. A sample was cut by a diamond pen to fit in the Tabletop-SEM sample holder (maximum diameter is 25 mm) and fixed on the SEM aluminum stub by a (sticky) carbon tape. The mounted sample was loaded into low vacuum load-lock chamber and placed below the electron gun, which is a long lifetime thermionic source with an accelerating voltage of 5 kV. In some cases, the low conductivity of glass slide substrate showed a charging effect under the Tabletop-SEM; so that a light coating of gold with 5 nm of thickness was used to improve the image quality. An alternative scanning electron microscope (SEM) (QuantaTM 250 FEG, FEI) was also used, whose electron optics has an accelerating voltage from 1 kV to 30 kV. Moreover, the chamber vacuum can be controlled from 10 to 2,600 Pa at low vacuum range (standard is high vacuum $< 6 \times 10^{-4}$ Pa). Low vacuum (nitrogen or water vapor) is helpful to reduce charging effects. Hence, the sample can be characterized without coating of gold or stained to avoid artifacts.

3.3.4 Scanning transmission electron microscopy (STEM)

To analyze an electrospun fiber with diameter below 20 nm, such as some small proteins and dsDNA fibers, samples were deposited onto a 400-mesh carbon-coated copper grid (Agar Scientific), and imaged in a scanning transmission electron microscope (STEM, Helios NanoLab Dual Beam, FEI, NL). Typically, a transmission electron microscope (TEM) can be used to characterize a sample at a high resolution of a few nm, but biological specimens are difficult to image in TEM because of their low contrast. One solution for increasing contrast is staining by the addition of heavy atoms [50]. However, to avoid artifacts from the staining, STEM was used in this work.

The principle of STEM is like the one of SEM: scanning the sample with a focused electron beam (20–30 kV, lower relative to typical TEM operating energies) and generating an image from the acquired signal. The samples must to be thin just like in case of TEM because the transmitted electrons that emerge from the opposite side of the sample will be captured by a detector and produce an image. There are two main possibilities to record the transmitted electrons; 1) using a bright field (BF) detector for collecting the transmitted electrons on axis, so that the resulting holes appear bright; 2) using an annular dark field (ADF) detector for recording scattered electrons, the holes appear dark and the sample is bright [50, 51].

3.3.5 Atomic force microscopy (AFM)

For the ultimate case of single molecular thickness (below 10 nm) nanofibers, their surface topographies were imaged with an atomic force microscope (AFM, 5500, Agilent Technologies) in AC mode with a tip frequency of 298.5 kHz. Silicons cantilevers were operated, with a spring constant of 42 N/m. The resolution was 512 pixels per line.

3.3.6 X-ray powder diffraction (XRD)

The crystallinity of the powders and fibers was determined via X-ray powder diffraction (XRD). The crystalline part of the sample gives sharp and narrow diffraction peaks and the amorphous component gives a very broad peak. These phenomena are based on diffraction of X-rays bombarded on the sample. The condition for diffraction is defined by the Bragg's law $n\lambda = 2d \cdot sin\theta$, where λ is the wavelength of X-rays, θ is scattering angle; n is an integer and d is spacing between planes in the atomic lattice. In this work, the samples were analyzed in a powder diffractometer (X'Pert, PANalytical). The λ is a fixed wavelength (0.154 nm, radiation of $Cu - K_\alpha$), and θ is variable. The X-ray tube voltage and current were 45 kV and 40 mA, respectively. Because some sample powders and fibers are available in amount of mg or μg, in order to achieve a good signal, the sample preparation and measurement setup were optimized as follows:

- Powder and fiber samples were placed homogenously on a silicon crystal zero background holder, covering an area of at least 10 x 10 mm.
- A certain constant rotation speed of the sample holder was set at 4 s/revolution with installation of a beam knife over the sample of 1 mm.
- For the incident beam, divergent X-rays from the source were controlled to irradiate a beam width of 10 mm onto the sample by using a programmable divergent slit (PDS), a fixed anti-scatter slit of 1°, a mask of 20 mm, and a soller slit of 0.04 rad.
- For the diffraction beam, a programmable anti-scatter slit, a nickel filter and a soller slit of 0.04 rad were installed before a detector recorded the diffraction beam.
- The scan range was defined from 5 to 45° (generally, a significant peak over this value was not observed in this work).
- "Time per step" value of the scan was set at 100 s/step or longer in order to obtain a high signal to noise ratio.

3.3.7 Vibrational spectroscopy

Vibrational spectroscopy is used to study molecular vibrations that occur when atoms in a molecule are in periodic motion, on top of the fact that the molecule as a whole can have constant translational and rotational motion. The frequency of the periodic motion is known as a vibrational frequency. The molecular vibration is excited when the molecule absorbs a quantum of energy E, corresponding to the vibrational frequency ν. The relation is

$$E = h\nu = hc.(\nu/c)\,, \tag{3.2}$$

where h is Planck's constant, c is the velocity of light and ν/c is quoted as wavenumbers. Two techniques that can be used to obtain vibrational data from solid state or gas phase samples are Infrared spectroscopy (IR) and Raman spectroscopy. The differences between these techniques are the photon energies transferred to the molecule and the instrumentation setup. For the IR technique, the molecule will absorb the photon, while there is both absorption and emission in the Raman technique. A qualitative description of the principles and selection rules of IR and Raman spectroscopies are given in [52] (see diagram in Fig. 3.8).

3.3.7.1 Infrared spectroscopy (IR)

The vibration in IR spectroscopy is excited by irradiating the sample with photon energies in the infrared region, generally in the range ν/c = 10000 to 200 cm^{-1}, although often only 4000 to 400 cm^{-1} are used. The molecule is excited to a higher vibrational state by directly absorbing the infrared radiation, as shown in Fig. (3.8). The selection rule of IR states that a vibration mode will be active when there is a change in the molecular dipole moment during the vibration.

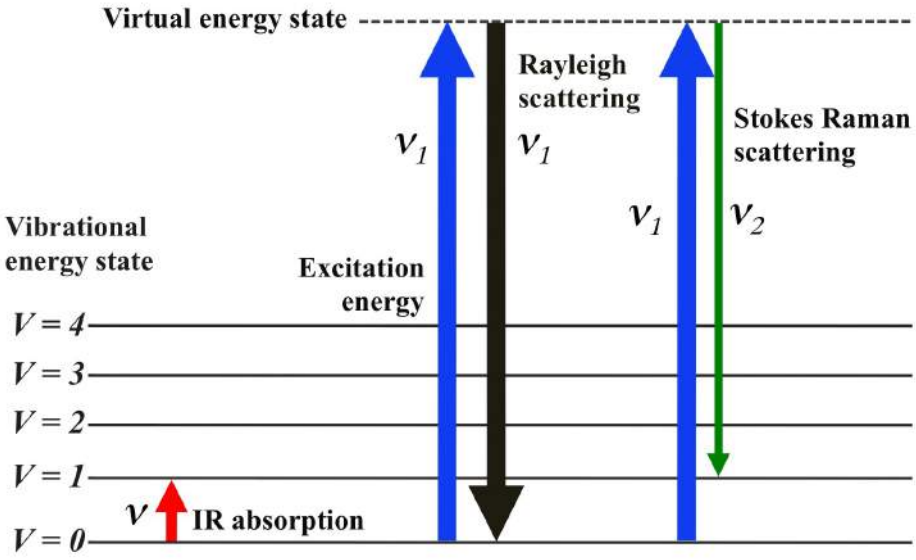

Figure 3.8: Energy level diagram showing the states involved in IR and Raman spectroscopies. For Raman, the arrow thickness indicates the signal strength from the different transitions. This diagram was adapted from [52].

In this work, a Fourier transform infrared (FTIR) spectrometer (Equinox 55, Bruker) equipped with attenuated total reflection (ATR) holder (Pike Technologies) was used to measure the vibrational mode of the samples in fiber and powder form. For ATR, infrared light is guided through an interferometer and then through a germanium (Ge) crystal in the ATR holder, allowing the infrared

radiation to reflect (from inside the Ge) at the Ge surface, where the sample is placed. Only the IR evanescent field just above the Ge surface illuminates the sample. For FTIR, a moving mirror inside the apparatus alters the distribution of infrared light that passes through the interferometer. The signal directly recorded (interferogram) represents light output as a function of mirror position. A Fourier transform from mirror position to frequency calculates a spectrum from the interferogram. In this thesis, the peak hights are not quantitative (the spectra were scaled and offset for clarity).

Curve fitting of IR spectra in the amide I region was performed using the OPUS software package (version 4.2) supplied by Bruker. The fitting is achieved by a damped least-squares optimization algorithm developed by Levenberg-Marquardt [53, 54], assuming Gaussian band envelopes of width 5 cm^{-1}. Assignment of amide I bands were done according to literature data related to peptide or protein. The percentage of each secondary structure was calculated to be the fractional area of the corresponding peaks, divided by the sum of the areas of all the compositions.

3.3.7.2 Raman spectroscopy

For Raman spectroscopy, a vibration is excited by monochromatic light, usually in the visible range of the electromagnetic spectrum, hence much more energetic than infrared. The Raman effect originates from inelastic scattering, although elastic scattering of radiation by the sample is also present. In the case of elastic scattering (Rayleigh scattering), the molecule is excited to a virtual energy state, and then relaxes to the original vibrational energy state by re-emitting a photon at the same frequency as the incident light (see Fig. 3.8). This frequency has to be blocked very efficiently from the detector by an edge filter. There is a very small fraction of molecules excited by inelastic scattering (Raman scattering), in which the excited molecule relaxes to a different vibrational level. The Raman spectrum shows a resonance when the frequency shift between the scattered light ν_2 and the excitation frequency ν_1 corresponds to a vibrational energy quantum (Eq. 3.3).

$$h\nu_1 = h\nu_2 + \Delta E_{vibration} = h\nu_2 + h\nu\,. \tag{3.3}$$

Figure 3.8 shows the vibrational energy states of a molecule. The Raman selection rule states that a vibrational mode will be active when there is a change in the molecular quadrupole moment, or of polarizability, during the vibration.

In this work, confocal Raman spectroscopy (Alpha300S, WITec) was used. The samples were deposited on a glass slide and excited with a frequency-doubled Nd:YAG laser at 532 nm (ν_1/c = 18797 cm^{-1}, green). The laser power was optimized (less than 56 mW) and focused on the sample through an objective lens (100X, NA 0.9), avoiding burning. Figure (3.9) shows the schematics of the beam path and important components of the machine. The Rayleigh scattering is filtered by an edge filter, while the Raman scattering is collected with the same objective and focused through

a pinhole. The core of the multi-mode optical fiber (100 μm core diameter[2]) acts as a pinhole for confocal microscopy. The collected Raman scattering is detected with a spectrometer (600 grooves/mm grating) and a CCD camera. The spectra were corrected by cosmic ray removal and background subtraction.

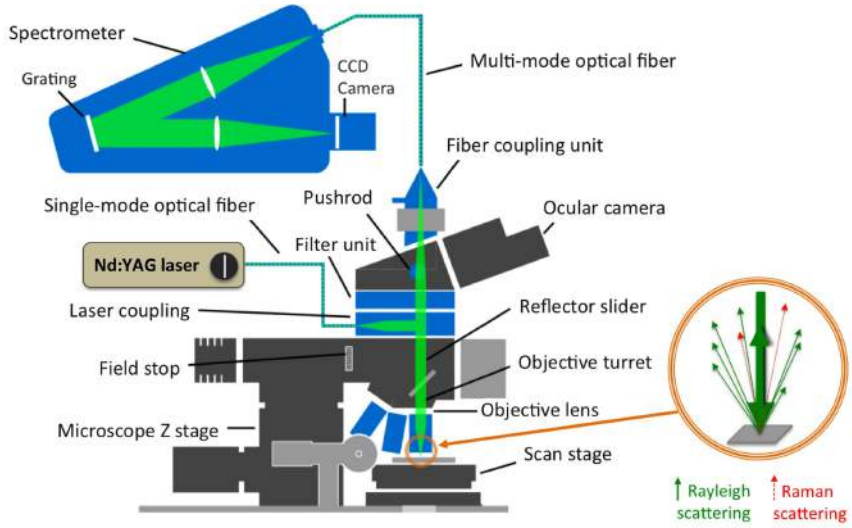

Figure 3.9: Schematics of the confocal Raman spectroscopy setup and its beam path (adapted from the manual of WITec confocal Raman tools).

3.3.8 Circular dichroism (CD) spectroscopy

As well as the vibrational spectroscopy methods described previously, circular dichroism (CD) is another excellent method for determining the secondary structure and folding properties of proteins, especially in solution form. Not only the electrospinning process can affect to the structure of the proteins, but also the solvents used in the dissolution process. Therefore, a CD spectrometer (J-815, Jasco, USA) was accounted to provide information about the secondary structure of the protein solutions.

When circular polarized light passes through chiral sample such as a protein solution, resulting left and right circular polarized light is differently absorbed, hence, a distinct CD spectrum can be presented. Circular polarized light used in this work is in the far ultraviolet (UV) region (190−250 nm), which corresponds to peptide bond absorption. Hence, the CD spectrum can be analyzed to provide the content of regular secondary structural features such as α-helices and β-sheets. The α-helices structure shows negative bands at 208 nm, 222 nm, and a positive band at 193 nm. Instead, β-sheets displays a negative band at 218 nm and a positive band at 195 nm. In addition, random structures show a negative band at 195 nm and a low ellipticity above 210 nm [55–57].

[2]A smaller pinhole of 50 or 25 μm diameter gives higher lateral and depth resolution, but the collection efficiency is strongly reduced.

Since the CD spectrum is based on an absorbance measurement, the sample solution must be in the correct concentration range. When the absorbance of the sample is too high, not enough light will be recorded by the detector, resulting in the spectrum not being displayed since the differential absorbance of left and right circularly polarized light is below the detection threshold. However, the CD spectrometer can gain this differential absorbance by applying a high tension (HT) voltage to the detector. This additional applied voltage is roughly proportional to absorbance. In case the HT voltage is above ~600 V, the detector will be saturated and the amplitude of the spectrum can oscillate wildly. Beyond 800 V, the noise will become disproportionate to the sample signal and the output CD spectrum will be completely unreliable.Thus, the sample solution needs to be reduced and optimized until a CD spectrum can be recorded. For this work, solution samples were diluted 1:1000 with water, and loaded into a cuvette of thickness 10 mm made of quartz (Hellma Analytics). A CD spectrum baseline was recorded with a blank cuvette or filled with water. The measurements were operated in continuous mode with a scanning speed of 200 nm/min, accumulated 10 times. The relative fraction of secondary structures was determined by fitting data with the help of the K2D3 software [58].

3.4 Computation of Molecular Vibrations

The infrared and Raman spectroscopy explained in the previous section provide information on molecular vibrations. The vibrational spectra of (solid) peptide fibers and powders were compared to simulation results of single molecules (in vacuum), obtained with a software package. The comparison can help to understand the vibrational modes of peptide electrospun fibers and assign the vibrational spectrum to the vibration of atoms and chemical groups in the peptide.

3.4.1 Computational details

The quantum chemical computations of single molecules were performed using the Gaussian09 program package [59] based on density functional theory (DFT) [60]. The calculations were performed using the B3LYP (Becke, 3-parameter, Lee-Yang-Parr [61,62]) exchange-correlation functional with standard 6-31G, 6-31G* or 6-311++G** basis sets, which are employed in linear combinations to create molecular orbitals (see table 3.4). The simulations were calculated on a high performance computing cluster (Arina Cluster, SGIker, UPV/EHU).

Firstly, the geometry of the single molecule was generated and converted (as explained in the next section) to atomic coordinates used for the input file of Gaussian09. Then, the optimized geometry corresponding to a minimum on the potential energy surface was obtained by solving the self-consistent field equation iteratively. After that, the harmonic vibrational wavenumbers of the optimized structure were calculated from analytic second derivatives of energy, to confirm the convergence to a minimum in the potential surface. Finally, the calculated quantum mechanical results were corrected by empirical scaling factors (according to the Pulay method [65]). This correction can improve the accuracy of the vibrational spectra prediction. However, this method

Table 3.4: Computational details of aromatic peptides and π-stacking unit, which is simulated and compared to experiments.

Computational details	**Phe-Phe**	**Fmoc-FG**	**Fmoc-G**	**9FM**
Exchange-Correlation functional	B3LYP	B3LYP	B3LYP	B3LYP
Basis set	6-311+G*	6-31+G*	6-31+G*	6-31G
Starting geometry	Görbitz [2]	Galaxy 3D [63]	PubChem [64]	Galaxy 3D [63]
Scaling factor	0.977	0.973[a]; 0.964[b]	0.973[a]; 0.964[b]	0.966[a]; 0.953[b]

[a] This scaling factor has been applied for wavenumbers 0−2000 cm^{-1} and
[b] for wavenumbers higher than 2000 cm^{-1}

must be carefully optimized using large databases of empirically corrected harmonic force fields (see recommendation in [66, 67]).

3.4.2 Structure development

A starting geometry of a single molecule has to be generated from the literature, a database or drawn using a molecule editor software (see detail in Table 3.4). Geometry of the Phe-Phe molecule was modified from the work of [2], Fmoc-G was downloaded from PubChem compound database [64] (CID=93124). For Fmoc-FG and 9FM no structure is published; therefore, their molecular geometries were created with the Galaxy 3D molecule building software [63].

▲ Summary

Self-assembling (in a specific condition) biomolecules such as short aromatic peptides and globular proteins are the main topics of this thesis. They must be dissolved in a suitable solvent and at optimized concentration so as to fulfill the inequality $Oh \geq 1$.

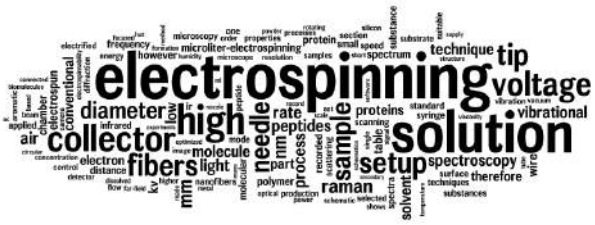

Much of this chapter discusses electrospinning setups, particularly, the conventional setup and microliter electrospinning. The later setup is a new nozzle-less design developed for this thesis. The tip is made from a Pt wire, onto which the solution can be directly dropped from a micropipette. This is convenient to do experiments and suitable for small amounts of solution. Furthermore, it can be combined with an air stream for production of sub-100 nm protein fibers. Infrared and Raman spectroscopy are mainly chemical characterization techniques. Instead, electron microscopes are important tools for studying the morphology of the biomolecular electrospun fibers.

The conventional electrospinning (ES), microliter electrospinning (μl-ES), microliter electrospinning at extremely far-field (EXFF μl-ES), and microliter electrospinning at extremely far-field with air stream (EXFF μl-ES + Air) will be used in Chapter 4 and 5 as described below.

• ES	Ch. 4.1	ES of self-assembling peptides
	Ch. 5.4	ES of hydrophobins
• μl-ES	Ch. 4.1, 4.2, 4.3	ES of aromatic peptides and TPP
	Ch. 5.1, 5.3	ES of globular proteins and insulin
• EXFF μl-ES	Ch. 5.2	ES of albumin into ultra small fibers
• EXFF μl-ES + Air	Ch. 5.2, 5.5	ES of albumin and double-stranded DNA

3.5 References

[1] C.H. Görbitz. Nanotube formation by hydrophobic dipeptides, *Chemistry A Euro. J.* **7**: 5153-5159, 2001.

[2] C.H. Görbitz. The structure of nanotubes formed by diphenylalanine, the core recognition motif of Alzheimer's β-amyloid polypeptide, *Chem. Comm.* 2332-2334, 2006.

[3] E. Gazit. Self Assembly of Short Aromatic Peptides into Amyloid Fibrils and Related Nanostructures, *Prion.* **1**: 32-35, 2007.

[4] J. Kim, et al. Role of Water in Directing Diphenylalanine Assembly into Nanotubes and Nanowires, *Adv. Mater.* **22**: 583-587, 2010.

[5] G. Singh, A.M. Bittner, S. Loscher, N. Malinowski, K. Kern. Electrospinning of Diphenylalanine Nanotubes, *Adv. Mater.* **20**: 2332-2336, 2008.

[6] V. Jayawarna, et al. Nanostructured Hydrogels for Three-Dimensional Cell Culture Through Self-Assembly of Fluorenylmethoxycarbonyl - Dipeptides, *Adv. Mater.* **18**: 611-614, 2006.

[7] D.J. Adams, M.F. Butler, M. Kirkland, L. Mullen, W.J. Frith. Influence of Molecular Structure on the Gelation Behaviour of Fmoc-Dipeptides, *AIP Conf. Proc.* **1027**: 555-557, 2008.

[8] D.M. Ryan, T.M. Doran, S.B. Anderson, B.L. Nilsson. Effect of C-Terminal Modification on the Self-Assembly and Hydrogelation of Fluorinated Fmoc-Phe Derivatives, *Langmuir* **27**: 4029-4039, 2011.

[9] G. Charalambidis, E. Kasotakis, T. Lazarides, A. Mitraki, A.G. Coutselos. Self-Assembly Into Spheres of a Hybrid Diphenylalanine-Porphyrin: Increased Fluorescence Lifetime and Conserved Electronic Properties, *Chem. Eur. J.* **17**: 7213-7219, 2011.

[10] K. Ladomenou, T. Lazarides, M.K. Panda, G. Charalambidis, D. Daphnomili, A.G. Coutsolelos. Meso-substituted Porphyrin Derivatives via Palladium-Catalyzed Amination Showing Wide Range Visible Absorption: Synthesis and Photophysical Studies, *Inorg. Chem.* **51**: 10548-10556, 2012.

[11] W. Wohlleben, T. Subkowski, C. Bollschweiler, B. von Vacano, Y. Liu, W. Schrepp, U. Baus. Recombinantly produced hydrophobins from fungal analogues as highly surface-active performance proteins, *Eur. Biophys. J.* **39**: 457-468, 2010.

[12] W.E. Teo, R. Inai, S. Ramakrishna. Technological advances in electrospinning of nanofibers , *Sci. Technol. Adv. Mater.* **12**: 013002, 2011.

[13] R. Nayak, R. Padhye, I.L. Kyratzis, Y.B. Truong, L. Arnold. Recent advances in nanofibre fabrication techniques, *Text. Res. J.* **82**: 129-147, 2012.

[14] D. Li, Y. Wang, Y. Xia. Electrospinning of Polymeric and Ceramic Nanofibers as Uniaxially Aligned Arrays, *Nano Lett.* **3**: 1167-1171, 2003.

[15] D. Li, Y. Xia. Electrospinning of Nanofibers: Reinventing the Wheel?, *Adv. Mater.* **16**: 1151-1170, 2004.

[16] V. Beachley, X. Wen. Effect of electrospinning parameters on the nanofiber diameter and length, *Mater. Sci. Eng. C* **29**: 663-668, 2009.

[17] L. Liu, Y.A. Dzenis. Analysis of the effects of the residual charge and gap size on electrospun nanofiber alignment in a gap method, *Nanotechnology* **19**: 355307, 2008.

[18] J.A. Matthews, G.E. Wnek, D.G. Simpson, G.L. Bowlin, Electrospinning of Collagen Nanofibers, *Biomacromolecules* **3**: 232-238, 2002.

[19] H.Y. Kim, M. Lee, K.J. Park, S. Kim, L. Mahadevan. Nanopottery: Coiling of Electrospun Polymer Nanofibers, *Nano Lett.* **10**: 2138-2140, 2010.

[20] D. Zhang, J. Chang. Electrospinning of Three-Dimensional Nanofibrous Tubes with Controllable Architectures, *Nano Lett.* **8**: 3283-3287, 2008.

[21] R. Rangkupan, D.H. Reneker. Electrospinning Process of Molten Polypropylene in Vacuum, *J. Metal. Mater. Miner.* **12**: 81-87, 2003.

[22] J.H. He, Y. Wu, N. Pang. A Mathematical Model for Preparation by AC-Electrospinning Process, *Int. J. Nonlin. Sci. Num.* **6**: 243-248, 2005.

[23] L.Y. Yeo, Z. Gagnon, H.C. Chang. AC electrospray biomaterials synthesis, *Biomaterials* **26**: 6122-6128, 2005.

[24] S. Sarkar, S. Deevi, G. Tepper. Biased AC Electrospinning of Aligned Polymer Nanofibers, *Macromol. Rapid Commun.* **28**: 1034-1039, 2007.

[25] S. Maheshwari, H.C. Chang. Assembly of Multi-Stranded Nanofiber Threads through AC Electrospinning, *Adv. Mater.* **21**: 349-354, 2009.

[26] I.G. Loscertales, A. Barrero, I. Guerrero, R. Cortijo, M. Marquez, A.M. Gañán-Calvo. Micro/Nano Encapsulation via Electrified Coaxial Liquid Jets, *Science* **295**: 1695-1698, 2002.

[27] D. Li, Y. Xia. Direct Fabrication of Composite and Ceramic Hollow Nanofibers by Electrospinning, *Nano Lett.* **4**: 933-938, 2004.

[28] N. Wang, H. Chen, L. Lin, Y. Zhao, X. Cao, Y. Song, L. Jiang. Multicomponent Phase Change Microfibers Prepared by Temperature Control Multifluidic Electrospinning, *Macromol. Rapid Commun.* **31**: 1622-1627, 2010.

[29] J.H. Park, P.V. Braun. Coaxial Electrospinning of Self-Healing Coatings, *Adv. Mater.* **22**: 496-499, 2010.

[30] A.K. Moghea, B.S. Gupta. Coaxial Electrospinning for Nanofiber Structures: Preparation and Applications, *Polymer Rev.* **48**: 353-377, 2008.

[31] I.C. Um, D. Fang, B.S. Hsiao, A. Okamoto, B. Chu. Electro-Spinning and Electro-Blowing of Hyaluronic Acid, *Biomacromolecules* **5**: 1428-1436, 2004.

[32] D.M. Rein, Y. Cohen, A. Ronen, K. Shuster, E. Zussman. Application of Gentle Annular Gas Veil for Electrospinning of Polymer Solutions and Melts, *Polym. Eng. Sci.* **49**: 774-782, 2009.

[33] J. Kameoka, R. Orth, Y. Yang, D. Czaplewski, R. Mathers, G.W. Coates, H.G. Craighead. A scanning tip electrospinning source for deposition of oriented nanofibres, *Nanotechnology* **14**: 1124-1129, 2003.

[34] J. Kameoka, S.S. Verbridge, H. Liu, D.A. Czaplewski, H.G. Craighead. Fabrication of Suspended Silica Glass Nanofibers from Polymeric Materials Using a Scanned Electrospinning Source, *Nano Lett.* **4**: 2105-2108, 2004.

[35] J. Kameoka, D. Czaplewski, H. Liu, H.G. Craighead. Polymeric nanowire architecture, *J. Mater. Chem.* **14**: 1503-1505, 2004.

[36] D. Sun, C. Chang, S. Li, L. Lin. Near-Field Electrospinning, *Nano Lett.* **6**: 839-842, 2006.

[37] C. Chang, K. Limkrailassiri, L. Lin. Continuous near-field electrospinning for large area deposition of orderly nanofiber patterns, *Appl. Phys. Lett.* **93**: 123111, 2008.

[38] C.H. Hellmann, J. Belardi, R. Dersch, A. Greiner, J.H. Wendorff, S. Bahnmueller. High Precision Deposition Electrospinning of nanofibers and nanofiber nonwovens, *Polymer* **50**: 1197-1205, 2009.

[39] G.S. Bisht, G. Canton, A. Mirsepassi, L. Kulinsky, S. Oh, D. Dunn-Rankin, M.J. Madou. Controlled Continuous Patterning of Polymeric Nanofibers on Three-Dimensional Substrates Using Low-Voltage Near-Field Electrospinning, *Nano Lett.* **11**: 1831-1837, 2011.

[40] H. Niu, T. Lin. Fiber Generators in Needleless Electrospinning, *J. Nanomater.* **2012**: Article ID 725950, doi:10.1155/2012/725950, 2012.

[41] H. Niu, X. Wang, T. Lin. Upward Needleless Electrospinning of Nanofibers, *J Eng. Fiber. Fabr.*: 17-22, 2012.

[42] S.A. Theron, A.L. Yarin, E. Zussman, E. Kroll. Multiple jets in electrospinning: experiment and modeling, *Polymer* **46**: 2889-2899, 2005.

[43] C.J. Luo, S.D. Stoyanov, E. Stride, E. Pelan, M. Edirisinghe. Electrospinning versus fibre production methods: from specifics to technological convergence, *Chem. Soc. Rev.* **41**: 4708-4735, 2012.

[44] O. Jirsak, F. Sanetrnik, D. Lukas, V. Kotek, L. Martinova, J. Chaloupek. A method of nanofibers production from a polymer solution using electrostatic spinning and a device for carrying out the method, WO 2005/024101 A1, 2005.

[45] S. Petrik, M. Maly. Production Nozzle-Less Electrospinning Nanofiber Technology, *MRS Proceedings* **1240**: 240-WW03-07, doi:10.1557/PROC-1240-WW03-07, 2009.

[46] O. Jirsak, P. Sysel, F. Sanetrnik, J. Hruza, J. Chaloupek. Polyamic acid nanofibers produced by needleless electrospinning, *J. Nanomater.* **2010**: Article ID 842831, doi:10.1155/2010/842831, 2010.

[47] H. Niu, T. Lin, X. Wang. Needleless Electrospinning. I. A Comparison of Cylinder and Disk Nozzles, *J. Appl. Polym. Sci.* **114**: 3524-3530, 2009.

[48] X. Wang, H. Niu, X. Wang, T. Lin. Needleless Electrospinning of Uniform Nanofibers Using Spiral Coil Spinnerets, *J. Nanomater.* **2012**: Article ID 785920, doi:10.1155/2012/785920, 2012.

[49] H. Niu, X. Wang, T. Lin. Needleless Electrospinning: Developments and Performances, Nanofibers, in the Production, Properties and Functional Applications, Dr. Tong Lin (Ed.), *InTech.* DOI: 10.5772/24999, 2011.

[50] A. Bogner, P.H. Jouneau, G. Thollet, D. Basset, C. Gauthier. A history of scanning electron microscopy developments: Towards wet-STEM imaging, *Micron* **38**: 390-401, 2007.

[51] S.J. Pennycook, A.R. Lupini, M. Varela, A. Borisevich, Y. Peng, M.P. Oxley, K.V. Benthem, M.F. Chisholm. Scanning Transmission Electron Microscopy for Nanostructure Characterization, *In Scanning microscopy for Nanotechnology*, W. Zhou, Z.L. Wang, Eds. Springer, New York: 152-191, 2007.

[52] D. Lin-Vien, N. B. Colthup, W. G. Fateley, J. G. Grasselli. The handbook of Infrared and Raman characteristic frequencies of organic molecules, *United Kingdom: Academic Press Limitted*, 1991.

[53] K. Madsen, N.B. Nielsen, and O. Tingleff. Methods for nonlinear least squares problems, Technical report, Informatics and Mathematical Modeling, Technical University of Denmark, 2004.

[54] H.P. Gavin. The Levenberg-Marquardt method for nonlinear least squares curve-fitting problems, Document from Department of Civil and Environmental Engineering, Duke University, 2013.

[55] S.M. Kelly, N.C. Price. The Use of Circular Dichroism in the Investigation of Protein Structure and Function, *Curr. Protein Pept. Sci.* **1**: 349-384, 2000.

[56] S.M. Kelly, T.J. Jess, N.C. Price. How to study proteins by circular dichroism, *Biochim. Biophys. Acta* **1751**: 119-139, 2005.

[57] N.J. Greenfield. Using circular dichroism spectra to estimate protein secondary structure, *Nat. Protoc.* **1**: 2876-2890, 2009.

[58] C. Louis-Jeune, M.A. Andrade-Navarro, C. Perez-Iratxeta. Prediction of protein secondary structure from circular dichroism using theoretically derived spectra, *Proteins* **80**: 374, 2012.

[59] M. J. Frisch, et al. Gaussian 09, Revision A.1, *Gaussian, Inc., Wallingford CT* , 2009.

[60] W. Kohn, A.D. Becke, R.G. Parr. Density Functional Theory of Electronic Structure, *J. Phys. Chem.* **100**: 12974-12980, 1996.

[61] K. Kim, K.D. Jordan. Comparison of Density Functional and MP2 Calculations on the Water Monomer and Dimer, *J. Phys. Chem.* **40**: 10089-10094, 1994.

[62] P.J. Stephens, F.J. Devlin, C.F. Chabalowski, M.J. Frisch. Ab Initio Calculation of Vibrational Absorption and Circular Dichroism Spectra Using Density Functional Force Fields, *J. Phys. Chem.* **45**: 11623-11627, 1998.

[63] Molinspiration Cheminformatics website: http://www.molinspiration.com/ (accessed 18 Feb. 2010).

[64] National Center for Biotechnology Information. PubChem Compound Database; CID93124, http://pubchem.ncbi.nlm.nih.gov/ (accessed 14 Sep. 2010).

[65] P. Pulay. Possibilities and limitations of *ab initio* calculation of vibrational spectra, *J. Mol. Struc.* **347**: 293-308, 1995.

[66] A.P. Scott, L. Radom. Harmonic Vibrational Frequencies: An Evaluation of Hartree-Fock, Møller-Plesset, Quadratic Configuration Interaction, Density Functional Theory, and Semiempirical Scale Factors, *J. Phys. Chem.* **100**: 16502-16513, 1996.

[67] J. Baker, A.A. Jarzecki, P. Pulay. Direct Scaling of Primitive Valence Force Constants: An Alternative Approach to Scaled Quantum Mechanical Force Fields, *J. Phys. Chem. A* **102**: 1412-1424, 1998.

Chapter 4

Electrospinning of Peptides

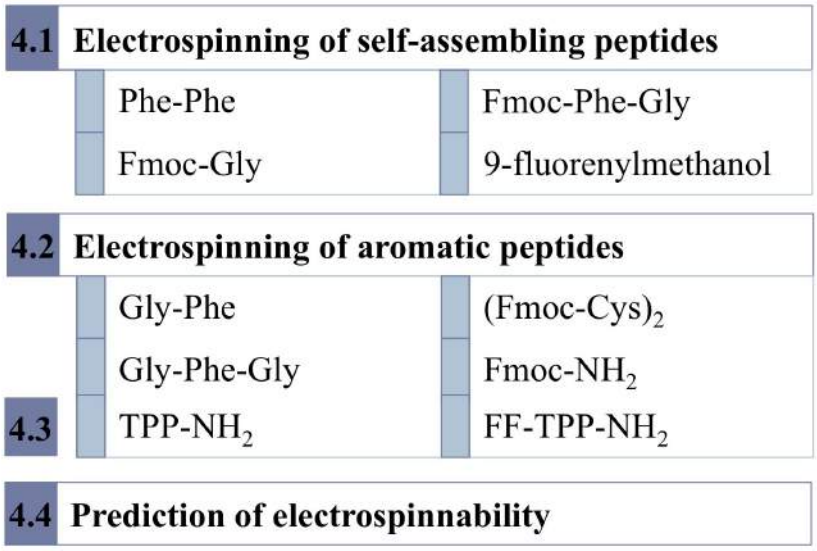

This chapter focuses exclusively on peptides. It is structured as follows: The first part will present and discuss electrospinning of several short aromatic peptides, i.e. Phe-Phe (FF), Fmoc-Phe-Gly (Fmoc-FG), and Fmoc-Gly (Fmoc-G), and compare them to the case of the simple π-stacking unit 9-fluorenylmethanol (9FM). Then, the electrospinning results of other short peptides will be reported, specifically Gly-Phe (GF), (Fmoc-Cys)$_2$ ((Fmoc-C)$_2$), Gly-Phe-Gly (GFG). The results are compared to electrospinning of Fmoc-NH$_2$, a fluorenyl compound. Optimized parameters and conditions for producing fibers from peptides are listed and discussed. In the final part, three prediction methods of the electrospinnability of peptide are proposed: The electron acceptor and donor number of the solvent, polarized Raman spectroscopy of the peptide powder, and rheological studies of the peptide solutions.

OBJECTIVE 2: Studying the possibility of electrospinning fibers from biomolecules; 2(a) starting from dipeptides containing phenyl side groups and 2(b) peptides containing larger aromatic groups.

4.1 Electrospinning of self-assembling peptides

As described in Chapter 2, there are four major classes of the biomolecules based on their structures and functions; proteins, nucleic acids, carbohydrates, and lipids. Proteins are the majority biomolecules produced in a living cell and have many functions. The subunit of the proteins is amino acids, so the beginning of this work was concentrated on the short peptides containing less than five amino acids. However, they can be self-assembled. The advantage of selecting short peptides for this work is that the chemical characterization and the peptide synthesis are easier than a long peptide. Because fiber fabrication processes might change chemical properties (mainly by unwanted chemical reactions), organic fibers call for chemical analysis methods, ideally on the nanoscale [1]. Vibrational spectroscopy experiments are, in this case, often more widely applicable than other methods because often the structures are not crystalline (no diffraction), and are easily destroyed by electron beams. However, fibers made up from molecular subunits may complicate spectroscopic experiments and their interpretation. The single molecules are, in most cases, not accessible for experiments because they cannot be evaporated. This is particularly true for organic molecules with strong hydrogen bonds (or even ionized groups), such as peptides. Hence, one is restricted to solid samples, where intermolecular interactions would be expected to make spectra rather complex (see e.g. [2]).

This work is especially interested in the very small nanofibers, produced almost exclusively by self-assembly, hence by a bottom-up approach. Such molecular assembly techniques mainly result in three-dimensional (3D) objects, e.g. crystallization of proteins; in 2D such as membrane proteins and graphene layers at low temperature; or in 1D fibers and tubes, e.g. a linear chain of ions [3], a single continuous structure of FtsZ (an essential cell division gene in *Escherichia coli.*) [4], based on intermolecular interactions of electrostatic, hydrogen bonds, or van der Waals. The latter come into play only for large molecules, or at very close distances, so they add up considerably for solids (including fibers and tubes). Depending on the details of the molecular structure, not only directional forces (caused by hydrogen bonds and by π-stacking, as a specific class of van der Waals interactions) but also all others can exert a directional assembly. In this way, self-assembling molecules arrange into well-ordered supramolecular structures, including nanofibers and nanotubes. Vibrational spectroscopy is one of the best methods to assess the extent of the various contributions of intermolecular forces. Note that in the case of intact molecular subunits (e.g. FF), the spectra of fibers or tubes have to be quite similar to those of single molecules, whereas, for example, polymers have spectra that are very different from the monomers, owing to formation of new covalent bonds.

The experiments in this section focus on the special case of peptides, whose composition of amino acids linked by peptide bonds allows for a rather simple and effective tuning of chemical and biochemical properties. Peptides and peptide hybrids have recently been fabricated in various structures and used as biomaterials, for example, filaments and fibrils, hydrogels, and surfactants [5]. Many peptides readily assemble to 1D nanostructures. For example, Ghadiri and coworkers described the formation of nanotubes from cyclic peptides [6–8] (see also [9]) that can assemble under favorable conditions into continuous hydrogen-bonded tubular structures. The tubes are able to form artificial transmembrane channels for an ion and a glucose transport, with an antibacterial activity [10]. Gazit and coworkers suggested and reported that π-stacking interactions are essential for the self-assembly of amyloid structures (which are energetically based mainly on hydrogen bonding). Amyloid fibrils are an important factor in neurodegenerative diseases, for example, Alzheimers and Parkinsons [11, 12]. Gazit and coworkers demonstrated that the short aromatic peptide diphenylalanine (FF), which is a motif in various amyloid-forming proteins, can assemble in solutions to form amyloid-like fibrils [13, 14]. These results encouraged further investigation into the role of π-stacking interactions in self- assembly, and in "forced" assembly by the electrospinning.

In addition to the natural aromatic side chains in peptides (Phe, Tyr, Trp), fluorenyl groups are easily available for peptides, because fluorenylmethoxycarbonyl (Fmoc) is widely used as the protection group for the amine terminus. Therefore, the Fmoc is chosen specifically for its ability to induce π-stacking and is expected to drive directional self-assembly. π-stacking is based on the weak attractive interactions between π electrons in aromatic rings, which may or may not be relevant for assembly. In the case of Fmoc, the aromatic fluorenyl system stacks nicely in a fluorene and in its compounds [13, 15], and thus exerts a sizeable influence on molecular assembly. This effect is well documented; Xu et al. reported that Fmoc-dipeptides can form nanofibrous hydrogels, with a phase transition that depends on ligand-receptor interactions [16], the Ulijn and Nilsson group showed the self-assembly of Fmoc-terminated dipeptides to nanofibers which was used as a scaffold material in 3D cell cultures [15, 17].

The first part of experimental results is based on the following molecules (Fig. 4.1): H-Phe-Phe-OH (FF), which can assemble into nanotubes or nanofibers, similar to amyloid fibrils [12, 18–20] and can be electrospun [21]; two Fmoc derivates Fmoc-glycine (Fmoc-G), and Fmoc-phenylalanylglycine (Fmoc-FG) that can assemble to nanofibers [13, 15] but had never been used in electrospinning experiments; 9-fluorenylmethanol (9FM), which contains the basic π-stacking unit (fluorenyl), selected for comparison. 9FM forms no fibers, so its powders were investigated which also tested for the other peptide derivates. The experiments combined confocal Raman microscopy, which allows us to obtain vibrational signals of fibers by minimizing the contributions from the background (a sample holder and a substrate), with infrared (IR) spectroscopy in the attenuated total reflection (ATR) configuration, which in turn allows us to probe solids in a rather simple way. A strong emphasis is the Appendix B with the simulated Raman and IR spectra, based on the single molecule subunits.

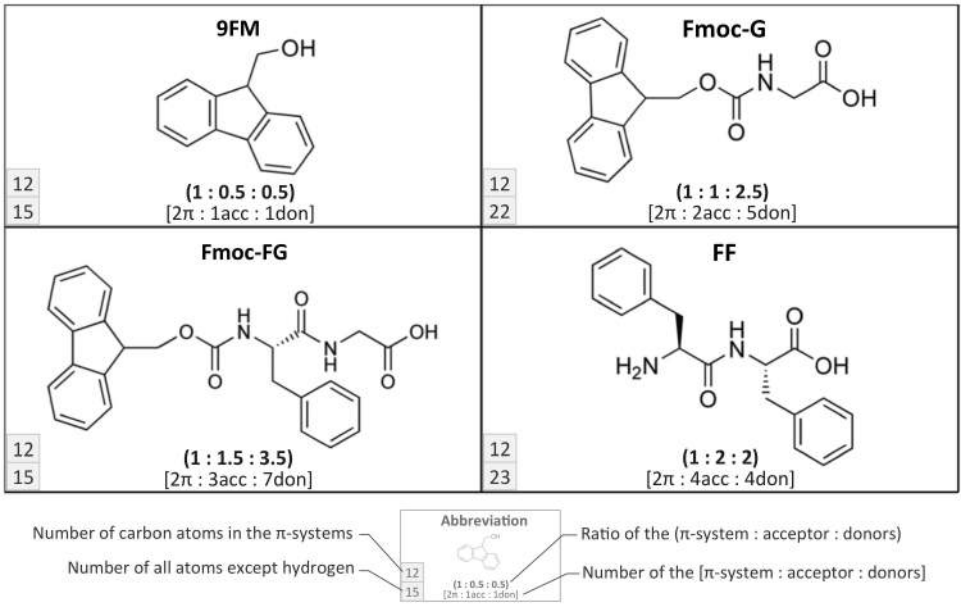

Figure 4.1: The peptides and peptide derivates used in this study.

4.1.1 Experimental

Chemicals: Dimethylsulfoxide (99.5%, Panreac) and N-methylpyrrolidone (99.8%, Technic France) are most suitable to dissolve the aromatic compounds. However, their low vapor pressures fail in the electrospinning process. In contrast, hexafluoroisopropanol (HFIP, 99.0%, Fluka) can completely dissolve most substances, has a high vapor pressure, and a low surface tension. HFIP's low viscosity causes a bead or a droplet formation in fibers (see Eq. 2.9 and the comment in Chapter 3.1.3). This problem can be improved by increasing the concentration of the substances as much as possible. FF (Sigma-Aldrich), Fmoc-G (Bachem), Fmoc-FG (Bachem), and 9FM (99%, Sigma-Aldrich) were dissolved in various solvents (listed in 3.3 or 4.5) at high concentrations, usually more than 15 %(wt/wt), by ultrasonication (USC300TH, VWR) for 30 min or more at the room temperature. The samples were additionally shaken (Titramax 1000, Heidolph) at 450−600 rpm for at least 3 h to obtain homogenous solutions. In some cases, the solutions were ultrasonicated at elevated temperatures (less than 60 °C) for 30 min, or until they were completely dissolved. Each solution was used aliquots of 0.5−1 ml for electrospinning. Dissolution and electrospinnability properties of each solvent for peptides are concluded in the section 4.3.1.

Electrospinning: The conventional electrospinning (ES) setup (detailed in Chapter 3, section 3.2.2.1) was used in this experiment. An aliquot of at least 0.1 ml was loaded into a 1 ml plastic syringe, connected to a metal needle through a teflon tube. A syringe pump was used to set the solution flow rate to 0.2−0.5 ml/h. Then a high voltage 10−30 kV was applied at the needle. A precleaned glass slide or wet cleaned oxidized silicon (111) wafer pieces were used to collect fibers for characterization by the optical and electron microscopy, respectively.

4.1.2 Results and discussion

The four substances considered here are 9FM, Fmoc-G, Fmoc-FG, and FF (Fig. 4.1). The solids are white powders, and in order to obtain structural information, 9FM was dissolved in HFIP and crystallized by slow evaporation. The crystal structure of Phe-Phe is well known [19]; it actually can form nanoscale tubes, with well-ordered sidewalls. However, the Fmoc derivates were unable to crystallize. Whereas electrospinning was not possible for 9FM to make the fibers (see Fig. 4.2a), only solidified droplets 1− 2.5 μm of diameter were observed. Figure 4.2b shows the result from the Fmoc-G solution which can be electrospun to fiber but very few. SEM micrograph indicates that the fiber has diameter of 100−300 nm, and some areas are smaller than 100 nm. The beads in the fibers are 1−2 μm of diameter. Figure 4.2c presents long and straight fibers produced from the solution of Fmoc-FG/HFIP at 18 %(wt/wt), the mean diameter is around 400−700 nm. Few droplets with diameter of 1−2 μm were observed in this sample, and a big droplet (diameter of about 10 μm) was dropped onto the fiber by chance. Note that, the coiled and straight part of a fiber can be observed together in the same sample when imaged at lower magnification. The case of FF is already documented [21], and also reproduces the results very nicely (see Fig. 4.2d) from the solution of FF/HFIP 16 %(wt/wt). With optical microscopy, extremely long (many mm) coiled and straight fibers were found in a single sample. The mean diameter of the fibers is 400−500 nm (neglecting the diffraction, described in section 3.3.2) without beads resulting from the optimization of the electrospinning parameters.

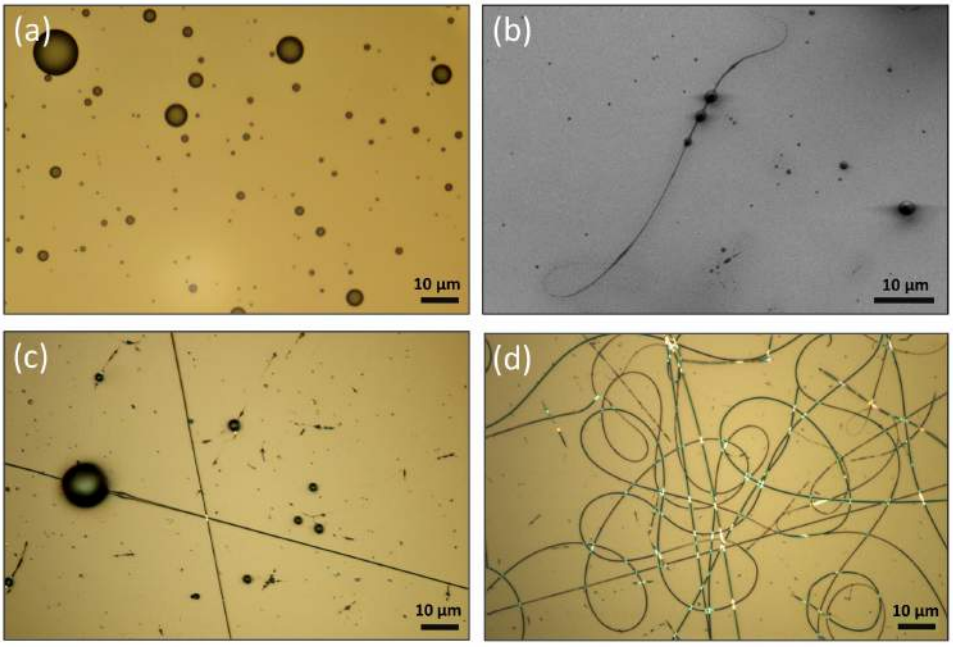

Figure 4.2: Optical micrograph (a) droplets of 9FM/HFIP 18 %(wt/wt), (b) SEM micrograph of Fmoc-G/TFA 25 %(wt/wt) fiber with beads, (c) optical image of Fmoc-FG/HFIP 18 %(wt/wt) long and straight fibers, and (d) FF/HFIP 16 %(wt/wt) long and coiled fibers.

OBJECTIVE 3: Evaluating molecular conformation of biomolecules, which are subjected to a high voltage.

The fact that it is possible to produce fibers from the solutions of the pure FF (no polymer blends) means that the intermolecular interactions are strong, and one would assume them being based on hydrogen bonds and π-stacking. This is equally true for the solution of Fmoc-G, Fmoc-FG, and other aromatic peptides or for aromatic peptide derivates, such as Fmoc-protected amino acids. To elucidate the relative roles of such intermolecular forces, and to assess possible chemical changes, an attenuated total reflection (ATR) infrared and Raman spectroscopy were performed on the powders and on the fibers. To develop the necessary background and for comparison, the simple case of 9FM will be firstly discussed.

4.1.2.1 9FM

The IR and also the Raman spectra of solid 9FM (powder) (see Fig. 4.3) show good agreement with literature data (see Table 4.1 for selected vibrations and full list in Appendix B) as expected because 9FM was neither modified nor contacted with solvents. The ATR technique has a cutoff at 600 cm^{-1}, such that low-wavenumber vibrations were not found. Similarly, the Raman microscope cuts off at 200 cm^{-1}. The simulations based on a single molecule model, connected a fluorenyl group of the usual dimensions to CH_2OH, and allowed for some structural optimization. The calculated vibrational data agree with the experimental ones (Table 4.1) although the experiment probes molecules in contact with a number of neighbors, whereas the simulations refer to single (free) molecules in vacuum. Also, the calculated intensities fit roughly, and they were used for the assignment. The local D2h symmetry (fluorenyl) means that vibrations localized in the fluorenyl system follow the mutual exclusion rule, for example, the strong Raman signal at 1610 cm^{-1} originates from symmetric C-H bending vibrations on both phenyl subsystems, whose dipole moment oscillations cancel out, such that the IR intensity is extremely low. There are, however, various differences between calculations and experiments, which will be detailed in the following.

Owing to the hydrogen bonds, they were expected shifts (between simulation and experiment) for all OH-related vibrations. The OH stretching vibration in a free molecule has one of the highest possible wavenumbers, here 3480 cm^{-1} (see Fig. 4.3 and Table 4.1). It is absent in Raman, as also known from benzyl alcohol [22, 23]. However, the OH stretching is easily detected in IR, where it is shifted (-230 cm^{-1}) and broadened [22, 23]. Indeed the crystal structure[1] (Fig. 4.4a) shows the

[1]Since 9FM can be crystallized from HFIP by slow evaporation, yielding slightly yellow needle-shaped crystals. They were analyzed in an ENRAF NONIUS CAD-4 Single Crystal X-Ray Diffractometer (Bruker), equipped with a low temperature system. This system is a fully automated four-circle instrument with an FR 590 generator, a goniometer, a CAD4F interface, and a MicroVAX3100. The detector was a scintillation counter. The data collection was performed at 20°C. Details of the structure are available

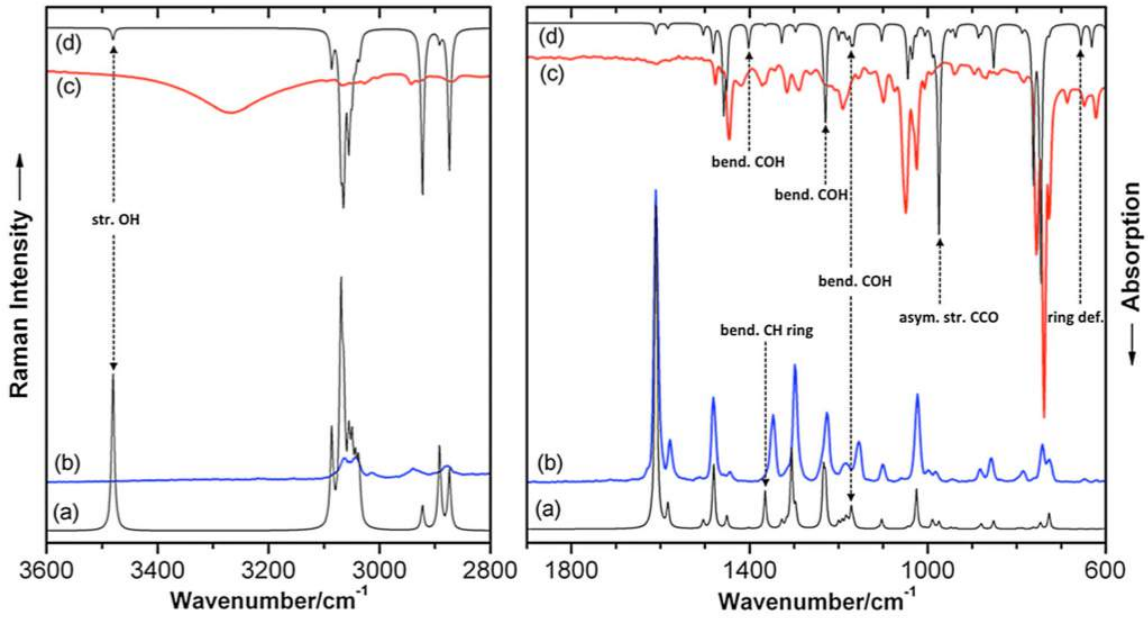

Figure 4.3: Raman spectrum (bottom trace) and IR spectrum (top trace) of 9FM. (a), (d) calculation; (b), (c) experimental results from powder. Spectra are scaled and offset for clarity.

Table 4.1 Observed and calculated spectral assignments for 9FM

Vibrational modes (9FM)	Experiments (cm^{-1})				Simulations (cm^{-1})				Shift	
	IR (Pow.)	IR (AIST)	Raman (Pow.)	Raman (Sigma)	Sim.	Scaled	IR inten.	Raman inten.	IR	Raman
str. OH		3323vs			3652	3480	3.78	235.90	↓	
wag. CH_2 + bend. COH	1418 m				1451	1402	6.80	1.33	↑	
i.p. CH ring bend.		1367w	1347 s	1348 s	1413	1365	0.63	48.84		↓
bend. COH + bend. CH(H)	1208w		1227 s	1226 s	1277	1234	5.55	69.73	↓	
i.p. CH ring bend. + bend. CH(H) + bend. COH	1155w		1154 m	1152 m	1213	1172	4.58	26.63	↓	↓
asym. str. CCO	940w	940w	983w	983w	1009	975	59.17	9.57	↓	
i.p. ring def.	648 m	622w	648vw		678	656	6.02	0.39	↓	
tor. COH			305w	304 m	248	240	132.72	7.16		↑

AIST, reference IR spectra from AIST (http://riodb01.ibase.aist.go.jp/sdbs/); Sigma, reference Raman spectra from Sigma–Aldrich (http://www.sigmaaldrich.com); i.p., in-plane; o.o.p., out-of-plane; sym., symmetric; asym., asymmetric; str., stretching; bend., bending; wag., wagging; twi., twisting; roc., rocking; tor., torsional; def., deformational; skel., skeleton; aliph., aliphatic; s, strong; m, medium; w, weak; v, very; Pow., experiment result from powder; Fibers, experimental result from fibers; inten., intensity; Sim., simulation; Scaled, the simulation wavenumbers are scaled by 0.966 and 0.953 for wavenumbers $< 2000\,cm^{-1}$ and $> 2000\,cm^{-1}$, respectively. ↓, ↑ vibrational wavenumber of solid, compared with the single molecule, is significantly downshifted or upshifted, respectively.

intermolecular hydrogen bond network that causes the described phenomena. The COH torsion (not detectable in IR) is upshifted (+65 cm^{-1}), as expected for an OH group that is tethered to a neighboring molecule. The remaining vibrations that involve the OH group also show some shifts (15−20 cm^{-1} up or down, the asymmetric CCO stretch even -35 cm^{-1}) in IR, because the C-O and O-H dipoles are rather strong and affected by hydrogen bonding.

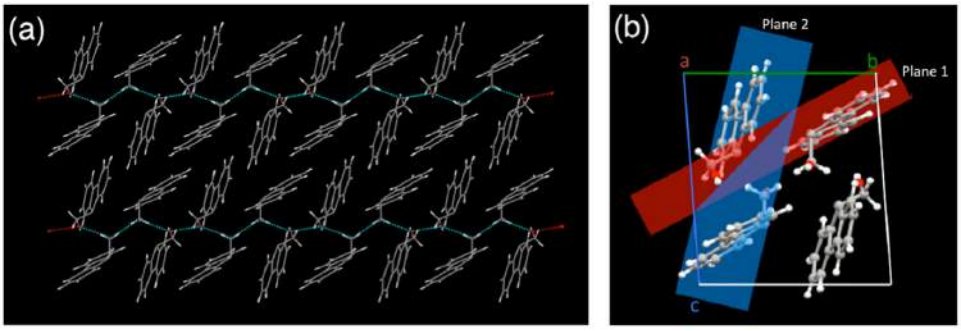

Figure 4.4: Experimentally determined crystal structure of 9FM. (a) The 9FM molecules form a layered structure based on p-stacking and on hydrogen bonds (shown as dashed lines). (b) The angle between two fluorene planes 1 and 2 from adjacent molecules is 52.7°

.

The hydrogen bonds cannot extend in 3D because of steric constraints of the molecular packing. Still, they appear to determine the two-dimensional layer-like molecular arrangement, layers of fluorenyl and of hydroxyl group, respectively. However, these layers are also based on π-stacking interactions between the flat fluorenyl systems, arranged at an angle of 52.7° (see Fig. 4.4b). Whereas large aromatic systems stack in parallel, such nonparallel stacking is typical for systems of this size (pure fluorene stacks at an angle of 67.6° [24]). The smallest systems (gas-phase benzene dimer) even stack perpendicularly [25]. Hence, one would expect that all ring and all CH vibrations in the fluorenyl system are affected by interaction with neighboring molecules. Such effects would be rather small in IR, because the dipole moments do not change much. They should be more pronounced in Raman, but there are only small shifts for some of the in-plane C-H bendings and one of the ring deformations (Table 4.1). The shifts are all negative, as expected from the presence of a rather large mass (neighboring molecule) close to the vibrating unit (C-H bond).

4.1.2.2 Fmoc-G

Raman spectra for this compound (which is, strictly speaking, not a peptide, but a carbamate) were obtained from powder and from spun fibers (using TFA solvent) (Fig. 4.5). Because they are virtually identical, be sure that the chemical identity, and even the molecular conformation did not change, despite the application of high voltages and organic solvents. This is not expected because Fmoc-G could attain a number of quite different conformations, which might be induced by contact with solvents, and especially by electrospinning, via exposure of the molecule to large

in the CCDC database code 843130.

local electrical fields. Figure 4.5 furthermore shows an IR spectrum; Raman and IR experiments show good agreement with literature data (see Table 4.2). In contrast, the agreement with the simulations is not perfect, as detailed in the following.

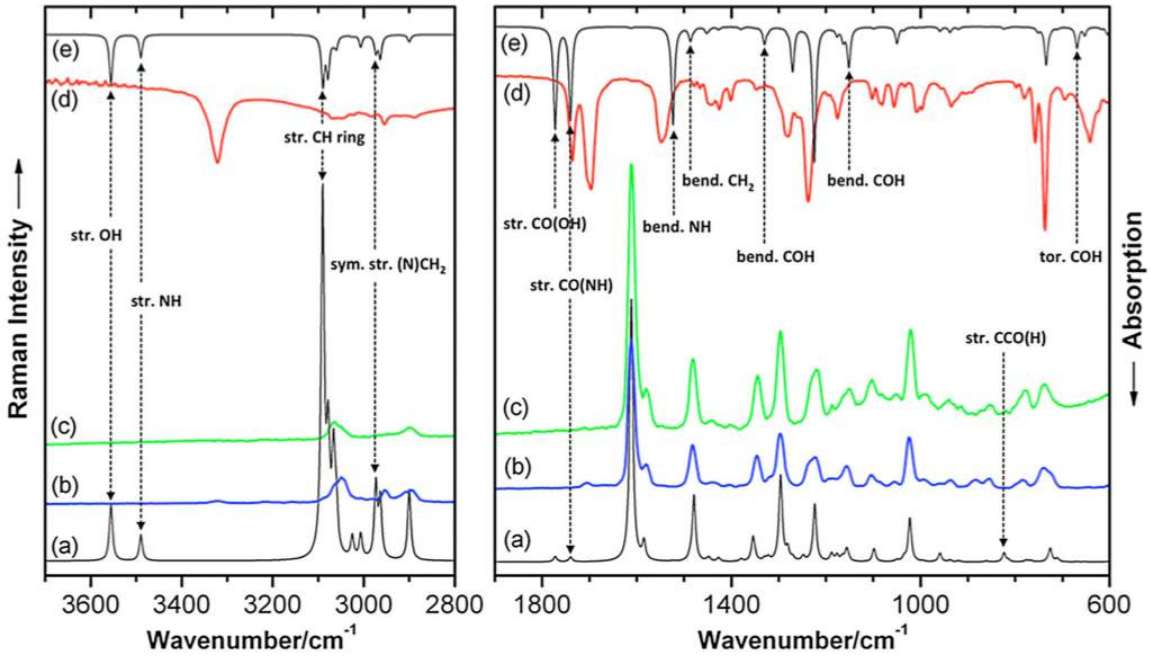

Figure 4.5: Raman (bottom) and IR spectra (top) of Fmoc-G. (a) and (e) are calculation results, (b) and (d) are experimental results from powder, and (c) from fibers (using TFA solvent). Spectra are scaled and offset for clarity.

All polar groups in Fmoc-G are able to form hydrogen bonds. These groups are O-CO-NH from the Fmoc linkage, and the COOH terminus. Similar to 9FM, those vibrations that involve hydrogen bonds deviate strongly from the single molecule behavior, and one would expect shifts for all related vibrations. The OH stretching is calculated at 3556 cm^{-1}. It is absent in Raman, as well known for many solid carboxylic acids, where the vibrational signature is barely detectable (when not exchanged with deuterium) [23, 26–28]. The OH band is shifted (-235 cm^{-1}) and broadened in IR (when assigned on the simulated large IR intensities). However, for this band, contributions from NH stretching (calculated at 3490 cm^{-1}) cannot be excluded. Because the absence of a peak is no direct proof of hydrogen bonds, one should also consider the CO stretching in the COOH terminus. Despite the shift caused by hydrogen bonding, the rather narrow and strong IR peak shows that COOH is present, not deprotonated COO^{-}. This is expected because contacting with water or bases was avoided.

The amide I band, here for simplicity called “str. CO(NH)”, is widely used for secondary structure analyses in proteins and peptides. As in most peptides, one can observe it easily in IR and Raman. It is somewhat shifted (-44 cm^{-1} for IR, -35 cm^{-1} for Raman). Conversely, the amide

Table 4.2 Observed and calculated spectral assignments for Fmoc-Gly

Vibrational modes (Fmoc-Gly)	Experiments (cm^{-1})					Simulations (cm^{-1})				Shift	
	IR (Pow.)	IR (AIST)	Raman (Pow.)	Raman (Fibers)	Raman (Sigma)	Sim.	Scaled	IR inten.	Raman inten.	IR	Raman
str. OH	3321 m	3320vs				3688	3556	63.85	98.36	↓	
str. NH						3620	3490	29.30	45.17		
str. CH ring				3063 m	3061 m	3206	3091	10.54	590.04	↓	
	3048w					3174	3060	12.22	74.01		↓
sym. str. (N)CH_2		2955 m	2953 m		2953 m	3084	2973	21.21	126.84		↓
str. CO(OH)	1736 s	1742vs				1822	1772	385.63	10.14	↓	
str. CO(NH) (am. I)	1696 s	1700vs	1705w	1708vw	1706w	1788	1740	348.96	9.24	↓	↓
bend. NH (amide II)	1548 s	1545vs				1566	1523	371.63	1.19	↑	
bend. CH_2(O)	1443 m	1450 s				1528	1487	50.24	8.03	↓	
bend. COH + str. CCO(H)	1346w					1367	1330	64.32	5.83	↑	
bend. COH	1175 m	1175 m				1183	1151	148.78	2.14	↑	
str. CCO(H)			856w	853w	853w	846	824	8.27	17.12		↑
tor COH	642 m	644 m				688	669	80.33	0.83	↓	

The simulation spectra are scaled by 0.973 and 0.964 for wavenumbers $< 2000\,cm^{-1}$ and $> 2000\,cm^{-1}$, respectively.

II band, which is called for simplicity "bend NH", is upshifted (+25 cm^{-1}) in IR, but absent in Raman. Both amide band shifts are typical for associated molecules [28]. For the CO stretch, the association with hydrogen atoms (hydrogen bonding) lowers the wavenumber; for amide II, the hydrogen bonding to a neighboring molecule tethers the hydrogen atom and increases the CNH bending wavenumber. Similar phenomena also in the other peptides will be found. Analogously, the COH bending at 1151 cm^{-1} is upshifted (+24 cm^{-1}) in IR. The COH torsion mode at 669 cm^{-1} is downshifted (-27 cm^{-1}) in IR, which is not expected.

Summing up, the Fmoc-G spectra show that the compound is intact, and that changes from the simulated single molecule signals are caused by intermolecular hydrogen bonding. This involves the terminal COOH group, and the amide group CONH. In contrast, nearly all other vibrations fit well to those in the single molecule in vacuum. Only in some cases found slight shifts, for example, the CH stretching in the fluorenyl system can be observed in Raman and IR, shifted by -12 cm^{-1} and -28 cm^{-1}, respectively. Hence, weak interactions, especially π-stacking of the fluorenyl moieties, do not manifest clearly in vibrational spectra, although this can expect them to sum up to important contributions, as learned from the case of 9FM.

4.1.2.3 Fmoc-FG

Different from Fmoc-G, the presence of two aromatic moieties (fluorenyl and phenyl) in a single molecule suggests considerable π-stacking, as clearly evident for FF (see next). Following 9FM and Fmoc-G, again took care to avoid any chemical changes, including deprotonation of the terminal COOH. Figure 4.6 compares IR and Raman spectra from experiment and simulation. Fibers show a spectrum that is virtually identical with that of the powder, it can be assured that neither the contact with organic solvents (HFIP, Raman peaks around 750 and 850 cm^{-1}) nor the electrospinning process are detrimental. However, many modes showed no intensity in either Raman or IR.

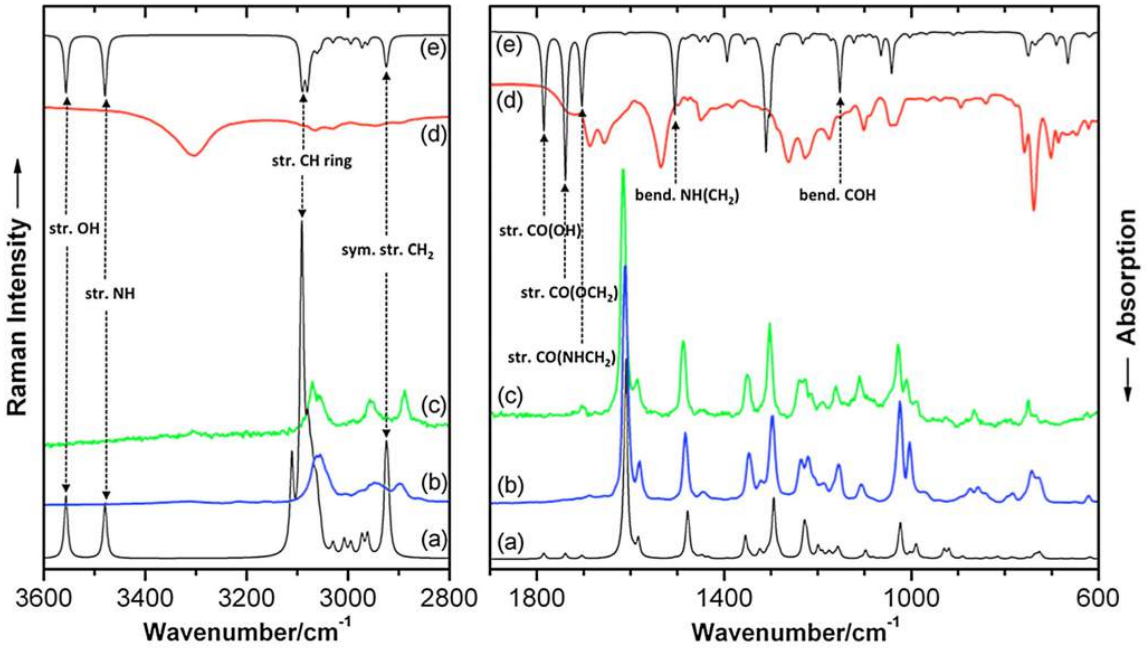

Figure 4.6: Raman (bottom) and IR spectra (top) of Fmoc-FG. (a) and (e) are calculation results, (b) and (d) are experimental results from powder, and (c) from fibers. Spectra are scaled and offset for clarity.

Table 4.3 Observed and calculated spectral assignments for Fmoc-Phe-Gly.

Vibrational modes (Fmoc-Phe-Gly)	Experiments (cm^{-1})			Simulations (cm^{-1})				Shift	
	IR (Pow.)	Raman (Pow.)	Raman (Fibers)	Sim.	Scaled	IR inten.	Raman inten.	IR	Raman
str. OH	3320 m			3689	3556	82.70	154.92	↓	
str. NH(CH) + str. $NH(CH_2)$				3609	3479	62.47	108.82		
str. CH f-ring, str. CH p-ring		3054 m	3070 m	3206	3091	29.63	398.69		↓
sym. str. CH_2(CO)		2898 m	2889 m	3035	2926	18.42	132.30		↓
str. CO(OH)	1720 m			1835	1785	363.02	15.29	↓	
str. $CO(OCH_2)$ (amide I)	1686 s			1787	1739	543.88	14.22	↓	
str. $CO(NHCH_2)$ (amide I)	1655 s			1751	1704	268.73	8.50	↓	
bend. $NH(CH_2)$ (amide II)	1536 s			1547	1505	305.52	1.58	↑	
bend. COH	1176 m			1185	1153	220.58	2.82	↑	

The simulation spectra are scaled by 0.973 and 0.964 for wavenumbers < 2000 cm^{-1} and > 2000 cm^{-1}, respectively.

The notation of atoms is defined as simple as possible, which sometimes gives rise to "chemically unsound" names such as "$CO(OCH_2)$" for an amide, which would read in detail "$NHCO(OCH_2)$"

All oxygen-containing and nitrogen-containing groups should be able to form hydrogen bonds, so first investigate the observed and relevant vibrations of Table 4.3. For the OH and NH stretching vibrations, the same arguments as for Fmoc-G apply (see the foregoing). Whereas the Raman signals even of the polar groups show very small shifts, some of the IR shifts in Fmoc-FG are noteworthy: The CO stretching in COOH (again protonated) and the amide I band for both amide groups $CO(OCH_2)$ and $CO(NHCH_2)$ at 1785, 1739, and 1704 cm^{-1} are strongly downshifted (-65, -53, and -49 cm^{-1}, respectively). As expected, the amide II band (for simplicity "NH bending" in $NH(CH_2)$) is upshifted (+31 cm^{-1}), and so is the COH bending at 1153 cm^{-1}. All this suggests considerable hydrogen bonding to neighboring molecules; these interactions sum up much more than in 9FM or Fmoc-G, so that a postulate is that they are the base for fiber formation of Fmoc-FG in electrospinning.

The CH stretching vibrations from the fluorenyl and phenyl rings are found very close to the simulated values, and this is generally true also for the aliphatic CH stretches. However, the Raman peak for the fiber at 2889 cm^{-1} is ambiguous; the CH_2 symmetric stretches at 2962 cm^{-1} and 2924 cm^{-1}, or the CH stretching at 2921 cm^{-1} might qualify, all with considerable shifts. All other observed modes show good agreement with the simulation, without any strong shift.

4.1.2.4 FF

FF (Phe-Phe) is a well-known short aromatic peptide, which can assemble to nanotubes in solutions or by electrospinning [21]. Görbitz [19] reported the structure of FF nanotubes based on X-ray analysis of powders composed of such fibers. This work used his molecular structure for simulations and also distinguished between the zwitterionic structure (H_3N^+-Phe-Phe-O^-), which is usually present in peptides, and a potential nonionic structure (H_2N-Phe- Phe-OH), with identical X-ray signature because only one proton is shifted.

The nonionic structure allowed to simulate spectra in the usual way (slight optimization of the structure in vacuum, resulting in a minimum on the potential energy surface). However, this structure is believed that not present in the solid phase because the spectra do not agree as well as with the simulation of the zwitterion. The CO stretching mode in the COOH terminus would have to shift by an unrealistic value of -100 cm^{-1} in IR (charges might cause such extreme shifts but there are no changes in the nonionic structure). The simulation based on the zwitterionic structure resulted in a potential energy 0.01578 eV (127 cm^{-1}) above the nonionic one. This structure is not stable in vacuum, which translates into partially negative vibration wavenumbers. Therefore, a model environment that stabilizes the charges was employed, defined by the dielectric constant of the solvent (the dielectric constant of HFIP is 17 at 20 °C) [29]. The potential energy is still 0.00357 eV (29 cm^{-1}) above the value for the nonionic form, but the vibrations can be computed, and the agreement with the experiment (Fig. 4.7) is now good. Therefore, this structure was decided to use for all further evaluations.

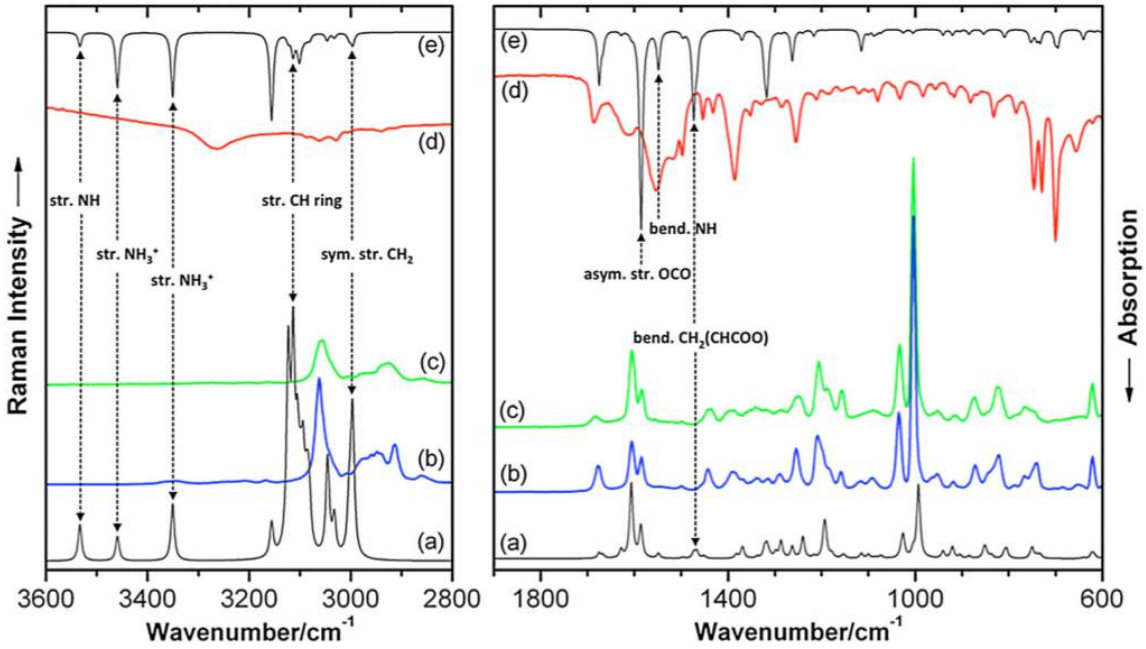

Figure 4.7: Raman (bottom) and IR spectra (top) of FF. (a) and (e) show calculated spectra based on the zwitterionic structure, (b) and (d) are recorded from powder, and (c) obtained from fibers. Spectra are scaled and offset for clarity.

Table 4.4 Observed and calculated spectral assignments for Phe-Phe (Zwitterionic form)

Vibrational modes (Phe-Phe, zwitterion)	Experiments (cm^{-1})					Simulations (solvent) (cm^{-1})				Shift	
	IR (Pow.)	IR (AIST)	Raman (Pow.)	Raman (Fibers)	Raman (Singh08)	Sim.	Scaled	IR inten.	Raman inten.	IR	Raman
str. NH						3616	3533	45.48	122.14		
str. NH_3^+						3541	3459	173.89	83.79		
str. NH_3^+	3264 m	3309 s				3430	3351	202.97	191.83		
str. CH ring	3086vw	3088w				3196	3123	40.78	784.15	↓	
			3062 s	3056 s	3054 s	3187	3114	82.64	847.69		↓
	3062vw	3063w				3174	3101	99.11	455.17	↓	
sym. str. CH_2(CHCOO) + str. CH(COO)			2914 m	2928 m		3074	3003	31.17	326.26		↓
sym. str. CH_2(CHCON)			2862w	2855w	2850 m	3066	2996	43.26	516.51		↓
i.p. CH ring bend. + asym. str. OCO	1553 s					1622	1585	1028.72	85.93	↓	
bend. NH (amide II)	1518 m					1585	1548	209.28	14.56	↓	
bend. CH_2(CHCOO)	1431w		1443w	1443w	1454w	1502	1467	264.87	24.41	↓	↓
bend. CH_2(CHCON) + i.p. CH ring bend.	1387 s	1387w				1487	1453	36.81	8.65	↓	
bend. CH_2(CHCOO) + i.p. CH ring bend.	1255 m	1261 s				1348	1317	350.08	45.49	↓	
bend. CH(COO)			1208 s	1206 s	1208 m	1270	1240	20.91	58.87		↓
o.o.p. CH ring bend. + skel.			873 m	874 m		942	920	31.30	31.78		↓
skel.	833 m					906	885	26.60	8.74	↓	

[Singh08], reference Raman from G. Singh, A. M. Bittner, S. Loscher, N. Malinowski, K. Kern, *Adv. Mater.* **2008**, *20*, 2332. The simulation spectra are scaled by 0.977. Simulation environment with dielectric constant 17 (as for solvent HFIP).

Figure 4.7 shows the vibrational simulation of the zwitterionic structure, and the recorded IR and Raman spectra. The NH stretching of zwitterionic structure is calculated at 3533 cm^{-1} (Table 4.4). It is absent in Raman and IR. The $NH_3{}^+$ stretching (only observed in the lit.) is downshifted (-87 cm^{-1}) by hydrogen bonding in IR. Note here that all vibrational signatures in this range could also be assigned to hydrogen bond stretchings in NH_2 and OH in the nonionic form, because in any event, hydrogen bonding would induce huge shifts. Clearer assignments are found in the amide II band range: The OCO asymmetric stretching at 1585 cm^{-1} is downshifted by -32 cm^{-1} in IR. The NH bending at 1548 cm^{-1} is downshifted by -30 cm^{-1} in IR, whereas hydrogen bonding should produce an upshift. Altogether, hydrogen bonding from NH and NH_3^+ to CO and COO^- is present, but the shifts are not as strong as in the Fmoc compounds, probably owing to the charges in the zwitterion. The CH ring stretching is downshifted 36 and 66 cm^{-1} in IR and Raman, respectively. The CH ring bending has a resonance at 1606 cm^{-1}; it is found in Raman, but not significantly shifted. Again, the π-stacking produces only small shifts in the spectra.

Because FF, as substructure of amyloid-forming proteins, is of biological relevance, despite its small size, the vibrational analysis has implications for amyloid-like peptide fibers. One would expect similar vibrational spectra in natural protein aggregates for the amide I and II band [30]. The basic motif in such cases is intersheet packing driven by intermolecular interactions such as hydrogen bonding and π-stacking.

4.1.3 Conclusions

In spite of their small size, short aromatic peptides and related compounds can assemble in solution or by electrospinning to 1D nanostructures, for example, nanotubes and nanofibers. These structures, as well as crystals or powders of the compounds, are based solely on noncovalent interactions. The results have shown that vibrational spectroscopy can probe the integrity of the molecular subunits, an important issue for possible applications, but also for research on functional properties in medicine and biochemistry. Results prove that the formation of hydrogen bonds and π-stacking together are the driving forces of the formation of fibers, although not all compounds can yield fibers. There are two phenyl rings in FF, and a fluorenyl and a phenyl ring in Fmoc-FG, both resulting in so strong intermolecular interactions that aggregates build up easily [14]. This claim can be proved by producing fibers with electrospinning this technique usually requires polymers to support fiber formation, but here monomers suffice, because their arrangement is aided by alignment in the local electrical fields.

Self-assembling amyloid fibrils are the hallmark of neurodegenerative diseases, e.g. Alzheimer's disease. Whereas aromatic amino acids are relatively rare in natural proteins, they play an important role in amyloids, and FF is one of the simplest model compounds. The extension to other aromatic peptides, including the non-natural fluorenyl group, shows that π-stacking is a recurrent motif to build up solid state structures of peptides. Whereas π-stacking has only minimal influence on the vibrational signatures, hydrogen bonding can easily be detected by IR or Raman spectroscopy. The use of Raman spectroscopy especially important because it gives straightforward access to

microscopy, including analysis of single fibers. Because the molecular subunits cannot usually be evaporated, simulation spectra of single molecules was employed, which allowed to contrast results with spectra from isolated units. The simulation is a very good agreement with experimental spectra, which helped to assign the vibrations and useful also for fibers of biological relevance. Whereas the majority of vibrations in a molecule is influenced by multiple interactions (of various types) with its environment, the overall spectra are surprisingly close to those of single molecules in vacuum (simulation). It is believed that this finding can be expanded to more complex unities such as biologically active oligopeptides. In this case, overlapping bands from similar chemical environments would cause problems, which hope to alleviate by identifying aromatic ring features, but by concentrating on vibrations affected by hydrogen bonds. Estimation of the limit for detailed assignment is three (similar) up to six (very different) amino acids.

4.2 Electrospinning of aromatic peptides

In this section, other peptides containing phenyl groups, i.e. Gly-Phe (GF), Gly-Phe-Gly (GFG) and containing fluorenyl groups (Fmoc-Cys)$_2$ ((Fmoc-C)$_2$) were investigated. Fmoc-NH_2, which contains the basic π-stacking unit (fluorenyl), was selected for comparison (see chemical structures in Fig. 4.8). The objective of this section is to test the electrospinnability of other aromatic peptides besides the substances that were used in the first section. Here, only the microliter electrospinning setup was used in order to study effects of concentration and applied voltage. The results help us to understand the electrospinning mechanism and improve the predictive power for the electrospinnability of peptides (the results are proposed in the next section). For this reason, the vibrational simulations of the peptide molecules are not studied. The characterizations with IR and Raman spectroscopy are also not discussed in any further detail. Both characterization techniques were used only for comparison between electrospun fibers and powder samples.

4.2.1 Experimental

Chemicals: All phenyl peptides and fluorenyl side group peptides were purchased from Bachem. Several solvents, e.g. DMF, HFIP, and TFA were tested to dissolve the selected substances. Solution samples were prepared by an ultrasonication (USC300TH) for at least 30 min at room temperature (up to 60 °C in some case). The samples were additionally shaken (Titramax 1000, Heidolph) at 450−600 rpm for at least 3 h to obtain homogenous solutions. Hexafluoroisopropanol (HFIP, 99.0% Fluka) and trifluoroacetic acid (TFA, 99%, Sigma-Aldrich) was found to be the most suitable to dissolve the compounds. *N*, *N*-Dimethylformamide (DMF, 99.8%, Sigma-Aldrich), dimethylsulfoxide (DMSO, 99.5%, Panreac), and *N*-methylpyrrolidone (NMP, 99.8%, Technic France) were also effective in dissolving the substances, but their low vapor pressures are not suitable for electrospinning.

Electrospinning: The microliter electrospinning (μl-ES) setup based on an electrified wire (detailed in Chapter 3.2.2.2) was used in this section. A high voltage is applied to a Pt wire, onto which only 2−5 μl of peptide solutions are directly dropped from a micropipette.

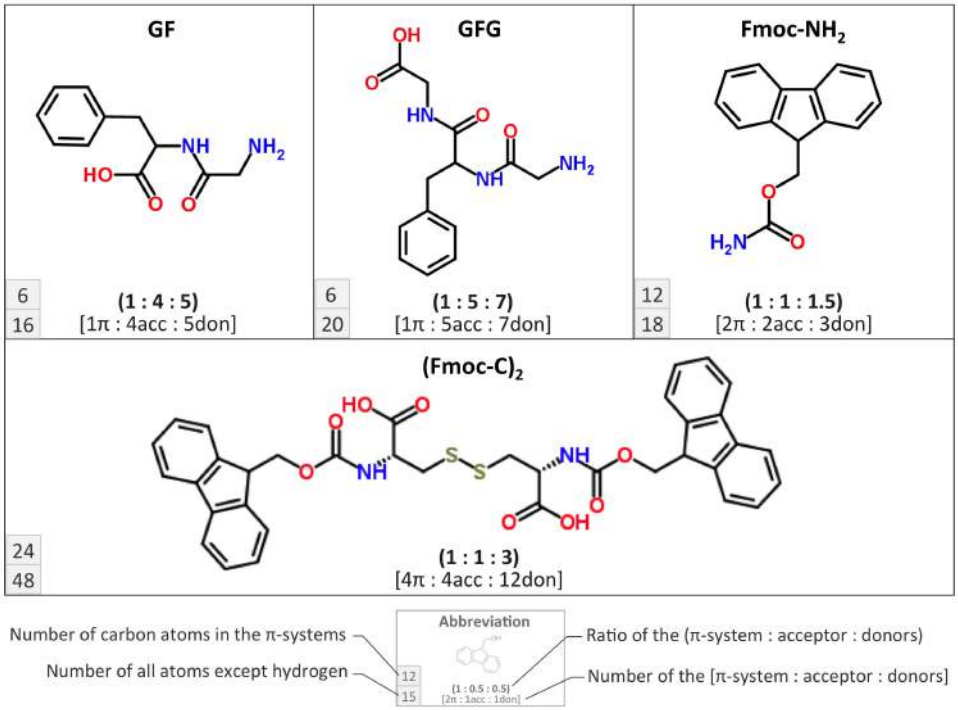

Figure 4.8: Chemical structures of peptides and peptide derivates used in this section.

4.2.2 Results and discussion

Electrospinning experiments were performed with various concentrations and at different parameters, i.e. applied voltage and distance between the needle and the collector in order to obtain optimized parameters. GF, GFG, and (Fmoc-C)$_2$ formed fibers with diameters ranging for 400 to 700 nm. Figure 4.9 shows optical micrographs of the electrospinning results. The electrospinnability of GF is very good, as is that of FF. Notice that in Fig. 4.9b, the GFG fibers are discontinuous because the GFG solution formed fibers (see inset of Fig. 4.9b) before the electrospinning process. So in this case, the electrospinning did not help to increase the self-assembly process, but only dispersed the preformed fibers on the substrate. As reviewed in Chapter 1, self-assembly of peptides in an organic solvent can be achieved simply by adding water. However, GFG can self-assemble (in a single step) by dissolution in HFIP at 0.4 %(wt/wt) by shaking and sonicating. Fmoc-NH$_2$ can be dissolved in HFIP, DMF, and TFA. However, Fmoc-NH$_2$ solutions cannot be electrospun. Only solidified droplets were observed (see Fig. 4.9d).

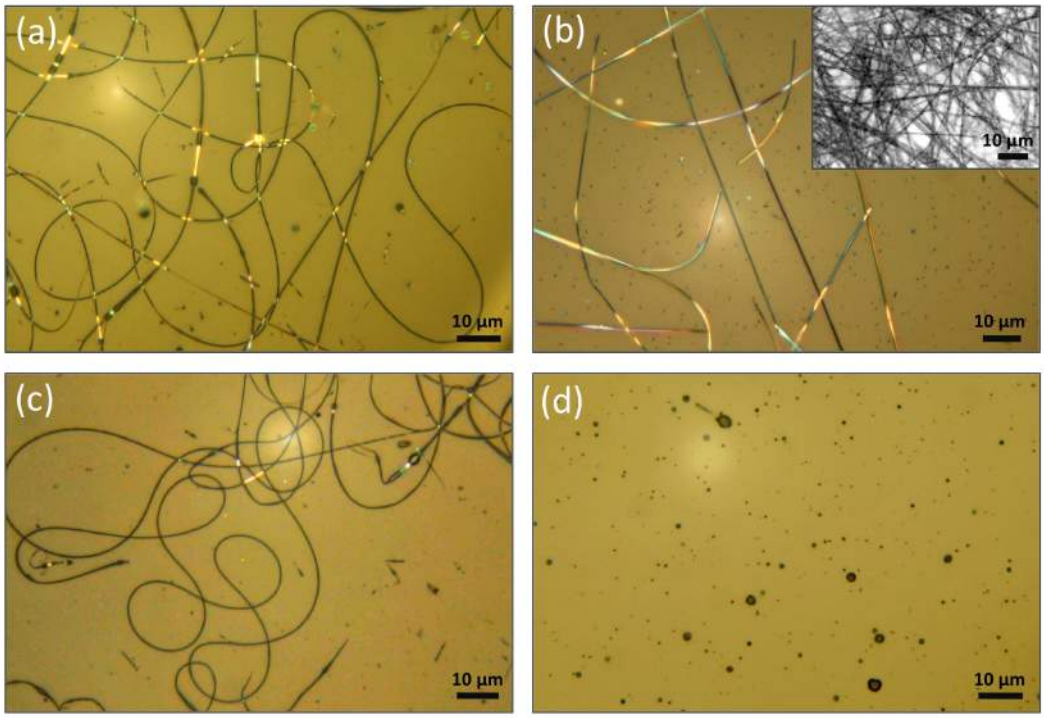

Figure 4.9: Optical micrographs of electrospinning results on a glass substrate; (a) long fibers of GF/HFIP 10 %(wt/wt) electrospun at V = 6 kV, H = 15 cm; (b) discontinuous fibers of GFG/HFIP 0.4 %(wt/wt) electrospun at V = 15 kV, H = 15 cm, inset is GFG fibers formed by self-assembly in the same solution; (c) long fibers of (Fmoc-C)$_2$/TFA 25 %(wt/wt) electrospun at V = 20 kV, H = 12 cm; and (d) solidified droplets of Fmoc-NH$_2$/TFA 15 %(wt/wt) electrospun at V = 15 kV, H = 12 cm.

4.2.2.1 Effect of solution concentration

Figure 4.10 shows the electrospinning results for GF/HFIP at various concentrations and applied voltages. At the concentration 5 %(wt/wt), the solution cannot be electrospun because the solution has a low viscosity. At 7.5 %(wt/wt), fibers are observed, since the viscosity is increased (the viscosity of the peptide solutions is discussed in detail in section 4.4.3). However, there are some droplets, and the fibers are not continuous. When the concentration was increased to 10 %(wt/wt), only fibers with very few beads were obtained. In this case, the solution whipping jet was continuously ejected. The solution jet did not break up into short fibers or tiny droplets. Thus the concentration 10 %(wt/wt) is high enough to obtain entanglement of the assembling molecules. This is similar to the entanglement found in polymer chains [31].

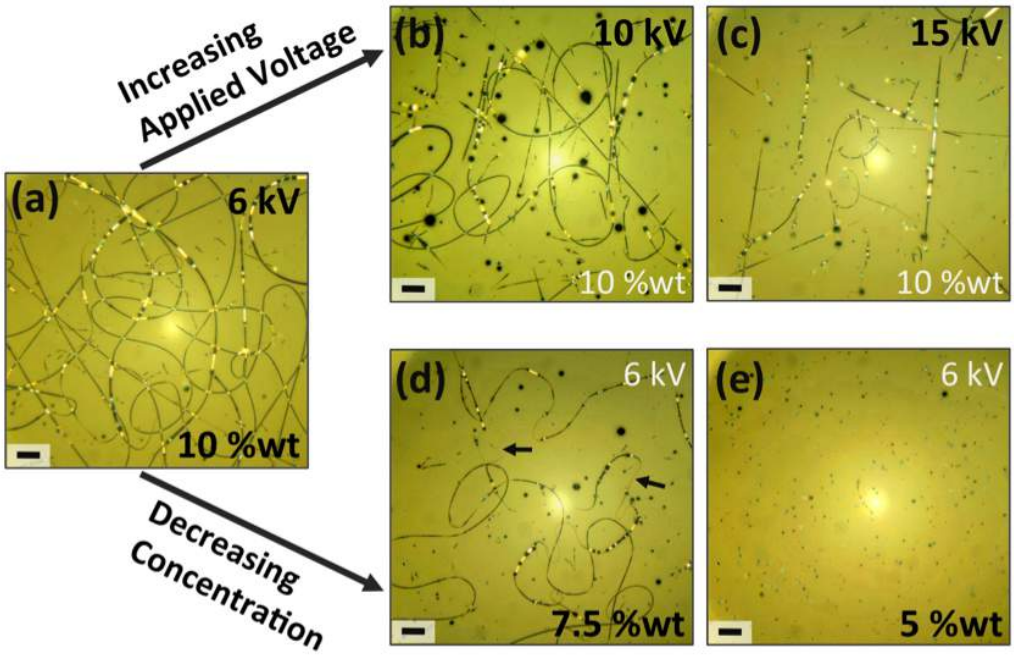

Figure 4.10: Optical micrographs show electrospinning results of the GF/HFIP solution at various concentrations and applied voltages. The distance between the tip and the collector was set at 15 cm. For (a-c) the applied voltage was set at 6 kV. The solutions concentrations were varied from (a) 5 %(wt/wt), (b) 7.5 %(wt/wt), and (c) 10 %(wt/wt). For (c-e) the concentration was set at 10 %(wt/wt). The applied voltages were varied from (c) 6 kV, (d) 10 kV, and (e) 15 kV. Scale bar is 10 μm.

4.2.2.2 Effect of applied voltage

Effect of applied voltage was studied by fixing the concentration of solution at 10 %(wt/wt) and the distance between the tip and the collector at 15 cm. The applied voltages were varied from 6 to 15 kV. Figure 4.10d-e show that the optimized voltage is 6 kV. When the applied voltage was increased to 10 kV, fibers with some solidified droplets were observed. At 15 kV, the fiber lengths are shorter than ~100 μm. It is possible that the fiber lengths are reduced because the electrostatic force is too high. At some points the jet diameter d_j is sharply reduced to zero or very small, causing the jet to break. The d_j is estimated by Eq. 4.1.

$$d_j = 4\left(\gamma\varepsilon_0\frac{Q^2}{I^2}\right)^{1/3} \tag{4.1}$$

Since the microliter electrospinning setup was used in this experiment, the solution was dropped from a micropipette with the flow rate of ≈0.5-1 μl/s. Here assumes that the flow rate Q is constant at about 1.0 x 10^{-9} $m^3.s^{-1}$ and the surface tension γ of the solution is the same with the solvent

Table 4.1: The estimation of jet diameter (d_j) for the GF/HFIP 10 %(wt/wt) solution.

Current (A)	**Flow rate** ($m^3.s^{-1}$)	**Surface tension** (mN/m)	d_j (m)
10^{-7}	10^{-9}	16.40	3.9 x 10^{-6}
10^{-6}	10^{-9}	16.40	8.3 x 10^{-7}
10^{-5}	10^{-9}	16.40	1.8 x 10^{-7}
10^{-4}	10^{-9}	16.40	3.9 x 10^{-8}

(see Table 3.3). The maximum current of the high voltage power supply is 2.5 x 10^{-4} A at 30 kV. However, the I that flow through the solution jet should be lower than the maximum value. With Eq. 4.1, the estimation of d_j for the GF/HFIP solution is shown in Table 4.1. The calculations show that the d_j reduced with increasing of the current. For example, at I is 1 μA, the d_j is estimated about 830 nm. When the voltage is higher, the greater number of charges causes the jet to move faster and the I also increases. If the I is 100 μA, the d_j is reduced to below 50 nm. The GF fibers with diameter of this range were not observed. However, ultrasmall fibers with diameter of below 50 nm can be produced in the case of albumin (see Chapter 5.2).

4.2.2.3 Vibrational spectroscopy of GF

Figure 4.11a shows the IR spectra of GF powders (solid line) and GF electrospun fibers (dash line). Only some bands are different (but $\leq$5 cm^{-1}). The highest vibrational frequency from the NH stretching is observed at 3213 cm^{-1}. The CH stretching vibrations appear in the region of 3061−2863 cm^{-1}. The strong intensity of Amide I band presents at 1684 cm^{-1} and the strongest intensity is observed at 1558 cm^{-1} due to Amide II band. Some strong intensity bands between 1521−1441 cm^{-1} and at 1281 cm^{-1} are assigned to CH bending. The vibration bands due to CO stretching are observed at 1412 and 1060 cm^{-1}. Some weak absorption bands are also assigned in the region 1207−1103 cm^{-1} due to in-plane CH ring vibration. In the low frequency region, the strong absorption at 746 cm^{-1} is assigned to out-of-plane CH bending [32]. The Raman spectrum of electrospun GF fibers is also very close to the GF powders. Figure 4.12a shows the highest vibration band, appearing at 3208 cm^{-1}, which is assigned to the NH stretching. The strong vibrations CH stretching band is located in the region 3053−2860 cm^{-1}. One strong vibration is observed at 1683 cm^{-1} due to Amide I band. A strong and medium vibration in the range 1605−1002 cm^{-1} reveals the presence of CH bending.

4.2.2.4 Vibrational spectroscopy of GFG

Figure 4.11b shows that most vibration bands of the electrospun GFG fibers are the same values compared to the GFG powders. The presence of OH stretching is revealed by weak absorption at 3456 cm^{-1}. One of very strong band is clearly observed at 3300 cm^{-1} due to NH stretching. Notice that the NH stretching presented in GFG features very strong absorption compared to infrared spectra of GF and (Fmoc-C)$_2$. Its possible that the hydrogen bondings in GFG molecules are

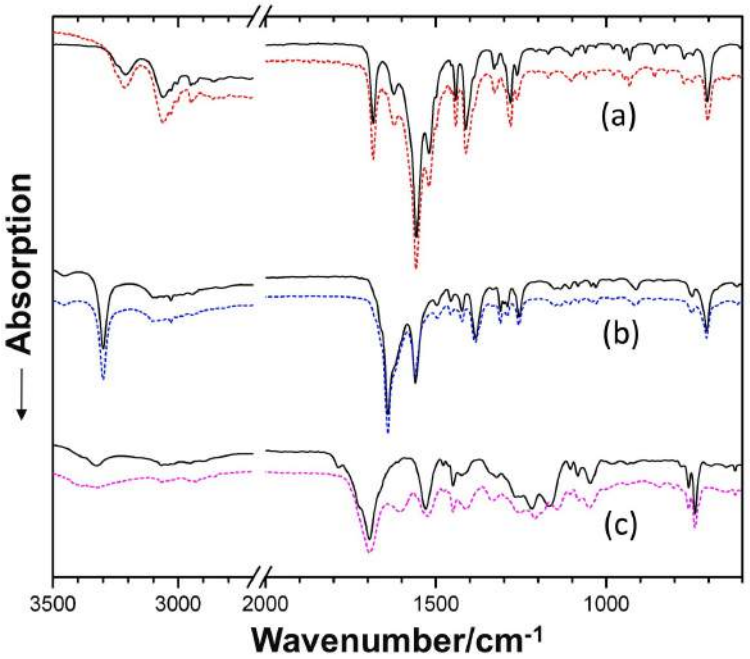

Figure 4.11: IR spectra of aromatic peptide compared between powder sample (solid line) and electrospun fibers (dash line) of (a) GF, (b) GFG, and (c) (Fmoc-C)$_2$. The spectra are scaled and offset for clarity comparison.

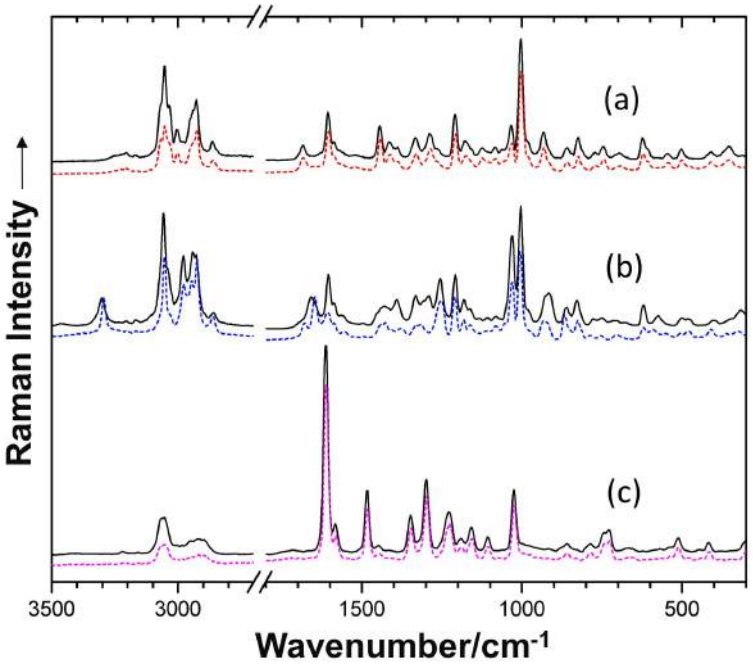

Figure 4.12: Raman spectra of aromatic peptide compared between powder sample (solid line) and electrospun fibers (dash line) of (a) GF, (b) GFG, and (c) (Fmoc-C)$_2$. The spectra are scaled and offset for clarity comparison.

stronger than GF and (Fmoc-C)$_2$, hence GFG can be self-assembled and formed fibers by shear force (sonication) before electrospinning process. While very strong absorption bands are also observed at 1640, 1561 cm^{-1} due to Amide I and II bands, respectively. At the 1495, 1456, 1384, 1290 and 1257 cm^{-1} are assigned to CH bending. One strong band from out-of-plane CH bending appears at 748 cm^{-1}. Figure 4.12b shows Raman spectrum of GFG electrospun fibers, which the solution can be self-assembled before applying with high voltage. The strong hydrogen bonded NH group is observed at 3295 cm^{-1} due to the NH stretching. The strong intensity of Raman peaks in the region 3055−2862 cm^{-1} which is assigned to CH stretching. Other vibration bands are in good agreement with the powder sample, without any strong shift CH bending bands that is located in the range 1428−1006 cm^{-1}. Except for the one Raman peak at 1647 cm^{-1} due to COO stretching that has slightly downshifted 12 cm^{-1} compared to the spectrum from the powder. Another difference is the vibration band from Amide I band at 1681 cm^{-1}, as it is not clearly observed in the powder sample. Both exceptions probably indicate the hydrogen bonding in the COO stretching and Amide I band [33].

4.2.2.5 Vibrational spectroscopy of (Fmoc-C)$_2$

In the case of electrospun (Fmoc-C)$_2$ fibers (see Fig. 4.11c), the OH stretching vibrates at 3329 cm^{-1} and the presence of CH stretching is located at 3066 cm^{-1}. Notice that both vibration bands have rather broad compared to GF and GFG at the same bands. Probably the broadened is by hydrogen bonds. Some CH bending bands at 1411, 1252, 1209, 1143 cm^{-1} are downshifted -9 to -24 cm^{-1} and upshifted 15 cm^{-1} at wavenumber 1336 cm^{-1} compared to the powder sample. Other vibration bands are almost the same values compared to the powder sample. The COO$^-$ stretching appears at 1695 and 1607 cm^{-1}. The strong absorption band out-of-plane CH bending is located at 739 cm^{-1}. Raman spectrum of electrospun (Fmoc-C)$_2$ shows good agreement with the powders sample (Fig. 4.11c). The vibration bands at high wavenumber are observed at 3055 and 2919 cm^{-1} due to the CH stretching. There is no vibration band from the NH stretching. The absence of NH or OH stretching is well known for many solid carboxylic acids, they might have very weak intensity or broadening. A very strong Raman peak at 1612 cm^{-1} is assigned to CO stretching. The presence of CH bending is revealed by strong and medium vibration peaks in the rage of 1580−1298 cm^{-1} and 1190−1025 cm^{-1}. Another band vibrates at 1226 cm^{-1} indicated to the OH bending.

4.2.3 Conclusions

The concentration of aromatic peptide solution plays an important role in the fiber formation. At low concentration the solution cannot form fiber, instead droplets were observed. IR and Raman spectra of the electrospun fibers reveal no signal from the C-F bond vibrations, which can be registered from the solvent, i.e. HFIP or TFA. Therefore, one can conclude that very little or no solvent is present. Furthermore, the spectra of electrospun fibers are in good agreement with the powders sample, except few vibration bands in GFG and (Fmoc-C)$_2$. This means that molecular conformation inside the electrospun fibers is changed very little compared to that powders sample. Thus, the function of the peptide would not be changed after electrospinning.

4.3 Electrospinning of tetraphenylporphyrin

Porphyrin derivates, especially tetraphenylporphyrin (TPP), are increasingly used in new types of photovoltaic devices [34–37]. Their advantages are their organic nature, hence availability, simple production, tunability of the optical properties, and potentially also mechanical flexibility. The advantage of porphyrins over other organic molecules is the combination of light absorption with separation of the charge carriers, and with good donor properties [34–36, 38–41]. However, this requires careful arrangement of the porphyrin rings, in order to achieve sufficient charge transfer rates. This normally requires crystals of the compounds, and ideally few grain boundaries. Furthermore, a complete photovoltaic (PV) device requires good contact to electron acceptors. For this, fullerenes are often mixed with the porphyrins [42, 43]. Such a blending of donor and acceptor in the devices requires careful mixing, down to the nanoscale, and both compounds need to exhibit charge transfer.

Alternative approaches aim at shaping both active materials, e.g. to defined 3D, 2D and 1D morphologies [44]. Indeed fullerene molecules would correspond to 0D (dots), but only in case of a perfect mixture, i.e. in absence of any aggregation. Typical problems are low charge transfer rates and also demixing of the donor and acceptor materials. Hence new methods for 1D and 2D nanofabrication are important to improve organic PV devices. Experiments in this section show a new approach based on electrospinning, which shapes porphyrin donors into a favorable 1D fiber [37]. This morphology is potentially more suitable for charge transfer to electrodes, even if the donor (or acceptor) molecules are some distance from the electrodes. It is also useful for mimicking natural photosynthesis [37, 41], and here solely concerned with the morphology of the donor, which includes simple, fast and effective processing methods.

4.3.1 Experimental

Electrospinning is practically exclusively used for polymeric materials, i.e. macromolecules. In this case, it would require a conductive polymer that mixes very well with the donor; this would require a totally new design of the molecular components. To avoid macromolecules altogether, and thus avoid demixing, TPP-NH_2 (monoamino-TPP) [45, 46] was employed and FF-TPP (diphenylalanine-TPP, NH_2-Phe-Phe-TPP) was selected as active materials [47], and used no polymer, but the small peptide diphenylalanine (FF, H_2N-Phe-Phe-COOH) to boost fiber formation (Fig. 4.13). The use of FF is motivated by its spinnability and high content of aromatic groups as demonstrated in section 4.1. The charge transfer of TPP and some of its derivates is based on π-stacking of the porphyrin moieties [46], which is also present in FF crystals (between the phenyl rings) [14, 19, 21, 48]. Additional to π-stacking, FF crystals are stabilized with an extensive network of hydrogen bonds, especially involving head-to-tail interactions between N- and C-terminal groups [49]. No crystal structure of NH_2-Phe-Phe-TPP exists yet, however a close analogue with blocked N-termini (Fmoc-FF-TPP) has been recently crystallized. Both π-stacking and hydrogen bonds between peptide moieties seem to stabilize the molecules in the crystal.

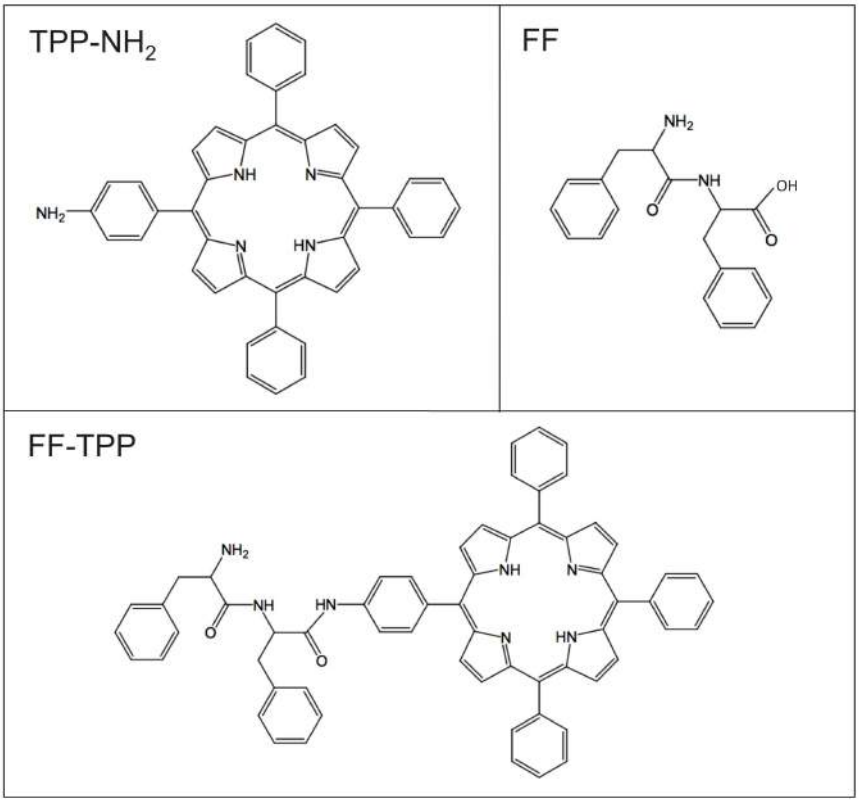

Figure 4.13: The tested porphyrin and diphenylalanine derivates.

The experiments are similar to previous section, firstly the substance was dissolved in organic solvents and tested their electrospinnability by using the microliter electrospinning setup (described in section 3.2.2.2). The electrospun fibers were analyzed with optical and electron microscopy, and with XRD and IR spectroscopy.

4.3.2 Results and discussion

Substance 1: TPP-NH_2, the pure TPP-NH_2 was dissolved in hexafluoroisopropanol (HFIP) (Fig. 4.14) at suitable concentrations of ~10 %(wt/wt) because they are simple to prepare, but already rather viscous. The viscosity can stabilize the droplet on the wire, and helps to avoid a break-up of the jet into droplets. It is thus a key parameter for the solutions, and easily controlled by the concentration, while the surface tension cannot be varied substantially. The second key parameter is the voltage: If it is too low (Fig. 4.14a, b), no jet forms, and if it is too high (Fig. 4.14d), the jet breaks up into droplets only (electrospraying). For properly adjusted conditions, some cm below the needle the jet starts to move sideways in ever larger distances. This irregular "whipping" is caused by the self-repelling charges on the jet surfaces. It stretches the jet and thins it to diameters well below μm. During this thinning the HFIP evaporates, and a submicroscale (or nanoscale) fiber forms (Fig. 4.14c).

Since the TPP-NH_2 is not a polymer, only intermolecular interactions should be able to stabilize a fiber. The crystal structure [46] suggests that π-stacking is an important interaction; it is certainly also responsible for the observed charge transfer rate of TPP [38, 39], and for the role of its derivates as donors in PV cells [43]. Intermolecular interactions are generally much weaker than the intramolecular covalent bonds in polymers, and consequently fibers tend to break up into rather short fragments. Nevertheless, electrospinning is a remarkably simple and generally applicable way to produce new fiber-like morphologies [21, 48]. Most of TPP-NH_2 fibers are shorter than 100 μm, and their needle-like shape (Fig. 4.14b), suggests incomplete electrospinning: During evaporation, molecules in the jet aggregate to an at least partially crystalline form, which has to induce axial shrinking. This force is opposed to the elongational force, which stems from the charging, and thus the jet breaks.

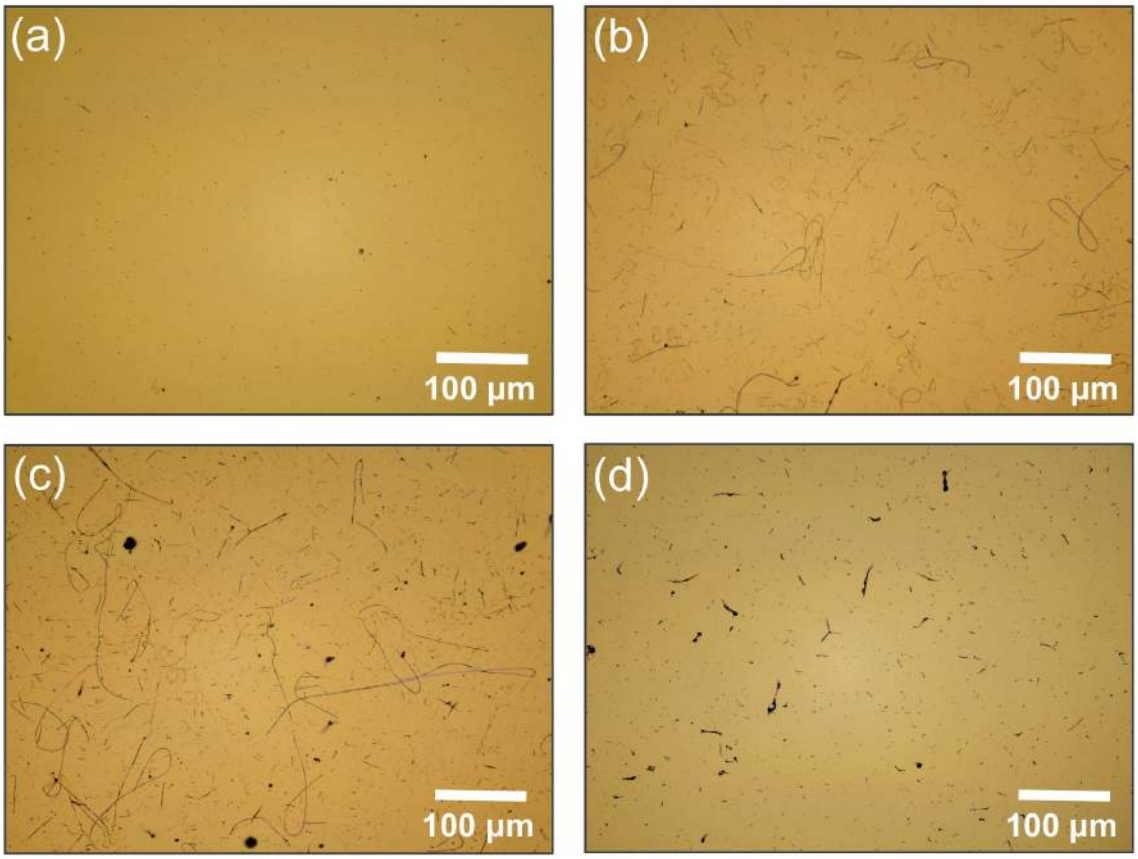

Figure 4.14: Optical images of TPP-NH_2 (9.1 %(wt/wt) in HFIP), electrospun at 12 cm distance wire-collector. The voltage was varied as follows: (a) 8 kV, no jet has formed, merely droplets; (b) 12 kV, the solution forms fibers; (c) 15 kV, optimal voltage, fiber length above 100 μm, diameters 500 to 2000 nm; (d) 20 kV, shorter fibers and droplets.

Substance 2: FF-TPP, the TPP derivate FF-TPP was tested because this compound contains six phenyl groups (see Fig. 4.13). It is expected that increasing of π-stacking (for the phenyl groups, but not necessarily of the porphyrin groups) can be produced longer fibers. Applying very high

voltages (above 30 kV), the spinnability is indeed better than for TPP-NH_2, and fibers long above 100 μm were observed (Fig. 4.15d). The length is now above the size of typical PV devices, which means that a highly porous fibrous solid (Fig. 4.15d) would substantially change the electrical characteristics of PV devices.

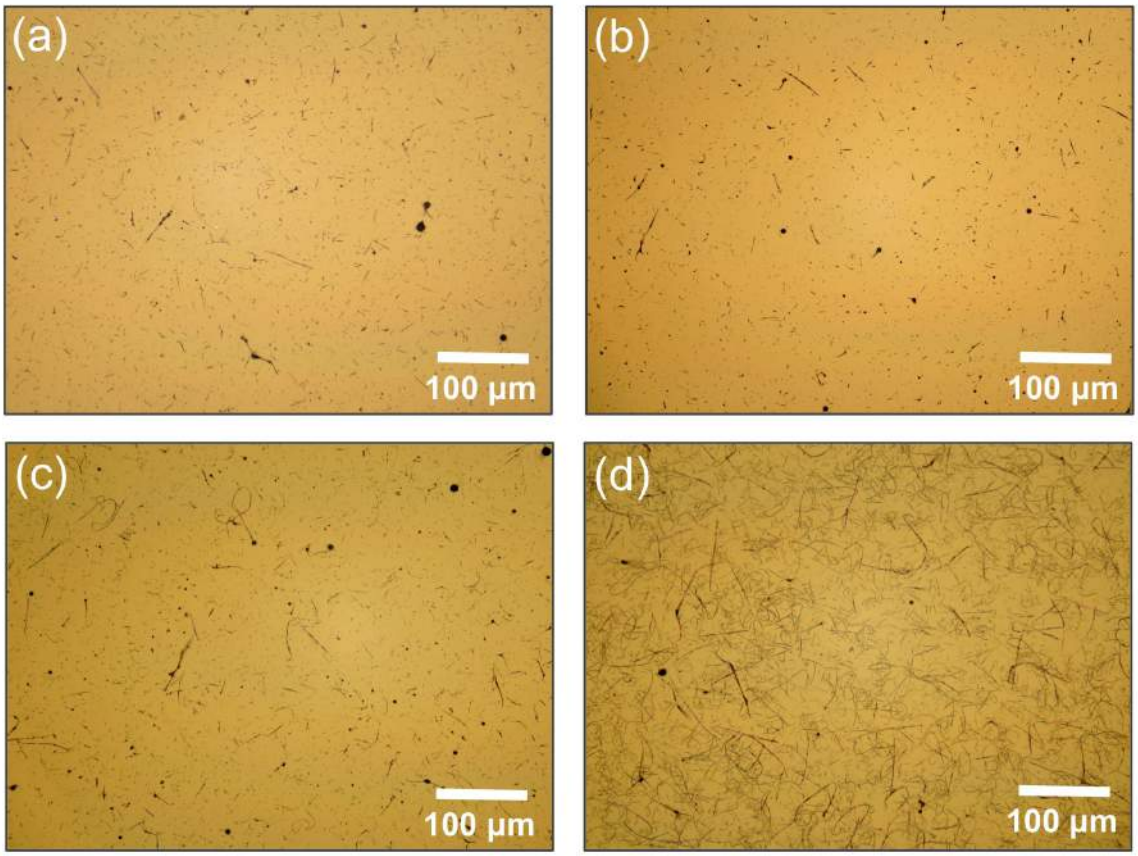

Figure 4.15: Optical images of FF-TPP (9.1 %(wt/wt) in HFIP), electrospun at 12 cm distance wire-collector. The voltage was varied as follows: (a) 12 kV, (b) 15 kV, (c) 20 kV, only fibers shorter than 100 μm, also droplets; (d) 35 kV (+25 kV at wire, -10 kV at collector), fibers longer than 100 μm, few droplets.

Substance 3: mixture of FF-TPP and FF (1:9), this mixture compound motivated by the excellent spinnability of FF [21], and by fiber formation in mixtures of peptides and porphyrins [50]. Indeed the high FF content leads to fiber morphologies (Fig. 4.16) that are typical for electrospinning of polymers [21, 48]. The parameters are however similar to those used for pure FF-TPP, and requires very high voltages. But the fibers are now quasi infinitely long (Fig. 4.16d). Here the advantage becomes very clear: Simple mixing, without the need of covalent binding, without the need to use polymers, allows to test promising compounds.

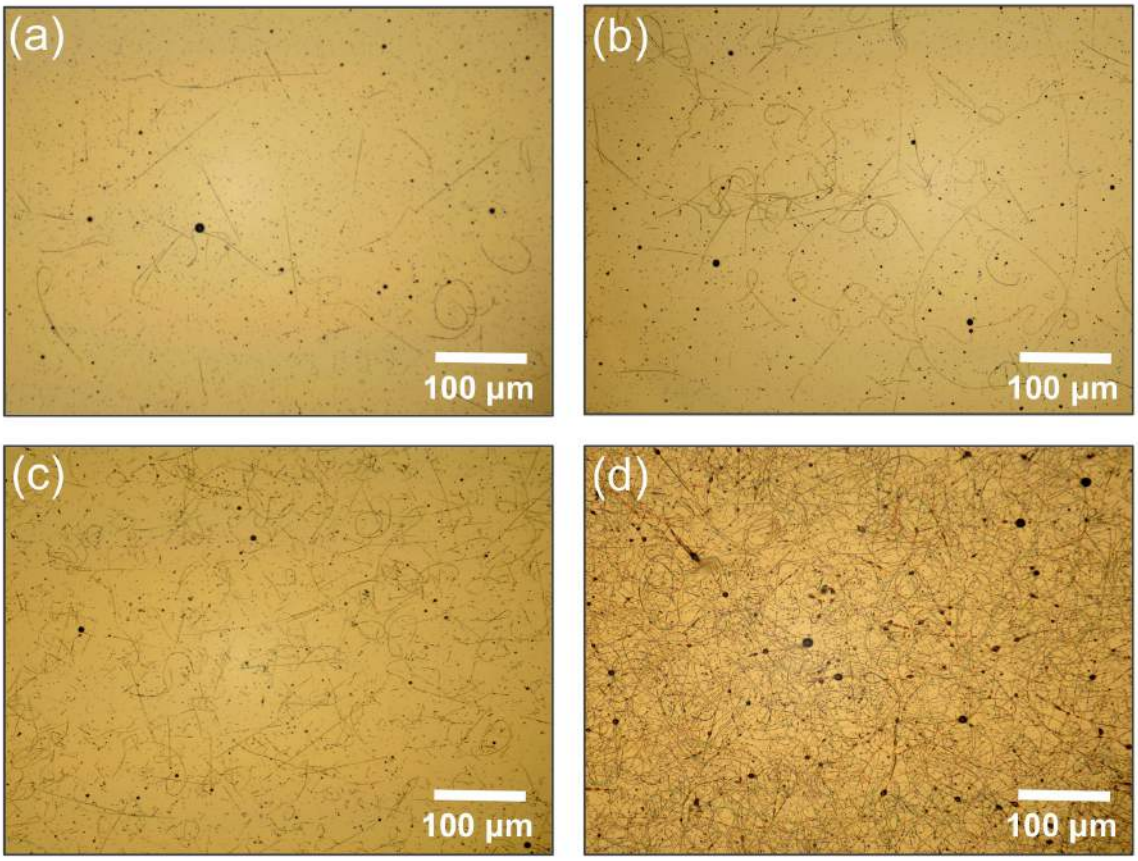

Figure 4.16: Optical images of a mixture of 1:9 (molar ratio) FF-TPP and FF (9.1 %(wt/wt) in HFIP), electrospun at 12 cm distance wire-collector. The voltage was varied as follows: (a) 12 kV, (b) 15 kV, (c) 20 kV, the solution forms fibers longer than 100 μm, and some droplets; (d) 35 kV, quasi infinite fibers with some beads (true electrospinning).

Electron micrographs (Fig. 4.17) show more details for the three cases (TPP-NH_2, FF-TPP, and FF/FF-TPP). For comparison, similar electrospinning parameters were employed. While fibers can be found in all cases, TPP-NH_2 (Fig. 4.17a) is fractured into rather short segments of irregular diameter, due to incomplete spinning. The ribbon-like morphology may be the result of drying. The diameter distribution is rather wide, large stretches measure 300 to 500 nm, but some more than 1000 nm. The presence of the FF moiety (Fig. 4.17b and 4.17c) induces long and thin fibers (on average below 500 nm). The mixed fiber has an especially narrow distribution of diameters (centered at 450 nm). A typical phenomenon for electrospinning is the presence of beads (short pearl-like stretches with increased diameter), which result from the first stages of droplet formation.

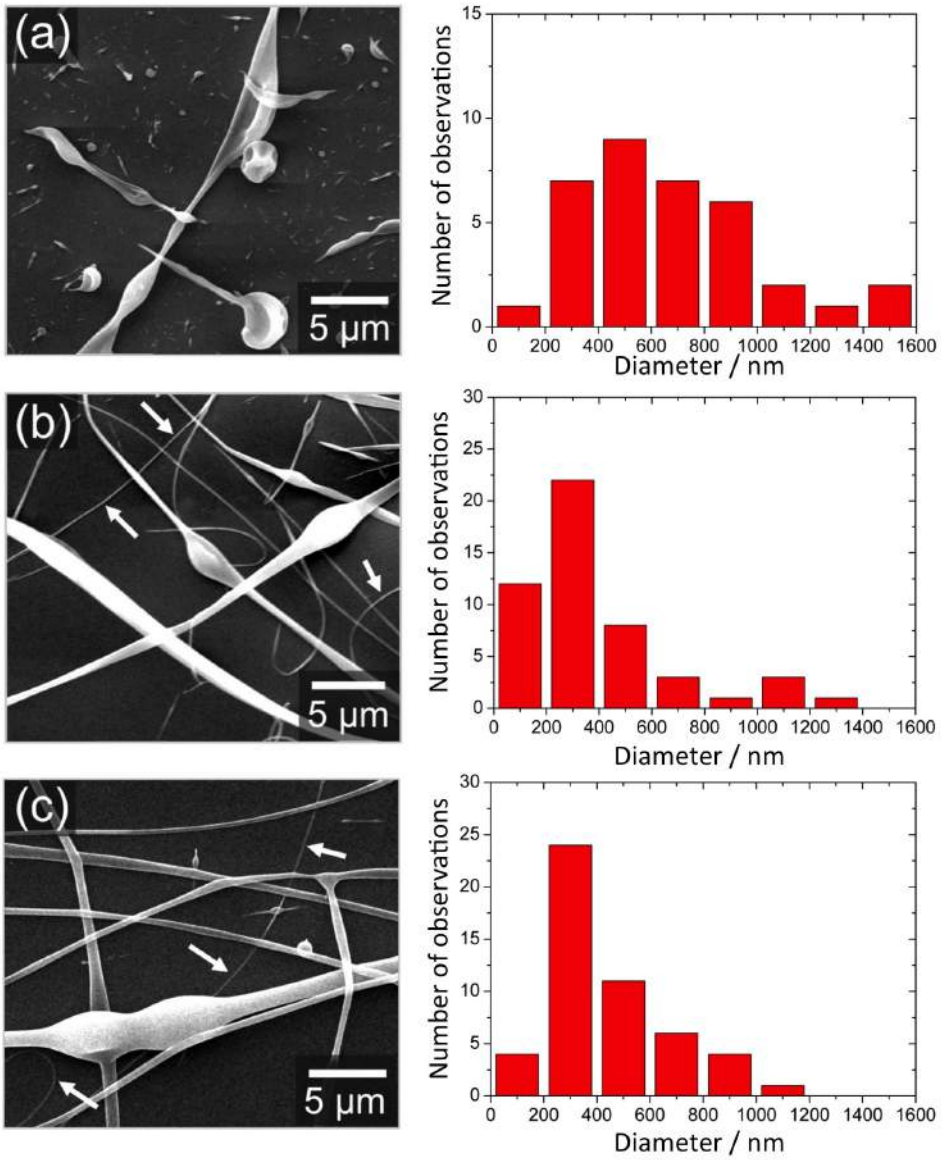

Figure 4.17: SEM micrographs and their histogram of the size distribution (on the right) of (a) very thick and short fibers of TPP-NH_2, diameter 840 ± 570 nm, and of (b) FF-TPP, diameter 400 ± 290 nm, and (c) FF-TPP mixed with FF (1:9), diameter 450 ± 240 nm. Both (b) and (c) show very long fibers of diameters of ~1000 nm, with some beads, but also some much thinner fibers (~100 nm, white arrows). All substances were electrospun at 35 kV, with 12 cm distance wire-collector. The size distribution was obtained from five SEM micrographs for each condition.

An important question concerns the internal structure. XRD was applied to obtain relevant information. Both FF and FF-TPP yield characteristic powder diffraction patterns with narrow peaks (Fig. 4.18a and 4.18b). The case of FF is well documented, and its structure is known [19], while for FF-TPP can be merely stated that it indeed forms crystals, but with an as yet unknown structure. When both powders are mixed, the pattern, too, resembles the added patterns (Fig. 4.18c). The high crystallinity of FF-TPP is likely responsible for breaking up the electrospinning jet, and thus for the short fiber length. In this respect, FF is an exception because it can form extremely long fibers that are crystalline. This is due to the very highly concentrated FF solution, which cannot be much affected by evaporation - the argument becomes obvious when considering not the standard technical weight% data, but mol% (and HFIPs high density of 1.6 kg/l): here obtain 158 mM for FF-TPP, but in the mixture 351 mM FF (and 39 mM FF-TPP).

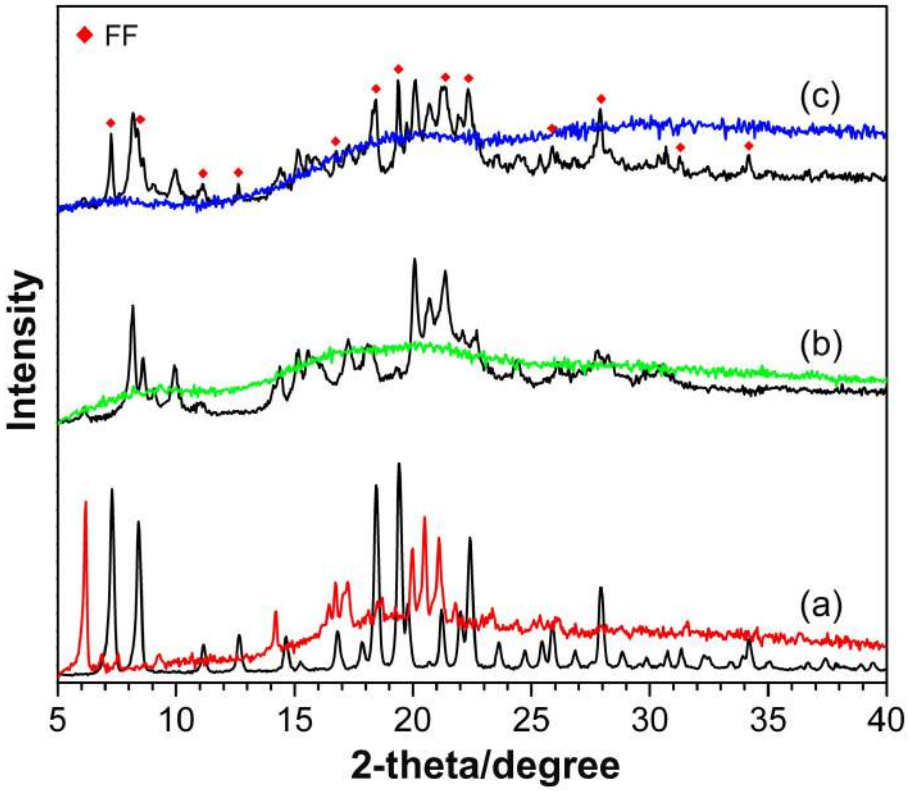

Figure 4.18: XRD patterns for (a) FF, (b) FF-TPP, (c) a 1:9 mixture of both powders FF and FF-TPP. The black traces correspond to the powder. The colored traces are patterns obtained from the corresponding electrospun fibers (12 cm distance; (a) 10 kV, (b) and (c) 35 kV). For (c) the black trace is a combination of (a) and (b), as expected; red squares mark the signals from FF.

The XRD pattern changes drastically for the spun mixture (Fig. 4.18d): It merely shows three extremely broad features of low intensity. Each feature spans a region of relatively strong signals from FF-TPP. This finding suggests that FF-TPP delivers the structural base, while altogether the structure is nearly amorphous. This is a direct consequence of the two incompatible crystal struc-

tures: No atomic distances match, FF is substantially smaller, and hence π-stacking of whichever parts of the molecules would produce a very open, unstable structure. A largely disordered arrangement is clearly preferred. Note that electrospinning, despite the elongational forces extended on the jet, does not usually produce new (semi)crystalline phases. Crystalline materials can preserve their structure [21, 48], but this is not guaranteed.

In order to show that especially the very broad patterns are no artifact, but stem from the electrospun fibers, the XRD diffractograms were presented in Fig. 4.18 again, but here each is plotted together with the background signal (three identical black traces). The background was recorded under identical conditions, but without sample, on the bare zero background holder (made of silicon).

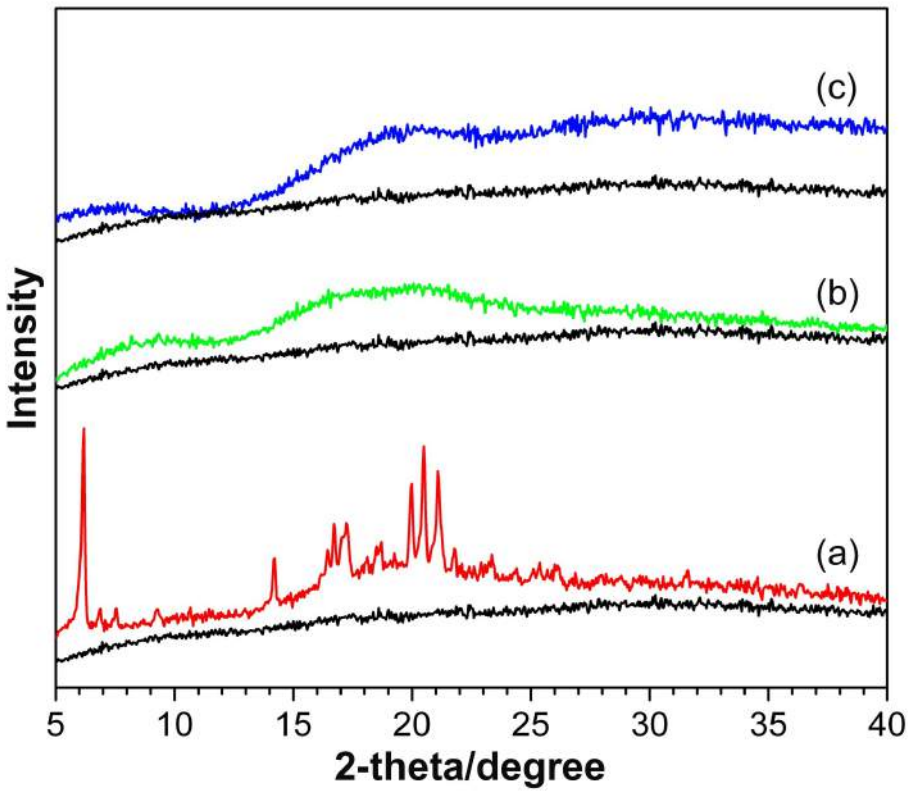

Figure 4.19: XRD patterns from (a) FF powder, crystalline; (b) FF-TPP powder, crystalline; (c) a mixture of both powders FF-TPP and FF compare to background, which recorded under identical conditions, but without sample, on the bare zero background holder.

Another potential cause of the loss of XRD would be the loss of molecular integrity. However, the 1:9 mixture of FF-TPP with FF fibers show all characteristic IR absorption peaks from both FF and from TPP-NH_2 (Fig. 4.20). The most prominent TPP-NH_2 peaks are 3435, 3315, 1595, 1470, 1440, 1350, 1000, 965, 800, 730, and 700 cm^{-1} [23]. Of these 3315, 1595, 1440, 965, and 800 cm^{-1} were found in the mixed fiber. These peaks can be defined as characteristic because all other

peaks are either too weak, or overlap with the well-known strong absorption peaks in FF (3265, 1555, 1520, 1430, 1385, 1255, 835 cm^{-1}) [48]; some additional bands, marked with discs, stem from the slowly evaporating residues from the solvent HFIP [23]. Note that the FF group is already present in the FF-TPP molecule, but that the free FF in the fiber heavily dominates the spectrum. In spite of this, the above-mentioned peaks from TPP-NH_2 are present in the electrospun mixture, so both molecules preserve their molecular integrity, in contrast to the very low integrity of mutual molecular orientation (i.e. the very low crystallinity).

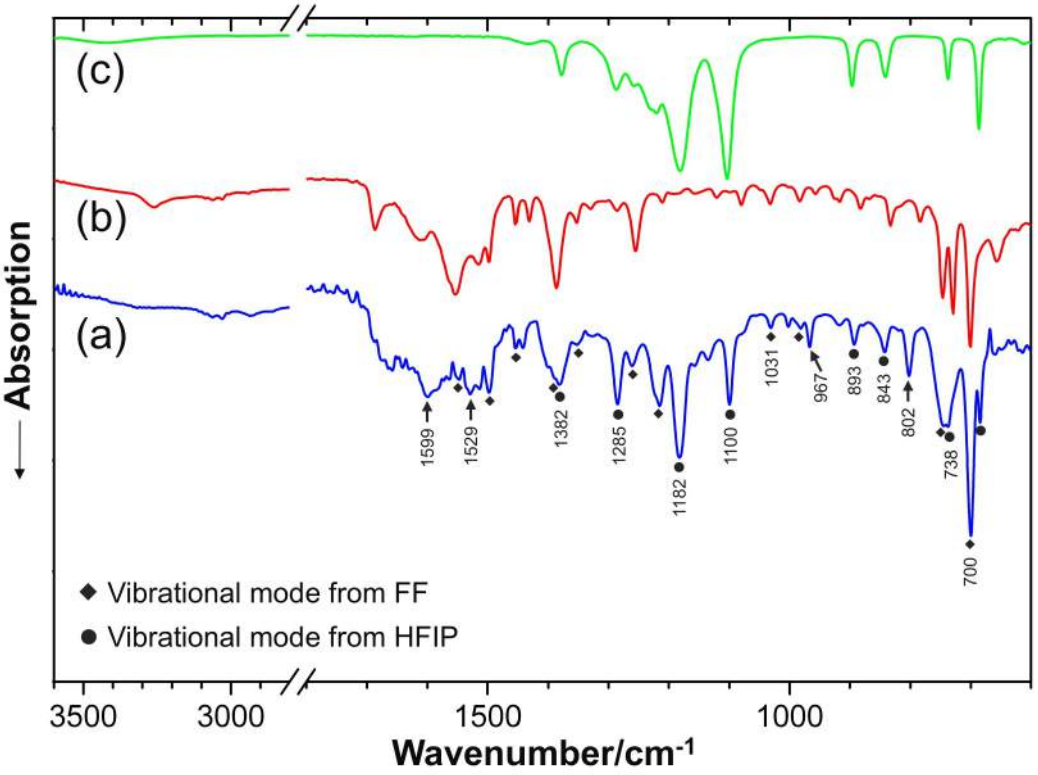

Figure 4.20: Infrared vibrational spectroscopic analysis of (a) electrospun fibers obtained from the 1:9 mixture of FF-TPP with FF (12 cm, 35 kV); (b) FF powder for comparison; (c) the pure solvent (HFIP). The spectra are scaled and offset for clarity.

4.3.3 Conclusions

The excellent electrospinnability of the mixture of FF-TPP with FF is based on preservation of the molecular structure, but induces loss of crystallinity. The combined effect of the presence of FF and the noncrystalline nature cannot induce charge transfer in the easily produced long fibers. The morphology, a quasi endless single fiber, curled up into a highly porous mesh, is very unusual for polymer-free molecular compounds, and will allow for incorporation of further structures. This simple and effective combination of blending and fiber formation will serve to finely tune electronic and optical properties of many more materials.

4.4 Prediction of electrospinnability

The fiber formation of peptides depends on the solution concentration and the electrospinning parameters. In addition to this, the type of solvent, type of substance, and rheology of the solution are also important factors. This section will propose methods for predicting the electrospinnability of peptides. First, a model based on dissolution and electrospinning results will be proposed. Second, polarized Raman spectra of peptide powders will be evaluated. Third, some notices on the high-speed images of a free falling drop test (rheology) will be compared.

4.4.1 Method 1: Electron acceptor and donor number of the solvent

Screening of solvents for the peptides (this work tested with FF, Fmoc-FG, $(Fmoc\text{-}C)_2$, Fmoc-G, $Fmoc\text{-}NH_2$, and 9FM) was investigated in order to find a suitable solvent for electrospinning. The results are concluded in Table 4.5. Each solvent was used to dissolve peptides at high concentrations (close to the limit of dissolution where precipitated or non-homogenous solution can be observed). Then the high concentrated solution was electrospun with various electrospinning parameters to obtain fibers. Some solvents can completely dissolve most of selected peptides (marked as +++) but the solution cannot be electrospun. Only droplets or short fibers (below 100 μm) are recognized. Though some solvents can completely dissolve some peptides (marked as ++), the solution can be electrospun and formed into fibers. Thus, electrospinnability might be predicted by the type of solvent as proposed below.

Table 4.5 summarizes solubility and electrospinnability of each solvent for peptides studied in this work, including their electron acceptor number (AN) and electron donor number (DN). The results point out that AN and DN affect electrospinnability of peptides. These two empirical parameters are proposed by Gutmann [51], which he calls the "two-parameter approach". The acceptor number describes electrophilic behavior (electron acceptor or hydrogen donor, δ^+, acid), while the donicity or donor number represents the nucleophilic behavior (electron donor or hydrogen acceptor, δ^-, lone pair, base) of the solvent. The AN and DN are generally used to determine the polarity of the solvent and explain the solubility of solvent, e.g. Malavolta et al. used these numbers for the interpretation of the insoluble β-amyloid peptide [52–54].

Example I: Fmoc-G can be dissolved in DMF at a high concentration but this solution cannot be electrospun into long fiber. Only short fibers (10−20 μm) were observed at a concentration of 20 %(wt/wt) with optimized electrospinning parameters (see Fig. 4.21a). Even though the concentration was increased to 50 %(wt/wt), only droplets were obtained. When the Fmoc-G was dissolved in TFA at 25 %(wt/wt) and electrospun at $V = \pm 15$ kV and $H = 15$ cm (μl-ES), long fibers with some solidified droplets $\approx$2−15 μm in diameter were observed. Figure 4.21b indicates that the fiber has diameter around 100−300 nm. The beads in fiber are 1−2 μm of diameter. Therefore, the electrospinnability of Fmoc-G can be improved by using TFA instead of DMF.

The AN value of TFA is high compared to HFIP and DMF; AN of TFA = 105, HFIP = 88, and DMF = 16 (see Table 4.5). This evidence supports the claim that the short aromatic peptides can be dissolved in a high AN solvent. The AN represents the dimensionless number expressing the electron acceptor or hydrogen donor property of the solvent. Conversely, DN represents the solvent electron donor character. It means TFA is a good hydrogen donor solvent, which increases hydrogen bonding in Fmoc-G solution. Possibly TFA helps Fmoc-G to remain protonated (COOH rather than COO^-), and COOH groups form strong hydrogen bonds. The increase of hydrogen bonding affects the increase of self-assembly, leading to fiber formation when electrospinning assists.

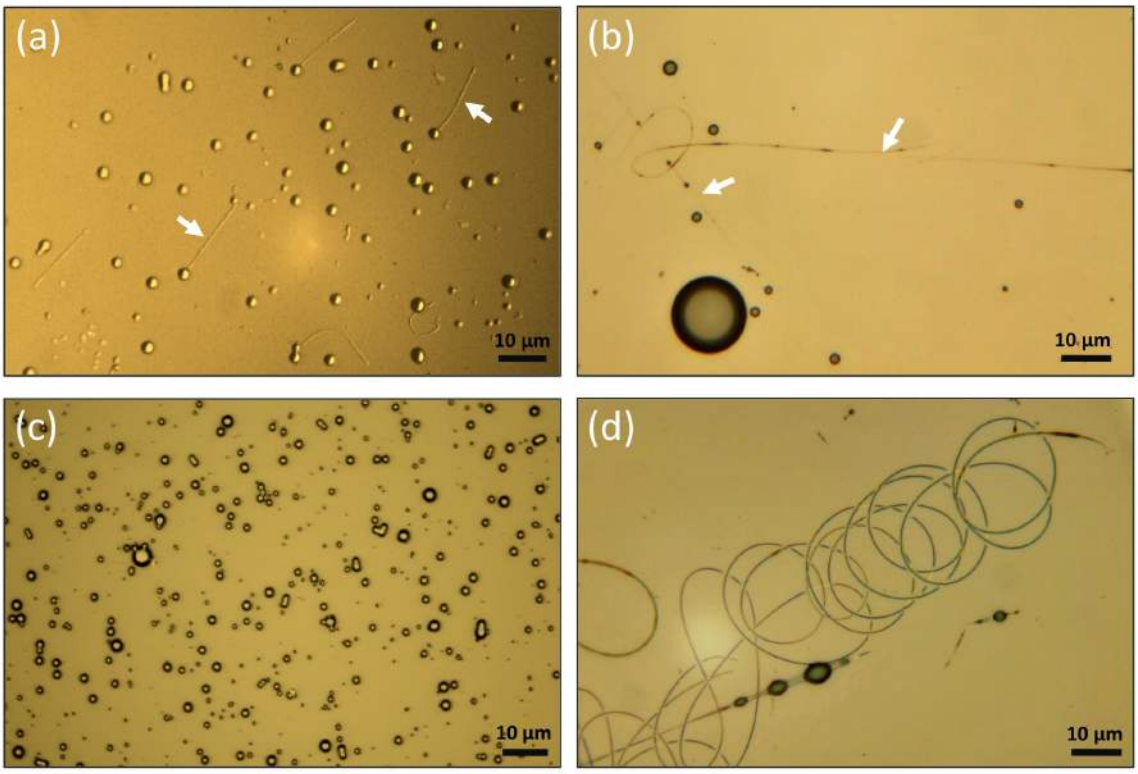

Figure 4.21: Optical images of the microliter electrospinning results: (a) arrows indicate short fibers of Fmoc-G/DMF 20 %(wt/wt), (b) long fibers of Fmoc-G/TFA 25 %(wt/wt), note that one huge solidified droplet diameter of ~10 μm at the left bottom was observed by chance because the solution was dropped from the needle, (c) solidified droplets of $(Fmoc\text{-}C)_2$/DMF 20 %(wt/wt), and (d) long fibers of $(Fmoc\text{-}C)_2$/TFA 25 %(wt/wt).

Example II: $(Fmoc\text{-}C)_2$ can be dissolved in DMF, DMSO, and NMP but the solutions cannot form fiber. Only solidified droplets were observed. Figure 4.21c shows solidified droplets with diameter of $\approx 1-3.5$ μm produced from $(Fmoc\text{-}C)_2$ dissolved in DMF at 20 %(wt/wt). The vapor pressure of DMF, DMSO, and NMP is much lower than HFIP, so this is a one reason why $(Fmoc\text{-}C)_2$ cannot form fiber by electrospinning. The electrospinnability of $(Fmoc\text{-}C)_2$ was improved by using TFA (AN = 105) as a solvent. Figure 4.21d shows long fibers with few beads of $(Fmoc\text{-}C)_2$ dissolved in TFA 25 %(wt/wt) and microliter electrospun at V = 20 kV and H = 12 cm. Table 4.5

Table 4.5: Electron acceptor number (AN) and electron donor number (DN) of selected solvents, and their solubility of short aromatic peptides and fluorene derivates.

Solvent[1]	pK_a[2]	AN	DN	(AN - DN)	Solubility[3]	Electrospinnability
THF	≫16	8.0	20.0	-12.0	++	Droplets
NMP	≫16	13.3	27.3	-14.0	+++	Droplets
DMF	>16	16.0	26.6	-16.0	+++	Droplets, Short fibers
DMSO	>16	19.3	29.8	-10.5	+++	Droplets
DCM	≫16	20.4	1.0	19.4	+	Droplets
EtOH	>16	37.1	32.0	5.1	+	Droplets
MeOH	>16	41.3	30.0	11.3	++	Droplets
TFE	≈12	53.5	0	53.5	0	-
HFIP	≈9	88.0	0	88.0	++	Long fibers
TFA	≈2	105.0	0	105.0	++	Long fibers

[1] solvent parameters from [52].
[2] see Eq. 2.13, for comparison, the pK_a of CH_3COOH ≈5, hydrochloric acid < -1, Gly ≈10, 2, and H_2O ≈15.
[3] the solubility results were determined by testing the dissolution of FF, Fmoc-FG, $(Fmoc\text{-}C)_2$, Fmoc-G, Fmoc-NH_2, and 9FM; +++ completely dissolves almost all peptides, ++ completely dissolves some peptides, + dissolves some peptides, 0 cannot dissolve.

indicates a relationship between the AN, DN, (AN - DN) of solvent and the electrospinnability. Notice that a solvent with negative (AN - DN) from -16.0 to -10.5 can dissolve the short aromatic peptides very well but it is not suitable for electrospinning. When a solvent has positive (AN - DN) ≥ 88, it is a suitable solvent for electrospinning of short aromatic peptides. Furthermore, the high (AN - DN) solvent (such as TFA and HFIP) has slightly high vapor pressure (see Table 3.3). This is a good property for the electrospinning because this technique needs a solution that easily evaporates.

Model: All previous results indicate that short aromatic peptides can be electrospun and form fibers with or without beads by dissolving them in a highly electrophilic solvent (AN ≥ 88) at high concentration. The choice of organic solvent has a significant influence on the electrospinnability and fiber formation. The solution has to achieve strong intermolecular interactions. In the case of aromatic peptides, the intermolecular interactions are from the aromatic residues in the peptide, causing π-stacking of the molecules and hydrogen bonding. To prove this, fluorene derivates 9FM and Fmoc-NH_2 were used in comparison with the short aromatic peptides. The results (see Fig. 4.2a and 4.9d) show that the fluorene derivates cannot form fibers. Only solidified droplets were observed.

4.4.2 Method 2: Polarized Raman spectra of the peptide powder

To evaluate intermolecular coupling, polarized Raman spectra of each substance from powder samples (hence random orientation) were recorded using the confocal Raman microscope (Alpha300S, WITec). Raman spectra can be measured as described in section 3.3.7.2. Additionally, a polarizer and analyzer were used in this experiment to provide a polarized Raman spectrum. The Raman intensities were measured in the vertical (I_{VV}) and horizontal (I_{VH}) components that refer to the 0°, 0° (polarizer, analyzer) orientation, and to 0°, 90°, respectively. The polarization ratio ρ is defined by I_{VH} / I_{VV}. Figure 4.22 shows the results. For 9FM, the ρ values close to the limit of 0.75 (depolarized bands) might be taken as an indication for rather small intermolecular interactions (except for the OH group, see earlier) because polarized bands would not appear in the absence of intermolecular coupling. However, depolarization can also arise from multiple scattering, which is a common problem for polarized Raman spectra of powders or of anisotropic or turbid materials [55].

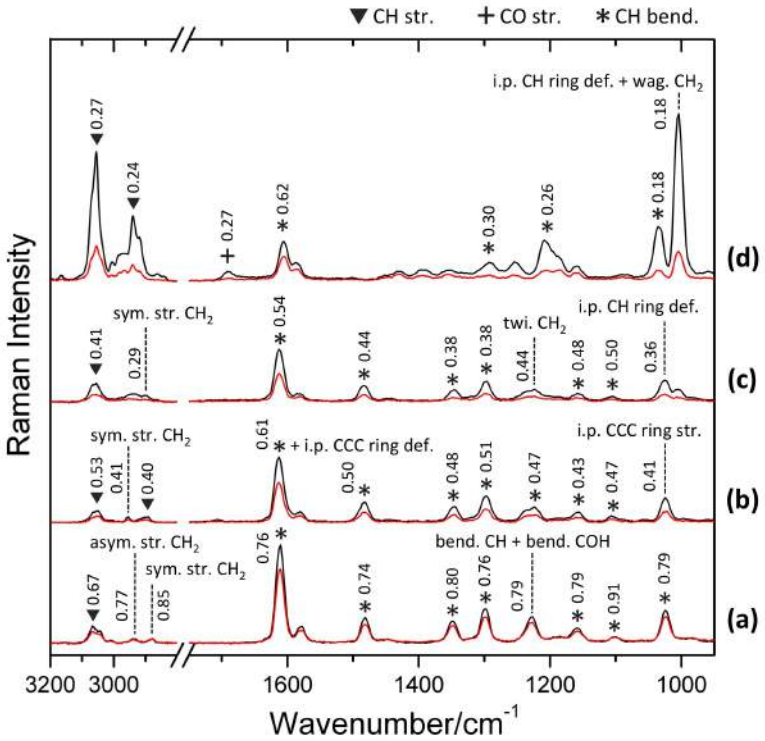

Figure 4.22: Polarized Raman spectra of powder samples, with the analyzer oriented parallel (black line) and perpendicular (lower red line) to the incident polarization. (a) 9FM, (b) Fmoc-G, (c) Fmoc-FG, and (d) FF. The spectra have been background subtracted and offset for clarity.

Concerning the other substances, the fact that their values don't reach below 0.18 suggests high (local) symmetries. As expected, all amide I bands are polarized [56] (e.g. ρ = 0.27 for the 1691 cm^{-1} band in Phe-Phe). Evaluation of wavenumber shifts as function of polarization, non-coincidence effect (NCE) [57–59] is defined as $\delta\nu = \nu_{aniso}$ - ν_{iso} , where the isotropic spectra were

calculated by $I_{iso}(\nu) = I_{VV}(\nu)$ - $(4/3)I_{VH}(\nu)$, and the anisotropic spectra intensity were assumed as $I_{aniso}(\nu) = I_{VH}(\nu)$. The NCE is zero for single molecules (see also the case of 9FM), and normally positive for molecular liquids such as *N*-methylacetamide [56]. Negative values can be found when the molecules interact stronger, for example, for the CO stretching in alcohols, pointing towards hydrogen bonding [60]. Considering the spectral resolution of 3 cm^{-1}, only a few of the bands show $\delta\nu \neq 0$ (not present here, see in [48]). Although there is no consistent trend, the NCE in some of the aromatic ring vibrations might be traced to π-stacking. The polarized Raman spectra of other short aromatic peptides support this method. Figure 4.23 shows the polarized Raman spectra of each substance from the powders sample. Most ρ values of GFG, GF and (Fmoc-C)$_2$ are smaller than Fmoc-NH$_2$ at the same vibration bands. Note that the ρ values of Fmoc-NH$_2$ are higher than the limit of depolarized bands (0.75), i.e. 0.84, 0.76, 0.77 because the multiple scattering of the powder materials [55].

Model: The electrospinnability of biomolecules (such as aromatic peptides and its derivates) may be predicted by comparing the ρ values of polarized Raman spectra. A substance can be electrospun when its ρ values are small (close to 0), rather than when it has high ρ values (close to 0.75).

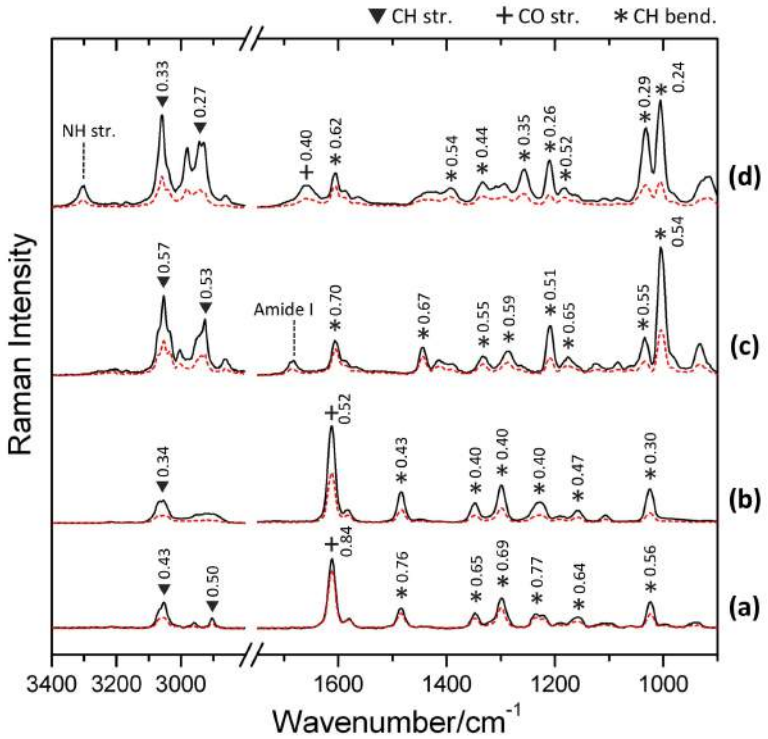

Figure 4.23: Polarized Raman spectra with the depolarization ratio of powder samples, with the analyzer oriented parallel (solid line) and perpendicular (dash red line) to the incident polarization. (a) Fmoc-NH$_2$, (b) (Fmoc-C)$_2$, (c) GF, and (d) GFG. The spectra have been background subtracted and offset for clarity.

4.4.3 Method 3: Rheology of the peptide solution

The concentration of solution is one of the most important factors for the electrospinning of small molecules. It should be high enough to achieve a sufficient viscosity. Solidified droplets were observed when the concentration is low or the viscosity is not suitable. Lagerwall pointed out that a fluid can be formed into fibers in the electrospinning process if the fluid presents non-Newtonian properties such as polymer solutions. The jet of water or other Newtonian liquids will break up into droplets by Rayleigh instability [61]. In addition, viscoelastic behavior of the liquid should have a long relaxation time for electrospinning [62, 63]. The knowledge of fiber formation and its relationship to the peptides solution, indeed even polymer solutions, has been lacking.

In Chapter 2, a high-speed camera was used to follow a mechanism of the electrospinning process. When a polymer solution was fed through a nozzle and applied a high voltage, the solution formed a Taylor cone and then a straight solution jet ejected. Finally, the jet unstable whipped (see Fig. 2.2f-j). If the voltage is zero, a free falling drop of the solution was observed. Figure 4.24 shows high-speed images at 20,000 fps of the free falling drop of solutions from a nozzle. A short solution jet was observed between the droplet and the nozzle, this jet is named "necking of a droplet" (indicated with black arrows). A necking length is defined as the maximum length of the jet before it is broken. The necking length of water and Fmoc-G/DMF 17 %(wt/wt) are shorter than PAN/DMF 4 %(wt/wt) and PEO/Water ≈3 %(wt/wt). In addition, the necking diameter (D_{Neck}) of water and Fmoc-G/DMF 17 %(wt/wt) are larger than both polymer solutions. Considering their electrospinnability, water and Fmoc-G/DMF 17 %(wt/wt) cannot form fiber, but the others can be electrospun to long fibers. This suggests that the electrospinnability of peptide solutions might be predicted using the free falling drop test. To prove this postulation, the necking of droplet of the solutions was studied.

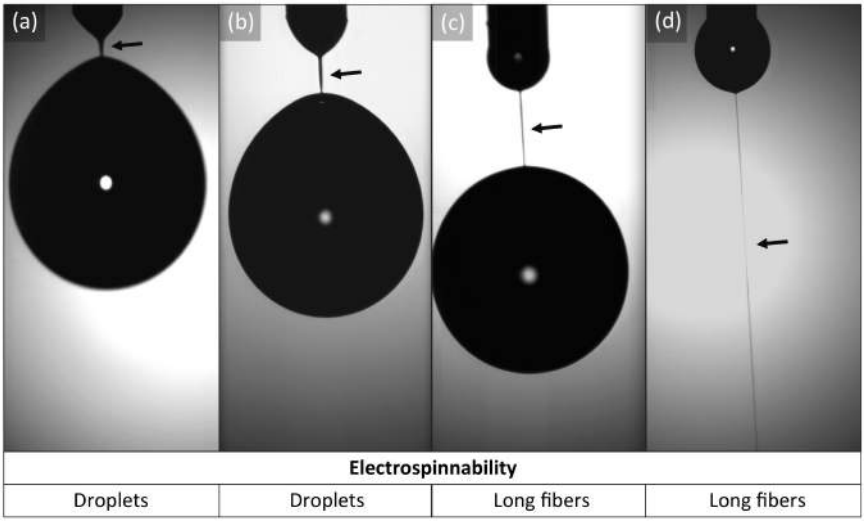

Figure 4.24: High speed images of the falling drop of solutions; (a) water, (b) Fmoc-G/DMF 38 %(wt/wt), (c) PAN/DMF 4 %(wt/wt), and PEO/water ~3 %(wt/wt) with their electrospinnability at the bottom, the arrows indicate the necking of droplet.

The high speed imaging technique has been extensively used for studies of the behavior of Newtonian and non-Newtonian drop detachment (see [64, 65]). For this thesis, a high-speed camera (Fastcam SA5, Photron) was used to follow the falling drops with resolution of 384 x 808 pixels at speed of 20,000 fps. The solution was slowly fed through a nozzle and controlled by a digital linear actuator because only the gravity and capillary forces are required for producing an affect on the falling drop. Figure 4.25 shows sequence images of the free falling drop test from the nozzle diameter (D_0) of 0.7 mm.

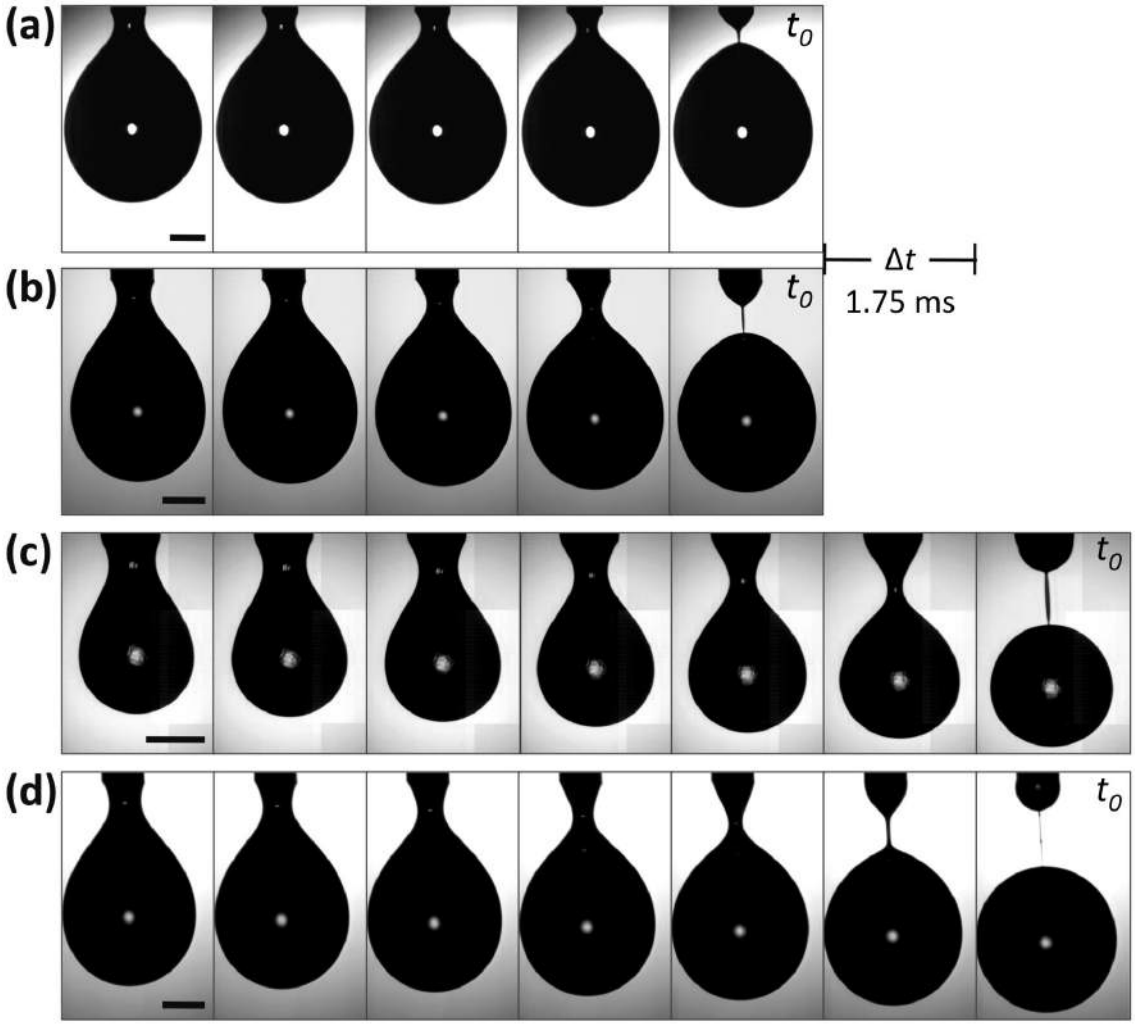

Figure 4.25: Sequence images of the free falling drop test of the solutions (a) water, (b) Fmoc-G/DMF 17 %(wt/wt), (c) FF/HFIP 14 %(wt/wt), and (d) polymer PAN/DMF 4 %(wt/wt). All images were recorded at the same speed of 20,000 fps and presented at the same interval amounts of Δt=1.75 ms. The scale bars are compared to the nozzle diameter of 0.7 mm.

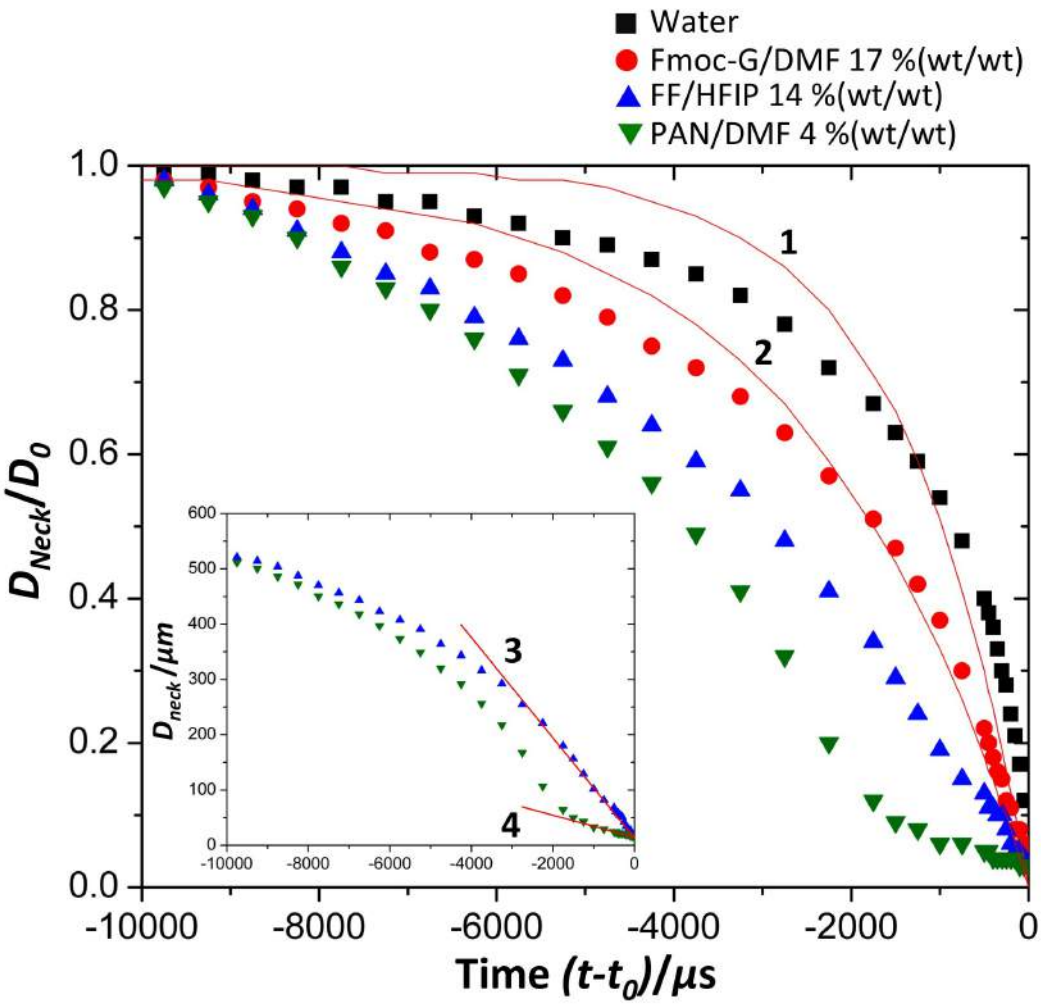

Figure 4.26: Time evolution of the necking diameter (D_{Neck}/D_0) versus shifted time ($t - t_0$) of water, Fmoc-G/DMF 17 %(wt/wt), FF/HFIP 14 %(wt/wt), and polymer PAN/DMF 4 %(wt/wt). The solid lines are the fitting curve of each time evolution. Number (1) and (2) are exponential decay functions of the water and Fmoc-G/DMF, respectively. Number (3) is linear fit according to the Stokes flow of the FF/HFIP and number (4) is linear fit in the Navier-Stokes flow of the PAN/DMF.

The image of the solution was captured and the necking diameter (D_{Neck}) was evaluated until the necking was broken (at time t_0). It assumes that the D_0 equals to the D_{Neck} at the first frame of the recording ($t - t_0$ = -10 ms). The D_{Neck}/D_0 was plotted versus the shifted time ($t - t_0$). Figure 4.26 shows the evolution time of the D_{Neck} of water and Fmoc-G/DMF 17 %(wt/wt), they are exponential decay functions. A model of the necking diameter reported by Clanet et al. was used, $D_{Neck}/D_0 = 1 - e^{(t-t_0)/\tau_n}$ where the τ_n is the characteristic time for the necking [66]. The fitting curve of the water (solid line 1) is

$$D_{Neck}/D_0 = 1 - e^{(t-t_0)/1400} \,, \tag{4.2}$$

and of the Fmoc-G/DMF 17 %(wt/wt) (solid line 2) is

$$D_{Neck}/D_0 = 1 - e^{(t-t_0)/2500} \,. \tag{4.3}$$

Both equations provide the τ_n of water (τ_n = 1.4 ms) and Fmoc-G/DMF (τ_n = 2.5 ms). Compared to the work of Rothert et al. [64], the FF/HFIP and the PAN/DMF solutions are linear fits corresponding to the Stokes flow and the Navier-Stokes flow, respectively. In the case of Stokes flow, the time evolution of the D_{Neck} is given by [67],

$$D_{Neck} = \chi \frac{\gamma}{\eta} (t_0 - t) \,, \tag{4.4}$$

where χ is the universal scaling factor, which is 0.0709 for the Stokes flow and 0.0304 for the Navier-Stokes flow [64], γ is the surface tension and η is the viscosity. To calculate the value of η, the D_{Neck} was plotted versus the shifted time $(t - t_0)$ (see inset of Fig. 4.26), the linear fits of the FF/HFIP is

$$D_{Neck} = 15 - 0.09\,(t - t_0) \,, \tag{4.5}$$

and of the PAN/DMF is

$$D_{Neck} = 15 - 0.02\,(t - t_0) \,. \tag{4.6}$$

Therefore, the slopes of the solid line number (3) and (4) are -0.09 and -0.02, respectively. Substituting the slopes into Eq. 4.4 and assuming that the surface tension of the solution is the same as the solvent, so that the η can be calculated and is shown in Table 4.3. The calculated η was also compared to values measured by a rheometer (DHR, TA Instrument) at temperature of 25 °C. In addition, the η was used to estimate the Oh of the solution by Eq. 2.9, assuming that the jet diameter (d) is ≈100 μm and the solution density (ρ) is $\approx \rho_{solvent} \cdot [1 + (\%\text{wt}/100)]$.

Table 4.3: The viscosity of solutions calculated by results from the free falling drop test and the estimation of the *Oh*.

Solution	**Viscosity** (mPa.s)	**Density** (kg/m^3)	**Surface tension** (mN/m)	*Oh*	**Electrospinnability**
Water	0.89*	1.00	71.99	0.3	Droplets
Fmoc-G/DMF 17 %wt	5.2*	1.11	37.76	2.5	Droplets
FF/HFIP 14 %wt	13	1.82	16.40	7.5	Long fibers
PAN/DMF 4 %wt	52*	0.99	37.76	27	Long fibers
PAN/DMF 4 %wt	57	0.99	37.76	30	Long fibers

* measured by the rheometer for comparison.

Table 4.3 shows that the η and *Oh* of the FF/HFIP solution can be estimated by using high-speed images of the free falling drop experiments. However, the solution should present the non-Newtonian behavior. For the polymer solution PAN/DMF, the η from this experiment agrees well with the value measured by the rheometer.

Model: By considering the electrospinnability of each solution, the result suggests that the *Oh* of solution should be above $\approx$10 in order to obtain long fibers. The *Oh* and the η of solutions will be mentioned again in Chapter 5.1.2. Note that the rheometer cannot provide the η of the FF/HFIP solution because this solution evaporated and dried before the measurement was finished. Therefore, the high-speed camera could be a technique that is used to solve the problem.

▲ Summary

This chapter focused on the electrospinning of the short aromatic peptides. Theses peptides can be electrospun without polymer blends when they are dissolved in a suitable solvent at a high concentration and when electrospinning parameters are optimized.

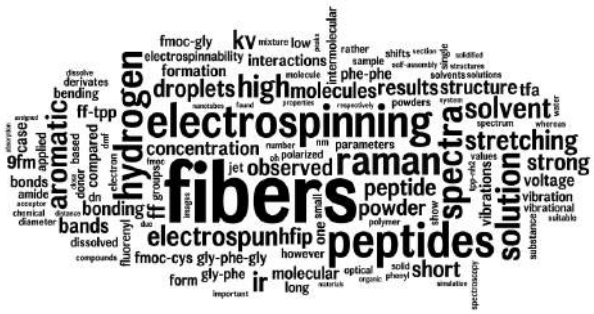

The results show that the short aromatic peptides can form long fibers but the fluorene derivates cannot obtain fibers. Therefore, the short aromatic peptides are the suitable substances for the electrospinning. In addition, a longer aromatic peptide should also be suitable. For the dissolution process, the short aromatic peptides should be dissolved in a strongly electrophilic solvent such as HFIP and TFA. The concentration should be high in order to reach strong intermolecular interactions and to achieve the suitable rheological properties. Moreover, the peptide has to be completely dissolved and there is no precipitate. In the case of a small volume solution (few μl), the microliter electrospinning works very well. Furthermore, this setup is more convenient than the conventional setup. In this Chapter, the optimization parameters are 10−15 kV, 12−15 cm, and 0.2−0.5 ml/h.

Noncovalent interactions (electrostatics, hydrogen bonds, or Van der Waals) that are proposed play a vital role in the stabilization of fiber formation. This appears similar to the self-assembly of aromatic peptides in solution (see examples 1−3 in Chapter 1.2). Figure 4.27a presents a schematic of a standard polymer electrospinning. Figure 4.27b is a proposed mechanism for a short aromatic peptide. Intermolecular interactions that are mainly from the hydrogen bonds and π-π stacking interactions determine the self-assembly. The electrostatic force applied by the electrospinning process assists assembled peptides to arrange into long fibers. Figure 4.27c shows mechanism of GFG solution self-assembles into fibers before the electrospinning process. For the fluorine derivates 9FM and Fmoc-NH_2, the solution jets breakup into droplets, which later solidify by solvent evaporation (Fig. 4.27d). This is possible because the molecular interactions are not strong enough for stabilizing structure of the fibers. Moreover, the viscosity of the solution is insufficient.

The conclusions on solvents and optimized parameters from this work can be applied to other small peptides and polypeptides. This means the choice of biomolecule substances for the electrospinning can be sharply increased, improving the potential applications of nanofibers in life science areas, e.g. wound dressing, tissue engineering, drug delivery, and applications in neurodegeneration. Electrospinnability of macrobiomolecules such as globular proteins will be studied in Chapter 5 based on the optimized parameters of this chapter.

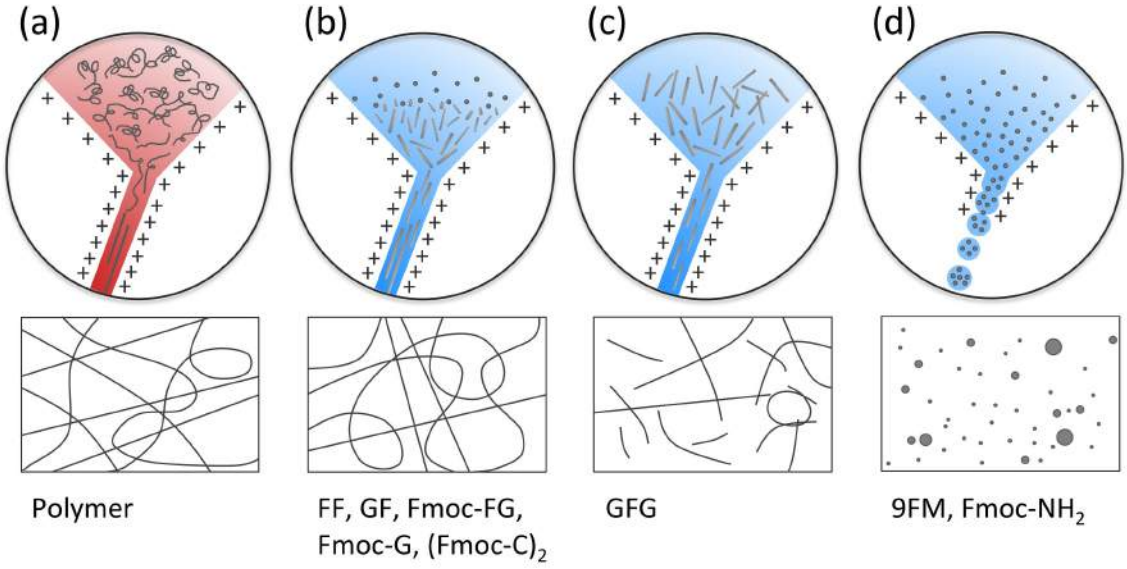

Figure 4.27: Schematic of the proposed mechanisms in electrospinning of (a) a standard polymer, (b) FF, GF, Fmoc-FG, Fmoc-G, $(Fmoc\text{-}C)_2$, (c) GFG, and (d) 9FM, Fmoc-NH_2.

4.5 References

[1] M. Brehm, T. Taubner, R. Hillenbrand, F. Keilmann. Infrared Spectroscopic Mapping of Single Nanoparticles and Viruses at Nanoscale Resolution, *Nano Lett.* **6**: 1307, 2006.

[2] W. Sasiadek, M. Maczka, E. Kucharska, J. Hanuza, A.A. Kaminskii, H. Klapper. Polarized IR and Raman study and DFT chemical quantum calculations of the vibrational levels for benzophenone single crystal, *J. Raman Spectrosc.* **36**: 912, 2005.

[3] Ch. Schneider, D. Porras, T. Schaetz. Experimental quantum simulations of many-body physics with trapped ions, *Rep. Prog. Phys.* **75**: 024401, 2012.

[4] J. Mingorance, G. Rivas, M. Vélez, P. Gómez-Puertas, M. Vicente. Strong FtsZ is with the force: mechanisms to constrict bacteria, *Trends Microbiol.* **18**: 348-356, 2010.

[5] R. Fairma, K.S. Akerfeldt. Peptides as novel smart materials, *Curr. Opin. Struct. Biol.* **15**: 453, 2005.

[6] J.D. Hartgerink, J.R. Granja, R.A. Milligan, M.R. Ghadiri. Self-Assembling Peptide Nanotubes, *J. Am. Chem. Soc.* **118**: 43-50, 1996.

[7] M.R. Ghadiri, J.R. Granja, L.K. Buehler. Artificial transmembrane ion channels from self-assembling peptide nanotubes, *Nature* **369**: 301-304, 1994.

[8] N. Ashkenasy, W.S. Horne, M.R. Ghadiri. Design of Self-Assembling Peptide Nanotubes with Delocalized Electronic States, *Small* **2**: 99, 2006.

[9] M. Yoshizaki, N. Nishio, J. Kuwahara, N. Nishino, T. Kato. Proceedings of the 4th International Peptide Symposium, 2007.

[10] K. Rosenthal-Aizman, G. Svensson, A. Unden. Self-Assembling Peptide Nanotubes from Enantiomeric Pairs of Cyclic Peptides with Alternating D and L Amino Acid Residues, *J. Am. Chem. Soc.* **126**: 3372-3373, 2004.

[11] S. Gilead, E. Gazit. Self-organization of Short Peptide Fragments: From Amyloid Fibrils to Nanoscale Supramolecular Assemblies, *Supramol. Chem.* **17**: 87-92, 2005.

[12] E. Gazit. Self Assembly of Short Aromatic Peptides into Amyloid Fibrils and Related Nanostructures, *Prion* **1**: 32-35, 2007.

[13] D.M. Ryan, T.M. Doran, B.L. Nilsson. Complementary π-π Interactions Induce Multicomponent Coassembly into Functional Fibrils, *Langmuir* **27**: 11145-11156, 2011.

[14] E. Gazit. A possible role for π-stacking in the self-assembly of amyloid fibrils, *FASEB J.* **16**: 77-83, 2002.

[15] V. Jayawarna, M. Ali, T.A. Jowitt, A.F. Miller, A. Saiani, J.E. Gough, R.V. Ulijn. Nanostructured Hydrogels for Three-Dimensional Cell Culture Through Self-Assembly of Fluorenylmethoxycarbonyl- Dipeptides, *Adv. Mater.* **18**: 611-614, 2006.

[16] Y. Zhang, H. Gu, Z. Yang, B. Xu. Supramolecular Hydrogels Respond to Ligand-Receptor Interaction, *J. Am. Chem. Soc.* **125**: 13680-13681, 2003.

[17] D.M. Ryan, T.M. Doran, S.B. Anderson, B.L. Nilsson. Effect of *C*-Terminal Modification on the Self-Assembly and Hydrogelation of Fluorinated Fmoc-Phe Derivatives, *Langmuir* **27**: 4029-4039, 2011.

[18] C.H. Görbitz. Nanotube formation by hydrophobic dipeptides, *Chem. Eur. J.* **7**: 5153-5159, 2001.

[19] C.H. Görbitz. The structure of nanotubes formed by diphenylalanine, the core recognition motif of Alzheimer's β-amyloid polypeptide, *Chem. Commun.* 2332-2334, 2006.

[20] J. Kim, T.H. Han, Y.I. Kim, J.S. Park, J. Choi, D.G. Churchill, S.O. Kim, H. Ihee. Role of Water in Directing Diphenylalanine Assembly into Nanotubes and Nanowires, *Adv. Mater.* **22**: 583-587, 2010.

[21] G. Singh, A.M. Bittner, S. Loscher, N. Malinowski, K. Kern. Electrospinning of Diphenylalanine Nanotubes, *Adv. Mater.* **20**: 2332-2336, 2008.

[22] D.A. Prystupa., A. Anderson, B.H. Torrie. Raman and infrared study of solid benzyl alcohol, *J. Raman Spectr.* **25**: 175-182, 1994.

[23] SDBSWeb: http://riodb01.ibase.aist.go.jp/sdbs/ National Institute of Advanced Industrial Science and Technology, (accessed 2 Sep. 2011).

[24] V.K. Belsky, V.E. Zavodnik, V.M. Vozzhennikov. Fluorene, $C_{13}H_{10}$, *Acta Cryst.* **C40**: 1210-1211, 1984.

[25] M.O. Sinnokrot, E.F. Valeev, C.D. Sherrill. Estimates of the Ab Initio Limit for π-π Interactions: The Benzene Dimer, *J. Am. Chem. Soc.* **124**: 10887-10893, 2002.

[26] H.T. Flakus, M. Jablonska, P.G. Jones. Study of polarized IR spectra of the hydrogen bond system in crystals of styrylacetic acid, *Spectrochim. Acta A* **65**: 481, 2006.

[27] W.W. Rudolph, G. Irmer. Vibrational spectroscopic studies and DFT calculations on tribromoacetate and tribromoacetic acid in aqueous solution, *Spectrochim. Acta A* **79**: 1483, 2011.

[28] D. Lin-Vien, N.B. Colthup, W.G. Fateley, J.G. Grasselli. The Handbook of Infrared and Raman Characteristic Frequencies of Organic Molecules, Academic Press, Boston, 1991.

[29] C. Dicko, D. Knight, J. Kenny, F. Vollrath. Conformational polymorphism, stability and aggregation in spider dragline silks proteins, *Int. J. Biol. Macromol.* **36**: 215-224, 2005.

[30] A.C. Leskovjan, A. Kretlow, A. Lanzirotti, L.M. Miller. Bioengineering Conference NEBC 07, IEEE 33 rd Annual Northeast: 54, 2007.

[31] S.L. Shenoy, W.D. Bates, H.L. Frisch, G.E. Wnek. Role of chain entanglements on fiber formation during electrospinning of polymer solutions: good solvent, non-specific polymer-polymer interaction limit, *Polymer* **46**: 3372-3384, 2005.

[32] SDBSWeb: http://riodb01.ibase.aist.go.jp/sdbs/ National Institute of Advanced Industrial Science and Technology, (accessed 3 Sep. 2012).

[33] W. Gallagher. FTIR analysis of protein structure, http://www.chem.uwec.edu (accessed 24 Jan. 2013).

[34] P.D.W. Boyd, C.A. Reed. Fullerene-Porphyrin Constructs, *Acc. Chem. Res.* **38**: 235-242, 2005.

[35] L.L. Li, E.W.G. Diau. Porphyrin-sensitized solar cells, *Chem. Soc. Rev.* **42**: 291-304, 2013.

[36] K.M. Panda, K. Ladomenou, A.G. Coutsolelos. Porphyrins in bio-inspired transformations: Light-harvesting to solar cell, *Coord. Chem. Rev.* **256**: 2601-2627, 2012.

[37] P.J. Meadows, E. Dujardin, S.R. Hall, S. Mann. Template-directed synthesis of silica-coated J-aggregate nanotapes, *Chem. Commun.* 3688-3690, 2005.

[38] Y. Harima, S. Furusho, K. Okazaki, Y. Kunugi, K. Yamashita. Charge transport in vacuum-sublimed films of metal-free tetraphenylporphyrin and its relation to capacitance and photocurrent measurements, *Thin Solid Films* **300**: 213-217, 1997.

[39] M.M. El-Nahass, H.M. Zeyada, M.S. Aziz, M.M. Makhlouf. Current transport mechanisms and photovoltaic properties of tetraphenylporphyrin/n-type silicon heterojunction solar cell, *Thin Solid Films* **492**: 290-297, 2005.

[40] G. Pagona, A.S.D. Sandanayaka, Y. Araki, J. Fan, N. Tagmatarchis, G. Charalambidis, A.G. Coutsolelos, B. Boitrel, M. Yudasaka, S. Iijima, O. Ito. Covalent Functionalization of Carbon Nanohorns with Porphyrins: Nanohybrid Formation and Photoinduced Electron and Energy Transfer, *Adv. Funct. Mater.* **17**: 1705-1711, 2007.

[41] J.H. Kim, M. Lee, J.S. Lee, C.B. Park. Self-Assembled Light-Harvesting Peptide Nanotubes for Mimicking Natural Photosynthesis, *Angew. Chemie Int Ed.* **51**: 517-520, 2012.

[42] G. Sedghi, V.M. Garca-Suárez, L.J. Esdaile, H.L. Anderson, C.J. Lambert, S. Martn, D. Bethell, S.J. Higgins, M. Elliott, N. Bennett, J.E. Macdonald, R.J. Nichols. Long-range electron tunnelling in oligo-porphyrin molecular wires, *Nat. Nanotechnol.* **6**: 517-523, 2011.

[43] T. Hasobe, K. Saito, P.V. Kamat, V. Troiani, H. Qiu, N. Solladié, K.S. Kim, J.K. Park, D. Kim, F. D'Souza, S. Fukuzumi. Organic solar cells. Supramolecular composites of porphyrins and fullerenes organized by polypeptide structures as light harvesters, *J. Mater. Chem.* **17**: 4160-4170, 2007.

[44] A.M. Bittner. Biomolecular rods and tubes in nanotechnology, *Naturwissenschaften* **92**: 51-64, 2005.

[45] K. Ladomenou, T. Lazarides, M.K. Panda, G. Charalambidis, D. Daphnomili, A.G. Coutsolelos. Meso-substituted Porphyrin Derivatives via Palladium-Catalyzed Amination Showing Wide Range Visible Absorption: Synthesis and Photophysical Studies, *Inorg. Chem.* **51**: 10548-10556, 2012.

[46] R. Luguya, L. Jaquinod, F.R. Fronczek, M.G.H. Vicente, K.M. Smith. Synthesis and reactions of meso-(*p*-nitrophenyl)porphyrins, *Tetrahedron* **60**: 2757-2763, 2004.

[47] G. Charalambidis, E. Kasotakis, T. Lazarides, A. Mitraki, A.G. Coutselos. Self-Assembly Into Spheres of a Hybrid Diphenylalanine-Porphyrin: Increased Fluorescence Lifetime and Conserved Electronic Properties, *Chem. Eur. J.* **17**: 7213-7219, 2011.

[48] W. Nuansing, A. Rebollo, J.M. Mercero, J. Zuñiga, A.M. Bittner. Vibrational spectroscopy of self-assembling aromatic peptide derivates, *J. Raman Spectrosc.* **43**: 1397-1406, 2012.

[49] C.H. Görbitz. Structures of dipeptides: the head-to-tail story, *Acta Cryst.* **B66**: 84-93, 2010.

[50] I.M.M. Carvalho, M.Y. Ogawa. Self-Organization of Porphyrin-Peptide Units by Metal-Mediated Peptide Assembly, *J. Braz. Chem. Soc.* **21**: 1390-1394, 2010.

[51] V. Gutmann. Empirical parameters for donor and acceptor properties of solvents, *Electrochimica Acta.* **21**: 661-670, 1976.

[52] L. Malavolta, E. Oliveira, E.M. Cilli, C.R. Nakaie. Solvation of polymers as model for solvent effect investigation: proposition of a novel polarity scale, *Tetrahedron* **58**: 4383-4394, 2002.

[53] L. Malavolta, C.R. Nakaie. Peptide dissociation in solution or bound to a polymer: comparative solvent effect, *Tetrahedron* **60**: 9417-9424, 2004.

[54] L. Malavolta, M.R. Pinto, J.H. Cuvero, C.R. Nakaie. Interpretation of the dissolution of insoluble peptide sequences based on the acid-base properties of the solvent, *Protein Sci.* **15**: 1476-1488, 2006.

[55] P.J. Hendra. In Handbook of Vibrational Spectroscopy, (Eds.: J.M. Chalmers, P.R. Griffiths), Wiley, Chichester, **2**: 1263, 2002.

[56] R. Schweitzer-Stenner, G. Sieler, N.G. Mirkin, S. Krimm. Intermolecular Coupling in Liquid and Crystalline States of *trans-N*-Methylacetamide Investigated by Polarized Raman and FT-IR Spectroscopies, *J. Phys. Chem. A* **102**: 118, 1998.

[57] C.H. Wang, J. McHale. Vibrational resonance coupling and the noncoincidence effect of the isotropic and anisotropic Raman spectral components in orientationally anisometric molecular liquids, *J. Chem. Phys.* **72**: 4039, 1980.

[58] P. Mirone. Comment on the influence of the dielectric constant upon the noncoincidence of the isotropic and anisotropiC Raman frequencies, *J. Chem. Phys.* **77**: 2704, 1982.

[59] M.G. Giorgini. Raman noncoincidence effect: A spectroscopic manifestation of the intermolecular vibrational coupling in dipolar molecular liquids, *Pure Appl. Chem.* **76**: 157, 2004.

[60] A. Morresi, M. Paolantoni, P. Sassi, R.S. Cataliotti, G. Paliani. Non-coincidence effect of aromatic ring vibrations, *J. Phys.: Condens. Matter* **12**: 3631, 2000.

[61] J.P.F. Lagerwall. Three facets of modern liquid crystal science (Habilitation thesis), Martin Luther University of Halle-Wittenberg, 2010.

[62] G.H. McKinley. Dimensional Analysis of Free Surface Flows, *Rheol. Bull.* **74**: 6, 2005.

[63] C. Clasen, P.M. Phillips, L. Palangetic, J. Vermant. Dispensing of Rheologically Complex Fluids: The Map of Misery, *AIChE J.* **58**: 3242, 2012.

[64] A. Rothert, R. Richter, I. Rehberg. Formation of a drop: viscosity dependence of three flow regimes, *New J. Phys.* **5**: 59.1-59.13, 2003.

[65] G. German, V. Bertola. Formation of viscoplastic drops by capillary breakup, *Phys. Fluids* **22**: 033101, 2010.

[66] C. Clanet, J.C. Lasheras. Transition from dripping to jetting, *J. Fluid Mech.* **383**: 307, 1999.

[67] D.T. Papageorgiou. On the breakup of viscous liquid threads, *Phys. Fluids* **7**: 1529, 1995.

Chapter 5

Electrospinning of Proteins and DNA

Small peptides can assemble or be electrospun into defined supramolecular structures such as fibers and tubes. The preceding sections showed that not only self-assembled, but also electrospun fibers can be interpreted based on the structure of the subunits; in this case, small peptides. This chapter moves onto much larger (bio)molecules, proteins and DNA. Proteins can be addressed as polypeptides, and DNA as polynucleic acid, so that the analogy to standard electrospinning of polymers is obvious. Electrospinning of pure proteins (and of DNA) is very poorly documented; thus, this chapter opens up a new field of research.

This Chapter will demonstrate that not only peptides but also globular proteins (which show little or no tendency for self-assembly) can be spun into practically endless fibers, in the absence of (artificial) polymers. In other words, the fibers are not blends, but made of pure biomolecules. Sections 1−4 cover electrospinnability into fibers of pure globular proteins, i.e. hemoglobin, albumin, casein, lysozyme, insulin, and hydrophobins will be reported. Section 2 specifically addresses

albumin fibers that can be shaped into extremely thin structures close to the ultimate limit of fibers, which is the diameter of a single molecule. Insulin is known to form β-amyloid fibrils upon denaturation in acids. These fibrils were studied and compared to insulin electrospun fibers (section 3) by using the amide I band from nanoscale and from global infrared spectra. Section 4 covers conventional electrospinning used for electrospinning of pure hydrophobins onto various substrates. The last section covers double-stranded DNA tested for electrospinning, and the relevant results are presented.

> **OBJECTIVE 2:** Studying the possibility of electrospinning fibers from biomolecules; 2(c) polypeptide chains such as globular proteins and also double-stranded DNA.

5.1 Electrospinning of globular proteins

Up to now, electrospinning of pure globular proteins have only reported for hemoglobin [1] and albumin [2]. It is no surprise that fiber-forming proteins (see Chapter 2.2.1), e.g. collagen, fibrinogen can be electrospun [3–5]. This thesis investigated the possibility of electrospinning other globular proteins. First, hemoglobin and albumin were reproduced, and new experiments are designed in order to obtain a fiber with smaller of diameter. Moreover, effects from solvent, solution concentration and applied voltage were also studied.

Many proteins are able to assemble naturally into thin fibers or tubes, the best known of which is polypeptides collagen [6] ("polypeptide" since it contains only three different amino acids). This normally requires an anisotropic and quite complex molecular structure, especially when the fiber diameter should be well defined and homogeneous. Given the complexity of proteins, there are many ways to form fibers, e.g. unfolding of a polypeptide chain, α-helices packing, the best known form probably being β-sheets, which are crucial for amyloid fibril formation [7]. Here, the protein structure is a simplified scheme based only on α-helices, β-sheets, turns, and unordered areas (see Chapter 2.2.1).

Since proteins are normally monomeric or oligomeric, diluted solutions do not exhibit strong viscoelasticity, and the requirements of high viscosity and high relaxation time can only be reached at high concentrations. This in turn asks for a careful selection of solvents, in relation to the discussion above (for peptides). A good solvent is even more important because most proteins are only available in very small amounts. In this section, four globular proteins were selected and investigated:

- **Hemoglobin** is the major component of red blood cells, and the most important respiratory globular protein of vertebrates by virtue of its ability to transport oxygen from the lungs to body tissues, and to facilitate the return transport of carbon dioxide. Hemoglobin is a tetramer composed of 2 pairs of polypeptide chains called "globins" (the first pair is α-chains, each with 141 amino acids, and the second pair is β-chains, each with 146 amino acids), and 4 heme groups. Each polypeptide chain is bound to one heme. Human hemoglobin was used in this work, its molecular weight being ~64.5 kDa (574 amino acids).
- **Albumin** consists of soluble proteins with multiple functions such as maintaining colloid osmotic pressure, ligand binding, and transporting [8]. The size of albumin is unusually large (>300 amino acids), and the shape can depend on the environment, for example on the pH. Albumins are abundant, e.g. in blood (serum albumins) and in eggwhite (ovalbumin, which is used here). Its molecular weight is ~44.3 kDa (385 amino acids).
- **Casein** is a protein that gives milk both its white color and unique "mouth feel" as well as being a carrier of calcium [9]. Whole casein is predominantly made up of four subunits that range from 19 to 25 kDa. In the presence of calcium (milk), casein forms micelles in the range of 50−500 nm, whereas in the absence of calcium the micelles disassemble into smaller assemblies, often called submicelles. Casein subunits are amphiphilic, and it has been suggested that casein acts as a stabilizer of protein structure, or even as a chaperone in promoting proper protein folding. Casein from bovine milk was used in this work, its molecular weight being ~24 kDa (~209 amino acids) [9]. One reason for selecting this protein is that casein can be produced from milk even from leftovers in large amounts, hence this fiber might be used for textile (for example, see products offered by the Qmilch company, en.qmilk.eu) and food fiber applications. Furthermore, pure casein has not yet been electrospun. It must be blended with PEO to archive fiber [10].
- **Lysozyme** is a compact protein, which folds into a compact globular structure. In addition, it is an enzyme found in tears, nasal secretions, and the white of avian eggs, which hydrolyzes the polysaccharides found in many bacterial cell walls. As such, it evokes a mild antibacterial action. Indeed, it was one of the first antibiotics studied by Sir Fleming who discovered penicillin. Hen egg white lysozyme has been studied in great detail. In this work, a recombinant human lysozyme ("lysobac") was used, its molecular weight being ~14 kDa (~129 amino acids). The lysobac has significantly higher bioactivity than hen egg white lysozyme) and is produced in an animal-free production system. Electrospinning of pure lysozyme has not been reported, there are only encapsulated with copolymers such as poly(ethylene glycol)-poly(DL-lactide) [11], or Poly(lactide-co-glycolic acid) [12]. The pure lysozyme electrospun fibers might be used for antimicrobial applications.

5.1.1 Experimental

Hemoglobin, albumin, casein and lysozyme were purchased from Sigma-Aldrich and used without any further purification. They were dissolved in hexafluoroisopropanol (HFIP, 99.0% Fluka), trifluoroacetic acid (TFA, 99%, Sigma-Aldrich), which are suggested in Chapter 4.[1] Then, the solution was tested with the microliter electrospinning setup (see section 3.2.2.2). To determine electrospinnability of each substance, solutions were prepared at various concentration (1−15 %(wt/wt)), the maximum value of which depends on solubility of each protein and solvent. For electrospinning process, distance between the tip and the collector was fixed at 12 cm, while the voltage was applied at 6−20 kV to optimize the process.

5.1.2 Results and discussion

Effect of solvent: All selected proteins can be dissolved in HFIP and TFA (including TFE for hemoglobin), the concentrated solutions can be formed fibers, when electrospinning at optimized parameters. Optical images shown in Fig. 5.1 summarizes that the morphology of pure protein fibers depends on the solvent. Note here that the optical images exhibit both dark and bright areas on the protein fibers deposited on a clean glass slide. The bright areas result from imaging artifacts in optical microscopy, where the fibers lie on each other. The dark areas can be observed where the fibers well in contacted on glass substrate.

HFIP solutions (see Fig. 5.1a, c, e, g) affect in slightly irregular fibers, i.e. straight segments are followed by curves of small radii (tens of micrometers), and the diameter can reach several micrometers (0.6−1 μm for hemoglobin, 0.6−2.5 μm for albumin, 2−3.5 μm for casein, and 0.5−1 μm for lysozyme). Continuous fibers were observed, except from lysozyme/HFIP 7 %(wt/wt) solution, most of the fibers are shorter than 100 μm. TFA solutions (see Fig. 5.1d, f, h) result in much better defined diameters of 200−800 nm (200−400 nm for albumin, 600−800 nm for casein, and 400−800 nm for lysozyme), in curves of large radii (hundreds of micrometers), and are continuous. This difference should be due to differences in solvent-protein interactions. Pure TFA protonates proteins to a large extent, and one would expect increased denaturation. Note here that the denaturing means the protein loss of structure, resulting in loss of function, e.g. denaturation of protein at high temperature or at low pH. One could explain the protein loss of structure by the unfolding of protein, which suggest that the secondary structure should be changed. The secondary structure of protein will be studied and presented in the next sections (using IR, Raman and CD spectroscopy). In case of hemoglobin, TFE solution (see Fig. 5.1b) results in more irregular fibers and a bigger diameter (1−3 μm) compared to HFIP solution. This means HFIP can denature hemoglobin better than TFE at the same concentration 5 %(wt/wt). Notice that TFA can dissolve hemoglobin at 5 %(wt/wt) but the viscosity is too high, hence it cannot be electrospun. Its worth mentioning here water can dissolve proteins, however, due to insufficient evaporation causes the solution cannot be electrospun.

[1] Notice that hemoglobin/TFA 5 %(wt/wt) solution has high viscosity (solid-like gel), and therefore cannot be spun and formed into fiber. Hence, trifluoroethanol (TFE) was tested at the same concentration 5 %(wt/wt).

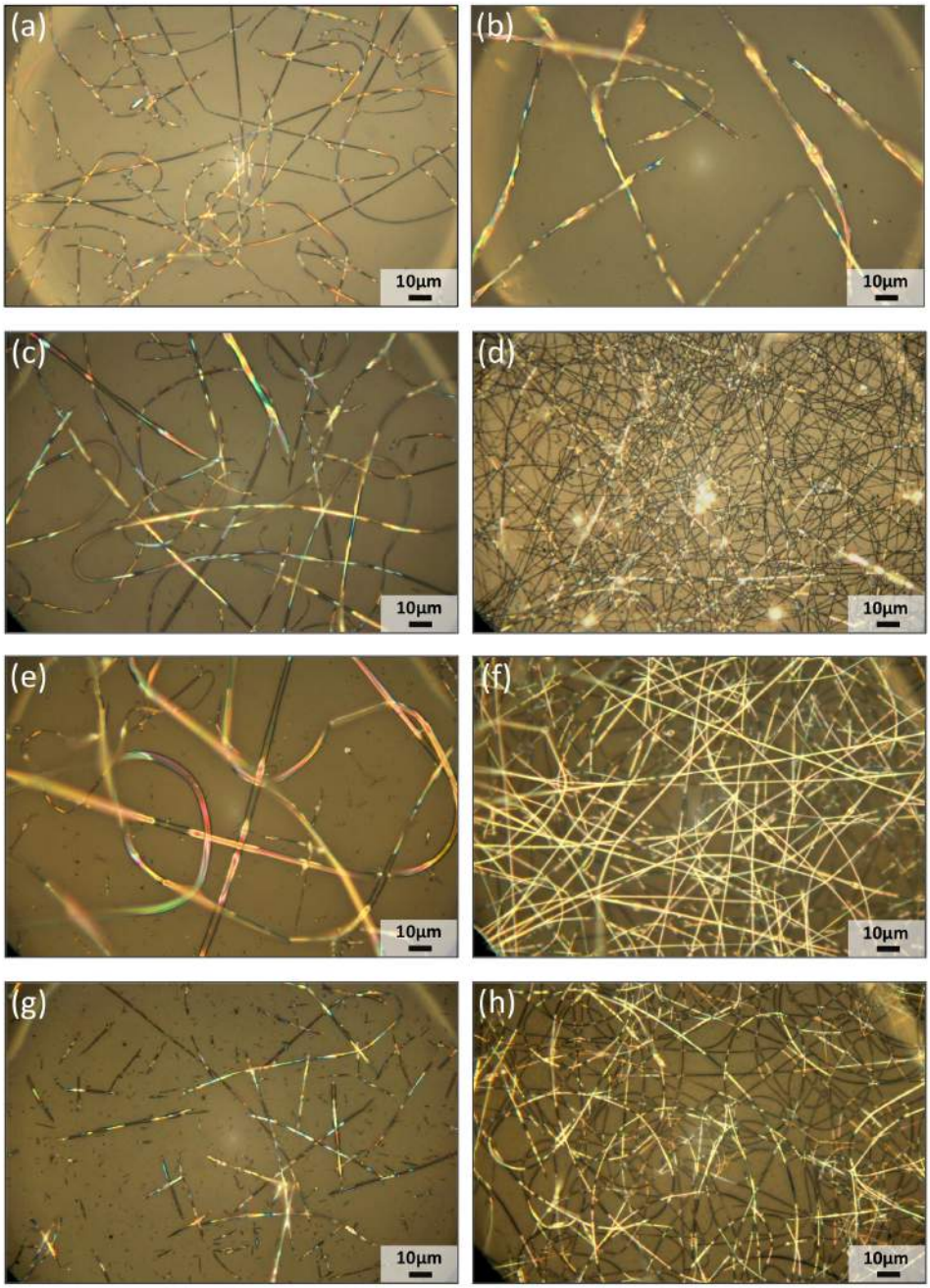

Figure 5.1: Optical micrographs of (a) hemoglobin/HFIP 5 %(wt/wt), (b) hemoglobin/TFE 5 %(wt/wt), (c) albumin/HFIP 7 %(wt/wt), (d) albumin/TFA 7 %(wt/wt), (e) casein/HFIP 5 %(wt/wt), (f) casein/TFA 7 %(wt/wt), (g) lysozyme/HFIP 7 %(wt/wt), and (h) lysozyme/TFA 15 %(wt/wt). All used microliter setup, electrospun at 12 cm, 10 kV, except (e), (g), and (h) at 15 kV.

Effect of concentration: Similar to peptide in the previous chapter, pure protein solution can form fibers when the concentration and electrospinning parameters are optimized. Figure 5.2a, b compares electrospinning results of casein/TFA 5 %(wt/wt) and 7 %(wt/wt) at the same electrospinning conditions (applied voltage is 15 kV, and distance to the substrate is 12 cm). At 5 %(wt/wt), droplets with diameter of 0.5−3 μm and few fibers with diameter of 200−500 nm were observed. When the concentration is increased to 7 %(wt/wt), the result is much better, obtains continuous and uniform fibers. However, droplets smaller than 500 nm of diameter were observed on substrate, they might be droplets from electrospraying or some residues in protein that cannot form fiber. In case of the lysozyme/TFA solution (see Fig. 5.2c, d), the minimum concentration to obtain fiber is higher compared to the casein. For lysozyme/TFA 10 %(wt/wt), only droplets with diameter of 0.5−3 μm were observed. Long fibers can be found at concentrations of 12 %(wt/wt) and 15 %(wt/wt) (Fig. 5.1h).

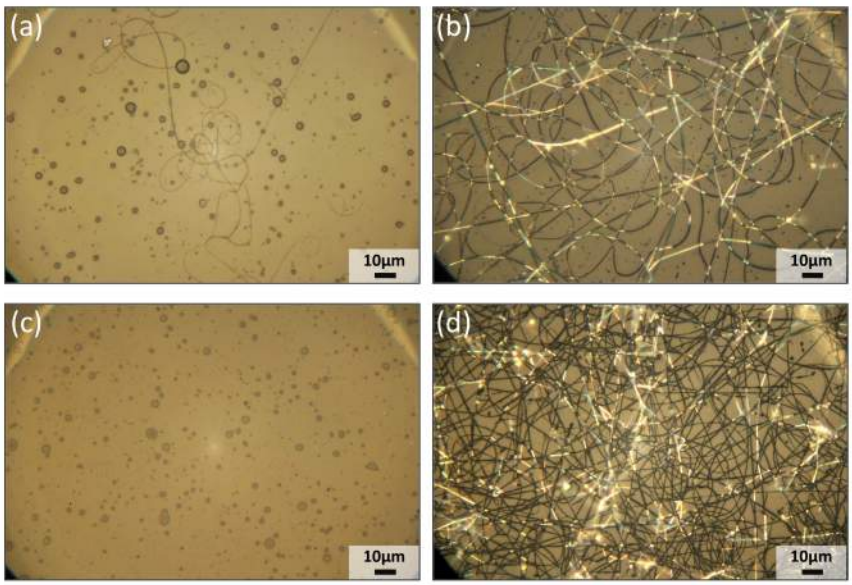

Figure 5.2: Optical micrographs of casein fibers from solution (a) 5 %(wt/wt), (b) 7 %(wt/wt), lysozyme fibers from solution (c) 10 %(wt/wt), and (d) 12 %(wt/wt), all dissolved in TFA and electrospun at 15 kV, 12 cm, microliter setup.

Now, there are two notable ideas concerning the effect of concentration. First, the molecular weight of lysozyme[2] (~14 kDa) is lower than casein (~24 kDa), so the lysozyme solution must be prepared at a higher concentration in order to achieve a sufficient entanglement. However, this is not true for the albumin, the molecular weight of albumin is ~44.3 kDa, it is higher than the casein (~24 kDa), but the albumin solution can be electrospun into continuous fibers at the same concentration (at 7 %(wt/wt) in TFA). This proposes that the flexibility of protein molecules might effect to this parameter. The casein structure could be more flexible than the albumin, hence, even though its molecular weight is lower, but it can electrospin into long fibers at the same concentration.

[2]Lysozyme and insulin are very small; insulin is often called “peptide”.

Table 5.1: The estimated *Oh* of the proteins solutions.

Solution	**Viscosity** (mPa.s)	**Density** (kg/m^3)	**Surface tension** (mN/m)	*Oh*	**Electrospinnability**
Water	0.89	1.00	71.99	0.3	Droplets
Fmoc-G/DMF 17 %wt	5.2	1.11	37.76	2.5	Droplets
Lysozyme/HFIP 7 %wt	10	1.71	16.40	6.0	Short fibers
Hemoglobin/HFIP 5 %wt	20	1.68	16.40	12	Long fibers
Albumin/HFIP 5 %wt	46	1.68	16.40	28	Long fibers
Casein/HFIP 5 %wt	200	1.68	16.40	121	Long fibers
PAN/DMF 4 %wt	52	0.99	37.76	27	Long fibers

The second notable idea is related to the viscosity of the solution. As discussed in the theoretical background Chapter 2.1 that electrospinning requires a fluid with $Oh \geq 1$. To estimate the *Oh*, viscosity of the protein solutions was measured by a rheometer (DHR, TA Instrument) at temperature of 25 °C. The viscosity values are listed in Table 5.1, where they are compared to water, peptide and polymer solutions. The *Oh* of each solution is estimated by Eq. 2.9, assumes that the jet diameter $d \approx 100$ μm, the solution density $\rho \approx \rho_{solvent} \cdot [1 + (\%wt/100)]$, and the surface tension of the solution γ is the same as the solvent. The results show that the *Oh* of a solution should be above ≈ 10 to obtain a long fiber via electrospinning. If the *Oh* is < 10, the solution jet tends to break up, resulting droplets or short fibers are observed. The Table 5.1 also indicates that the *Oh* increases with increased the viscosity. To increase the *Oh*, the surface tension of solution should be low. The water and the peptide solution (Fmoc-G/DMF 17 %wt) have low viscosity and high surface tension, hence, they cannot be electrospun into long fiber. For the lysozyme/HFIP 7 %wt, its *Oh* is close to 10, so this solution forms short fibers. To improve the electrospinnability, the lysozyme should be dissolved in HFIP at a higher concentration in order to increase the viscosity and raise the *Oh* to above ≈ 10.

Effect of applied voltage: Figure 5.3 exhibits fibers from hemoglobin/HFIP 5 %(wt/wt) solution, electrospun at 6, 10, 15, and 20 kV, distance to substrate was fixed at 12 cm. All conditions obtain slightly irregular fibers with diameter 400−800 nm. The longest fibers (>100 μm) were found at the applied voltage of 10 kV, which is an optimized value. When the applied voltage is increased to 15 kV, the fiber length is not longer than 100 μm. In addition, most of the fibers are shorter than 100 μm at 20 kV. This can be interpreted as the electrostatic force being too hight, and thus, the solution jet is broken. However, the fiber diameter was not significantly different when the solution was electrospun at various applied voltages of 10, 15, and 20 kV. This is unlike the electrospinning of the polymer, for which the diameter typically reduces with increasing applied voltage. When the applied voltage is higher, the solution jet is able to accelerate faster and more instability, yields greater stretching into a smaller fiber. In the case where the applied voltage was 6 kV, only a few short fibers (<100 μm) were observed on the substrate because the electric force wasn't not high enough to stretch the solution and form long fiber.

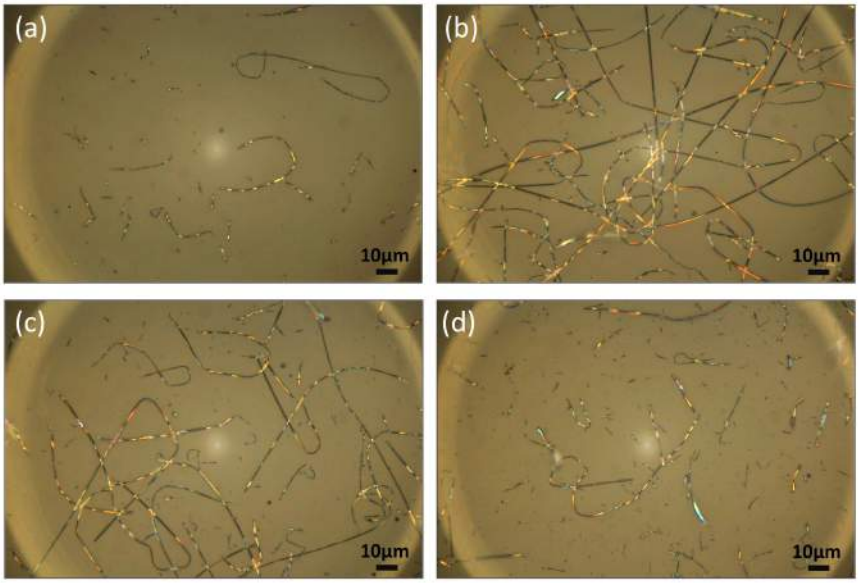

Figure 5.3: Optical micrographs of hemoglobin fibers obtained from 5 %(wt/wt) solution in HFIP, electrospun at 12 cm, microliter setup, (a) 6 kV, (b) 10 kV, (c) 15 kV, and (d) 20 kV.

5.1.3 Conclusions

Electrospinning of pure globular protein is possible; continuous fibers can be spun using microliter setup, which necessitates only small amounts of solution. The protein must be dissolved in a suitable solvent. Fluorinated solvents of high vapor pressure are also known to be suitable for peptides, namely TFA and HFIP as concluded in Chapter 4 HFIP and TFA. They are also very suitable solvents for globular proteins. However, the solution should be prepared at high concentrations around 5 %(wt/wt) up to 15 %(wt/wt), depending on molecular weight and type of proteins in order to obtain a high viscosity of the solution. In addition, the applied voltage has to optimized for other parameters, i.e. distance between the tip and the collector.

A key difference between a globular protein and a polymer in electrospinning is that fiber diameter does not reduce with increasing applied voltage. To obtain a small fiber diameter, another technique must be used, e.g. reducing concentration (as found example in Fig. 5.2a), increasing distance between the tip and the collector (which will be reported in the next section). Pure protein electrospun fibers without polymer blends can be a new candidate for biomaterial application. For example, casein (from milk) fiber is good for textile application, lysozyme fiber might provide a good antimicrobial property.

OBJECTIVE 4: Reducing the diameter of biomolecule fibers close to the size of a single molecule.

5.2 Electrospinning of albumin into ultrasmall fibers

Electrospinning can enhance or even induce assembly of materials that do not naturally assemble to fibers. The previous section demonstrated that globular proteins show little or no tendency for self-assembly, but can be electrospun to practically endless fibers in the absence of polymers. As mentioned in the previous section, the proteins might be partially denatured in the solvent. In this section, microscopy and spectroscopy techniques were used for studying the secondary structure of albumin samples. Moreover, reducing the diameter of albumin fiber into extremely thin structures was investigated. The biomolecule fibers with ultrasmall diameters present a possible opportunity to understand or study properties of a single molecule rather than bulk molecules, which interact with each other.

5.2.1 Experimental

Albumin from chicken egg white (ovalbumin, it was purchased from Sigma-Aldrich) was dissolved in hexafluoroisopropanol (HFIP, 99.0% Fluka) and trifluoroacetic acid (TFA, 99%, Sigma-Aldrich), by ultrasonication and shaking in order to achieve homogenous solutions. Then, the solution was tested with the microliter electrospinning setup. To assess ultrasmall fiber formation from μg or mg amounts of proteins or peptides, advanced microliter electrospinning setup was used (see detail in section 3.2.2.3) based on increasing distance between the tip and the substrate (mentioned in the previous section). Briefly, a platinum wire of 0.25 mm diameter as a tip was placed vertically 30−80 cm above the collector (standard value is around 10−30 cm). The voltage was applied to the wire, onto which only ~2 μl solution was directly dropped from a micropipette. The droplet attached to the wire was stretched, causing the formation of a fiber. Additionally, in some cases, an air stream from a hot air generator (HLG 2000, Würth master) was employed, from above the tip, pointing downwards (see detail in section 3.2.2.4).

5.2.2 Results and discussion

Microscopy: Electrospinning of albumin from HFIP and TFA solution provide continuous fibers, which are imaged by optical microscopy shown in Fig. 5.1c, d. For both solvents, a small fraction of the fibers has diameters below 100 nm, which requires SEM or AFM for visualization (Fig. 5.4). Specifically for the albumin/TFA solution, the fraction of ultrasmall diameter can be expanded to larger area. Note here that in order to avoid any artifacts, the fibers did not stain or use metal sputtering. Not surprisingly, the longer tip to substrate distances resulted in thinner fibers.

Since the solvents certainly have evaporated (especially at the SEM vacuum conditions), this effect should be due to the fiber elongation in the whipping jet. Figure 5.4c shows an AFM image of two adjacent stretches of an ultrathin fiber, with heights down to 5 nm (the width of >20 nm rather reflects the diameter of the AFM tip, while the height data is reliable). Such thin segments are only known from branched fibers. Indeed, the smallest diameters can be observed close to branches. Note that the SEM can destroy the ultrasmall fibers, hence the AFM was used.

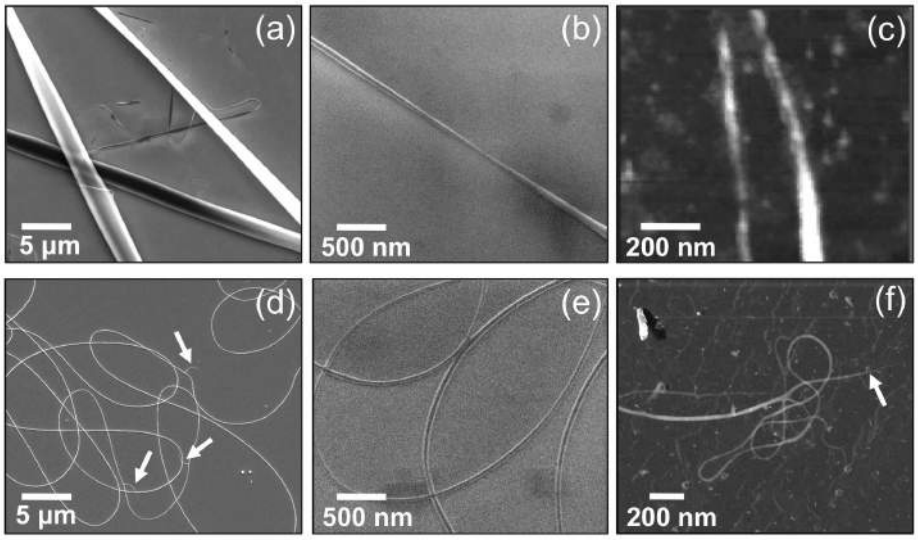

Figure 5.4: Micrographs of albumin. A ribbon-like morphology was observed by SEM for fibers from a 7 %(wt/wt) solution in HFIP, electrospun in the microliter setup at (a) 15 kV (12 cm), and at (b) 6 kV (20 cm). (c) AFM image showing albumin fibers of 5 nm and 11 nm height. (d-e) Albumin fibers with diameters below 100 nm can be observed with SEM (albumin was dissolved in TFA and electrospun at 25 kV, at distances of 60 and 40 cm, respectively), arrows indicate thorn-like protrusions in Fig. 5.4d. (f) STEM image; the diameter is reduced to <20 nm; in some areas the fiber is broken (white arrow). The fiber was produced at 20 kV and 75 cm with application of an air stream.

Branching is a rare phenomenon in electrospinning [13–15] and might be associated with higher-charged densities on the fiber. To obtain the branched fiber, high voltages are required, but in addition it is possible to induce branching in a controlled way by blowing air from the top, along the jet (see the setup in section 3.2.2.4). One would expect a deformation of the fiber in the whipping jet, in the direction of the jet (i.e. towards the collector). However, this should produce loops and similar structures, while thorn-like protrusions were found when using TFA (Fig. 5.4d, see arrows). Another mechanism can be based on increased evaporation of the solvent. If this effect is very localized, branching might be induced at this point. The most fascinating aspect of the thorn-like structures is that the branch diameters decrease already over lengths <1 μm to extremely small values (<20 nm). As mentioned, they occur regularly, and can be detected easily (also with an optical microscope). The thorns can be covered by more fiber material deposited on top, and thus apparently connect two big fibers, or it can break (Fig. 5.4f). In either case fibers of <20 nm in diameter were observed.

Raman and IR spectroscopy: To improve the characterization results, spectroscopic methods were employed. Figure 5.5 presents an overview, and illustrates the analogy to the peptide case. The Raman spectrum shows features expected for proteins: The bands are much broader than those of a simple peptide, and rather hard to interpret. Most intensity is in the hydrogen stretching vibrations above 2700 cm^{-1}, while the presence of the amide I band (around 1650 cm^{-1}) and its large width proves the protein nature. The value of Raman spectroscopy is that it can be easily obtained from a microscale region that contains only a few fibers. Between such regions, but also in comparison to the albumin powder, no significant spectral differences (Fig. 5.5f, g) were indentified. Infrared spectra are probably more useful as will be shown. First, by comparison with the pure solvent TFA (Fig. 5.5a), the C-F stretching region is established around 1200 cm^{-1} as a quantitative probe for the presence of the solvent (also the carbonyl peak at 1780 cm^{-1} is useful). All IR spectra of the fibers (Fig. 5.5c, d, e) show the presence of the solvent, even in dried fibers, but not in the pure albumin (Fig. 5.5b). This is expected since the strong acid TFA protonates albumin, and the anion should remain in the solid as counterion.

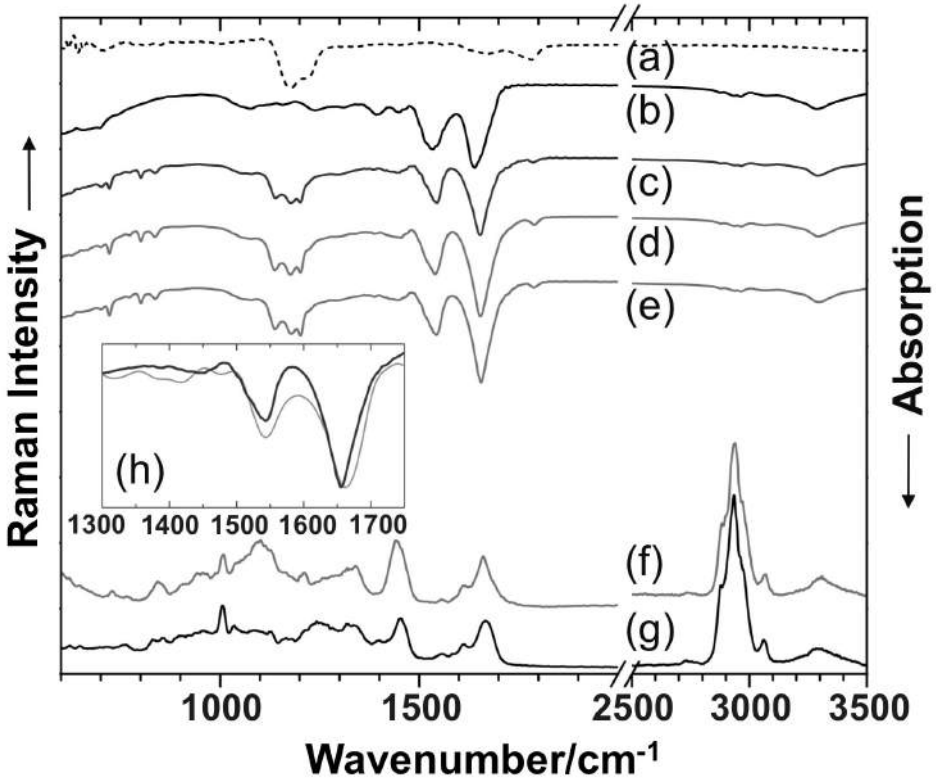

Figure 5.5: Vibrational spectroscopic analysis of albumin samples. IR spectrum of (a) TFA solvent, (b) albumin powder, (c) 7 %(wt/wt) albumin in TFA, dried on glass, (d) electrospun fibers from 7 %(wt/wt) albumin in TFA, stored for 3 h, (e) similar, but stored for 3 d. Raman spectrum of (f) electrospun fibers and (g) powder. Inset (h): Comparison of the amide I band region of albumin fibers recorded by IR (black line as in trace (d)), and local spectrum from a ca. 10 nm wide spot recorded by scanning near field IR microscopy (grey line).

Most useful, however, are the amide I and amide II regions (around 1650 and 1550 cm^{-1}, for ovalbumin [16], where even fine details in the IR spectra can be interpreted safely. For albumin fibers, the amide I band gains intensity (compared to amide II), and both bands exhibit a blueshift. This is exactly the same for a dried solution (spots) and an electrospun solution (fibers). From this result it can conclude that the albumin structure is different from the original protein, that the solvent is incorporated, and that the protein in the fibers is in the same state as post-contact with solvent (without electrospinning).

All of the IR data feature rather broad amide bands, as often seen for proteins. The reason is the presence of many amide groups in very similar environments. The exact location of the amide I band will depend very much on denaturation, as in the case of amyloid-like self-assembly of ovalbumin [17]. In TFA the pH is lower than considered elsewhere [17, 18] and hence not only the peak shifts, but also the peak shape changes, compared to ovalbumin powder. Fitting procedures (described in Chapter 3) allow to assign relative amounts of secondary structure elements: Ovalbumin powder, despite a rather low-frequency peak at 1640 cm^{-1}, shows a balanced mixture of 25% α-helices, 30% β-sheets, 25% turns, and 20% unordered areas (Fig. 5.6a), in accordance with the crystal structure [19].

The fiber amide I band (from HFIP solution) has its maximum at 1655 cm^{-1}. The fit yields 50% α-helices, 15% β-sheets, and 35% turns (Fig. 5.6b), so the original structure changed significantly towards a high α-helices content. This also means the fiber cannot simply address as "albumin" any longer. Fibers electrospun from TFA also show a maximum at 1655 cm^{-1}, but the band is highly asymmetric. The fit yields 25% α-helices, 45% β-sheets, and 30% turns (Fig. 5.6c), so it appears more ordered, and with an increased fraction of β-sheets [17]. In view of the expected denaturation in TFA, this result is rather surprising. Obviously the spun fiber has a structure that is not very different from the original substance, and certainly it is not completely unfolded.

IR nanospectroscopy: The observed spectral changes (from albumin to electrospun albumin) can be interpreted as a global effect in a homogeneous sample, as normally expected [1–4, 17, 20]. However, local spectra occasionally find differences in apparently homogeneous samples, e.g. with tip-enhanced Raman spectroscopy [21]. To measure local infrared spectra of a fiber, Fourier transform IR nanospectroscopy (nano-FTIR) [22, 23] was operated, based on a scattering-type scanning near-field optical microscope (s-SNOM, [24,25] Neaspec GmbH, DE). A noncontact atomic force microscope (AFM) tip is illuminated by a coherent-continuum IR source. The light scattered by the tip is detected by an asymmetric Fourier Transform (FT) spectrometer, yielding the imaginary part of the scattered field that corresponds in good approximation to the local IR absorption. The same setup was used to obtain AFM images of fibers. The IR spectrum in Fig. 5.5h (grey trace) was obtained on top of a single 100 nm thick fiber. It exhibits strong similarity to the global IR spectrum (black trace) for both the amide I and the amide II bands, thus confirming thin fibers for the protein structure derived from the global spectra.

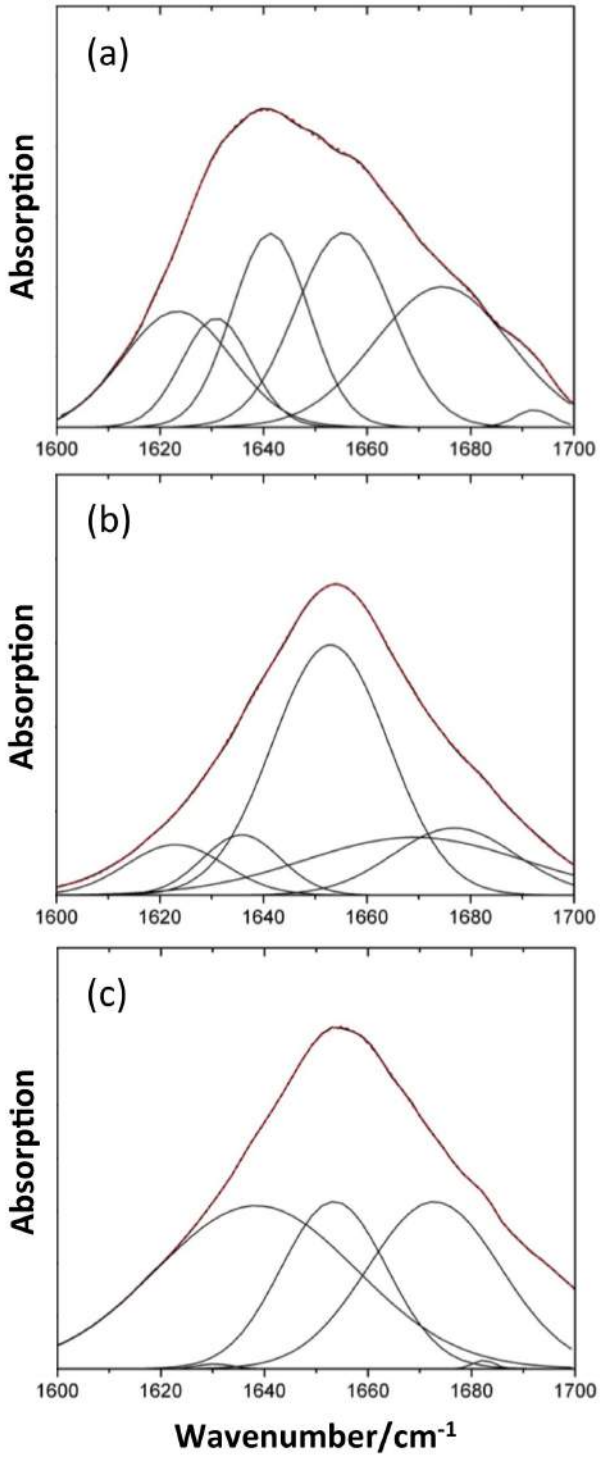

Figure 5.6: Curve fitting of amide I band, IR (ATR) of (a) albumin powder, (b) albumin fibers electrospun from HFIP solution, and (c) albumin fibers electrospun from TFA solution.

CD spectroscopy: After elucidating salient features of the fiber structure, the question is how the structure forms. Hints about the very loosely defined term "spinnability" (see the section on peptides in Chapter 4), and about the structure in solution, can be found with CD spectroscopy (Fig. 5.7). Ovalbumin in water (black trace) [19, 26] can be fit [27] to a structure with ~45% α-helices and ~10% β-sheets (the remaining 45% cannot easily be separated into turns and unordered areas); the literature spectrum (dashed trace) yields ~35% α-helices and ~15% β-sheets. In contrast to the IR spectrum (see above), the CD results are not well compatible with the ovalbumin crystal structure, probably due to minor conformational changes in solution [19]. The result is quite similar for the HFIP solution (grey trace) with ~50% α-helices and ~10% β-sheets, hence HFIP induces no or minor denaturation. It is likely that the flexibility increases, which would explain the good results for electrospinning, in analogy to polymers.

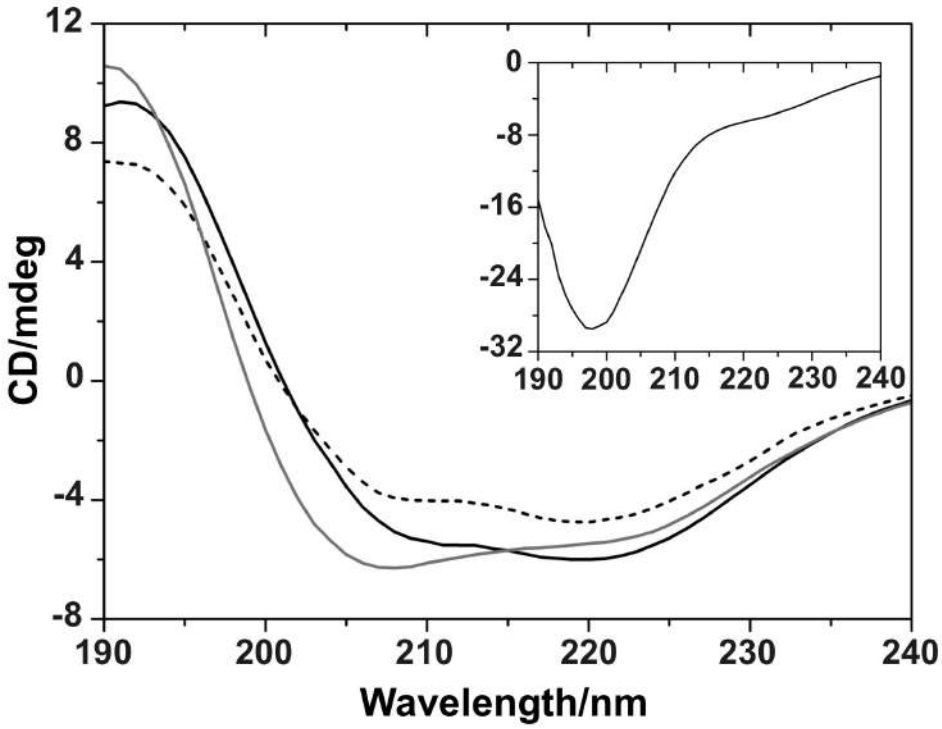

Figure 5.7: CD spectra of albumin samples (diluted 1:1000 in water): Black trace, after dissolution in water (7 %(wt/wt)); dashed trace, literature data [26]; grey trace, after dissolution in HFIP (3 %(wt/wt)). Inset: After dissolution in TFA (7 %(wt/wt)).

After being dissolved in TFA (Fig. 5.7 inset), at much lower pH values, the structural changes are so large (and obviously irreversible) that fits to existing structures are impossible (fits rely on data bases of structured proteins with rather large contents of helices and sheets - in case of unordered and random structures, very few crystal structures exist, and the flexible nature of such proteins means that the crystal structure might not even be optimal for fits). The purely negative CD values, with a minimum close to 195 nm, indicate a predominantly unordered structure. TFA thus induces a nearly complete opening of the structure, without β-sheets, and with few α-helices

remaining, which are here addressed already as denaturation. The reason is the combination of protonation of many residues, together with the excellent solvation of most amino acids and peptides. This structure is compatible with that of very flexible polymers, which explains the good results for electrospinning, especially for ultrathin fibers. The fact that the spun (dry) fiber does not exhibit similar denaturation (see the IR spectra) could mean that the protein partially refolds after electrospinning. Such behavior would also explain the observed brown color of electrospun hemoglobin [1], which is tightly linked to the functionality (oxygen binding).

5.2.3 Conclusions

The results show that electrospinning of pure albumin is not only possible, but that fibers can be obtained with homogenous widths in the 100 nm range, and that their chemical behavior is homogeneous. Stretches of albumin fibers were produced, with thicknesses down to the ultimate limit of single molecule widths (<10 nm), which can be reproducibly obtained in thorn-like branches. This requires a special spinning/air flow setup, and albumin denaturation in trifluoroacetic acid (TFA), which is also very useful as electrospinning solvent. In addition, various global and local analysis methods are combined in order to address the denaturation, and also the more subtle changes of the protein structure observed in HFIP. Albumin fibers from TFA solution exhibit an increase in β-sheets, and a decrease in unordered areas, compared to albumin powder.

5.3 Electrospinning of insulin

Insulin is a very small protein (is often called peptide). Its quaternary structure consists of 2 chains polypeptide, joined by two interchain disulfide bonds (see details in Chapter 2.2.1 and Fig. 2.8). Insulin is one of the most important hormones in the human body produced by the β-cells of pancreatic islets and used for decreasing blood sugar. Type 1 diabetes is caused by insufficient or non-existent production of insulin; people need synthetic insulin by injection into the blood stream. Repeated insulin injection seems to cause amyloid fibrils formation, and moreover, do not depend on site of injection. Self-assembled insulin fibrils can be found at or around the site of repeated injections, e.g. in the shoulders, arms, or abdominal walls of patients [28]. Since insulin can form amyloid-like fibrils, it is a widely used model system for neurodegenerative disease research, e.g. Alzheimer's disease, Parkinson's disease [29–32]. Electrospinning of pure insulin has not yet been reported; only insulin encapsulated in polymer has been demonstrated [33]. Insulin was incorporated into polyvinyl alcohol (PVA), and then was coaxially electrospun with polycaprolactone (PCL) as a sheath, developing for tissue engineering and clinical delivery applications. Thus, this thesis tested electrospinnability of pure insulin. Furthermore, secondary structure of electrospun insulin fibers was characterized and compared to insulin fibrils.

5.3.1 Experimental

Insulin fibers (electrospinning): Human insulin powder was purchased from Sigma-Aldrich and used without any further purification, molecular weight is ~5.8 kDa. They were dissolved in hexafluoroisopropanol (HFIP, 99.0% Fluka) and trifluoroacetic acid (TFA, 99%, Sigma-Aldrich), by ultrasonication and shaking in order to achieve homogenous solutions. Then, the solution was tested with the microliter electrospinning setup (see section 3.2.2.2 and 3.2.2.3). For microscopy, insulin fibers were electrospun on a clean silicon wafer. For ATR-FTIR measurements, insulin fibers were electrospun on an aluminum disk diameter of 3 mm, which is fit to the sensor surface of the ATR-FTIR. Fibers cover the whole top surface of the substrate.

Insulin fibrils (protein aggregates): Insulin solution was prepared solubilizing 20 mg dehydrated human insulin (Sigma-Aldrich) in 1 ml of 1 mM HCl solution. The solution was then re-diluted in 10 mM HCl/KCl at 2 mg/ml, and incubated at 60 °C for 24 h in a thermomixer (Eppendorf), followed by 2 years storage at 4 °C (less is sufficient). Then 20 μl of insulin aggregate solution was deposited on a silicon wafer using spin-coating method, the sample was dried and rinsed with water. For ATR-FTIR measurements, an aluminum disk diameter of 3 mm was used.

5.3.2 Results and discussion

Insulin solution can be prepared in TFA at 7 %(wt/wt), in HFIP at 5 and 10 %(wt/wt). However, Insulin/HFIP 5 %(wt/wt) and insulin/TFA 7 %(wt/wt) solution cannot form long fiber because their viscosity are too low, their *Oh* should be lower than 10. Note that the solutions cannot be measured their viscosity because the substance is available in small amounts. The solutions are not enough for the rheometer. Droplets and fibers shorter than 10 μm were observed. Only the insulin/HFIP 10 %(wt/wt) can be electrospun and formed fibers longer than 100 μm. Figure 5.8a shows insulin fibers on an aluminum disk, electrospun at 12 cm, applied voltage 8 kV. The fibers completely cover the substrate, diameter of fibers are 0.4−1 μm. SEM micrograph (see Fig. 5.8b) of the fibers on the silicon wafer provides clearly morphology, ribbon-like fibers with diameter 300-750 nm, smallest diameter of ~100 nm observed at the end of fiber (white arrow). In addition, some fraction of the fibers has a small diameter below 200 nm (Fig. 5.8c, the fiber has diameter of 160 nm).

To study denaturation by HFIP as found in the case of albumin (previous section), IR spectroscopy was employed. Figure 5.9 shows IR spectra of insulin powder, fibrils and fibers in region of amide I band (1600−1700 cm^{-1}) and amide II band (1500−1580 cm^{-1}). At the amide II band region, all samples have peaks around 1520 and 1540 cm^{-1}, which are combination of the vibration modes from CN stretching, NH bending and with small contribution from the CC stretching [34, 35]. Comparison of the peaks are not clearly different because the vibrations in the amide II band are not much affected by side-chain vibrations, hence secondary structures of each sample were estimated from the amide I band.

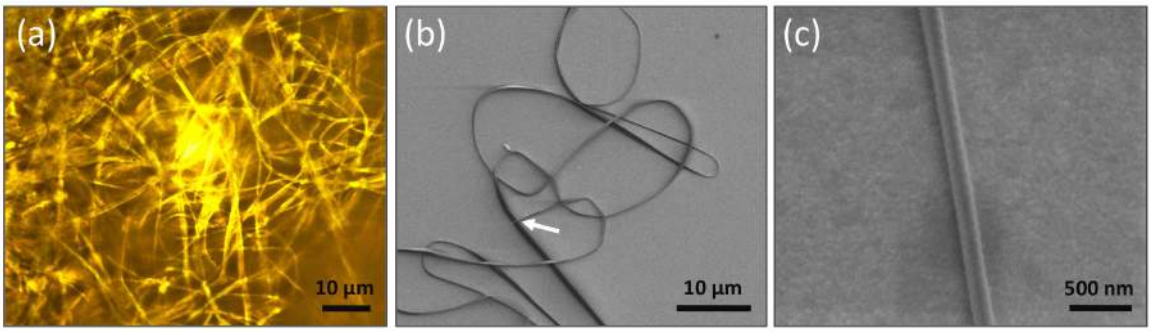

Figure 5.8: (a) Optical micrographs of INS/HFIP 10 %(wt/wt) microliter electrospinning at 12 cm, 8 kV on an aluminum disk diameter of 3 mm. (b) and (c) SEM micrograph of insulin fibers produced with the same parameters on a cleaned silicon wafer. The white arrow indicates the end of fiber, wherein diameter is ~100 nm.

Insulin powder and electrospun fiber have the strongest peak at around 1650 and 1655 cm^{-1}, respectively. Both peaks are in the amide I band region and assigned to α-helices. While, the predominantly peak near 1630 cm^{-1} of insulin fibrils sample is assigned to β-sheets. This suggests that the insulin fibril structure is different from the original powder but is not clear for the insulin fiber. To quantify the secondary structure, curve fitting of amide I band was determined [35–38] and presented in Fig. 5.10 (see procedure in the chapter 3). Note that the curve fitting results give different IR peak widths depending on the relative strength of intermolecular, intramolecular and solvent-molecule interactions of each secondary structure [38]. For spectroscopy, the peak width is inversely proportional to the effective lifetime, and also the presence of two or more peaks. For example, water molecule has strong hydrogen bonding network allows the molecules to relax very fast, so O-H peaks are enormously broad. Therefore, if α-helices structure of protein is not distorted (weak interaction) results the molecules to relax slow, the peak width is small.

Curve-fitting result of insulin powder shows a mixture of about 50% α-helices, 35% β-sheets, and 10% turns (Fig. 5.10a). The insulin fiber (from HFIP solution) amide I band has its maximum at 1654 cm^{-1}. The fit yields 50% α-helices, 25% β-sheets, and 25% turns (Fig. 5.10b), hence the β-sheets is slightly reduced (10%), whereas the turns structure is increased (15%) compared to the original structure. This can be interpreted that the denaturation of insulin in HFIP is not too much, and means the insulin is not completely unfolded, which is similar to the case of albumin/TFA (see the previous section). Reasons may involve the compact structure of these proteins or disulfide bonds. The insulin fibril shows a maximum at 1633 cm^{-1}, the fit yields major component of the 65% β-sheets, 25% α-helices, and 10% turns (Fig. 5.10c). This clearly shows that the fibril appears more ordered, and with an increased fraction of β-sheets [29].

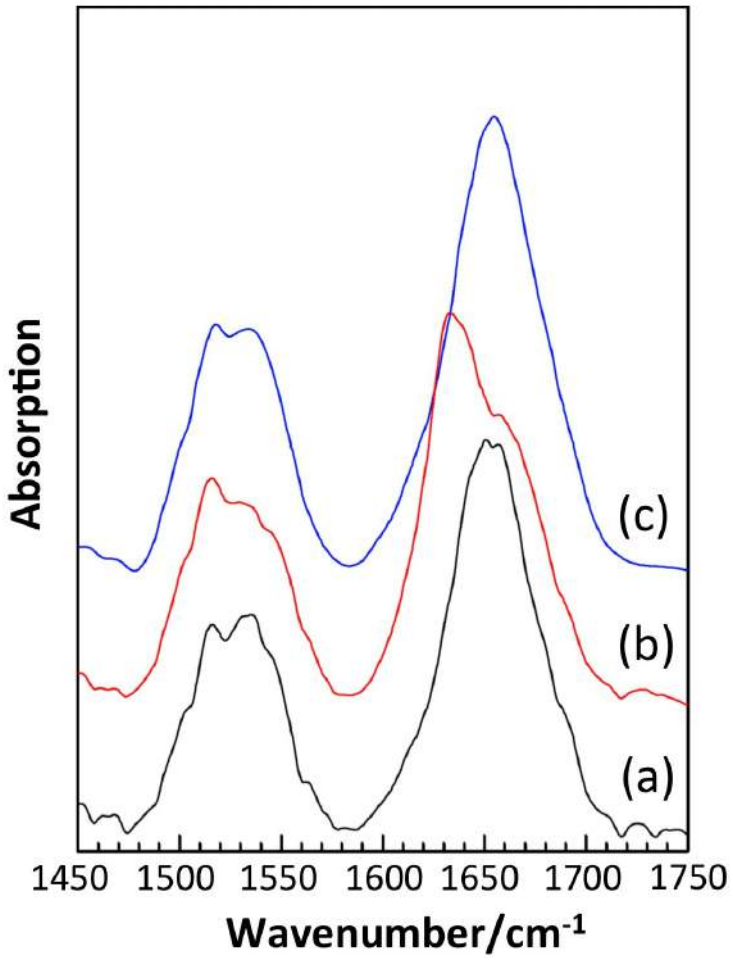

Figure 5.9: IR spectra of (a) insulin powder, (b) acids-treated insulin fibrils, and (c) insulin fibers electrospun from INS/HFIP 10 %(wt/wt) solution at 12 cm, 8 kV on an aluminum disk diameter of 3 mm.

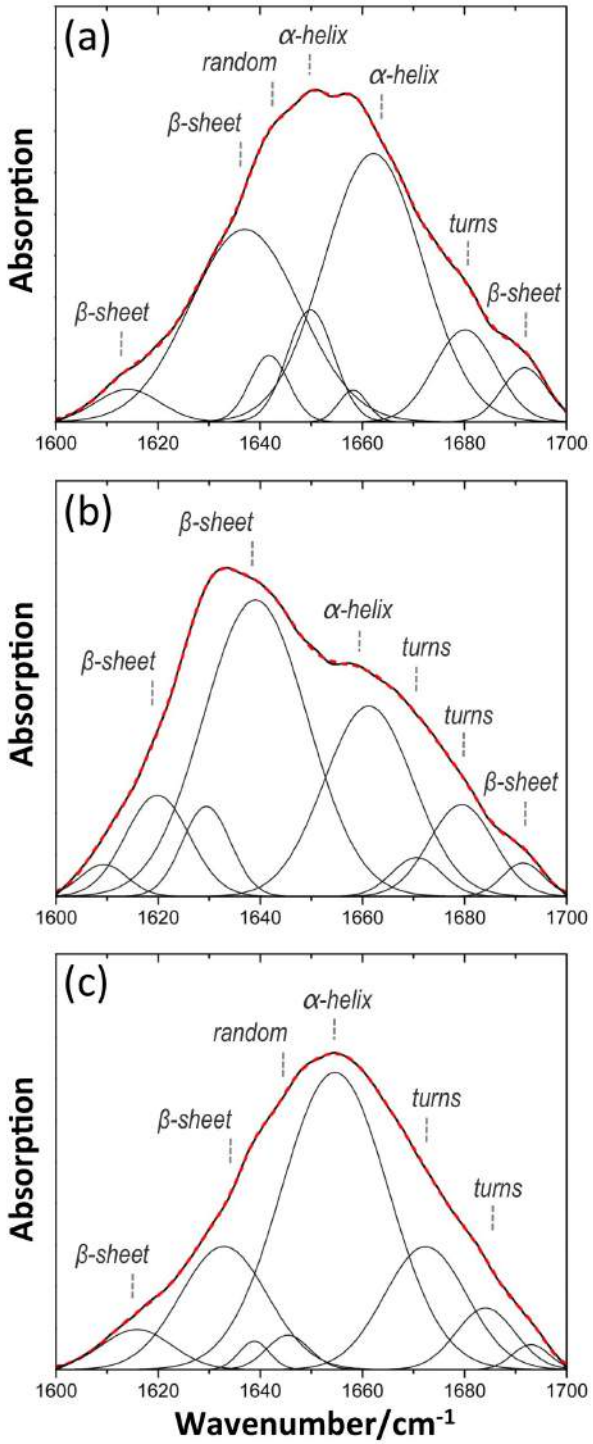

Figure 5.10: Curve fitting of amide I band, IR (ATR) of (a) insulin powder, (b) insulin fibrils, and (c) insulin fibers electrospun from HFIP solution.

Local IR spectra of a single insulin fiber and fibril were employed using the nano-FTIR (see detail in the previous section, IR nanospectroscopy of albumin). Figure 5.11a shows insulin fibrils (black arrow) on a clean silicon wafer, not clearly observed under optical microscope because their diameter is small (30−50 nm). Then, insulin fiber was produced onto the same sample. A continuous fiber (white arrow) has diameter of 400 nm (~200 in some area) electrospun from insulin/HFIP 10 %(wt/wt) solution at distance of 60 cm, applied voltage at the tip 20 kV and the collector -10 kV. Apart the long fiber, some short fibers (~10 μm) were observed. Since the distance between the tip and the collector is very far, it is possible that some fibers are too much elongated and then broken. Inset of Fig. 5.11a is AFM topography of the sample, small fractions are thick insulin fibrils composed of several protofilaments, the length is not longer than 500 nm because they aggregated from a 2 years storage at 4 °C solution (the length of fresh insulin fibrils is in range of few μm, see in [23]). Insulin fiber (marked P2) has a diameter of ~200 nm and the height values around the width is 160 nm, so the small fiber tends to have a round shape, rather than a ribbon-like structure observed as in the case a fiber electrospun at 12 cm, 8 kV (see SEM micrograph in Fig. 5.8b). The local IR spectra in Fig. 5.11b were obtained on top of a single 200 nm thick fiber (at P2, red trace) and insulin fibril (at P1, orange trace), compared to the global IR spectrum of the fibers (blue trace) and fibrils (black trace). Both the amide I and the amide II bands of local spectra correspond very well to the global spectra, thus confirming the characterization results from the ATR-FTIR.

5.3.3 Conclusions

Optical and electron microscopy results confirmed that electrospinning of pure insulin is possible by dissolution in HFIP at 10 %(wt/wt) and using microliter electrospinning setup. Secondary structures of the insulin powder, electrospun fiber and aggregated fibril were determined by curve fitting analysis of the amide I bands in the IR spectra. The α-helices and β-sheets content of the fiber are not very different from the original substance. Thus the insulin is denatured by HFIP but its structure is not absolutely unfolded. The fibril has strong increasing of β-sheets content because the fibril is more ordered, caused by the intermolecular hydrogen bonds, as the peptides. Furthermore, nano-FTIR provides a local spectra, which are substantially similar to global spectra. This supports the conclusion on secondary structures of the insulin fiber and fibril.

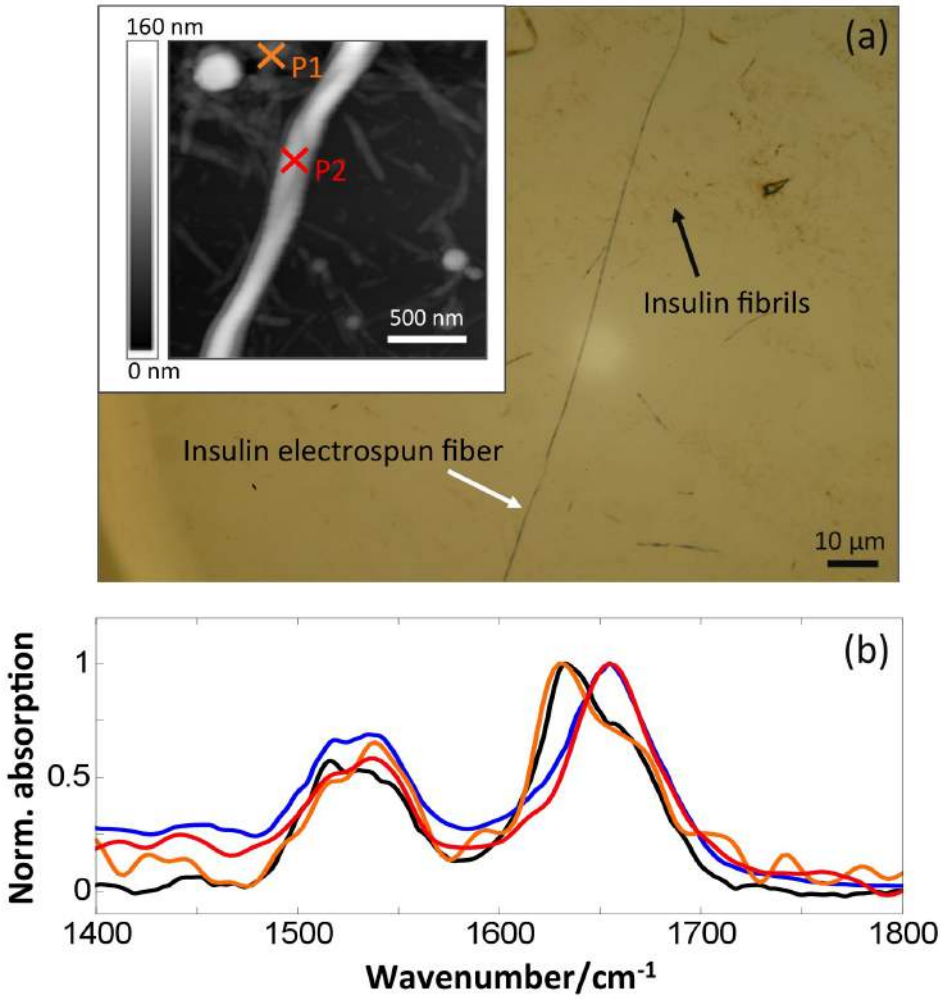

Figure 5.11: (a) Optical micrograph of insulin fiber (white arrow) and insulin fibril (black arrow) deposited on the same cleaned silicon substrate. Inset is AFM micrograph shows insulin fiber (red mark) and insulin fibril (orange mark). (b) Local IR spectra at P1 (red is insulin fiber) and P2 (orange is insulin fibril) compared to global ATR-FTIR spectra (blue is insulin fiber, black is insulin fibril).

5.4 Electrospinning of hydrophobins

Hydrophobins (HPs) are small with low molecular weight of about 10 kDa, cysteine-rich and moderately hydrophobic proteins. HPs are naturally found on fungi, where they determine the very hydrophobic nature of the fungus cap. Hence, this protein is introduced by the name "hydrophobins" [39, 40]. The principal function is to reduce the surface tension of water based on the property to self-assemble at hydrophilic/hydrophobic interface into an amphipathic membrane. These proteins have several key roles in fungal development, for example 1) acting to allow the emergence of aerial hyphae from the mycelial growth medium and providing a water-repellent coating to spores that are aerally dispersed; 2) allowing fungi to escape their aqueous environment, as well as the hydrophobization of spores facilitating improved dispersal of the conidiospores [41].

HPs are identified into Class I and Class II depending on their hydropathy patterns and solubility characteristics. But both classes of HPs can self-assemble on both hydrophilic and hydrophobic surfaces into amphipathic membranes [42, 43]. 2D assembly of HPs can adapt surface characteristics for use of various applications, e.g. biosensors, separation technologies [44, 45]. In particular, stable assembly of hydrophobins Class I is an attractive substance for surface modifications and coating applications. Moreover, their biocompatibility can increase wetting property of coated surface or enhance attachment of cells in tissue engineering applications [40].

Assembly of hydrophobins into fibers (1D) would offer a new application. However, electrospinning of hydrophobins into fiber have not yet reported. There are only coating of hydrophobin HFBI onto electrospun fiber scaffolds poly(lactide-co-glycolide) (PLGA) [46] and poly(ε-caprolactone) (PCL) [47]. The coating of hydrophobin HFBI can improve the hydrophilicity and water permeability of the three-dimensional electrospun scaffolds. Thus, this work tried to find an optimized parameter to electrospin pure hydrophobins. Furthermore, this section will consider the possibility of electrospun pure hydrophobin fiber onto various substrates. A recombinant hydrophobins (can produce in kilogram scale, donated from BASF, Germany) class I hydrophobins named H*Protein A (HP-A) and H*Protein B (HP-B) was used in this work. Both hydrophobins were synthesized from the coding sequence of hydrophobin DewA (*A. nidulans* FGSCA4, gene ID 2869124, see detail in [41]).

5.4.1 Experimental

Hydrophobins in powder form (free flowing fine granules) were used without purification. The HP-A and HP-B were screening dissolved by ultrasonication and shaking in various solvents, i.e. mixture of water and methanol (water:MeOH), ethanol (water:EtOH), tetrahydrofuran (water:THF), hexafluoroisopropanol (HFIP), and trifluoroacetic acid (TFA). In case a solvent can dissolve the HPs, a homogenous solution was tested with the conventional and the microliter electrospinning setup (see section 3.2.2.1 and 3.2.2.2). Effects from humidity inside the chamber were studied by using a hot air gun to control the humidity (see detail in the section 3.2.4).

5.4.2 Results and discussion

Mixture of water and solvent, i.e. (water:MeOH), (water:EtOH), (water:THF) and HFIP are not suitable for HP-A and HP-B. Only mixture of water and methanol (water:MeOH) can completely dissolve HP-B at 4 %(wt/wt). However, this solution cannot form fiber by electrospinning, droplets were observed. Only TFA can dissolve both HP-A and HP-B at high concentration, resulting homogenous, dark brown color and high viscosity solution. TFA can dissolve both HPs very well because they are classified in hydrophobin Class I, which is very insoluble assemblies and can only be dissolved in strong acids, e.g. TFA or formic acid. While assemblies of HPs Class II are amphipathic and can be dissolved in EtOH or sodium dodecyl sulfate (SDS) [44].

Electrospinning was only possible from highly concentrated solutions (above ≈5 %(wt/wt) or even some ten %(wt/wt) depending on the substance and the solvent). This required TFA as solvent, with the advantage of fast evaporation during spinning. To achieve continuous fiber, electrospinning parameters, i.e. applied voltage, distance from tip to collector must be optimized. Furthermore, fiber formation of HPs is sensitively affected by humidity of the chamber. Figure 5.12 illustrates optical micrographs of HP-B/TFA 20 %(wt/wt) solution electrospun at varying humidity from 35−27 %(wt/wt) (distance to collector 12 cm, applied voltage 12 kV, flow rate 0.5 ml/h). The comparison shows that unwanted electrospraying of droplets can be avoided by decreasing the humidity of the air in the electrospinning chamber. Continuous fibers can be formed when the humidity is lower than 30 %. At higher values, droplets with diameter of 2−10 μm and few fibers were observed. High air humidity can prevent electrostatic charging. In addition, the solvent can be evaporated faster in the case of lower humidity. Therefore, the humidity inside the chamber was controlled below 30 %.

To evaluate the effects from concentration, the HPs were dissolved in TFA at around 10 and 20 %(wt/wt), which are closed to minimum and maximum concentrations. At concentrations of 5 %(wt/wt), only droplets were observed on the substrate. In contrast, when the concentrations is too high, the solution has a very high viscosity, hence cannot electrospin (the solution is solid-like gel). The solution was electrospun at an optimized parameters listed below;

- HP-A/TFA 8 %(wt/wt) electrospun at 12 cm, 12 kV, 0.2 ml/h
- HP-A/TFA 22 %(wt/wt) electrospun at 12 cm, 12 kV, 0.5 ml/h
- HP-B/TFA 10 %(wt/wt) electrospun at 12 cm, 15 kV, 0.5 ml/h
- HP-B/TFA 21 %(wt/wt) electrospun at 12 cm, 12 kV, 0.5 ml/h

The HPs fibers were analyzed by scanning electron microscope (SEM) after sputtering the surface with a thin film of gold (~5 nm). Figure 5.13a, b show that the average diameter of HP-A depends strongly on the concentration of the TFA solutions. Average diameter is 280 nm for 8 %(wt/wt) and increasing more than two times (630 nm), when the concentration is 22 %(wt/wt). In addition, the fibers from the 22 %(wt/wt) solution are smooth, bead-less and continuous. While

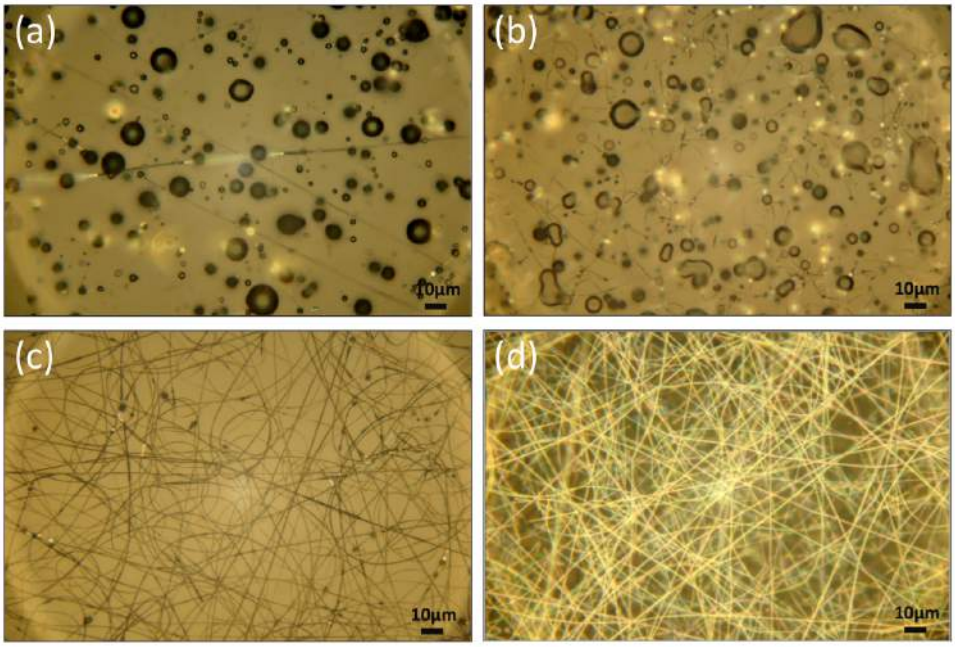

Figure 5.12: Optical micrographs of HP-B/TFA 20 %(wt/wt) electrospun at 12 cm, 12 kV, flow rate 0.5 ml/h under humidity of (a) 35 %, (b) 33 %, (c) 30 %, and (d) 27 %. Notice that the sample (d) electrospun from HP-A/TFA 18 %(wt/wt) solution and the fibers was deposited on substrate longer than other samples, resulting with more density of the fibers.

beads diameter about 2 μm was observed in the 8 %(wt/wt) sample. In the case of HP-B (see Fig. 5.13c, d), the average diameter of fibers from 10 %(wt/wt) and the 21 %(wt/wt) solution is not different, the values are 320 nm and 310 nm, respectively. However, HP-B fibers from the 21 %(wt/wt) solution are slightly smoother than the lower concentration and has very few bead (clearly seen in the first column of Fig. 5.13). Therefore, optimized concentration of HPs dissolved in TFA is about 20 %(wt/wt).

The surface structure of HPs fibers is not clearly visible because the samples were coated with gold and imaged by a low magnification electron microscope (a desktop SEM). To overcome this, the fiber samples were characterized by a higher resolution scanning electron microscope without sputtering or stain obtains detail on the surface of HPs electrospun fiber. Figure 5.14a shows detail at high magnification of HP-A fiber electrospun from solution of HP-A/TFA 20 %(wt/wt) at 20 cm, 12 kV (microliter setup). The fibers are covered by protrusions (unknown mechanism) diameter of 30−70 nm. From the IR spectra (Fig. 5.14) can exclude substantial amounts of liquid TFA because vibration mode of the solvent at around 1780−1790 cm^{-1} is very weak compare to vibrational from protein. Furthermore, the liquid TFA should be completely evaporated, when the fibers were characterized in a vacuum chamber of the SEM microscope.

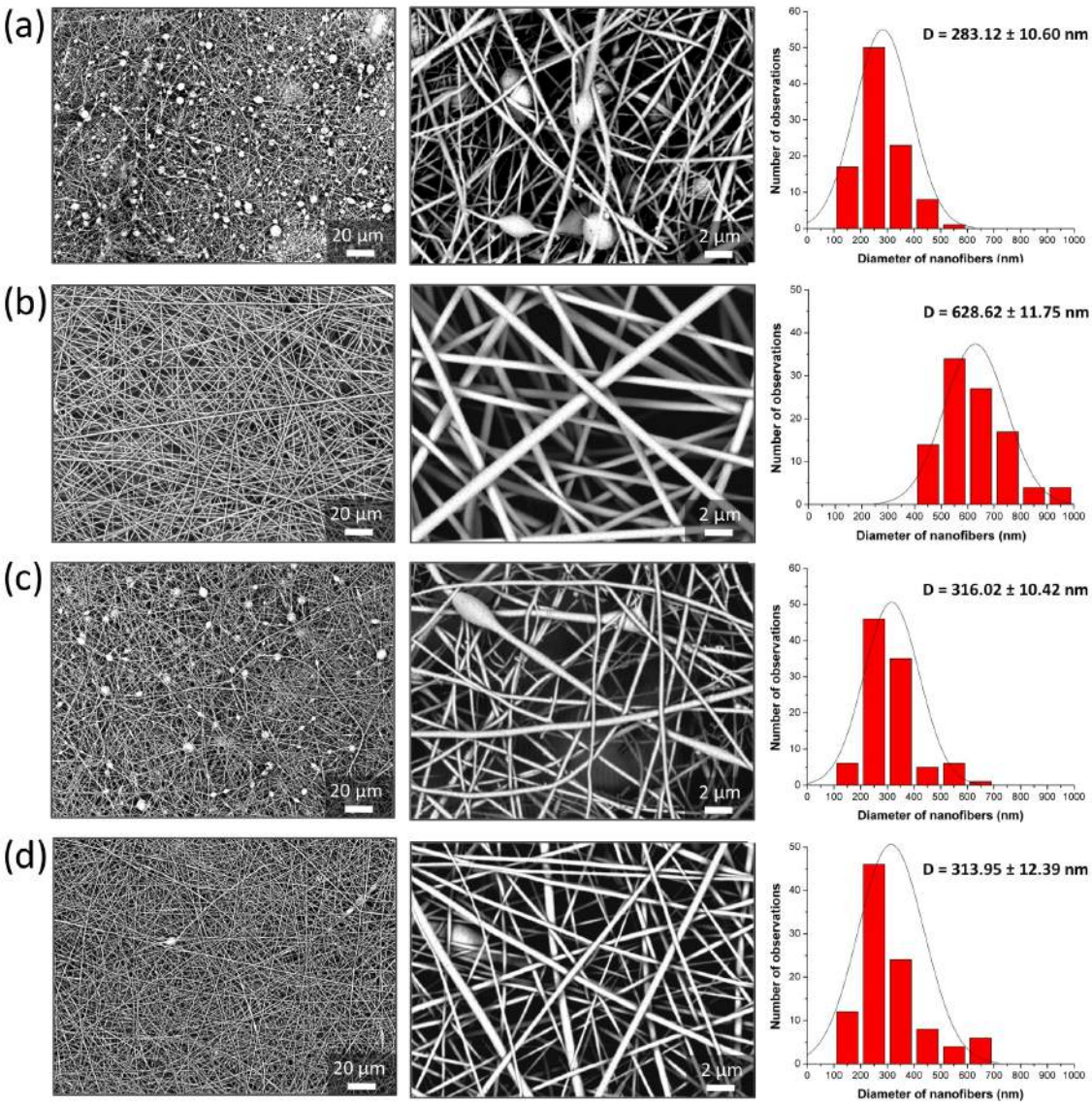

Figure 5.13: SEM micrographs at magnification of 1000X (left), 10000X (center) with the histogram (right) showing the size distribution of electrospun hydrophobins nanofibers. (a) HP-A/TFA 8 %(wt/wt) electrospun at 12 cm, 12 kV, 0.2 ml/h; (b) HP-A/TFA 22 %(wt/wt) electrospun at 12 cm, 12 kV, 0.5 ml/h; (c) HP-B/TFA 10 %(wt/wt) electrospun at 12 cm, 15 kV, 0.5 ml/h; and (d) HP-B/TFA 21 %(wt/wt) electrospun at 12 cm, 12 kV, 0.5 ml/h.

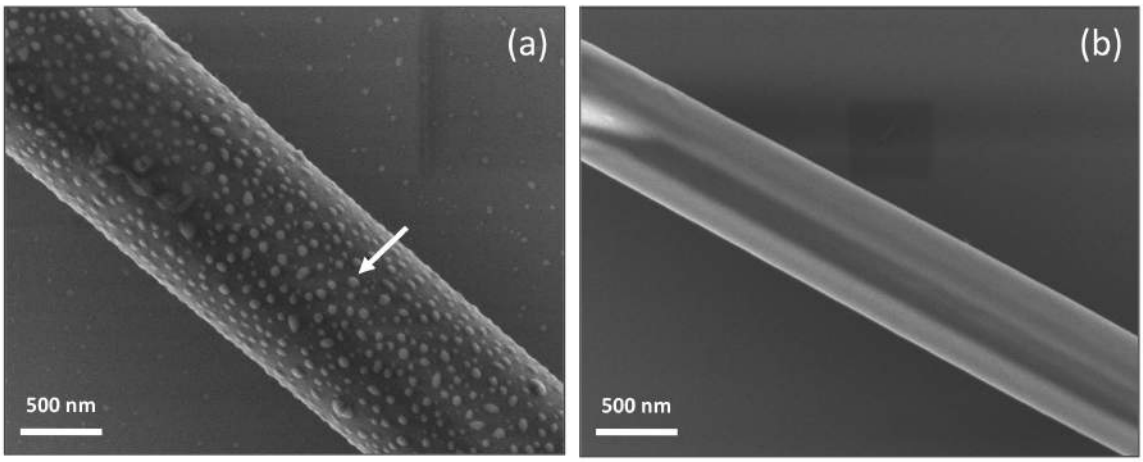

Figure 5.14: SEM micrographs of (a) HP-A/TFA 20 %(wt/wt) and (b) HP-B/TFA 20 %(wt/wt), both produced by microliter electrospinning at 20 cm, 12 kV on a clean silicon wafer. White arrow indicates a protrusions (unknown mechanism) diameter of 30−70 nm, observed only on the HP-A fiber.

IR spectroscopy was employed to probe the changes in secondary structure of hydrophobins after being dissolved in TFA and electrospun to fibers. Figure 5.15 shows IR spectra of HP-A (solid line) and HP-B (dash line) powders (trace a), after dissolved in TFA and evaporation (trace b), and fibers (trace c). The ATR-FTIR spectra of HPs after dissolved in TFA were recorded after drying the HPs/TFA solution on a cleaned glass slide. IR spectra of HPs present two prominent bands in amide I region (1600−1700 cm^{-1}) and amide II region (1520−1550cm^{-1}). Looking first at amide II band, HPs powder samples have the strongest component near 1530 cm^{-1} corresponds to β-sheets structure [48]. In the case wehre the HPs were dissolved in TFA and after electrospun, the highest peaks are found around 1545 cm^{-1}, representing some α-helices structure. This means the HPs are dissociated with TFA, which also unfolds the HPs [43], resulting the α-helices content is increased. This may be a reason why the solution can be electrospun and form fibers. and maybe a reason why the solution can be electrospun and formed fiber. To quantify the changing of secondary structure, amide I band of the IR spectra was characterized as following

As previously mentioned, the amide I band (1600−1700 cm^{-1}) is sensitive to secondary structure, i.e. α-helices, β-sheets, random coils and turns. The IR spectra of HP-A are strongly similar to HP-B. When comparing powder samples to others, however, there is a shift of the amide I band toward higher frequency for the HPs in TFA and electrospun fibers. This means the secondary structure of HPs (after dissolving in TFA and electrospun to fibers) is changed from the original powder. Curve fitting elucidates to relative amounts of secondary structure elements (see Fig. 5.16). HP-A and HP-B powder show a mixture of about 10% α-helices, 45% β-sheets, and 45% turns. The fit of HPs in TFA solution yields an increasing of α-helices to 25%, while content of β-sheets strongly decreases to 10-15%. The turns structure was slightly reduced to 30-40% and 20-40% random coil was observed. The increasing of α-helices and random coil supports that the HP-A and HP-B can be unfolded (and might including the dissociation) after dissolved in TFA as found in another

hydrophobins Class I, e.g. SC3 [43, 49–51]. Comparison amide I band of HPs after dissolved in TFA and after electrospinning, the IR spectra are similar but curve fitting yields increasing of β-sheets content to 20-25%. In addition, the content of random coil strongly reduces to 5%. This can be represented that the HP-A and HP-B are refolded (but cannot specific that they refolded to original form of the powder or others) after electrospinning process. This mechanism is similarly observed when a class I hydrophobins SC3 assembled at the water-air interface, resulting rich β-sheets structure was obtained [43, 49–51]. Note that the content of turns structure is not clearly changes, probably because there is a contribution in amide I band of the TFA centered around 1670 cm^{-1} [48].

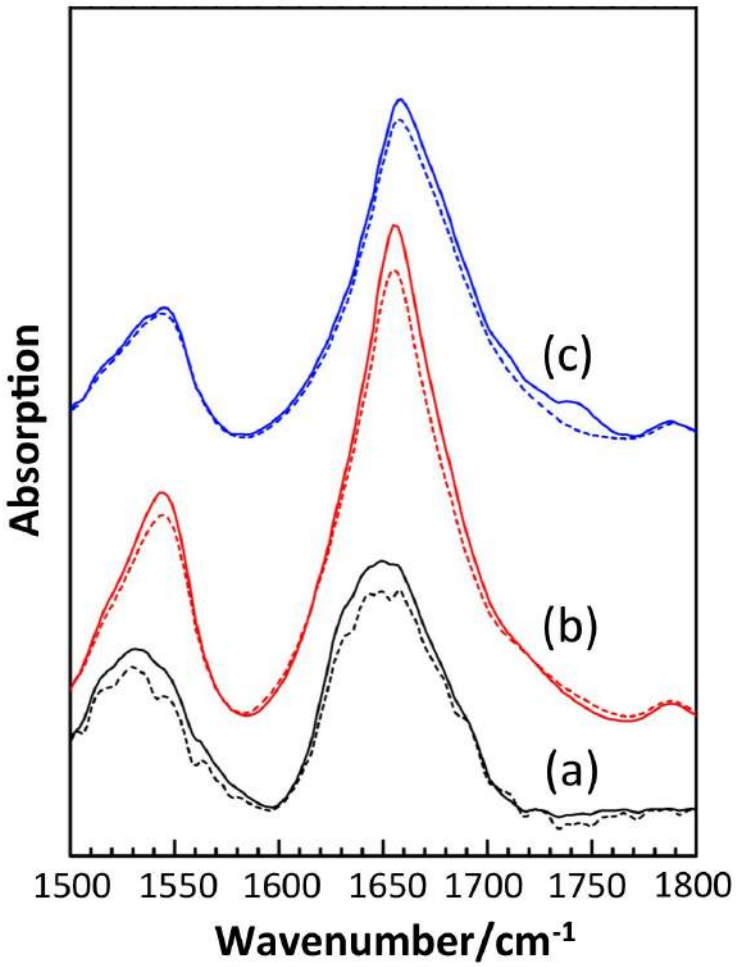

Figure 5.15: IR spectra of HP-A (solid trace) and HP-B (dash trace), (a) powder, (b) after dissolved in TFA, and (c) electrospun fibers.

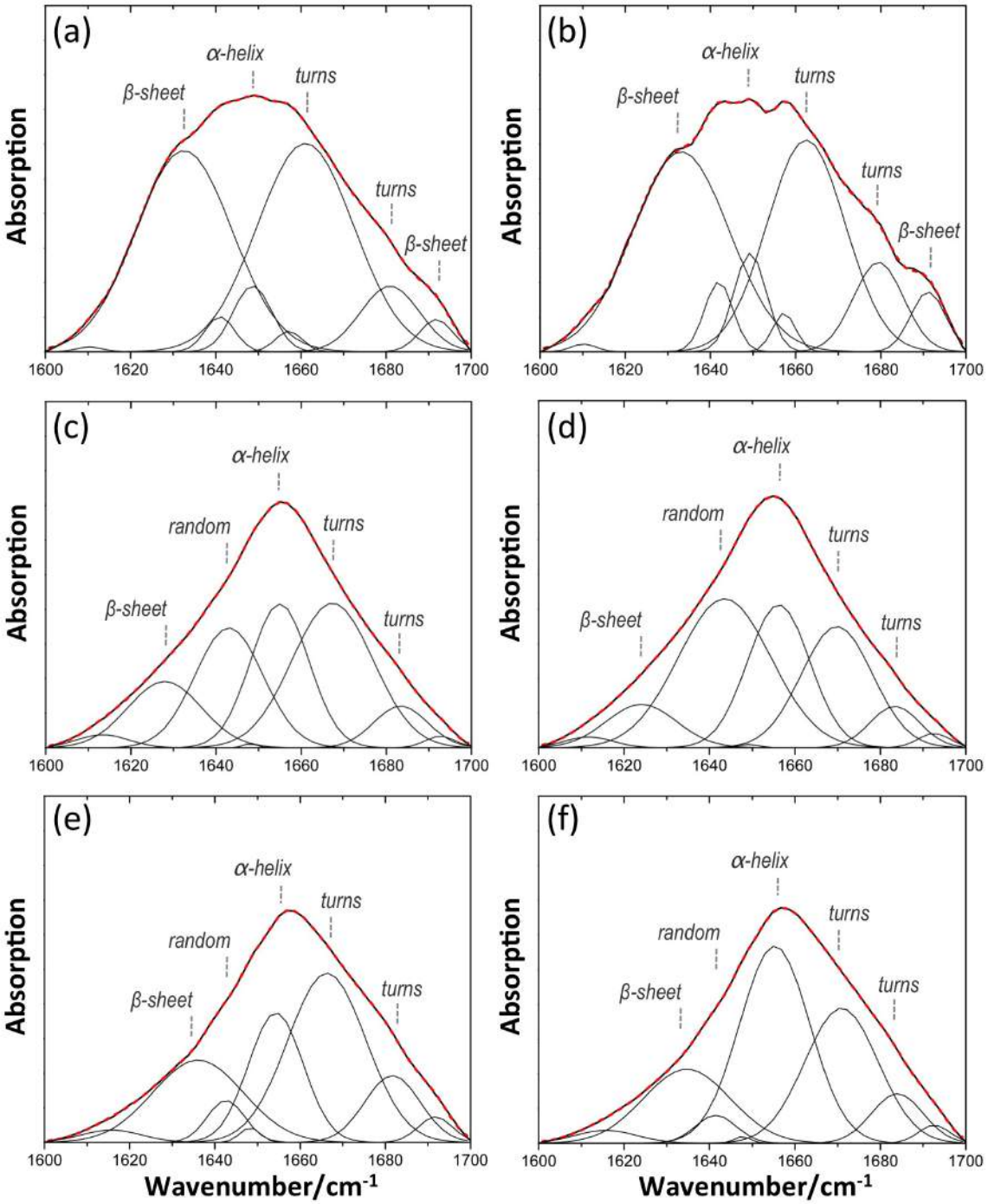

Figure 5.16: Curve fitting of the amide I band of (a) HP-A powder, (b) HP-B powder, (c) HP-A in TFA solution, (d) HP-B in TFA solution, (e) HP-A electrospun fibers, and (f) HP-B electrospun fibers.

Since HPs is one of attractive biomolecule for surface modification and coating applications, so electrospinning of HPs into 2D fiber mat was tested on various substrate. Figure 5.17 shows a possibility to deposit HPs fibers onto a fabric, paper, polymer film, plastic sheet, and plastic mesh. In this experiment, HP-B was donated in aqueous solution form, lyophilization was employed to dried the substance. Then the lyophilized powder was dissolved in TFA at 20 %(wt/wt) and electrospun at 15 kV, 20 cm with flow rate of 0.4 ml/h. A substrate was place over collector below the needle in order to collecting fibers. The electrospinning process was carried for 5−10 min, resulting a homogenous 2D fiber mat covers the substrate (Fig. 5.17a-f). Some solution droplets were observed on the fiber mat when the electrospinning parameters are not optimized. Fabrication of 3D scaffold, the HP-B/TFA 21 %(wt/wt) solution was electrospun at 12 kV, 20 cm over the collector, with flow rate of 0.4 ml/h for 10 min. Hydrophobin fibers formed 3D over the collector, then harvested (see Fig. 5.17g).

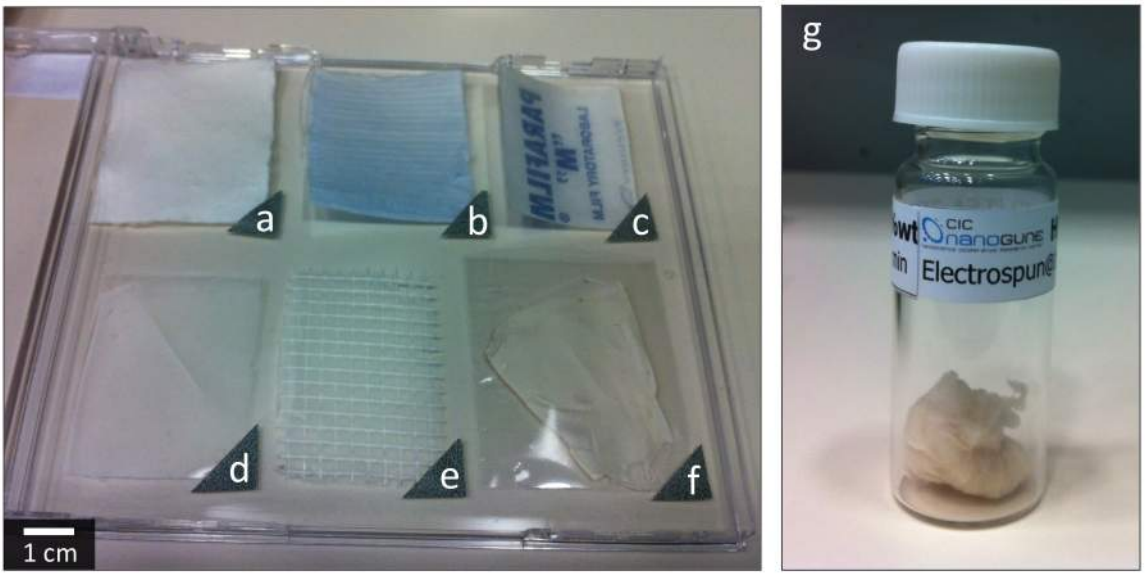

Figure 5.17: Digital photo of HP-B/TFA solution 20 %(wt/wt) was electrospun at 15 kV, 20 cm with flow rate of 0.4 ml/h for 5−10 min, electrospun fibres can be deposited on any substrate (a) fabric, (b) paper, (c) polymer film, (d) plastic, (e) plastic mesh, (f) without substrate), and (g) the electrospun scaffold, which can be processed into a 2D fiber mat or a 3D scaffold (electrospun parameters are 15 kV, 20 cm, with flow rate of 0.4 ml/h for 10 min).

5.4.3 Conclusions

Hydrophobins (HP-A and HP-B) can be electrospun to 1D nonwoven fibers without the normally required synthetic polymers or supports by optimizing solvent, concentration, humidity of chamber, and electrospinning parameters. TFA is suitable to dissolve HPs at high concentration, result suggests at about 20 %(wt/wt), and the electrospinning should be done under humidity of lower than 30 %. IR spectroscopy shows that the HPs unfolds after dissolved in TFA and slightly refolds when electrospun and forms fiber. Since the HP-A and HP-B can easily be produced in kg amounts

by biotechnological fermentation techniques, its possible to scale up to industrial scale and the fibers can coat on various surfaces. However, wetting properties of HPs fibers mat does not clearly or only depend on type of substrate. Based on some preliminary experiments of HPs fibers on a glass slide and a polytetrafluoroethylene (PTFE) film (a teflon tape), they present only hydrophilic properties rather than amphiphilic as found in the self-assembly monolayer of hydrophobins. Its possible that the fiber is too thick and mechanism in electrospinning of hydrophobins is slightly different to self-assembly. However, the electrospinning process of pure hydrophobins works exactly as with the usual polymer solutions. Thus, electrospun fibres of HPs without polymer blends might be used for multiple applications in biotechnology, e.g. as highly biocompatible (non toxic after the solvent removal) scaffold materials, cell growth support, tissue engineering, water absorption, a template in the production of ceramic nanofibers.

5.5 Electrospinning of DNA

As seen in Chapter 4 and section 5.1−5.4, peptides and proteins were electrospun into fibers. The last experiment of this thesis studied electrospinning of another building block: nucleotides, subunits of nucleic acids such as deoxyribonucleic acid (DNA) and ribonucleic acid (RNA). Apart from proteins, carbohydrates, and lipids, DNA is an essential macromolecule, important for all known forms of life. DNA serves as the primary unit of heredity in organisms. Since living cells or isolated cell components can synthesize this biomolecule DNA the result is the production of molecules that are exactly the same number of monomers and same sequence [52]. These molecules serve as good building materials for nanostructures such as DNA origami [53–56] and DNA metamaterial [57].

The right-handed double helices structure of DNA in B-form (see Fig. 5.18a) was discovered by Watson and Crick [58, 59]. Each monomer of DNA is composed of a phosphate group, a five-carbon sugar (ribose), and one of four bases; adenine (A), thymine (T), cytosine (C), and guanine (G). These four bases can interact with each other with hydrogen bonds and π-stacking interactions. Besides the original Watson-Crick model, other biologically active double helical structures DNA are A-DNA (can be found in a dehydrated sample) and Z-DNA (formed by stretches of alternating purines and pyrimidines or negatively supercoiled DNA) [60]. Chemically and structurally much less variable than peptides, only 4, 16, 64 are possible molecules.

Electrospinning of pure DNA was first reported by Fang et al., electrospun DNA fibers had smallest diameter of 30 nm from a solution of calf thymus Na-DNA 0.3−1.5 %(wt/wt) dissolved in a mixture of EtOH/water (3:7). The DNA fibers contained beads diameter of 80−300 nm. TEM image supposed that a single DNA fiber diameter of 62 nm consists of ~600 DNA molecules [61]. Another work reported by Takahashi et al., solution of salmon testes DNA (200,000−900,000 base pairs) was electrospun onto a mica substrate. Using AFM, four different types of DNA nanofibers were observed on the same sample consist of; 1) intricately-twisted shape, 2) twisted and stretched shape, 3) curved shape, and 4) straight shape. A stretched DNA fiber with average height of 1.8 nm

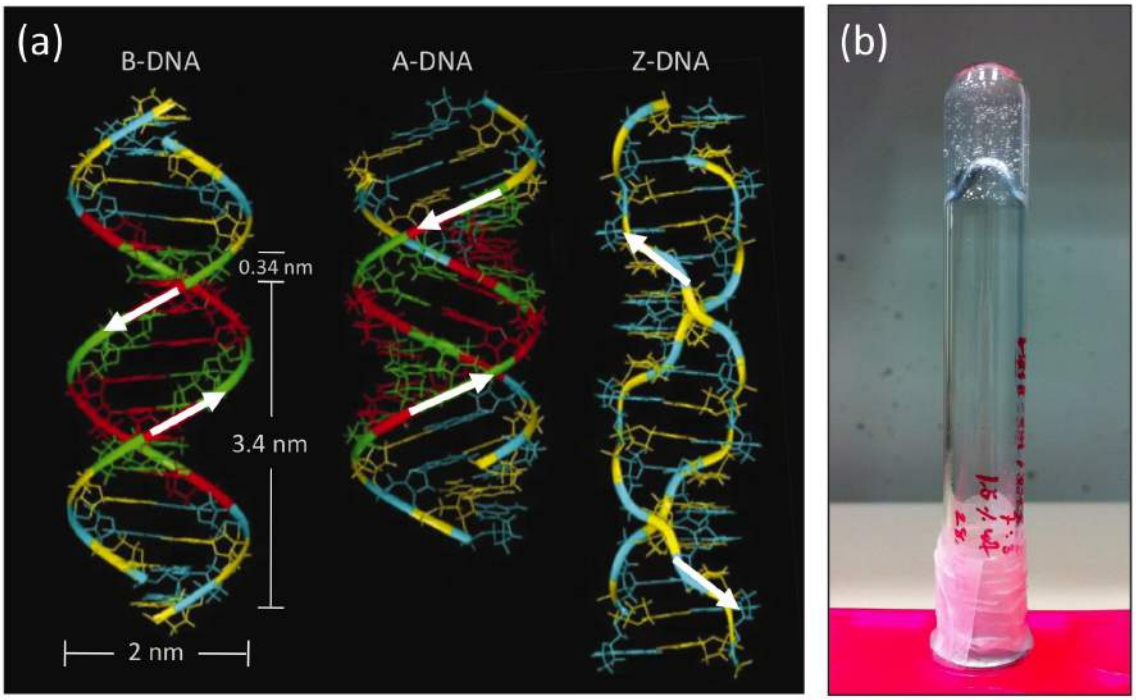

Figure 5.18: (a) Molecular structures model of B-DNA, A-DNA, and Z-DNA demonstrated in stick. Cytosine is represented in yellow, guanine in cyan, thymine in green and adenine in red. A- and B-DNA are right-handed, while Z-DNA is a left-handed double helices (adapted from [60]). (b) Double-stranded DNA sodium salt from salmon testes forms a hydrogel after it was dissolved in mixture of ethanol/water 30 %(v/v) at 1.5 %(wt/wt). This solution was used for electrospinning.

(one double-stranded) and average length of ~1 μm can be obtained under optimized conditions, solution concentration 1.5 %(wt/wt), applied voltage 20 kV, and distance 25 cm [62]. Moreover, the fluorescently labeled DNA was also electrospun onto a photolithographically patterned. Imaging with fluorescence microscopy, SEM and AFM presented that the DNA fibers have diameter approximately 27 nm. The Young's modulus of an electrospun DNA fiber (diameter of 39 nm) was estimated ~13 GPa using AFM [63]. DNA was incorporated or mixed into electrospun of polymer nanofibers, e.g. nanofiber mats produced from mixture of DNA, PEO and single-walled carbon nanotubes used for glucose biosensor [64], incorporated of DNA to electrospun nanofibers for gene delivery [65], and hybrid nanofibers of DNA, magnetite nanoparticles, and cetyltrimethylammonium (CTMA) bromide for water detoxification [66]. Fluorescently labeled bacteriophage λ-DNA mixed with poly(ethylene oxide) (PEO) was electrospun into fiber with diameter of 100−350 nm [67].

In this work, a solution of salmon testes DNA (~2,000 base pairs, estimation in Da is ≈74 kDa or higher) will be electrospun using the microliter electrospinning at an extremely far distance with air stream onto a silicon and a TEM grid substrate. A new shape of DNA fibers and their wetting properties were characterized with SEM, STEM and ESEM.

5.5.1 Experimental

Double-stranded DNA sodium salt from salmon testes with approximately 2,000 base pairs was purchased from Sigma-Aldrich. The DNA was dissolved in EtOH/water 30 %(v/v). The mixture at 1.5 %(wt/wt) forms hydrogel after shaken overnight (see Fig. 5.18b). The microliter electrospinning setup was employed for this experiment with an air stream (see detail in section 3.2.2.4). Silicon wafers and carbon-covered Cu grids were used for collecting DNA fibers. Typically, the collector will be placed far from the tip in range of 10−20 cm or 0.5−3.0 mm in case of near-field electrospinning [68–71]. In this experiment, the DNA solution will be electrospun at long collector distance is 75 cm in order to obtain a small DNA fiber.

5.5.2 Results and discussion

The dsDNA from salmon testes can be completely dissolved in EtOH7water 30 %(v/v) after shaken overnight, at concentrations of 0.1 and 1.5 %(wt/wt). However, the later concentration forms hydrogel (see Fig. 5.18b) with very high viscous and does not drip down. Viscosity of the hydrogel 1.5 %(wt/wt) was measured by a rheometer (TA Instrumental) at 25 C. The value is approximately 100 Pa.S (the same as a sour cream) at shear rate 0.1 rad/s, and reduced to 0.3 Pa.S at shear rate 100 rad/s. The dsDNA hydrogel was sucked up a small amount (~10 μl) via a micro-pipette and then slowly punched onto the tip of microliter electrospinning setup. The process was tested at various parameters. Observation with optical microscopy found that solution of 1.5 %(wt/wt) yields long fibers with some beads, while lower concentration of 0.1 %(wt/wt) also provides fibers but with a lot of beads. Hence, this study focused on the DNA solution of 1.5 %(wt/wt).

Optimized electrospinning conditions were found, when a positive voltage 20 kV was applied at the tip and negative 10 kV at the collector. The substrate was placed 75 cm below the tip, with air stream over the tip (detail in section 3.2.2.4). Figure 5.19a shows optical image of stretched and curved fibers deposited on silicon wafer. Diameter of the fibers is 300−500 nm, which is much bigger than the size of a single dsDNA molecule (about 2 nm). This means several of the dsDNA molecules are bundled and forms fibers [62]. However, the bundle of DNA fibers does not homogenous, provides several diameters. Some area on the same sample show a very small fiber. Using STEM, thin dsDNA bundled fibers were found from 35 nm down to 10 nm of diameter (Fig. 5.19b). The smallest bundle whose diameter is 10 nm, can be formed by 19 dsDNA (see inset of Fig. 5.19b). The difference diameters and shapes (stretched and curved) of dsDNA fibers may be due to non-homogenous nature of the hydrogel of the solution (electrospinning of pure peptide or pure protein requires a homogenous solution).

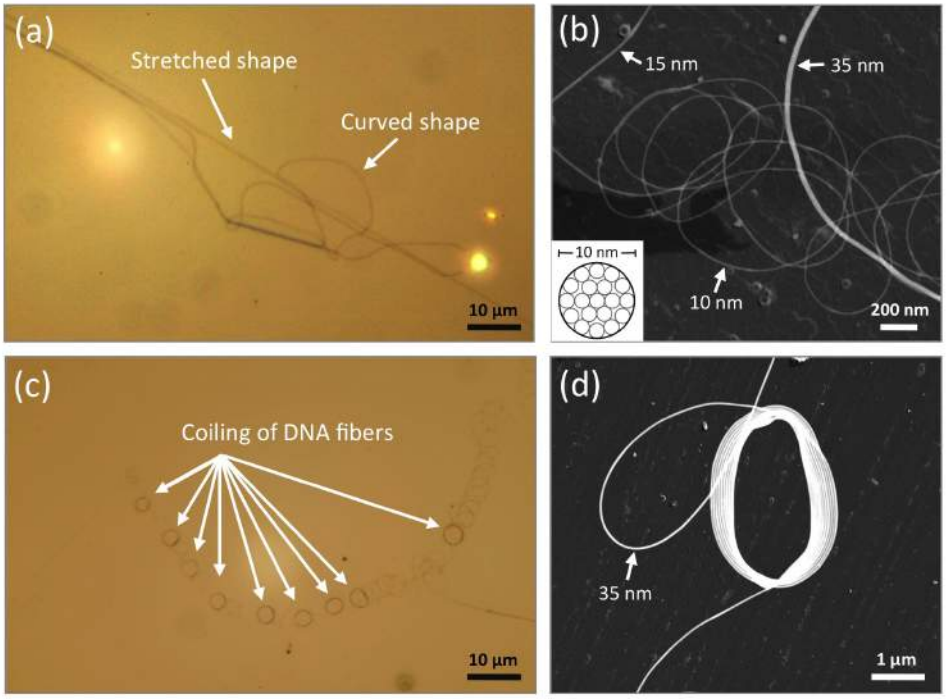

Figure 5.19: Electrospinning result of dsDNA dissolved in EtOH 30 %(v/v) at concentration of 1.5 %(wt/wt); (a) optical image presents stretched and curved fibers diameter of 300−500 nm formed by bundles of dsDNA, (b) STEM micrograph of dsDNA with diameter 10−35 nm, inset demonstrates model of smallest fiber 10 nm bundled from 19 dsDNA molecules, (c) optical image of dsDNA fiber coiling with diameter of 2−3 μm, and (d) STEM micrograph shows high magnification image of fiber coiling in a clockwise direction, which consists fraction of dsDNA fiber 35 nm of diameter. Notice that the coilings were observed both in a clockwise and a counter clockwise direction. Characterization with STEM, dsDNA fibers were deposited on a carbon-coated copper grid.

Besides stretched and curved fiber, a coiling of DNA fiber was observed in some area of the same sample (see arrows in Fig. 5.19c). Optical image shows the coiling fibers with diameter of 2−3 μm. This structure can be observed when the hydrogel was electrospun at very far from substrate (75 cm) and an air stream was applied over the tip. Without air stream and closer distance (20 cm), only few fibers and some droplets were observed on substrate. It's possible that the air stream increases evaporation rate of EtOH/water. To obtain detail of the coiling fibers, STEM was used and focused on the coiling structure. Figure 5.19d shows the coiling of dsDNA fibers with diameter of 2−3 μm. The fiber 35 nm of diameter turns around 10 times and then moves to form the next coiling structure. Characterization with AFM provides the same, dsDNA fiber coiled up from about 10 turns, forming similar a pool with diameter of 3 μm and height ~250 nm. The mechanism of coiling is not clearly yet. It is possible that this coiling is superimposed on electrically driven bending instability [72]. Another reason may be the effect of charging on the dsDNA fiber (applying 20 kV to the tip). The positively charged fiber neutralizes, when relied on the negatively charged substrate (applying -10 kV to grounded collector below the substrate). However, when the fibers are coiled up, the positive charge cannot transfer to the substrate (DNA is non conductive), so they move to form a new coiling (see schematic model in Fig. 5.20c). With this argument, conductivity of the substrate would affect the coiling fiber. Figure 5.20a, b shows optical micrographs of dsDNA coiling structures observed on a silicon wafer and a silicon wafer coated with 150 nm gold. The coilings in both samples have diameter around 2−3 μm, but small coilings diameter ~1 μm were observed on the conductive substrate. The numbers of coiling on the gold-coated silicon is about four times higher than on the silicon wafer.

There is no report about the coiling structure of DNA fibers but this structure typically is founds in honey or high viscosity fluid [73–77]. However, this phenomenon can be observed in a special electrospinning setup reported by Kim et al. [78]. Buckling of PEO fiber (see Fig. 3.1c in Chapter 3.2.1.1) forms like a nanopottery of diameter approximately 6 μm and height 40 μm, when the polymer solution is electrospun onto an electrode pin (apex diameter of 50 μm) placed below the tip at 2 mm. Surprisingly, similar structure was found in the case of DNA solution, even though, the distance to the collector is 75 cm for this experiment and there is no pin. Although, the height of fiber coiling (~250 nm) is less than the nanopottery (40 μm). However, several coilings of dsDNA structures can be found on the substrate, while the nanopottery formed one structure per pin. The structure of electrospun DNA fiber is not clear but probably B-form, which is found when Na-DNA dissolved in EtOH/water concentration of 0−50 %(v/v) [79]. However, the structure of electrospun DNA might be directly evaluated using aberration-corrected high resolution TEM, without staining [80].

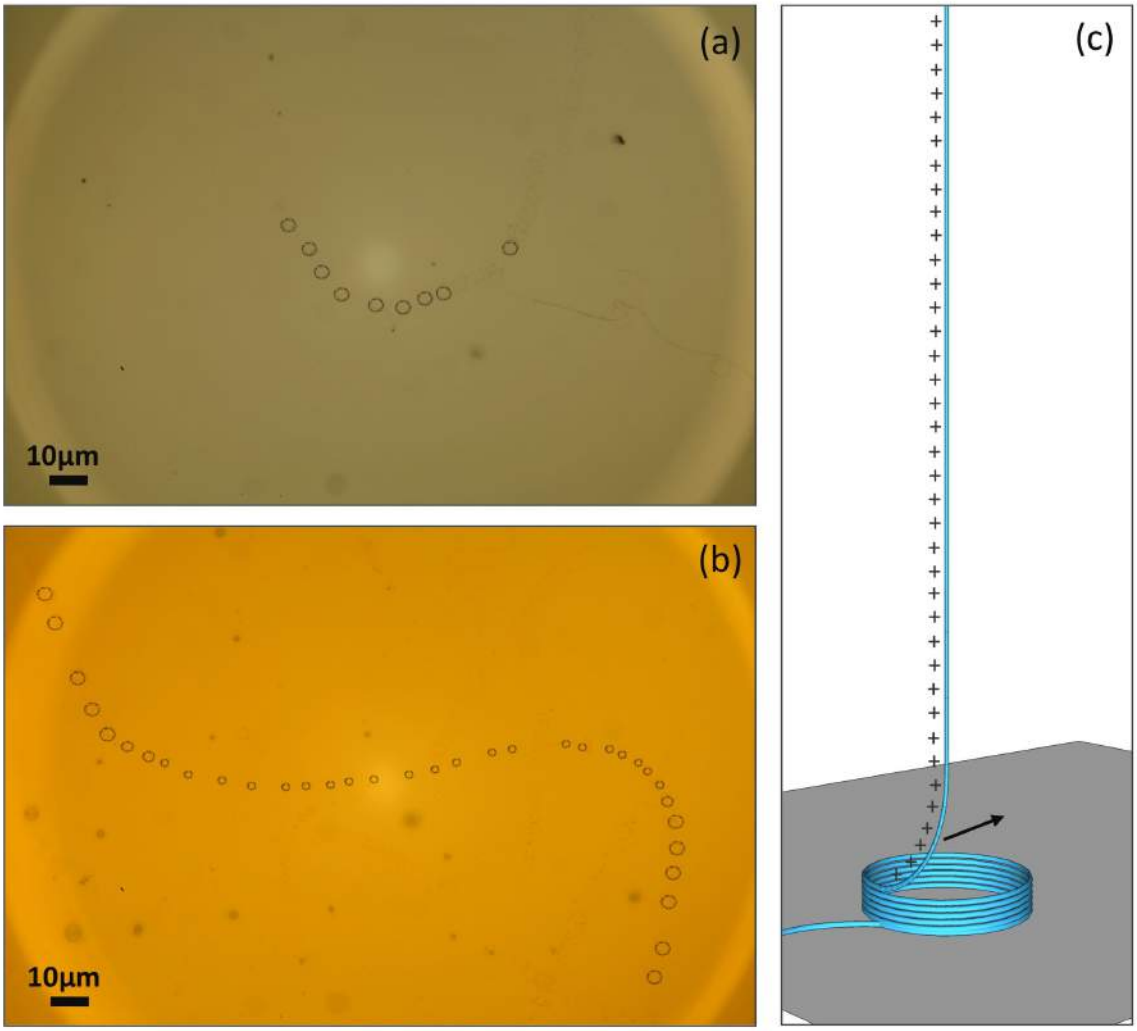

Figure 5.20: Optical micrograph of dsDNA coiling structures (shown with dash lines to clarify) observed on (a) silicon wafer and (b) silicon wafers coated with 150 nm gold. The coilings have diameter of 1−3 μm, number of observation on the gold-coated silicon is higher than silicon wafer about 4 times. (c) schematic model of coiling fiber formation, positively charged fiber coiled up until the charge cannot move to the substrate, then forms a new coiling (along the arrow direction).

To study wetting property, dsDNA coiling structures were deposited onto a wet cleaned silicon wafer (without plasma treatment) then characterized with ESEM. Figure 5.21a shows coiling P1 (diameter of the coiling is approximately 4 μm, and of fiber 60 nm) and P2 (diameter of coiling is approximately 5 μm, and of fiber 70 nm). On the same area, curve fibers were observed below and around the coiling structure. These fibers were deposited before and after forming a new coiling structure. A big droplet of dsDNA solution diameter of 1 μm or bigger can be found (marked with a cross symbol), since the hydrogel does not homogenize as a polymer solution. Figure 5.21b, c show coiling P1 and P2 imaged at higher magnification, dark contrast of the ring was observed around the coiling because of the superposition of the fibers, while the top of the coiling showed in bright contrast. Other bright spots in Fig. 5.21d represent small condensed water droplets form inside the coiling P1 and P2, when the humidity of environment is increased to 100 %. After then 45 s, the size of bright spots are increased means water full fill inside the structure (Fig. 5.21e). Therefore, dsDNA fibers are hydrophilic and coiling structures are not destroyed after drying (Fig. 5.21f).

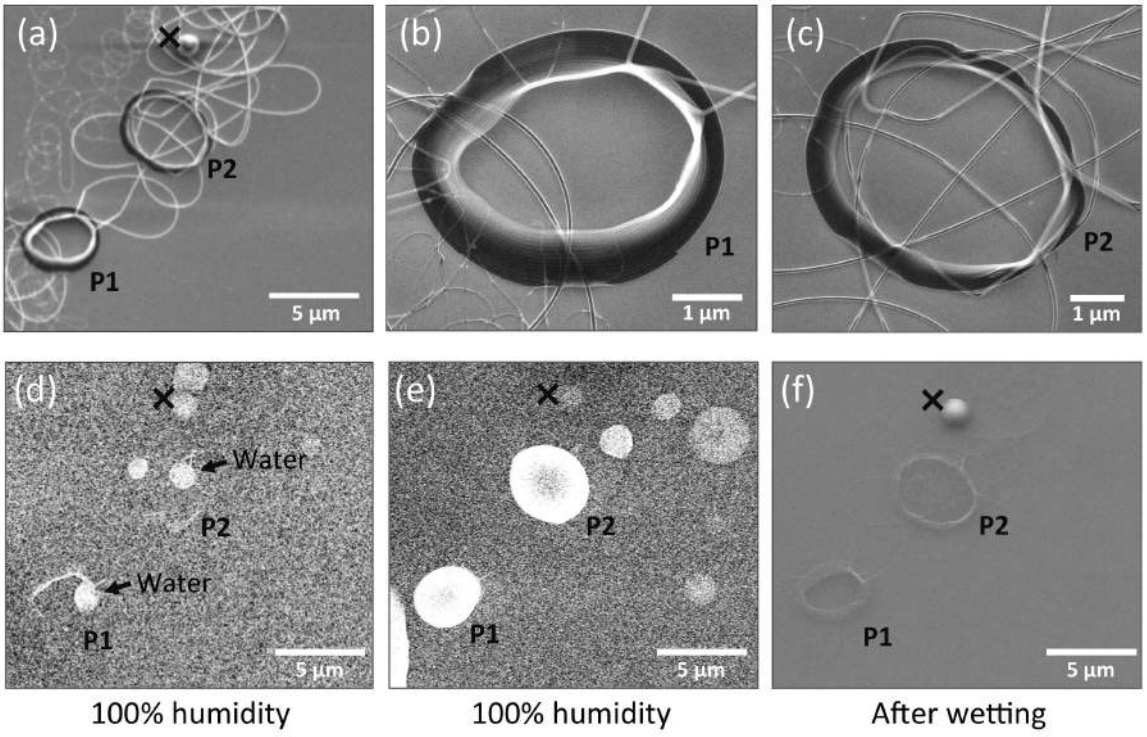

Figure 5.21: SEM micrographs of dsDNA fiber coiling on a silicon substrate; (a) The fiber coiling P1 and P2 were observed, (b, c) zooming at P1 and P2, respectively. Their wetting properties investigated using ESEM under temperature of 1 °C; (d) forming of water droplets inside the fiber coiling at 100 % of humidity, pressure 665 Pa, (e) 45 s later, water fulfilled inside the coiling structures, and (f) the structure of fiber coiling remains after dried at 0 % of humidity, pressure 8 mPa (vacuum).

5.5.3 Conclusions

In analogy to synthetic polymers, DNA molecules appear to bundle into nanoscale fibers of practically infinite length; centimeter-long fibers with diameters down to 10 nm (see Fig. 5.19b) were observed. Electrospinning of DNA provides bundle stretched fiber and coiling structure and would be a useful technique for preparing thin ultralong DNA fibers onto a substrate for further characterization. Molecular combing is an efficient method for stretching and the alignment of DNA [81], however the length is not infinite compared to production by electrospinning. In addition, the advantage of electrospinning over a standard adsorption method is the DNA fiber can be deposited over a small hole, which suitable for characterization by TEM [80]. For applications, adsorption of DNA on a planar substrate or curved surface (gold nanoparticle) has been a very popular for biosensor applications because DNA can selectively bind to other molecules or metal ions and more stable than antibodies [82]. Thus, centimeter-long DNA fibers and the possibility to deposit them on various substrates (demonstrated in the case of the hydrophobin) might be used for producing a biosensor (multi-bindings along centimeter fiber or the coiling structure).

▲ Summary

This chapter uses the optimized parameters from Chapter 4 for electrospinning of pure globular proteins. Much of this chapter presents the fibers that produced from the solution of protein without adding polymers.

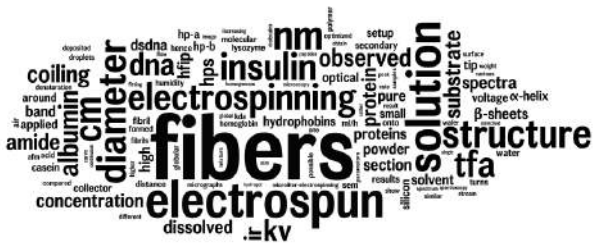

The diameter of albumin fiber can be reduced to below 10 nm by using the microliter electrospinning at extreme far from the collector with an air stream. The secondary structure of proteins fibers was studied in comparison to powders. The results indicate denaturation of proteins when they were dissolved in the solvent. In addition, rheology property of the protein solution suggests a minimum value of the *Oh*. Important parameters and conclusions of this thesis will be mentioned in more detail in the next chapter.

5.6 References

[1] C.P. Barnes, M.J. Smith, G.L. Bowlin, S.A. Sell, T. Tang, J.A. Matthews, D.G. Simpson, J.C. Nimtz. Feasibility of Electrospinning the Globular Proteins Hemoglobin and Myoglobin, *J. Eng. Fiber Fabr.* **1**: 16, 2006.

[2] Y. Dror, T. Ziv, V. Makarov, H. Wolf, A. Admon, E. Zussman. Nanofibers Made of Globular Proteins, *Biomacromolecules* **9**: 2749, 2008.

[3] J.A. Matthews, G.E. Wnek, D.G. Simpson, G.L. Bowlin. Electrospinning of Collagen Nanofibers, *Biomacromolecules* **3**: 232-238, 2002.

[4] G.E. Wnek, M.E. Carr, D.G. Simpson, G.L. Bowlin. Electrospinning of Nanofiber Fibrinogen Structures, *Nano Lett.* **3**: 213, 2003.

[5] M. Li, M.J. Mondrinos, M.R. Gandhi, F.K. Ko, A.S. Weiss, P.I. Lelkes. Electrospun protein fibers as matrices for tissue engineering, *Biomaterials* **26**: 5999, 2005.

[6] C. Branden, J. Tooze. Introduction to Protein Structure 2nd Edition, New York: Garland Publishing Company, 1998.

[7] O.S. Makin, E. Atkins, P. Sikorski, J. Johansson, L.C. Serpell. Molecular basis for amyloid fibril formation and stability, *PNAS* **102**: 315, 2005.

[8] S. Klammt, S. Mitzner, J. Stange, B. Brinkmann, B. Drewelow, J. Emmrich, S. Liebe, R. Schmidt. Albumin-binding function is reduced in patients with decompensated cirrhosis and correlates inversely with severity of liver disease assessed by model for end-stage liver disease, *Eur. J. Gastroenterol. Hepatol.* **19**: 257, 2007.

[9] T. Ozeki, V. Verma, M. Uppalapati, Y. Suzuki, M. Nakamura, J.M. Catchmark, W.O. Hancock. Surface-Bound Casein Modulates the Adsorption and Activity of Kinesin on SiO_2 Surfaces, *Biophys. J.* **96**: 3305-3318, 2009.

[10] J. Xie, Y.-L. Hsieh. Ultra-high surface fibrous membranes from electrospinning of natural proteins: casein and lipase enzyme, *J. Mater. Sci.* **38**: 2125, 2003.

[11] Y. Yang, X. Li, S. He, L. Cheng, F. Chen, S. Zhou, J. Weng. Biodegradable ultrafine fibers with core-sheath structures for protein delivery and its optimization, *Polym. Adv. Technol.* **22**: 1842, 2011.

[12] S.K. Tiwari, S. Venkatraman. Electrospinning pure protein solutions in core-shell fibers, *Polym. Int.* **61**: 1549, 2012.

[13] S. Koombhongse, W. Liu, D.H. Reneker. Flat Polymer Ribbons and Other Shapes by Electrospinning, *J. Polym. Sci. B Polym. Phys.* **35**: 2598, 2001.

[14] S. Maheshwari, H.-C. Chang. Assembly of Multi-Stranded Nanofiber Threads through AC Electrospinning, *Adv. Mater.* **21**: 349, 2009.

[15] A.L. Yarin, W. Kataphinan, D.H. Reneker. Branching in electrospinning of nanofibers, *J. Appl. Phys.* **98**: 064501, 2005.

[16] T. Güler, K. Sahbudak, S. Cetinkaya, U. Akdemir. Electrochemical study of pyrite-ovalbumin interaction in relation to flotation, *Trans. Nonferrous Met. Soc. China* **23**: 2766, 2013.

[17] C. Lara, S. Gourdin-Bertin, J. Adamcik, S. Bolisetty, R. Mezzenga. Self-Assembly of Ovalbumin into Amyloid and Non-Amyloid Fibrils, *Biomacromolecules* **13**: 4213, 2012.

[18] H.Y. Hu, H.N. Du. α-to-β Structural Transformation of Ovalbumin: Heat and pH Effects, *J. Protein Chem.* **19**: 177, 2000.

[19] J.A. Huntington, P.E. Stein. Structure and properties of ovalbumin, *J. Chromatography B* **756**: 189, 2001.

[20] K.-I. Minato, K. Ohkawa, H. Yamamoto. Chain Conformations of Poly(γ-benzyl-*L*-glutamate) Pre and Post an Electrospinning Process, *Macromol. Biosci.* **6**: 487, 2006.

[21] D. Cialla, T. Deckert-Gaudig, C. Budich, M. Laue, R. Mller, D. Naumann, V. Deckert, J. Popp. Raman to the limit: tip-enhanced Raman spectroscopic investigations of a single tobacco mosaic virus, *J. Raman Spectrosc.* **40**: 240, 2009.

[22] F. Huth, A. Govyadinov, S. Amarie, W. Nuansing, F. Keilmann, R. Hillenbrand. Nano-FTIR Absorption Spectroscopy of Molecular Fingerprints at 20 nm Spatial Resolution, *Nano Lett.* **12**: 3973, 2012.

[23] I. Amenabar, S. Poly, W. Nuansing, E.H. Hubrich, A.A. Govyadinov, F. Huth, R. Krutokhvostov, L. Zhang, M. Knez, J. Heberle, A.M. Bittner, R. Hillenbrand. Structural analysis and mapping of individual protein complexes by infrared nanospectroscopy, *Nat. Commun.* **4**: doi:10.1038/ncomms3890, 2013.

[24] M. Brehm, T. Taubner, R. Hillenbrand, F. Keilmann. Infrared Spectroscopic Mapping of Single Nanoparticles and Viruses at Nanoscale Resolution, *Nano Lett.* **6**: 1307, 2006.

[25] F. Keilmann, R. Hillenbrand. Nano-Optics and Near-Field Optical Microscopy, Artech House, Boston/London, 2008.

[26] L. Whitmore, B. Woollett, A.J. Miles, D.P. Klose, R.W. Janes, B.A. Wallace. PCDDB: the protein circular dichroism data bank, a repository for circular dichroism spectral and metadata, *Nucleic Acids Res.* **39**: D480, 2011.

[27] C. Louis-Jeune, M.A. Andrade-Navarro, C. Perez-Iratxeta. Prediction of protein secondary structure from circular dichroism using theoretically derived spectra, *Proteins* **80**: 374, 2012.

[28] M. Muzaffar, A. Ahmad. The Mechanism of Enhanced Insulin Amyloid Fibril Formation by NaCl Is Better Explained by a Conformational Change Model, *Plos One* **6**: e27906, 2011.

[29] M. Bouchard, J. Zurdo, E.J. Nettleton, C.M. Dobson, C.V. Robinson. Formation of insulin amyloid fibrils followed by FTIR simultaneously with CD and electron microscopy, *Prot. Sci.* **9**: 1960-1967, 2000.

[30] I. Arada, J.L.R Arrondo. An Infrared Study of Fibril Formation in Insulin from Different Sources, in the Supramolecular Structure and Function 9, Editor by G. Pifat-Mrzljak, Springer Netherlands, ISBN 978-1-4020-6465-4, 2007.

[31] M.I. Ivanova, S.A. Sievers, M.R. Sawaya, J.S. Wall, D. Eisenberg. Molecular basis for insulin fibril assembly, *Proc. Natl Acad. Sci.* **106**: 18990-18995, 2009.

[32] O.M. Selivanova, O.V. Galzitskaya. Structural polymorphism and possible pathways of amyloid fibril formation on the example of insulin protein, *Biochemistry* **77**: 1237-1247, 2012.

[33] A. Raheja, A. Agarwal, V. Muthuvijayan, T.S. Chandra, T.S. Natarajan. Studies on Encapsulation of Bovine Serum Albumin, Lysozyme and Insulin Through Coaxial Electrospinning, *J. Biomater. Tissue Eng.* **3**: 669-672, 2013.

[34] A. Barth, C. Zscherp. What vibrations tell us about proteins, *Quart. Rev. Biophys.* **35**: 369-430, 2002.

[35] A. Adochitei, G. Drochioiu. Rapid characterization of peptide secondary structure by FT-IR spectroscopy, *Rev. Roum. Chim.* **56**: 783-791, 2011.

[36] D.M. Byler, H. Susi. Examination of the secondary structure of proteins by deconvolved FTIR spectra, *Biopolymers* **25**: 469-487, 1986.

[37] J.T. Pelton, L.R. McLean. Spectroscopic Methods for Analysis of Protein Secondary Structure, *Anal. Biochem.* **277**: 167-176, 2000.

[38] E. Bramanti, E. Benedett. Determination of the secondary structure of isomeric forms of human serum albumin by a particular frequency deconvolution procedure applied to Fourier transform IR analysis, *Biopolymers* **38**: 639-653, 1996.

[39] J.G.H. Wessels. Fungal hydrophobins: proteins that function at an interface, *Trends in Plant Sci. Rev.* **1**: 9-15, 1996.

[40] M.B. Linder, G.R. Szilvay, T. Nakari-Setälä, M.E. Penttilä. Hydrophobins: the protein-amphiphiles of filamentous fungi, *FEMS Microbiology Rev.* **29**: 877-896, 2005.

[41] W. Wohlleben, T. Subkowski, C. Bollschweiler, B. von Vacano, Y. Liu, W. Schrepp, U. Baus. Recombinantly produced hydrophobins from fungal analogues as highly surface-active performance proteins, *Eur. Biophys. J.* **39**: 457-468, 2010.

[42] H. Wosten, O. De Vries, J. Wessels. Interfacial Self-Assembly of a Fungal Hydrophobin into a Hydrophobic Rodlet Layer, *Plant Cell* **5**: 1567-1574, 1993.

[43] H.A. Wösten. Hydrophobins: Multipurpose Proteins, *Annu. Rev. Microbiol.* **55**: 625-646, 2001.

[44] H.J. Hektor, K. Scholtmeijer. Hydrophobins: Proteins with potential, *Curr. Opin. Biotechnol.* **16**: 434-439, 2005.

[45] P.W. Cox, P. Hooley. Hydrophobins: New prospects for biotechnology, *Fungal Biol. Rev.* **23**: 40-47, 2009.

[46] S. Hou, X. Li, X. Li, X. Feng. Coating of hydrophobins on three-dimensional electrospun poly(lactic-co-glycolic acid) scaffolds for cell adhesion, *Biofabrication* **1**: 035004, 2009.

[47] M. Zhang, Z. Wang, Z. Wang, S. Feng, H. Xu, Q. Zhao, S. Wang, J. Fanga, M. Qiao, D. Kong. Immobilization of anti-CD31 antibody on electrospun poly(ε-caprolactone) scaffolds through hydrophobins for specific adhesion of endothelial cells, *Colloids. Surf. B* **85**: 32-39, 2011.

[48] E. Goormaghtigh, V. Raussens, J.M. Ruysschaert. Attenuated total reflection infrared spectroscopy of proteins and lipids in biological membranes, *Biochim. Biophys. Acta.* **1422**: 105-185, 1999.

[49] M.L. de Vocht, K. Scholtmeijer, E.W. van der Vegte, O.M. de Vries, N. Sonveaux, H.A. Wösten, J.M. Ruysschaert, G. Hadziloannou, J.G. Wessels, G.T. Robillard. Structural characterization of the hydrophobin SC3, as a monomer and after self-assembly at hydrophobic/hydrophilic interfaces, *Biophys. J.* **74**: 2059-2068, 1998.

[50] X. Wang, M.L. de Vocht, J. de Jonge, B. Poolman, G.T. Robillard. Structural changes and molecular interactions of hydrophobin SC3 in solution and on a hydrophobic surface, *Protein Sci.* **11**: 1172-1181, 2002.

[51] M.L. de Vocht, I. Reviakine, W.P. Ulrich, W. Bergsma-Schutter, H.A. Wösten, H. Vogel, A. Brisson, J.G. Wessels, G.T. Robillard. Self-assembly of the hydrophobin SC3 proceeds via two structural intermediates, *Protein Sci.* **11**: 1199-1205, 2002.

[52] A. Mashaghi, A. Katan. A physicist's view of DNA. *De Physicus* **3**: 59-61, 2013.

[53] E.S. Andersen, M. Dong, M.M. Nielsen, K. Jahn, R. Subramani, W. Mamdouh, M.M. Golas, B. Sander, H. Stark, C.L. Oliveira, J.S. Pedersen, V. Birkedal, F. Besenbacher, K.V. Gothelf, J. Kjems. Self-assembly of a nanoscale DNA box with a controllable lid, *Nature* **459**: 73-77, 2009.

[54] D. Han, S. Pal, Y. Liu, H. Yan. Folding and cutting DNA into reconfigurable topological nanostructures, *Nat. Nanotechnol.* **5**: 712-717, 2010.

[55] A.V. Pinheiro, D. Han, W.M. Shih, H. Yan. Challenges and opportunities for structural DNA nanotechnology, *Nat. Nanotechnol.* **6**: 763-772, 2011.

[56] A. Kuzyk, R. Schreiber, Z. Fan, G. Pardatscher, E.M. Roller, A. Högele, F.C. Simmel, A.O. Govorov, T. Liedl. DNA-based self-assembly of chiral plasmonic nanostructures with tailored optical response, *Nature* **483**: 311-314, 2012.

[57] J.B. Lee, S. Peng, D. Yang, Y.H. Roh, H. Funabashi, N. Park, E.J. Rice, L. Chen, R. Long, M. Wu, D. Luo. A mechanical metamaterial made from a DNA hydrogel, *Nat. Nanotechnol.* **7**: 816-820, 2012.

[58] J.D. Watson, F.H.C. Crick. Molecular Structure of Nucleic Acids, *Nature* **171**: 737-738, 1953.

[59] J.D. Watson, F.H.C. Crick. Genetical Implications of the Structure of Deoxyribonucleic Acid, *Nature* **171**: 964-967, 1953.

[60] A. Ghosh, M. Bansal. A glossary of DNA structures from A to Z, *Acta Cryst.* **D59**: 620-626, 2003.

[61] X. Fang, D.H. Reneker. DNA Fibers by Electrospinning, *J. Macromol. Sci. Phys.* **B36**: 169-173, 1997.

[62] T. Takahashi, M. Taniguchi, T. Kawai. Fabrication of DNA Nanofibers on a Planar Surface by Electrospinning, *Jpn. J. Appl. Phys.* **44**: L860-L862, 2005.

[63] L.M. Bellan, E.A. Strychalski, H.G. Craighead. Electrospun DNA nanofibers, *J. Vac. Sci. Technol. B* **25**: 2255, 2007.

[64] Y. Liu, J. Chen, N.T. Anh, C.O. Too, V. Misoska, G.G. Wallace. Nanofiber Mats from DNA, SWNTs, and Poly(ethylene oxide) and Their Application in Glucose Biosensors, *J. Electrochem. Soc.* **155**: K100-K103, 2008.

[65] M. Hadjiargyrou. Incorporation of DNA into Electrospun Nanofibrous Scaffolds: Fundamental Characterization Studies and Gene Delivery, in the Nanofibers - Production, Properties and Functional Applications, T. Lin (Ed.), ISBN: 978-953-307-420-7, *InTech.* 383-400, 2011.

[66] D. Navarathne, Y. Ner, M. Jain, J.G. Grote, G.A. Sotzing. Fabrication of DNA-magnetite hybrid nanofibers for water detoxification, *Mater. Lett.* **65**: 219-221, 2011.

[67] L.M. Bellan, J.D. Cross, E.A. Strychalski, J. Moran-Mirabal, H.G. Craighead. Individually Resolved DNA Molecules Stretched and Embedded in Electrospun Polymer Nanofibers, *Nano Lett.* **6**: 2526-2530, 2006.

[68] D. Sun, C. Chang, S. Li, L. Lin. Near-Field Electrospinning, *Nano Lett.* **6**: 839-842, 2006.

[69] C. Chang, K. Limkrailassiri, L. Lin. Continuous near-field electrospinning for large area deposition of orderly nanofiber patterns, *Appl. Phys. Lett.* **93**: 123111, 2008.

[70] C.H. Hellmann, J. Belardi, R. Dersch, A. Greiner, J.H. Wendorff, S. Bahnmueller. High Precision Deposition Electrospinning of nanofibers and nanofiber nonwovens, *Polymer* **50**: 1197-1205, 2009.

[71] G.S. Bisht, G. Canton, A. Mirsepassi, L. Kulinsky, S. Oh, D. Dunn-Rankin, M.J. Madou. Controlled Continuous Patterning of Polymeric Nanofibers on Three-Dimensional Substrates Using Low-Voltage Near-Field Electrospinning, *Nano Lett.* **11**: 1831-1837, 2011.

[72] D.H. Reneker, A.L. Yarin. Electrospinning jets and polymer nanofibers, *Polymer* **49**: 2387-2425, 2008.

[73] G. Barnes, J. Mackenzie. Height of Fall Versus Frequency in Liquid Rope-Coil Effect, *Am. J. Phys.* **27**: 112-115, 1959.

[74] T. Han, D.H. Reneker, A.L. Yarin. Buckling of jets in electrospinning, *Polymer* **48**: 6064-6076, 2007.

[75] S.W. Morris, J.H.P. Dawes, N.M. Ribe, J.R. Lister. The meandering instability of a viscous thread, *Phys. Rev. E* **77**: 066218, 2008.

[76] Y. Xin, D.H. Reneker. Garland formation process in electrospinning, *Polymer* **53**: 3629-3635, 2012.

[77] Y. Xin, D.H. Reneker. Hierarchical polystyrene patterns produced by electrospinning, *Polymer* **53**: 4254-4261, 2012.

[78] H-Y. Kim, M. Lee, K.J. Park, S. Kim, L. Mahadevan. Nanopottery: Coiling of Electrospun Polymer Nanofibers, *Nano Lett.* **10**: 2138-2140, 2010.

[79] J. Piškur, A. Rupprechtb. Aggregated DNA in ethanol solution, *FEBS Lett.* **375**: 174-178, 1995.

[80] F. Gentile, M. Moretti, T. Limongi, A. Falqui, G. Bertoni, A. Scarpellini, S. Santoriello, L. Maragliano, R.P. Zaccaria, E. Fabrizio. Direct Imaging of DNA Fibers: The Visage of Double helices, *Nano Lett.* **12**: 6453-6458, 2012.

[81] A. Bensimon, A. Simon, A. Chiffaudel, V. Croquette, F. Heslot, D. Bensimon. Alignment and Sensitive Detection of DNA by a Moving Interface, *Science* **265**: 2096-2098, 1994.

[82] J. Liu. Adsorption of DNA onto gold nanoparticles and graphene oxide: surface science and applications, *Phys. Chem. Chem. Phys* **14**: 10485-10496, 2012.

Chapter 6

Conclusions

The objectives, hypotheses, and theories, laid out in Chapters 1 and 2, were combined with a large array of techniques (Chapter 3) to find new methods, new materials, and new structures, based on electrospun self-assembling peptides and proteins (Chapters 4 and 5).

Four electrospinning setups were constructed (see schematics in Fig. 6.1 and descriptions in Chapter 3.2). The conventional setup is suitable for studying electrospinning of peptides and proteins, when concentrated solutions of at least 0.1 ml volume are available, However, some substances are available only in small amounts, and generally testing new processes under various parameters is simpler and faster from small amounts: This requires the microliter electrospinning setup, which works down to some μl of solution. The third and fourth tools were developed specifically to reduce the diameter of protein fibers to below 10 nm.

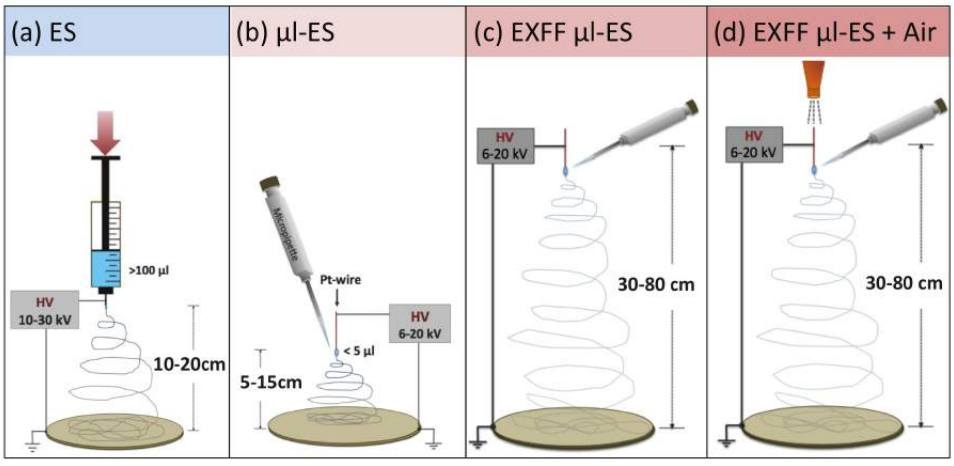

Figure 6.1: Schematics of the electrospinning setups used in this work. (a) Conventional electrospinning setup, (b) microliter electrospinning, (c) microliter electrospinning at extreme far-field, and (d) microliter electrospinning at extreme far-field with an air stream.

The results from both Chapter 4 and 5 (see the summary in Fig. 6.2) support the hypothesis of this work: electrospinning of pure biomolecules without polymer blends is possible, when they show self-assembly in 1D, 2D, or 3D; when they can be dissolved in a suitable organic solvent at high concentration; and when the electrospinning parameters (voltage, distance, flow rate, air humidity) are optimized. For the aromatic peptides, intermolecular interactions (mainly the hydrogen bonds and π-π stacking interactions) determine the self-assembly. The electrostatic force exerted by the electrospinning process assists assembled peptides to arrange into long fibers. The electrospinning of pure globular proteins is possible; however, they are usually denatured: their secondary structures (α-helices, β-sheets, etc.) are changed already by dissolution in the organic solvent. The electrospinning itself appears to be much less damaging.

It is notoriously difficult to predict electrospinning parameters, so they are usually totally based on empirical tests. It is even harder to predict the electrospinnability - probably all substances can be spun, depending on as yet not tested parameters. For peptides, the spinnability might be predicted with three methods, as proposed in Chapter 4.4. Method 1) is based on the electron acceptor (AN) and on the donor number (DN) of the solvent; method 2) uses polarized Raman spectra of the peptide as it is usually provided (i.e. in powder form); and method 3) employs rheological characterization of the peptide solution. The third method was applied and tested for peptides and globular proteins; the results indicate that a minimum value of the Ohnesorge number (Oh), $\approx$10, is required for electrospinning.

General rules for suitable solvents, optimization conditions and parameters are summarized in the following.

- **Substance selection:** The peptide should be self-assembling, so it should have ample options for intermolecular bonds, especially hydrogen bonds. Aromatic side groups can direct assembly, but they appear to leave less options for hydrogen bonds, hence short aromatic peptides are preferable (their end groups can then dominate assembly). Globular proteins such as albumin, hemoglobin, casein, lysozyme and insulin can also be electrospun without adding polymers. Fibrous proteins (not tested here) should behave rather similar to polymers, and are supposed to be spun without problems.
- **Dissolution:** Aromatic peptides and globular proteins should be dissolved in a strongly electrophilic solvent (AN - DN $\geq$ 88), e.g. in hexafluoroisopropanol (HFIP) or in trifluoroacetic acid (TFA). The solution concentration should be high (above $\approx$5 %(wt/wt) or even some ten %), in order to reach strong intermolecular interactions, and to achieve suitable rheological properties (the results suggest an Ohnesorge number (Oh) above 10.
- **Electrospinning:** The applied voltage, the distance to the collector, the flow rate, and the air humidity (especially for electrospinning of proteins) are important parameters, affecting the morphology of the fibers. For the studied biomolecules, typical optimization conditions are 10−15 kV, 12−15 cm, 0.2−0.5 ml/h (flow rate as small as possible for the microliter electrospinning setup), and below 30 % humidity. For ultrathin protein fibers (< 20 nm diameter), electrospinning should proceed at an extreme distance (60−75 cm), with 20−35 kV, and with an additional air stream of $\sim$1 m.s^{-1} (from above the tip).

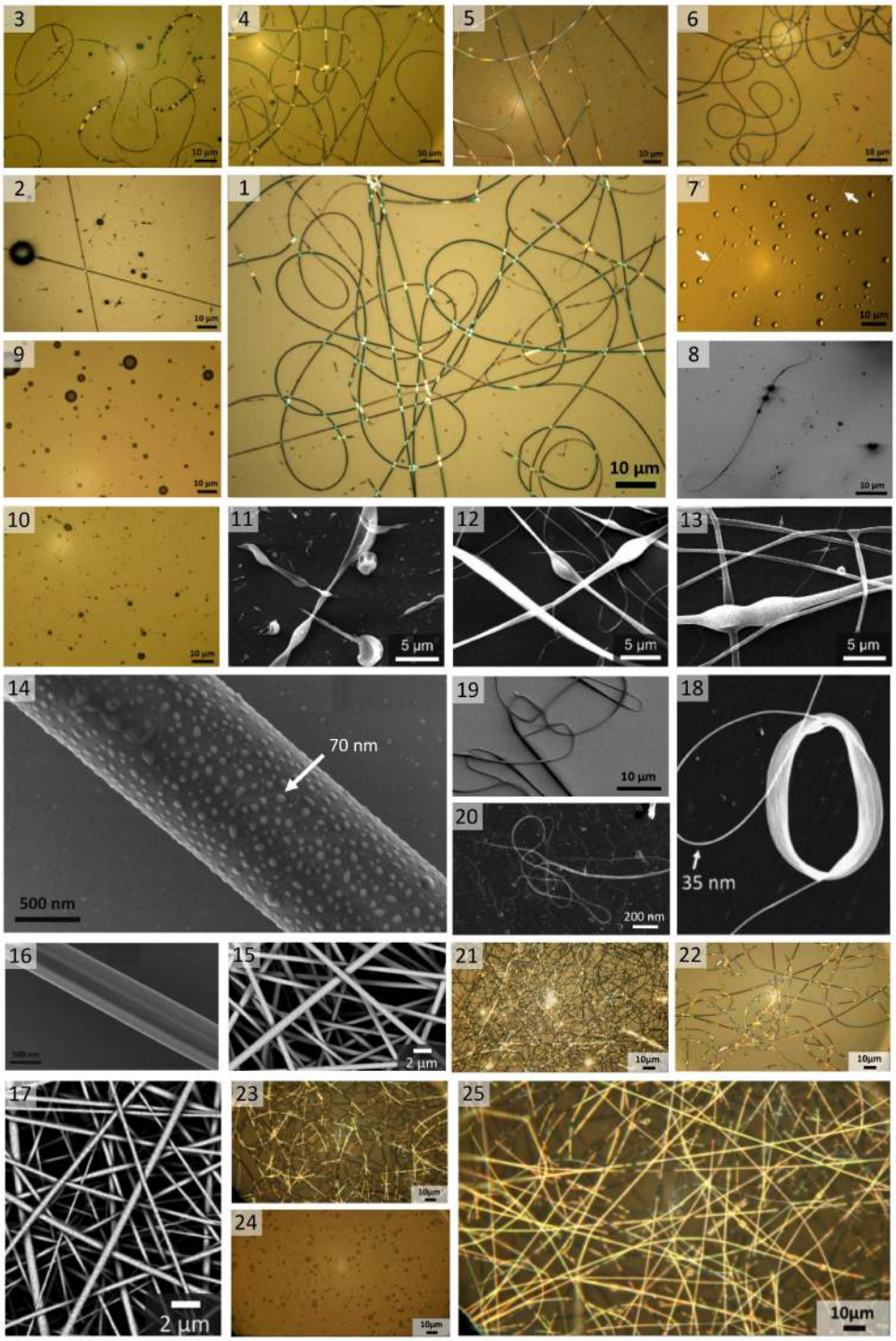

Figure 6.2: Summary of electrospinning results, optical (color) and electron micrographs (black/white), (1) FF, (2) Fmoc-FG, (3-4) GF, (5) GFG, (6) $(Fmoc\text{-}C)_2$, (7-8) Fmoc-G, (9) 9FM, (10) $Fmoc\text{-}NH_2$, (11) TPP, (12) FF-TPP, (13) FF/FF-TPP, (14-15) HP-A, (16-17) HP-B, (18) ds-DNA, (19) insulin, (20-21) albumin, (22) hemoglobin, (23-24) lysozyme, and (25) casein.

For the possible application of purely biomolecular electrospun fibers, it is interesting that peptide and protein fibers (100 nm up to micrometers) show morphologies similar to those of typical biocompatible polymer fibers. In addition, their chemistry suggests a very high biocompatibility that should allow use for highly critical biological and medical applications, e.g. the proliferation and differentiation of stem cells. Scaffolds made from pure proteins or peptides fibers present naturally occurring chemical groups to the cells; moreover, selecting proteins (or amino acid sequences) from families of proteins that naturally attach to cells, would allow to construct a morphologically and biochemically optimized environment. Relevant experiments have been carried out recently at nanoGUNE, and several publications are now being prepared; a detailed discussion is outside the scope of this thesis.

More generally, electrospun biofunctional scaffolds are discussed for many more medical uses, e.g. wound dressing, tissue engineering, drug delivery, drug release, and applications in neurodegeneration. Many of these fields are now moving from research to development.

For biomolecules of less specific functionality, the fiber morphology, mechanics and surface chemistry can provide an advantage over polymers. Such molecules have to be available in large amounts, such as casein from milk, sugars from plants, and hydrophobins (from fungi, but produced in bacteria). They can be electrospun and applied e.g. in the textile applications, for protective clothing, for packaging, or as filter media. In the same way that ceramic nanofibers are formed on templates of electrospun polymer fibers (see Chapter 1.1), also these biomolecules can serve as natural polymer sources for the production of mineralized nanofibers. In this case the ceramic coating provides the functionality, which can be targeted to a vast range of energy applications and electronics devices.

▼ Future work

The conclusions of this work show that the electrospinning of pure biomolecules is possible for short peptides containing aromatic residues, and for globular proteins. They also indicate that nonaromatic peptides and fibrous proteins can be spun with less optimization effort. The difference between standard electrospinning of polymers and small molecules such as peptides is that they can only be spun, when they are able to assemble. As described in the expected impact of this thesis (Chapter 1.4), future work will combine the experience, parameters and results from electrospinning of other biomolecules, e.g. peptide amphiphiles, cyclic peptides, membrane proteins. The number of biomolecular substances for electrospinning can further increase, even above the number of useful polymers, so the potential applications in life science will likely increase.

"Biomolecules" can also include sugars, or complex mixtures, and even edible substances (see an example in Fig. 6.3). This could bring electrospinning into food science and technology. Electrospinning processes and tools based on this work could be incorporated in food processing, or used in creative/innovative restaurants, or even at home.

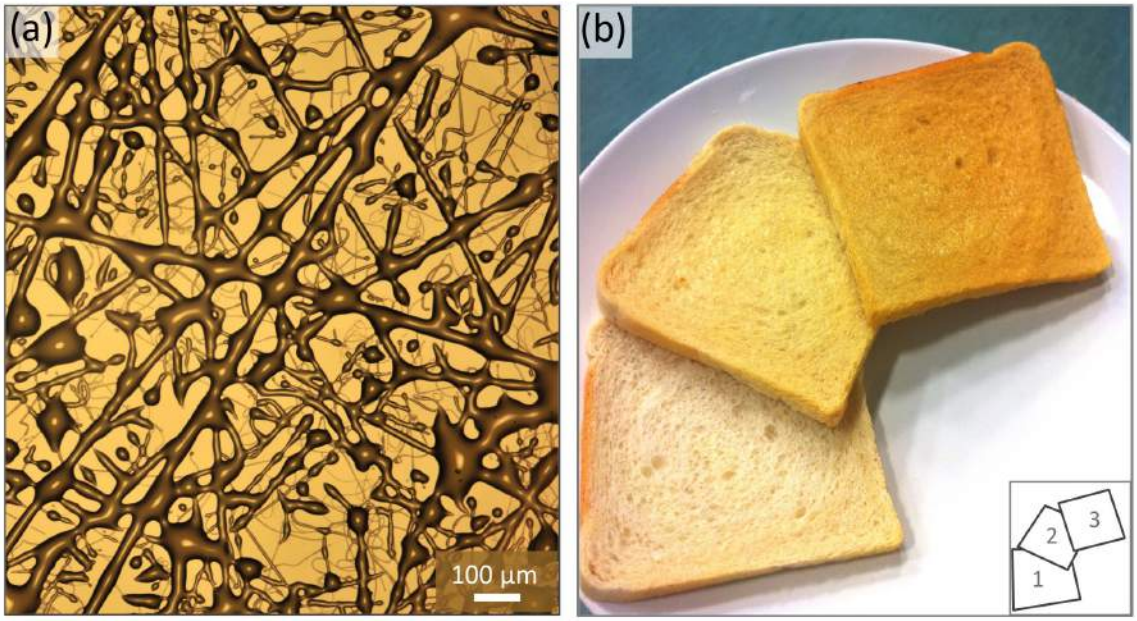

Figure 6.3: Example results of edible electrospun fibers, (a) optical micrograph of caramel fibers electrospun on glass, (b) photos of the caramel fibers collected on bread: (1) a fresh bread, (2) caramel volume 1/20 tea spoon, and (3) caramel volume 1/10 tea spoon.

The microliter electrospinning setup is simple and requires less equipment than the conventional setup. Moreover, it is more convenient and suitable for preliminary tests. This setup can be further designed and developed towards a commercial device, tailored for microscale applications (substances available in small amounts), or for a simple setup used in a high school (see a prototype of a portable setup in Fig. 6.4).

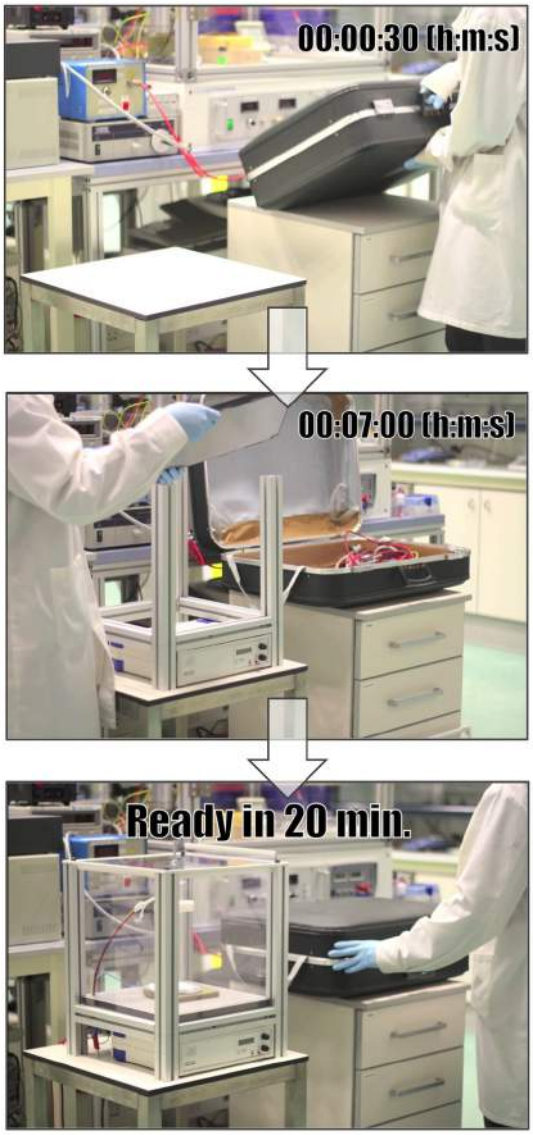

Figure 6.4: Prototype of a portable electrospinning setup that can be assembled (ready to use) in 20 min. The design and operation principles were developed from the microliter setup.

List of publications

This thesis is based on the following publications:

1. W. Nuansing*, A. Rebollo, J.M. Mercero, J. Zuñiga, A.M. Bittner. Vibrational spectroscopy of self-assembling aromatic peptide derivates, *J. Raman Spectrosc.* **43**: 1397, 2012. *(Ch. 4)*
2. W. Nuansing*, E. Georgilis, T. Oliveira, G. Charalambidis, A. Eleta, A.G. Coutsolelos, A. Mitraki, A.M. Bittner. Electrospinning of tetraphenylporphyrin compounds into wires, *Part. Part. Syst. Charact.* **31**: 88, 2014. *(Ch. 4)*
3. W. Nuansing*, D. Frauchiger, F. Huth, A. Rebollo, R. Hillenbrand, A.M. Bittner. Electrospinning of peptide and protein fibres: Approaching the molecular scale, *Faraday Discuss.* **166**: 209, 2013. *(Ch. 5)*

Other publications:

- F. Huth, A. Govyadinov, S. Amarie, W. Nuansing*, F. Keilmann, R. Hillenbrand. Nano-FTIR absorption spectroscopy of molecular fingerprints at 20 nm spatial resolution, *Nano Lett.* **12**: 3973, 2012.
- I. Amenabar, S. Poly, W. Nuansing*, E.H. Hubrich, F. Huth, R. Krutokhvostov, L. Zhang, M. Knez, J. Heberle, A.M. Bittner, R. Hillenbrand. Nano-FTIR for secondary structure analysis of single protein complexes, *Nat. Commun.*, 2013, DOI: 10.1038/ncomms3890.

Acknowledgements

I would like to express my gratitude to all who supported and helped me finish this thesis, namely six groups of people along **six directions** of my life.

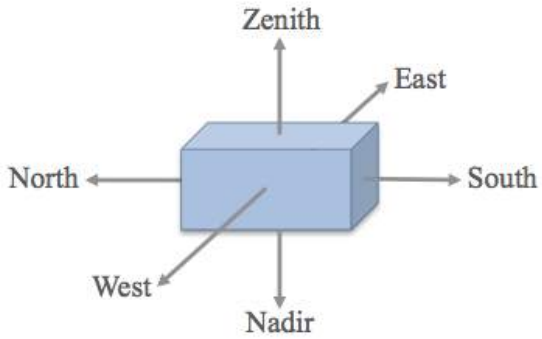

South: Thanks to all my TEACHERS, a very special thanks to my research supervisor Prof. Alexander M. Bittner for his support and motivation throughout this work and his helpful suggestions. I humbly thank Prof. José M. Pitarke and Prof. Andreas Berger for giving me the opportunity to work at nanoGUNE. Thanks to all professors in nanoGUNE for motivating and inspiring me to pursue science. I would like to thank professors in the Master in Nanoscience program at the University of the Basque Country (UPV/EHU), Prof. Angel Alegría and Prof. José M. Asua for all their support, especially at the beginning of my studies in Donostia. Thanks to Prof. Angel Rubio, Dr. Marius Wanko and Dr. Yann Pouillon (nano-bio spectroscopy group, UPV/EHU), Dr. Txema Mercero (Arina cluster) for help with computer simulations. Thanks to Prof. Javier Zuñiga and Prof. Gotzon Madariaga (Condensed Matter Physics Dept., UPV/EHU) for their collaboration involving the single crystalline characterization, and Prof. Anna Mitraki and co-workers for their collaboration in the electrospinning of TPP.

Thanks to all professors affiliated with the Department of Physics, Faculty of Science, Khon Kaen University (KKU). Thanks especially to my former supervisor Prof. Santi Maensiri for your patience, enthusiasm, and research skills. I would like to thank all teachers and professors in the Development and Promotion of Science and Technology Talents Project (DPST) and the Thailand Graduate Institute of Science and Technology (TGIST). Many thanks to all teachers who inspire greatness and who changed my life at the Kaen Nakhon Witthayalai School (KNW), Phangkhon Witthayakhom School (PVK), Phangkhon Jampasamakkheewitthaya School (PKJ), as well as my first teacher in electronics and science, A. Pornsak Kasemsan.

North: Thanks to all my FRIENDS! I would like to acknowledge the entire self-assembly group and every "nanopeople" at nanoGUNE for their funny, informative conversations, and for making me feel at home. I was very happy and never felt alone, even while living in a new country. Thanks so much to my friends at nanoGUNE, KKU, and KNW for proofreading this thesis. I would like to express special thanks to Dr. Amaia Rebollo the postdoc of self-assembly group for a very hard work to find a suitable solvent and preparing the solutions and basically helping me with everything, and with every problem. Last but not least, many thanks to all my friends in the Master program, PhD program, classmates at the UPV/EHU, KKU, KNW, PVK, PKJ, and my flatmates at Zabaleta 34, Berio 31, Villa Bat for those happy moments and making this a very good time in my life.

East: Best of thanks to my PARENTS, the only ones who could have loved me before and after I was born. Their love does not depend on any parameters, e.g. distance (> 10K km), time (>1 year). I would like to express my deepest thanks to my dear parents, as well as my grandmother, my brother, and all my family members for their never-ending support and love for me.

West: Thanks to my LOVE, "Men marry women with the hope they will never change. Women marry men with the hope they will change. Invariably they are both disappointed." — (A. Einstein). Thank you very much for being "just the way you are". You have always inspired and motivated me to be happy and enjoy life. I have a similar theory to M. Faraday rather than A. Einstein.

Nadir: Thanks to all WORKERS, this work cannot have been completed without support from all people who work behind the scenes, such as the support staffs at nanoGUNE and UPV/EHU. In particular, thanks to Miguel Odriozola, Maria Rezola, Itziar Otegui Feliz, and Ralph Gay. Special thanks to the security staff who work overnight and the cleaning staff who work early every morning. Thanks to all employees in Donostia, thanks to all chefs, waiters, waitresses, and everyone doing their best. These people make the city a clean, safe, and nice place to live. Many thanks to all internship students: Daniela Frauchiger, Amaia Benitez Andonegui, and Evangelos (Vangelis) Georgilis. There are many things that I have learned from your works and some results were also included in this thesis.

Zenith: Thanks to all SPIRITUAL LEADERS, we are all subject to birth, old age, sickness, and death. Whether we posses a lot of material things or have nothing, we are subject to the same things. Finally, I want to thank everyone who supported me and who wasn't mentioned herein. I offer you my help and assistance in whatever you do. I wish you all the very best of luck and a very happy :-)

Appendix A

Fibers via the ruler drawing technique

Around 1990s, the “ruler drawing technique” is a mysterious experiment for kids in Thailand. At that time, I was a child, I want to be older, so I made fibers from an orange peel and a plastic ruler. I put them over my upper lip, I had feeling that I have a beard. More than 20 years, I believed that the fibers are spread out from the orange peel. However, vibrational spectroscopy results, Infrared and Raman spectra (see Fig. A.1) concluded that the fibers are polystyrene. This means organic natural solvent (limonene) spread out from the orange peel dissolved polystyrene. Then it is stretched and leaving micro- and nanofibers (see Fig. A.2).

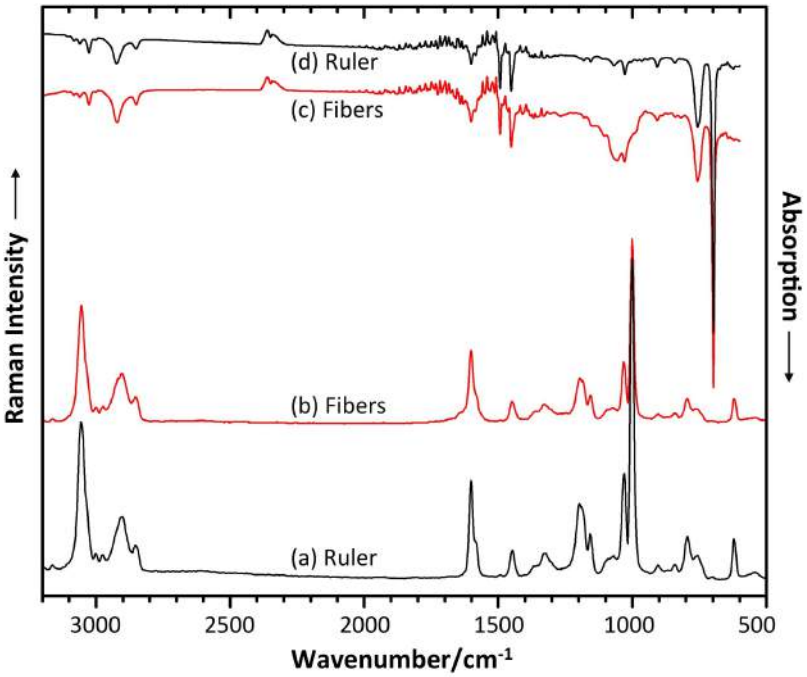

Figure A.1: Vibrational spectroscopy results, Raman (bottom) and IR spectra (top) of (a), (d) a ruler made from polystyrene, and (b), (c) fibers produced by the ruler drawing technique.

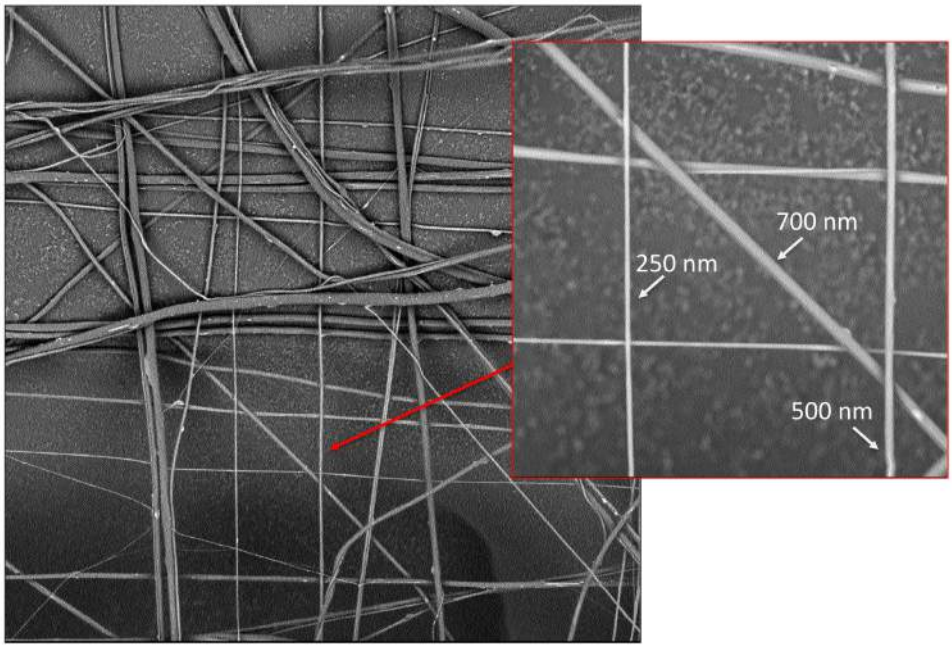

Figure A.2: SEM micrographs of the micro- and nanofibers produced by the ruler drawing technique on a carbon tape.

Appendix B

Infrared and Raman configurations

Table B.1: Vibrational assignment of 9FM.

Vibrational Modes	IR (Exp.)	IR (AIST.)	Raman (Fibers)	Raman (Lit.)	Frq. Sim.	Frq. Scaled.	Int. IR	Int. Raman
str. OH		3323vs			3652	3480	3.78	235.90
	3250vs							
i.p. sym. str. CH ring	3095vw	3145w	3063m	3070m	3238	3086	10.77	140.49
		3098w			3221	3070	35.54	325.58
i.p. asym. str. CH ring	3065w	3063w			3216	3064	44.36	162.42
	3049w	3039m	3040m	3048m	3206	3055	31.39	106.08
	3028w		3014vw		3200	3049	14.74	101.84
					3193	3043	7.06	71.07
					3188	3038	1.50	60.09
					3186	3036	6.22	33.68
asym. str. CH_2 + str. C_9H	2943w		2939w	2943w	3067	2922	53.95	36.05
	2930vw	2926w			3034	2892	3.70	125.22
sym. str. CH_2	2870w	2877w	2877w	2883w	3016	2874	45.14	90.34
i.p. bend. CH ring			1610s	1613vs	1667	1610	3.03	81.61
			1578m	1578s	1667	1610	0.11	343.56
					1640	1584	0.82	16.15
					1638	1582	0.70	15.13
bend. CH_2			1513vw		1557	1504	3.05	10.84
i.p. bend. CH ring	1477m	1477w	1481s	1483s	1534	1485	7.27	27.36
	1447s	1467m	1444w	1443w	1532	1482	1.02	63.53
		1451s			1509	1480	23.37	0.86
		1443s			1501	1451	15.22	16.62
wag. CH_2 + bend. COH	1418m				1451	1402	6.80	1.33
i.p. CH ring bend.		1367w	1347s	1348s	1413	1365	0.63	48.84
i.p. CH ring bend. + bend. C_9H	1316m	1329w			1374	1328	5.48	10.05
		1316w			1363	1317	0.30	7.09
i.p. CH ring bend.			1299s	1300s	1352	1306	0.26	104.71
bend. C_9H	1289m	1284w			1342	1296	2.31	24.88
bend. COH + bend. CH(H)	1208w		1227s	1226s	1277	1234	5.55	69.73
					1273	1229	26.42	57.21
bend. CH(H)	1190m	1187w			1242	1200	4.12	8.49
twi. CH_2 + bend. C_9H					1234	1192	1.60	9.46
i.p. CH ring bend.		1178w	1183w	1187w	1225	1184	2.38	12.21
					1221	1179	2.78	6.54
i.p. CH ring bend. + bend. CH(H) + bend. COH	1155w		1154m	1152m	1213	1172	4.58	26.63
i.p. CH ring bend.	1100m	1098w		1104w	1208	1166	4.77	7.76
					1151	1112	0.42	1.52
					1142	1103	4.88	12.31
i.p. CH ring bend. + roc. CH_2	1049s	1060s			1081	1045	14.90	2.46
		1043s						
i.p. CH ring bend. + roc. CH_2 + bend. COH	1025s	1034m			1071	1035	8.40	2.04
i.p. CH ring bend.		1022s	1023s	1022s	1061	1025	2.23	51.62
		1017vs						
i.p. ring def.	1007w	1012s			1041	1006	2.53	1.07
o.o.p. CH ring bend. + bend. CH + roc. CH_2	992w		999w	1000w	1024	989	5.99	10.79
o.o.p. CH ring bend.					1021	986	1.11	1.66

Table B.2: Vibrational assignment of 9FM (continued).

Vibrational Modes	IR (Exp.)	IR (AIST.)[1]	Raman (Fibers)	Raman (Lit.)[2]	Frq. Sim.	Frq. Scaled.	Int. IR	Int. Raman
o.o.p. CH ring bend.					1016	982	3.68	1.51
asym. str. CCO	940w	940w	983w	983w	1009	975	59.17	9.57
o.o.p. CH ring bend.	895w		881w	883w	982	948	1.43	2.05
					971	938	3.45	1.34
					917	886	3.47	1.78
					911	880	2.21	6.67
i.p. ring def.	868w	855w	857m	857m	882	852	12.31	10.82
o.o.p. CH ring bend. + bend. C_9H					825	797	0.10	1.35
i.p. ring def. + roc. CH_2	784w		786w	787w	816	788	1.79	1.42
o.o.p. CH ring bend.	756s	758vs	743m	743m	790	763	43.15	2.16
	739s	747m	728m	726m	774	748	6.84	5.13
		741s						
	728s	730s			772	727	65.91	3.74
		725m						
i.p. ring def.	648m	622w	648vw		753	698	1.69	20.48
	622m				678	656	6.02	0.39
					654	631	6.55	0.38
i.p. ring def. + roc. CH_2		594m	593vw	591w	618	597	5.56	3.37
o.o.p. ring def.		544w	543m	543m	589	569	0.37	0.59
		537w		513m	556	537	11.68	4.85
i.p. ring def.					528	510	0.38	3.98
o.o.p. CH ring bend. + bend. C_9H					469	453	0.10	2.04
o.o.p. ring def.					447	432	4.98	0.29
i.p. ring def.			416m	417m	427	412	0.24	7.22
o.o.p. ring def. + bend. CCO				391w	380	368	7.19	1.14
bend. CCO				343w	341	329	2.46	3.35
o.o.p. ring def. + bend. CCO					303	293	2.57	8.88
tor. COH			305w	304m	248	240	132.72	7.16
i.p. ring def.				213w	214	207	7.58	0.97
tor. CCC				196w	186	179	9.32	3.66
				157w	140	135	9.87	1.53
tor. ring				130m	123	119	1.08	1.20
					109	105	0.83	0.12
					72	70	0.33	7.57

[1] reference IR spectra downloaded from AIST (http://riodb.ibase.aist.go.jp/riohomee.html)
[2] reference Raman spectra downloaded from Sigma-Aldrich (http://www.sigmaaldrich.com)
C_9., the carbon atom connected to CH_2OH group; i.p., in-plane; o.o.p., out-of-plane; sym., symmetric; asym., asymmetric; str., stretching; bend., bending; wag., wagging; twi., twisting; roc., rocking; tor., torsional; def., deformational; s, strong; m, medium; w, weak; v, very; Exp., experiment; Lit., literature; Int., intensity; Frq., frequency; Sim., simulation; Scaled., the simulation spectra are scaled by 0.966 and 0.953 in frequency for wavenumbers < 2000 cm^{-1} and > 2000 cm^{-1}, respectively.

Table B.3: Vibrational assignment of Fmoc-G.

Vibrational Modes	IR (Powders)	IR (AIST.)	Raman (Powders)	Raman (Fibers)	Raman (Lit.)	Frq. Sim.	Frq. Scaled.	Int. IR	Int. Raman
str. OH	3321m	3320vs				3688	3556	63.85	98.36
str. NH						3620	3490	29.30	45.17
str. CH ring				3063m	3061m	3206	3091	10.54	590.04
	3069w	3069m				3205	3090	51.95	39.86
		3059m		3052w		3194	3079	42.81	115.18
						3192	3077	6.64	85.66
						3182	3067	3.14	55.62
			3049m	3046w	3044m	3180	3066	3.01	121.34
	3048w					3174	3060	12.22	74.01
						3174	3060	2.33	0.04
asym. str. (N)CH_2						3138	3025	1.79	38.38
asym. str. CH_2(O)		2966w				3119	3006	15.12	42.00
sym. str. (N)CH_2		2955m	2953m		2953m	3084	2973	21.21	126.84
sym. str. CH_2(O)	2954w					3074	2964	28.10	100.40
str. CH	2888vw	2891vw	2896m	2900w	2901m	3008	2900	9.05	122.68
str. CO(OH)	1736s	1742vs				1822	1772	385.63	10.14
str. CO(NH)	1696s	1700vs	1705w	1708vw	1706w	1788	1740	348.96	9.24
i.p. CCC ring def. + CH ring bend.						1657	1612	4.90	14.91
			1612vs	1611vs	1611vs	1656	1611	0.15	485.24
						1634	1590	0.80	0.68
			1580m	1580m	1581s	1629	1585	0.50	34.08
bend. NH	1548s	1545vs				1566	1523	371.63	1.19
		1540vs							
bend. CH_2(O)	1443m	1450s				1528	1487	50.24	8.03
i.p. CH ring bend.						1520	1479	6.83	8.44
			1482s	1481s	1481s	1520	1479	0.35	115.06
	1425m	1425m				1493	1452	20.07	1.49
			1440w	1443vw		1488	1448	7.55	7.26
(N)CH_2 bend.	1400m	1402m	1404vw	1403vw	1403vw	1467	1427	9.96	7.36
wag. CH_2(O)						1418	1380	9.13	4.69
i.p. CCC ring def. + CH ring bend. + wag. (N)CH_2			1346m	1344m	1347m	1392	1354	0.44	44.32
wag. (N)CH_2						1388	1351	2.32	6.71
bend. COH + str. CCO(H)	1346w					1367	1330	64.32	5.83
i.p. CH ring bend. + twi. CH_2(O)						1359	1322	11.58	7.21
						1339	1303	0.01	1.61
i.p. CH ring bend. + bend. CH			1297s	1297s	1299s	1332	1296	0.20	160.94
bend. CH						1316	1281	8.63	22.38
twi. (N)CH_2	1280m	1284s				1306	1270	166.98	6.10
twi. CH_2(O)						1283	1248	0.52	9.40
bend. CNH	1237s	1241vs			1239m	1259	1225	490.38	4.13
i.p. CH ring bend.			1223m	1222m	1221m	1258	1224	25.98	104.18
bend. CH + twi. CH_2(O)				1187vw		1221	1188	1.93	14.78
i.p. CH ring bend. + bend. CH						1209	1176	27.67	11.92
						1198	1166	2.91	7.58
i.p. CH ring bend. + str. CN						1196	1163	44.51	1.73
i.p. CH ring bend.			1156m	1151m	1152m	1188	1156	1.29	21.54
i.p. CH ring bend. + bend. CH						1185	1153	0.07	3.70
bend. COH	1175m	1175m				1183	1151	148.78	2.14

Table B.4: Vibrational assignment of Fmoc-G (continued).

Vibrational Modes	IR (Powders)	IR (AIST.)[1]	Raman (Powders)	Raman (Fibers)	Raman (Lit.)[2]	Frq. Sim.	Frq. Scaled.	Int. IR	Int. Raman
i.p. CH ring bend.			1104m	1104m	1104m	1136	1105	0.00	0.03
	1081m	1081m			1083vw	1129	1098	5.92	24.68
roc. $(N)CH_2$	1055m	1057m	1055w	1051vw	1052vw	1079	1050	63.64	3.40
roc. $CH_2(O)$ + i.p. CH ring bend.						1065	1036	3.69	1.52
aliph. skel. str.	1032w					1063	1034	7.15	5.68
i.p. CCC ring str.			1024s	1021s	1022s	1051	1022	1.04	83.06
roc. $CH_2(O)$	1008m	1010m				1037	1009	3.35	0.50
i.p. CCC ring str.	997m	996m	995w	990w	992vw	1023	996	2.38	1.59
o.o.p. CH ring bend.						991	964	0.02	0.08
						989	962	0.01	0.70
str. (CH)CCO	957w		960vw			986	959	16.94	16.03
roc. $(N)CH_2$ + o.o.p. CH ring bend.	935m		936w	940w	936w	964	938	21.57	3.45
o.o.p. CH ring bend.						951	925	0.04	0.17
	905m			914vw		945	920	9.33	2.14
						886	862	0.11	0.02
			883w		884w	885	861	1.10	2.03
str. CCO(H)			856w	853w	853w	846	824	8.27	17.12
o.o.p. CH ring bend.				820vw		838	815	2.67	3.44
roc. $CH_2(O)$						809	787	1.06	0.18
o.o.p. CH ring bend.			783w	780w	780w	798	777	0.33	3.65
i.p. CCC ring def.						788	767	0.08	2.95
aliph. skel. bend.	757m	757s				773	752	15.99	0.33
o.o.p. CH ring bend.	736s	739vs				755	734	144.24	0.61
						751	731	0.03	2.01
i.p. CCC ring def.			739m	739m	741m	746	726	4.09	25.01
o.o.p. CCC ring def.	694w					731	711	5.45	6.40
tor COH	642m	644m				688	669	80.33	0.83
	622m	622m				670	652	30.28	0.81
i.p. CCC ring def.						635	618	6.78	0.34
aliph. skel. bend.						621	604	28.77	0.83
roc. $CH_2(O)$ +						583	567	0.25	2.25
o.o.p. CCC ring def.									
aliph. skel. bend.			593w			579	563	37.35	2.87
o.o.p. CCC ring def.						571	556	0.04	2.33
aliph. skel. bend.						565	550	30.99	3.21
tor. CNH						519	505	63.57	0.17
tor. CNH + i.p. CCC ring def.			512w		511w	517	503	6.57	3.84
tor. CNH + roc. $(N)CH_2$ +						496	482	18.38	0.71
tor. COH									
o.o.p. CCC ring def.						467	454	1.41	0.24
						454	442	0.20	0.59
						428	416	4.87	0.45
i.p. CCC ring def.			416w	416w	416m	418	407	0.03	6.99
aliph. skel. bend.			385vw		386vw	383	373	5.44	4.01
o.o.p. CCC ring + tor. CCO(C)			310w		312w	304	295	0.35	2.48
tor. CCN						297	289	15.94	0.20
aliph. skel. bend.						289	281	0.56	0.30
tor. CCO(C)						245	238	1.37	1.32
i.p. CCC ring def.						227	221	0.60	1.14
						198	192	0.90	1.96
o.o.p. CCC ring def.						153	149	0.35	0.14
aliph. skel. bend.						141	137	5.19	0.84
o.o.p. CCC ring def.						124	121	0.17	0.17
						90	88	0.47	1.33
aliph. skel. bend.						61	59	4.02	1.81
						48	47	1.61	2.93
						37	36	0.37	2.98
tor. (C)COH						32	31	2.83	4.03
aliph. skel. bend.						17	17	0.02	5.72
						10	10	1.23	1.64

[1] reference IR spectra downloaded from AIST (http://riodb.ibase.aist.go.jp/riohomee.html)
[2] reference Raman spectra downloaded from Sigma-Aldrich (http://www.sigmaaldrich.com)
i.p., in-plane; o.o.p., out-of-plane; sym., symmetric; asym., asymmetric; str., stretching; bend., bending; wag., wagging; twi., twisting; roc., rocking; tor., torsional; def., deformational; skel., skeleton; aliph., aliphatic; s, strong; m, medium; w, weak; v, very; Lit., literature; Int., intensity; Frq., frequency; Sim., simulation; Scaled., the simulation spectra are scaled by 0.973 and 0.964 in frequency for wavenumbers < 2000 cm^{-1} and > 2000 cm^{-1}, respectively.

Table B.5: Vibrational assignment of Fmoc-FG.

Vibrational Modes	IR (Exp.)	Raman (Fibers)	Frq. Sim.	Frq. Scaled.	Int. IR	Int. Raman
str. OH	3320m		3689	3556	82.70	154.92
str. NH(CH) + str. NH(CH_2)			3611	3481	28.18	33.26
			3609	3479	62.47	108.82
str. CH f-ring, str. CH p-ring			3227	3111	0.91	224.59
			3208	3092	19.74	320.66
		3070m	3206	3091	29.63	398.69
			3204	3088	31.19	147.45
			3196	3081	34.44	55.07
	3064vw		3194	3079	31.28	129.53
			3191	3076	8.32	90.57
		3060m	3187	3072	6.73	110.48
			3183	3068	3.40	66.09
			3178	3064	3.85	67.52
			3176	3062	6.29	35.87
			3174	3060	8.63	48.93
			3168	3054	11.34	46.77
asym. str. CH_2(O)	3033m		3143	3030	9.18	29.60
asym. str. CH_2(CO)			3120	3008	4.01	41.33
str. CH(N)			3106	2995	11.31	33.34
sym. str. CH_2(O)			3084	2973	16.46	51.16
asym. str. CH_2(p)		2957m	3072	2962	11.12	53.84
sym. str. CH_2(CO)		2889m	3035	2926	18.42	132.30
sym. str. CH_2(p)			3033	2924	26.32	114.74
str. CH(f)			3030	2921	7.66	115.77
str. CO(OH)	1720m		1835	1785	363.02	15.29
str. CO($OCCH_2$)	1686s		1787	1739	543.88	14.22
str. CO($NHCH_2$)	1655s		1751	1704	268.73	8.50
i.p. CH p-ring bend.			1658	1614	3.61	46.67
i.p. CH f-ring bend.			1656	1611	5.59	20.79
		1616s	1655	1610	0.61	475.17
i.p. CH p-ring bend.			1638	1594	0.79	10.23
i.p. CH f-ring bend.			1632	1588	0.83	2.28
		1585m	1627	1583	1.69	45.15
bend. NH(CH_2)	1536s		1547	1505	305.52	1.58
i.p. CH p-ring bend.			1541	1500	6.04	0.76
sci. CH_2(O)			1524	1483	13.77	7.81
i.p. CH f-ring bend.		1488m	1520	1479	1.11	83.32
i.p. CH f-ring bend. + sci. CH2(O)			1517	1476	1.69	40.95
sci. CH_2(p)			1516	1475	7.47	8.83
sci. CH_2(CO)			1504	1463	2.56	3.14
i.p. CH p-ring bend.			1497	1456	4.12	1.24
i.p. CH f-ring bend.	1450m		1492	1452	27.70	2.59
			1486	1446	6.55	7.06
bend. NH(CH)			1474	1434	33.01	4.57
wag. CH_2(O)	1382w		1432	1394	109.74	1.46
wag. CH_2(CO)			1393	1356	36.86	9.57
i.p. CH f-ring bend.		1352m	1392	1354	0.63	50.37
wag. CH_2(CO) + wag. CH_2(p)			1383	1346	11.96	8.74
bend. CH(N)			1377	1339	5.19	1.54
i.p. CH p-ring bend.			1363	1327	4.09	2.54

Table B.6: Vibrational assignment of Fmoc-FG (continued).

Vibrational Modes	IR (Exp.)	Raman (Fibers)	Frq. Sim.	Frq. Scaled.	Int. IR	Int. Raman
bend. CH(f) + twi. CH_2(O)			1361	1324	5.06	17.04
bend. COH			1357	1321	37.84	4.66
bend. CH(N)			1347	1311	374.08	4.15
bend. CH(f) + twi. CH_2(CO)			1343	1307	50.64	11.01
bend. CH(N)	1262s		1338	1302	222.79	9.84
i.p. CH f-ring bend.		1303m	1330	1294	8.70	152.23
bend. CH(f) + twi. CH_2(O)			1323	1287	0.05	9.93
bend. CH(N) + twi. CH_2(f)			1318	1282	32.54	10.82
twi. CH_2(CO)	1227s		1266	1232	39.26	12.19
twi. CH_2(O)		1239m	1263	1229	2.24	76.30
bend. CH(f) + twi. CH_2(O)			1257	1223	7.37	44.71
bend. $NH(CH_2)$ + twi. CH_2(CO)			1253	1219	14.41	4.11
i.p. CH p-ring bend. + str. C-(p-ring)			1233	1199	4.64	31.42
bend. CH(f)			1223	1190	3.02	14.55
i.p. CH p-ring bend.			1213	1180	1.02	4.23
bend. CH(f)			1209	1176	1.17	12.87
twi. CH_2(p)			1205	1172	21.45	5.41
i.p. CH f-ring bend.			1196	1164	1.50	8.12
i.p. CH p-ring bend.			1191	1159	0.42	3.21
i.p. CH f-ring bend.		1161m	1189	1157	0.36	23.89
sci. COH	1176m		1185	1153	220.58	2.82
i.p. CH f-ring bend.			1184	1152	1.67	4.40
str. HN-CH	1102m		1154	1123	35.47	0.35
str. H-CH_2			1141	1110	8.92	2.05
i.p. CH f-ring bend.			1138	1107	0.38	1.60
		1111m	1128	1098	12.16	22.27
i.p. CH p-ring bend.			1112	1082	12.51	3.80
str. CH_2(O)-(f-ring)			1095	1065	82.61	2.11
str. O-CH_2	1043m		1071	1042	150.44	2.40
i.p. CH f-ring bend.			1060	1031	10.73	0.48
i.p. CH f-ring def.			1055	1027	5.51	23.18
		1029m	1052	1023	3.86	81.16
str. (N)CH-CH_2(p)			1031	1004	18.64	11.54
i.p. CH f-ring def.			1025	997	1.25	2.39
			1022	994	1.19	3.16
		1011m	1018	990	0.99	28.60
roc. CH_2(CO)			1016	988	5.40	7.69
o.o.p. CH f-ring bend.			1003	976	0.55	0.54
o.o.p. CH p-ring bend.			1001	973	0.28	0.08
roc. CH_2(CO) + roc. CH_2(p)	967vw		995	968	8.44	1.22
o.o.p. CH f-ring bend.			991	964	0.01	0.40
o.o.p. CH p-ring bend.			976	950	0.07	0.08
o.o.p. CH f-ring bend.			966	940	1.71	1.30
			956	930	2.74	24.22
			945	920	0.69	25.03
o.o.p. CH p-ring bend.	895w		935	910	12.40	1.14
			915	890	6.60	7.26
o.o.p. CH f-ring bend.			895	870	0.61	0.25
			886	862	0.61	1.97
i.p. CH f-ring def.			863	840	0.46	3.98

Table B.7: Vibrational assignment of Fmoc-FG (continued).

Vibrational Modes	IR (Exp.)	Raman (Fibers)	Frq. Sim.	Frq. Scaled.	Int. IR	Int. Raman
o.o.p. CH p-ring bend.			854	831	0.23	0.68
aliph. skel. bend.			846	823	1.70	2.10
i.p. CH p-ring def.			838	815	1.89	6.36
i.p. CH f-ring def.			808	786	0.38	4.43
			800	779	1.20	2.40
o.o.p. CH f-ring bend.			774	753	25.57	2.11
o.o.p. CH p-ring bend.			772	752	23.74	1.12
o.o.p. CH p-ring bend. + o.o.p. CH f-ring bend.	739s		769	749	53.61	0.68
o.o.p. CH f-ring bend.			758	737	24.85	7.84
			753	733	25.37	7.06
i.p. CH f-ring def.		749w	747	727	11.72	14.90
o.o.p. CH p-ring bend.			741	721	13.39	5.17
	702s		709	690	45.67	0.08
aliph. skel. bend.			699	680	3.49	1.60
tor. COH			684	666	116.57	0.14
tor. COH + aliph. skel. bend.			674	656	3.41	1.81
aliph. skel. bend.			657	639	1.73	0.39
			639	621	13.69	2.03
i.p. CH p-ring def.			635	617	0.98	3.43
i.p. CH f-ring def.			634	617	7.28	0.65
roc. CH_2(O)			596	580	0.20	2.73
aliph. skel. bend.			592	576	53.67	1.32
i.p. CH p-ring def.			578	562	9.04	0.54
o.o.p. CH f-ring def.			574	558	5.04	1.62
tor. NH(CH_2) + tor. NH(CH)			560	544	111.28	0.59
tor. NH(CH_2)			547	532	11.74	2.12
tor. COH + roc. CH_2(CO)			524	509	20.72	3.03
i.p. CH f-ring def.			517	503	3.36	3.81
aliph. skel. bend. + o.o.p. CH p-ring def.			512	498	11.07	1.66
tor. NH(CH_2) + tor. NH(CH)			485	472	38.71	1.10
aliph. skel. bend.			470	457	46.23	2.51
o.o.p. CH f-ring def.			458	427	0.16	0.50
			439	410	8.28	0.18
aliph. skel. bend.			422	407	9.12	0.83
i.p. CH f-ring def.			418	503	2.53	7.61
o.o.p. CH p-ring def.			414	403	0.16	0.11
o.o.p. CH f-ring def.			388	378	5.57	0.55
aliph. skel. bend.			368	358	6.20	0.89
			352	342	0.67	0.13
o.o.p. CH f-ring def.			302	294	2.12	1.54
aliph. skel. bend.			276	269	1.26	1.41
			266	259	1.75	0.75
			259	252	5.70	0.28
			235	229	3.20	4.49
			224	218	5.83	1.89
			202	196	6.64	1.40
			197	192	3.57	1.07
aliph. skel. bend. + i.p. CH f-ring def.			184	180	3.82	1.55
o.o.p. CH f-ring def.			150	146	0.60	0.43
aliph. skel. bend.			138	134	1.49	3.62
			124	121	0.50	0.42
o.o.p. CH f-ring def.			104	101	0.82	0.12
aliph. skel. bend.			95	92	3.46	0.52
			86	83	0.80	2.95
			76	74	10.98	1.62
			61	59	0.53	0.98
			58	57	0.79	3.53
			46	45	1.46	1.39
			33	32	0.20	4.51
aliph. skel. tor.			30	29	2.15	2.47
			29	28	0.38	2.99
			23	23	0.20	2.33
			13	12	0.13	1.64
			10	9	0.08	4.14
			8	8	0.02	4.60

i.p., in-plane; o.o.p., out-of-plane; sym., symmetric; asym., asymmetric; str., stretching; bend., bending; sci., scissoring; wag., wagging; twi., twisting; roc., rocking; tor., torsional; def., deformational; skel., skeleton; aliph., aliphatic; f-ring, fluorenyl ring; p-ring, phenyl ring; s, strong; m, medium; w, weak; v, very; Exp., experiment; Lit., literature; Int., intensity; Frq., frequency; Sim., simulation; Scaled., the simulation spectra are scaled by 0.973 and 0.964 in frequency for wavenumbers < 2000 cm^{-1} and > 2000 cm^{-1}, respectively.

Table B.8: Vibrational assignment of FF.

Vibrational Modes	IR (Exp.)	IR (AIST.)	Raman (Fibers)	Raman (Lit.)	Frq. Sim.	Frq. Scaled.	Int. IR	Int. Raman
str. NH					3616	3533	45.48	122.14
str. NH_3^+					3541	3459	173.89	83.79
str. NH_3^+	3264m	3309s			3430	3351	202.97	191.83
str. NH_3^+					3230	3156	276.72	135.78
str. CH ring	3086vw	3088w			3196	3123	40.78	784.15
			3056s	3054s	3187	3114	82.64	847.69
					3187	3113	83.40	845.93
					3178	3105	70.35	555.59
	3062vw	3063w			3174	3101	99.11	455.17
					3172	3099	83.42	445.84
					3167	3094	46.31	468.27
					3160	3088	33.68	370.75
					3156	3083	30.61	356.06
					3153	3080	27.96	251.87
asym. str. CH_2(CHCOO)	3028vw	3032w			3119	3047	26.80	320.73
str. CH(CON)					3117	3045	24.62	356.73
asym. str. CH_2(CHCON)					3104	3032	19.13	171.68
sym. str. CH_2(CHCOO) + str. CH(COO)			2928m		3074	3003	31.17	326.26
					3068	2998	42.38	525.27
sym. str. CH_2(CHCON)			2855w	2850m	3066	2996	43.26	516.51
str. CO + bend. NH_3^+	1686m	1694s	1684w		1714	1675	287.72	16.80
bend. NH_3^+					1706	1667	131.03	12.93
					1666	1628	33.12	28.88
i.p. CH ring bend.	1612m	1661vs	1605s	1605s	1645	1607	55.96	191.21
					1644	1606	60.41	197.53
					1624	1587	894.95	86.45
i.p. CH ring bend. + asym. str. OCO			1585m	1585m	1623	1586	1012.51	89.96
	1553s				1622	1585	1028.72	85.93
bend. NH	1518m				1585	1548	209.28	14.56
i.p. CH ring bend.	1479m		1501vw	1502w	1533	1497	46.39	4.56
					1531	1495	46.43	4.38
bend. NH_2^+	1454w				1508	1473	468.30	21.54
sci. CH_2(CHCOO)	1431w		1443w	1454w	1502	1467	264.87	24.41
sci. CH_2(CHCON)					1501	1466	240.69	22.81
sci. CH_2(CHCON) + i.p. CH ring bend.	1387s	1387w			1487	1453	36.81	8.65
sci. CH_2(CHCOO) + i.p. CH ring bend.					1484	1450	28.49	8.11
bend. CH(CON)					1415	1382	21.83	13.56
bend. CH(COO) + roc. CH_2(CHCON)					1404	1372	54.08	23.90
	1353w				1401	1369	54.19	32.07
bend. CH(COO) + i.p. CH ring bend.					1370	1338	36.88	8.40
					1369	1338	36.88	8.40
bend. CH_2(CHCOO) + i.p. CH ring bend.					1353	1322	269.08	39.51
	1255m	1261s			1348	1317	350.08	45.49
twi. CH_2(CHCON) + i.p. CH ring bend.					1341	1311	119.45	22.37
bend. CH(COO) + i.p. CH ring bend.					1329	1298	25.76	23.67
bend. CH(CON)					1317	1287	24.19	48.72
bend. CH(CON) + bend. NH					1293	1263	164.20	34.23
bend. CH(COO)			1206s	1208m	1270	1240	20.91	58.87
bend. CH(CON) + twi. CH_2(CHCON)					1245	1217	36.08	11.55
i.p. CH ring bend.					1223	1194	6.12	100.10

Table B.9: Vibrational assignment of FF (continued).

Vibrational Modes	IR (Exp.)	IR (AIST.)[1]	Raman (Fibers)	Raman (Lit.)[2]	Frq. Sim.	Frq. Scaled.	Int. IR	Int. Raman
i.p. CH ring bend.					1220	1192	6.53	99.38
twi. CH_2(CHCOO) + i.p. CH ring bend.					1219	1191	6.38	90.93
i.p. CH ring bend.					1207	1179	3.93	20.85
					1202	1174	3.16	12.48
					1182	1155	2.91	11.67
					1178	1151	3.04	11.29
bend. NH_3^+			1091w		1141	1115	113.35	14.80
					1126	1100	29.38	12.56
bend. NH_3^+ + i.p. CH ring bend.					1114	1088	36.13	5.96
i.p. CH ring bend.					1107	1082	27.53	5.92
					1098	1073	21.09	9.48
					1054	1030	10.77	46.78
			1033s	1034s	1050	1026	18.84	66.92
					1047	1023	15.52	46.52
i.p. CH ring def. + wag. CH_2(CHCOO)			1004s	1000vs	1029	1005	21.01	40.37
i.p. CH ring def.					1017	994	5.46	184.00
					1016	993	5.19	193.48
o.o.p. CH ring bend.					1013	990	3.94	126.61
					1002	979	2.23	16.41
					993	971	2.65	8.31
					982	959	2.78	4.65
skel.					963	941	31.07	21.11
o.o.p. CH ring bend.					944	922	28.60	30.32
o.o.p. CH ring bend. + skel.			874m		942	920	31.30	31.78
o.o.p. CH ring bend.					926	905	12.37	11.69
skel.	833m				906	885	26.60	8.74
wag. CH_2(CHCOO) + skel.					875	854	26.29	30.02
o.o.p. CH ring bend. + skel.			824m		871	851	17.57	35.40
o.o.p. CH ring bend.					866	846	7.78	19.68
					857	838	3.56	13.00
i.p. CH ring def. + skel.					828	809	42.97	24.64
					823	804	19.81	28.26
o.o.p. CH ring bend. + skel.	747s	748s			771	754	63.49	18.98
o.o.p. CH ring bend.					767	750	61.49	31.06
					757	740	68.95	15.22
o.o.p. CH ring bend. + skel.	729s				750	733	74.94	13.82
o.o.p. CH ring bend.					717	701	82.94	1.08
	700s	698s			711	695	97.57	1.19
o.o.p. CH ring bend. + skel.	656m				656	641	54.46	4.16
i.p. CH ring def. + skel.					638	623	10.81	17.25
i.p. CH ring def.			621m		636	621	11.43	18.04
i.p. CH ring def. + skel.					631	617	14.12	13.41
bend. NH + skel.					612	598	38.55	6.46
					593	580	91.32	5.45
					579	566	30.91	2.23
skel.					555	542	39.13	4.89
i.p. CH ring def. + skel.			484w		492	481	23.97	10.79
o.o.p. CH ring bend.					489	477	22.73	8.08
skel.					451	441	13.49	3.64
					431	421	13.49	3.17
o.o.p. CH ring def.					421	411	16.06	1.02
					415	406	13.39	0.88
Multiple combinations					403	394	88.69	3.51
					381	372	30.22	0.75
wag. CH_2(CHCOO)					346	338	5.03	1.83
Multiple combinations					336	329	16.93	2.73
					332	325	19.28	3.29
bend. NH_3^+					264	258	28.52	3.87
Multiple combinations					229	224	9.38	4.27
bend. NH_3^+					221	216	15.79	2.81
Multiple combinations					209	204	14.41	3.04
					153	149	6.28	3.66
					146	142	5.56	1.56
					101	98	26.53	5.18
					96	94	20.34	8.31
					90	88	9.50	5.63
					62	61	20.84	6.81
					53	52	20.47	12.96
					48	47	17.15	17.96
					47	46	16.37	16.57
					34	33	4.80	5.40
					22	21	5.53	5.22
					16	15	12.84	5.82

[1] reference IR spectra downloaded from AIST (http://riodb.ibase.aist.go.jp/riohomee.html)

[2] G. Singh, A.M. Bittner, S. Loscher, N. Malinowski, K. Kern. Electrospinning of Diphenylalanine Nanotubes, *Adv. Mater.* **20**: 2332-2336, 2008.

i.p., in-plane; o.o.p., out-of-plane; sym., symmetric; asym., asymmetric; str., stretching; bend., bending; sci., scissoring; wag., wagging; twi., twisting; roc., rocking; tor., torsional; def., deformational; skel., skeleton; s, strong; m, medium; w, weak; v, very; Exp., experiment; Lit., literature; Int., intensity; Frq., frequency; Sim., simulation; Scaled., the simulation spectra are scaled by 0.977 in frequency.